

Measuring and Modeling Interactions Between Groundwater, Soil Moisture, and Plant
Transpiration in Natural and Agricultural Ecosystems

by

Gretchen Rose Miller

B.S. (University of Missouri, Rolla) 2002

M.S. (University of Missouri, Rolla) 2003

A dissertation submitted in partial satisfaction of the

requirements for the degree of

Doctor of Philosophy

in

Engineering-Civil and Environmental Engineering

in the

GRADUATE DIVISION

of the

UNIVERSITY OF CALIFORNIA, BERKELEY

Committee in Charge:

Professor Yoram Rubin, Co-chair

Professor Dennis Baldocchi, Co-chair

Professor Fotini Katopodes Chow

Professor Gregory Biging

Spring 2009

The dissertation of Gretchen Rose Miller is approved:

Co-chair Date

Co-chair Date

Date

Date

University of California, Berkeley

Spring 2009

Measuring and Modeling Interactions Between Groundwater, Soil Moisture, and Plant
Transpiration in Natural and Agricultural Ecosystems

© 2009

by Gretchen Rose Miller

Abstract

Measuring and Modeling Interactions Between Groundwater, Soil Moisture, and Plant
Transpiration in Natural and Agricultural Ecosystems

by

Gretchen Rose Miller

Doctor of Philosophy in Engineering – Civil and Environmental Engineering

University of California, Berkeley

Professor Yoram Rubin, Co-chair

Professor Dennis Baldocchi, Co-chair

Plant transpiration serves a critical function in the terrestrial hydrologic cycle, acting as the primary link between the atmosphere and subsurface stores of water. To properly manage our water resources under changing and uncertain climate conditions, we will first need to understand the complex interactions and feedbacks between vegetation, soil moisture, groundwater, and the atmosphere. This dissertation focuses on measuring and modeling the flow of water through these connections.

The primary study site is a semi-arid oak savanna in California, located in the foothills of the Sierra Nevada. Here, a suite of tree and stand scale ecohydrological measurements are collected. The measurements, taken at half-hourly to biweekly intervals over the 2007 and 2008 growing seasons, include individual tree transpiration (from sap flow), stand evapotranspiration (using the eddy-covariance method), soil moisture content, soil and leaf water potential, tree diameter, stable isotope ratios, and depth to groundwater. This work develops and tests a novel method for locating the sap

flow and soil moisture sensors – based on a geostatistical analysis and an artificial intelligence algorithm. It uses the resulting data to quantify the proportion of evapotranspiration due to groundwater uptake by woody vegetation, finding that the blue oaks at the site are heavily dependent on deep sources of water during the dry summer months.

Two modeling studies explore the dynamic relationships between soil moisture, vadose zone processes, evapotranspiration, and groundwater recharge. The first tests the applicability of an analytical, stochastic soil moisture model to the data from the oak savanna and several other micrometeorological sites. It illustrates the importance of understanding the relationship between soil moisture and the onset of plant stress and notes the benefits and drawbacks to using simple, point models of the water budget. The second uses a numerical, reactive flow and transport code to describe the application of food-processing wastewater to agricultural lands in California's Central Valley. It indicates that the biosphere and its control over the nitrogen-carbon-oxygen system may highly influence salinity attenuation, demonstrating the necessity of including multiple plant, soil, and microbial processes in order to capture the complexity of their interactions.

Professor Yoram Rubin
Dissertation Committee Co-Chair

Professor Dennis Baldocchi
Dissertation Committee Co-Chair

To my family

Table of Contents

Chapter 1: Introduction	1
Chapter 2: Soil Moisture Dynamics at AmeriFlux Sites	7
2.1 Introduction.....	7
2.2 Description of Sites.....	9
2.3 Methods	12
2.3.1 Data Collection	12
2.3.2 Data Analysis	13
2.3.3 Model Description	16
2.3.4 Model Application and Modifications	21
2.3.5 Model Parameter Estimation.....	23
2.3.6 Model Testing and Calibration	29
2.3.7 Forward Predictions Using the Soil Moisture Dynamics Model	31
2.4 Discussion.....	34
2.4.1 Water Content Time Series and Histograms.....	34
2.4.2 Hydraulic Redistribution.....	38
2.4.3 Inverse Soil Texture Effect	40
2.4.4 Probability Density Functions.....	41
2.4.5 Soil Moisture Under Climate Change Scenarios	43
2.5 Conclusions.....	46
Chapter 3: Hydrogeological Characterization of Tonzi Ranch.....	50
3.1 Introduction.....	50
3.2 Soils	51
3.3 Geology and Geochemistry	56
3.4 Hydrogeology	61
3.5 Summary	70
Chapter 4: Groundwater Uptake in a Semi-Arid Oak Savanna	73
4.1 Introduction.....	73
4.2 Data Collection	77
4.2.1 Site Description.....	77

4.2.2 Hydrological Measurements	79
4.3 Data Analysis.....	82
4.3.1 Uptake from Groundwater Measurements.....	83
4.3.2 Stand-level Uptake from Water Balance Closure.....	86
4.3.3 Tree-level Uptake from Water Balance Closure.....	88
4.3.4 Water Potential Data	89
4.3.5 Stable Isotope Analysis.....	92
4.4 Results and Discussion	93
4.4.1 Groundwater Uptake from Hydrological Measurements.....	93
4.4.2 Evidence of Uptake in Water Potential.....	107
4.4.3 Isotopic Signature of Soil Water versus Groundwater	109
4.5 Conclusions.....	110
Chapter 5: Upscaling Transpiration from Sap Flow Measurements.....	112
5.1 Introduction.....	112
5.2 Methods	116
5.2.1 Site Description and Characterization	116
5.2.2 Design of a Sap Flow Sensor Network	118
5.2.3 Upscaling from Tree to Stand Transpiration.....	127
5.3 Results and Discussion	131
5.3.1 Sap Flow by Cluster and Season.....	131
5.3.2 Cluster Selection: Was it Representative of the Study Area?.....	134
5.3.3 Is the Tower Footprint Representative of the Study Area?.....	140
5.3.4 Comparison of the Tower and Sap Flow Stand Transpiration.....	142
5.4 Conclusions and Future Work	149
Chapter 6: Plant Water and Solute Uptake in Wastewater Recharge.....	152
6.1 Introduction.....	152
6.2 Methods	154
6.2.1 Conceptual Model.....	154
6.2.2 Scenario Development.....	161
6.2.3 Numerical Modeling	164
6.3 Results and Discussion	173

6.3.1 Nitrogen Compounds	174
6.3.2 Salinity Reaching the Water Table	177
6.3.3 Comparison to Groundwater Data	181
6.3.4 Root Zone Soil Salinity	183
6.3.5 Model Sensitivity Analysis	187
6.3.6 Application to Additional Industries	192
6.4 Conclusions	194
Chapter 7: Summary	196
References	202
Appendix A: Tonzi Ranch Maps	221

List of Figures

Figure 2.1: Average Water Content at Studied Sites	14
Figure 2.2: Soil Moisture Depth-averaging Methods	17
Figure 2.3: Soil Water Loss Function for Water-stressed Environments	19
Figure 2.4: Water Retention Curve for Silt Loam	20
Figure 2.5: Soil Moisture as a Function of Depth.....	36
Figure 2.6: Measured versus Modeled Histograms	37
Figure 2.7: Diurnal Fluctuations in Soil Moisture	39
Figure 2.8: Soil Moisture Distributions Under Climate Change	44
Figure 3.1: Soil Texture at Tonzi Ranch.....	52
Figure 3.2: Bulk Soil Properties at Tonzi Ranch	53
Figure 3.3: Water Retention Curve for Tonzi Ranch Soils.....	54
Figure 3.4: Soil Hydraulic Conductivity Curve.....	56
Figure 3.5: Geologic Map of the Tonzi Ranch Area	58
Figure 3.6: Rock Outcrops at Tonzi Ranch	59
Figure 3.7: Well Locations and Hydrologic Features.....	62
Figure 3.8: Profiles from Supply Wells	63
Figure 3.9: Profiles from Monitoring Wells	64
Figure 3.10: Drawdown and Recovery during Slug Tests	66
Figure 3.11: Normalized Head during Slug Tests	67
Figure 3.12: Understory Well Hydraulic Conductivity as a Function of Depth.....	71

Figure 4.1: Tonzi Ranch Site Map.....	79
Figure 4.2: Temporal Patterns of Water Flux and Storage.....	83
Figure 4.3: Water Balance at the Stand and Tree level.....	87
Figure 4.4: Annual Variation in Water Balance.....	94
Figure 4.5: Groundwater Uptake from Stand Water Balance.....	96
Figure 4.6: Annual Variation in Percentage of ET from Groundwater Uptake.....	98
Figure 4.7: Diurnal Groundwater Fluctuations.....	100
Figure 4.8: Correlation between Groundwater Uptake and Meteorological Variables .	101
Figure 4.9: Daily and Monthly Groundwater Uptake from Fluctuation Method.....	103
Figure 4.10: Groundwater Uptake from Tree Level Water Balance.....	106
Figure 4.11: Water Potential Across the GSPA Continuum.....	108
Figure 5.1: Site Characterization Maps.....	119
Figure 5.2: Sap Flow Monitoring Station.....	120
Figure 5.3: Maps of Tree Locations, Size, and Cluster Membership.....	124
Figure 5.4: Sapwood Area.....	126
Figure 5.5: Example Flux Footprints for Tonzi Site.....	130
Figure 5.6: Cluster Sap Flow.....	132
Figure 5.7: Relationship between Nighttime Sap Flow and Vapor Pressure Deficit.....	134
Figure 5.8: Statistical Distribution of Tree Diameter and Cluster Soil Moisture.....	136
Figure 5.9: Comparison of Sap Flow from Midsize Trees.....	137
Figure 5.10: General Linear Model of Sap Velocity.....	139

Figure 5.11: Proportion of Footprint Covered by Trees	141
Figure 5.12: Hourly Stand Transpiration for Selected Periods.....	143
Figure 5.13: Daily Stand Transpiration	145
Figure 5.14: Comparison of Inner and Outer Sap Velocity Rates	148
Figure 6.1: Conceptual Model of Land Application.....	156
Figure 6.2: Footprint Analysis of Selected Wine and Grape Processors.....	165
Figure 6.3: Breakthrough Curves of Contaminants Reaching the Water Table	174
Figure 6.4: Nitrogen Mass Balance for Wine and Grape Industry	175
Figure 6.5: FDS Mass Balance for Wine and Grape Industry	178
Figure 6.6: Fraction of FDS Contributed by Individual Components	179
Figure 6.7: FDS and Nitrates Measured in Groundwater	183
Figure 6.8: 30-year Simulated Soil Salinity for Scenario 2	185
Figure 6.9: Year 10 Simulated Soil Salinity Levels	186

List of Tables

Table 2.1: Site Characteristics	11
Table 2.2: Precipitation Patterns.....	24
Table 2.3: Soil Characteristics and Critical Soil Moisture Points	26
Table 2.4: Mean Potential and Actual Evapotranspiration	28
Table 2.5: Degree of Saturation at Stress Point	42
Table 3.1: Soil Properties at the Tonzi Ranch Site.....	52
Table 3.2: Distributed Soil Texture and Density Measurements.....	52
Table 3.3: Geochemical Analysis of Greenstone.....	60
Table 3.4: Tonzi Ranch Well Completion Data.....	65
Table 3.5: Hydraulic Conductivity	69
Table 3.6: Slug Test Results in Understory Well	70
Table 4.1: Daily Uptake from Groundwater Fluctuations for July 2007.....	101
Table 4.2: Comparison of Groundwater Uptake Method	105
Table 4.3: Oxygen Isotope Ratios ($\delta^{18}\text{O}$ in ‰) for Water in Ecosystem.....	110
Table 5.1: Results of Cluster Analysis.....	123
Table 5.2: Weight of Cluster Contribution to Canopy Area.....	142
Table 6.1: Concentration Ranges in Wastewater by Industry.....	155
Table 6.2: Biogeochemical Reactions and their Parameters.....	157
Table 6.3: Overview of Scenarios.....	162
Table 6.4: Water Balance at Hypothetical Discharge Site.....	168

Table 6.5: Model Input Concentrations for Wine and Grape Processors	170
Table 6.6: Active Root Uptake Parameters.....	172
Table 6.7: Ten Most Influential Model Parameters for Scenarios 1 and 2.....	190

Acknowledgements

I would first like to sincerely thank my advisors, Professors Yoram Rubin and Dennis Baldocchi. Their guidance has been invaluable; their wisdom, creativity, and dedication inspiring. I am particularly grateful that they allowed me the freedom to explore all the possibilities in my research while gently steering me in the most fruitful of directions. I would also like to thank the other faculty members who have contributed to the success of my career here at Berkeley: my dissertation committee members, Professors Tina Chow and Greg Biging; my exam committee members, Professors John Dracup, Jim Hunt, and Mark Stacey; and my numerous classroom instructors.

I would next like to acknowledge my graduate student colleagues, who have, by turns, been supporters, mentors, co-conspirators, and field hands, particularly Felipe de Barros, Pascual Benito, Xingyuan Chen, Jenny Druhan, Zhangshuan Hou, Jessica Osuna, Youngryel Ryu, and Ben Runkle. Of these, I perhaps owe the largest debt of gratitude to Xingyuan Chen, who has contributed much to this work, through long discussions, brainstorming, and, of course, sap flow sensor assembly. Her excellent work on sap flow sensor calibration and inverse modeling of ecohydrological processes have been very useful to this research.

Next, I would like to thank my family. My husband, Joe Miller, who has the disposition and patience of a saint, unfailingly supported me during this process. My parents, Linda and Gary Gawer, who kindled my love of science and education, have been the best of cheerleaders. I would also like to thank my grandmother, Rita Gawer

for her continued encouragement and prayers, and my grandparents Rosie and Elroy Pfautsch, who urged me to start a Ph.D. but were sadly unable to see me finish it.

Research is not done in a vacuum (unless speaking literally), and as such, there have been many scientific contributors to this work. I would like to acknowledge them here: Ted Hehn, Joe Verfaillie, and Dave Ball for technical and field support; Siyan Ma, Rodrigo Vargas, and Liukang Xu for kindly sharing their data; Stefania Mambelli, Todd Dawson, and Aline Sengchannavong for their stable isotope data, training, and lab support; Qi Chen for access to his Lidar data and his advice on using it; and Slav Hermanowicz, Jatal Mannapperuma, John McLaughlin, Dennis Corwin, David Russo, and Gia Destouni for advice and data related to the Central Valley salinity project. Mr. Russell Tonzi deserves much appreciation for the use of his land for this research and for his advice on locating and drilling wells. I would also like to thank the following for their administrative and moral support: Shelly Okimoto and the CEE Academic Affairs Office and Mariko Yasuda and the Engineering Research and Support Office.

Now, the financial and copyright matters: This material is based upon work supported under a National Science Foundation Graduate Research Fellowship and a Jane Lewis Fellowship from the University of California, Berkeley, both awarded to the author. Additional support has been provided by the US Department of Energy's Terrestrial Carbon Project (DE-FG02-03ER63638) in the form of a grant to Dennis Baldocchi, a National Science Foundation grant to Yoram Rubin, and an American Geophysical Union Horton Research grant to Xingyuan Chen.

Portions of this dissertation have been reprinted, with permission, from previously published materials. “Chapter 2: Soil Moisture Dynamics at AmeriFlux Sites” has been reprinted from *Advances in Water Resources*, 30(5), Gretchen R. Miller, Dennis D. Baldocchi, Beverly E. Law, and Tilden Meyers, “An analysis of soil moisture dynamics using multi-year data from a network of micrometeorological observation sites,” pages 1065-1081, Copyright 2007, with permission from Elsevier. “Chapter 6: Plant Water and Solute Uptake in Wastewater Recharge” has been reprinted from the *Journal of Environmental Quality*, 37(5), Gretchen R. Miller, Yoram Rubin, K. Ulrich Mayer, and Pascual H. Benito, “Modeling Vadose Zone Processes during Land Application of Food-Processing Waste Water in California's Central Valley,” pages S43-S57, Copyright 2008, with permission from ASA-SSSA-CSSA Journals.

Chapter 1: Introduction

The focus of this research is, at its heart, ecohydrology, defined here as the study of the movement, storage, and quality of water, as it controls and is controlled by vegetation. Very broadly, ecohydrology concerns itself with questions like:

- How do plants regulate water and respond to water stress? What mechanisms do they use to control their water usage? How do they compete with each other for water resources?
- What impact will climate and land use change have on terrestrial and aquatic ecosystems? How will changing precipitation regimes influence the distribution and ranges of ecosystems?
- Can we allocate water to sustain both human consumption and natural ecosystems? What services do ecosystems provide and can we assign a monetary value to these services?

We know that precipitation acts as a main external driver of ecosystems, with the amount and timing of rain and snowfall being critical to which plants and animals can survive and flourish in a region. Precipitation is inarguably a well studied phenomenon, with individual meteorological stations recording its temporal patterns and radar able to remotely detect its large scale spatial distribution.

Conversely, plant transpiration serves as the primary mechanism for vegetative control of water by transferring water stored in the subsurface to the atmosphere. Transpiration, and its relatives soil and water surface evaporation, form a predominant portion of the global water balance, returning almost two-thirds of precipitation that falls

over land masses to the atmosphere [Dingman, 2002]. Although its contribution is dramatic, in traditional hydrology, evapotranspiration (ET) has often simply been estimated from easier to measure variables of precipitation (P), runoff (R), and infiltration (I), combined with the water balance equation [Brutsaert, 2005]:

$$P - R - I = ET \quad (1.1)$$

Understanding and accurately predicting evapotranspiration is necessary for water resources management, especially under an uncertain climatic future. One key unknown is the how ET will be affected by global climate change: will increasing temperatures “ramp-up” the hydrological cycle and increase ET [Huntington, 2006], or will a CO₂ enriched atmosphere lead to more efficient water use by plants [Gedney *et al.*, 2006] and cause it to decline? Much depends on the feedbacks that are considered by global climate models [Betts *et al.*, 1997]. While these models show agreement in their precipitation predictions for polar and equatorial regions, they often predict vastly different responses by the water cycle in key mid-latitude areas [Bates *et al.*, 2008]. Will these places begin to experience drought while others have newfound surpluses? How will the quantity and timing of precipitation change, and how will this change affect the natural vegetation and agricultural production? Adequately modeling plant transpiration, with appropriate soil and atmospheric feedbacks, continues to be key to answering these questions.

Two complementary approaches to ecohydrology have attained recent prominence in the literature. The first approach, typically referred to as environmental biophysics or biometeorology, centers around the “biophysical relationships between ambient climate and the form and function of the associated vegetation” [Eagleson,

2002]. Work in this area began with the studies of agricultural sites, progressed to observations of forested environments, and then on to measurements of dry-land ecosystems. This approach primarily uses the energy budget equation:

$$R_n = H + \lambda E + G - M \quad (1.2)$$

where R_n is the net radiation absorbed by the earth's surface; H is turbulent sensible heat exchange, heat exchanged due to temperature differences in air parcels; λE is turbulent latent heat exchange, energy lost due to the evaporation of water; G is the sensible heat transfer to soil; and M is the metabolism of energy for photosynthesis [Campbell and Norman, 1998]. The traditional tool of this method is the micrometeorological measurement station, operated by individual scientists, but standardized and networked by FLUXNET [Baldocchi *et al.*, 2001]. These stations include: high-frequency wind speed and direction gauges, air and soil temperature sensors, gas analyzers to measure CO₂ and H₂O concentrations in air, relative humidity sensors, and soil moisture probes. While this scientific community has developed around the measurement of carbon fluxes in order to address climate change problems, its contribution to the understanding of ecohydrology and the role of water-stress in ecosystem productivity cannot be overstated.

The second approach focuses on soil moisture, the primary reservoir for water available to vegetation and the “key variable synthesizing the action of climate, soil, and vegetation on the water balance” [Rodríguez-Iturbe and Porporato, 2004]. These methods rely heavily on dynamic models of the water budget at the land surface, first introduced by Eagleson's series of papers [Eagleson, 1978a; b; c] and much later refined significantly by Rodríguez-Iturbe and Porporato, in their recent papers and books [Laio

et al., 2001; *Rodriguez-Iturbe et al.*, 1999; *Rodriguez-Iturbe and Porporato*, 2004]. The defining equation of this technique is the water balance at a point in the soil, often referred to as the bucket model:

$$nZ_r \frac{ds(t)}{dt} = R(t) - I(t) - Q[s(t), t] - E[s(t)] + L[s(t)] \quad (1.3)$$

where n is the soil porosity, Z_r is the root zone depth, s is the soil moisture (its volumetric water content normalized by porosity, making it soil saturation), R is precipitation, I is infiltration, Q is runoff, E is evapotranspiration, and L is leakage. These terms are all time dependent, as noted by the (t) , and some are additionally dependent on the soil moisture at a given time, denoted as $s(t)$. Since rainfall must be described as a random process, the equation is treated stochastically and is generally transformed into a probability density function for soil moisture. Once developed, this framework was applied to model nutrient cycling [*D'Odorico et al.*, 2004], photosynthesis dynamics [*Daly et al.*, 2004], and vegetative response to climate change [*Porporato et al.*, 2004]. While fairly robust, this approach may be limited by its lack of spatial considerations.

With this work, I would like to highlight a third, previously underemphasized realm of investigation in ecohydrology – groundwater. The first approach, the land surface energy balance developed by meteorologists and ecophysicists, is primarily atmos-centric in its philosophy, using an advanced toolset developed to study atmospheric fluxes and meteorological patterns. The second approach, with its stated focus on the soil moisture component of the subsurface water balance, takes its cues from the soil physics community, using principles like soil matric potential and soil

texture to describe the influence of the shallow subsurface on plants. While both perspectives are highly valuable, they essentially do not consider processes occurring more than a meter below the surface of the earth, despite the interconnected nature of the terrestrial water cycle. This raises the question: what techniques and viewpoints can the field of hydrogeology contribute?

In the first chapter, I explore the soil moisture dynamics in four different field sites, asking: How broadly can current probabilistic models of soil moisture be applied to ecosystems? What major constraints does the water balance at a point have? How do these affect the efficacy of the probabilistic soil moisture model? At one of these sites, I find that the models do not accurately predict soil moisture patterns; the conceptual model of the water balance in the California oak savanna must somehow be incomplete.

Focusing on this site, the Tonzi Ranch, the next two chapters aim to confirm the suspected source of this discrepancy – the uptake of groundwater by woody vegetation. In Chapter 3, I characterize the subsurface at the site, asking what is known about the soils and geology, and making measurements and observations to supplement the literature. The main findings presented in this chapter are fundamentals about the site's groundwater system: the type of rocks hosting the groundwater, their hydraulic conductivity, and the depth to the groundwater table.

In Chapter 4, I use this information, along with two years of nearly continuous field data, to directly and indirectly demonstrate that the blue oaks at the site reach and rely on stores of water 10 meters or more below the surface. After spring rains cease, the trees rapidly deplete their soil moisture supplies, and groundwater becomes the more accessible source of moisture. During very dry summer months, 80 to 100% of the

water transpired by the trees comes from groundwater. This finding implies that the response of blue oaks to reduced precipitation regimes may be less dramatic than anticipated, if their access to groundwater does not change.

Chapter 5 uses geostatistical techniques, familiar to the groundwater community, to improve the measurement of water vapor fluxes from individual trees. Here, I present the design of a sap flow monitoring system that incorporates existing information about tree and soil properties at the site. The system allows for the strategic upscaling of point to stand scale water fluxes in a unique manner – by locating sensors on the most representative trees, a priori.

Finally, in Chapter 6, I present an engineering application of ecohydrology that explores how plants can influence groundwater quality. This work addresses a practical problem: the application of food processing wastewater for the irrigation of cropland in the Central Valley. Does this practice negatively impact groundwater immediately below the discharge site or does land application work as effective bioremediation? Which discharge practices, such as maintaining oxygenated conditions, growing salt tolerant crops, or selecting for specific site properties, have the largest impact on groundwater? In order to answer these questions, I use a geochemical fate and transport model, developed for groundwater remediation, adding in the consideration of vegetation, particularly how crops uptake the applied water and the plant nutrients it contains. The results demonstrate the importance of plant activity in such systems, as well as the influence of the microbial ecosystems contained within the soil and groundwater.

Chapter 2: Soil Moisture Dynamics at AmeriFlux Sites¹

2.1 Introduction

The complex interactions between soil, vegetation, and the atmosphere play critical roles in the global hydrologic cycle and the functioning of ecosystems. Mounting evidence suggests that these interactions play a larger role in regulating atmospheric conditions than initially assumed. As more sophisticated climate models are being developed, researchers are becoming increasingly aware of the critical role of soil water availability in simulating water fluxes over land surfaces [Feddes *et al.*, 2001]. Models that do not consider the impacts of rainfall pulses and precipitation regime changes on evapotranspiration [Porporato *et al.*, 2004] and total ecosystem respiration [Xu *et al.*, 2004] will not accurately model the accompanying climatic responses. Spatial and temporal variations in soil moisture can have a lasting impact on climate factors such as precipitation [Pielke, 2001], and the inclusion of sub-grid scale soil moisture heterogeneity can improve the performance of global climate models [Gedney and Cox, 2003]. Numerous soil moisture models have been developed in an attempt to quantify and predict fluxes through the Soil-Plant-Atmosphere Continuum (SPAC). Accurate models should, in some manner, account for all components of the terrestrial water balance: precipitation, evaporation, transpiration, runoff, leakage, and storage. Portions of the balance have well-defined models: the Richards equation (and its various analytical solutions) for the flow of water in the vadose zone [Hillel, 1998], the Penman-

¹ This chapter is reprinted, with permission, from the original journal article: Miller, G. R., D. D. Baldocchi, B. E. Law, and T. Meyers (2007), An analysis of soil moisture dynamics using multi-year data from a network of micrometeorological observation sites, *Adv. Water Resour.*, 30(5), 1065-1081.

Monteith equation for evaporation [Mcnaughton and Jarvis, 1984], and the Poisson arrival process for rainfall [Onof *et al.*, 2000]. The main difficulty remains in uniting the models of these various components. Several solutions have been tendered, including a notable probabilistic method originally proposed by Rodriguez-Iturbe *et al.* [Rodriguez-Iturbe *et al.*, 1999] and improved in a series of papers by Laio *et al.* [Laio *et al.*, 2001]. Daly and Porporato provide a review of current research into soil moisture dynamics and emphasize its control on meteorological process, soil biogeochemistry, plant conditions and nutrient exchange [Daly, 2005].

Micrometeorological measurement sites record half-hourly exchanges of carbon dioxide, water vapor, and energy between the biosphere and the atmosphere, as well as state variables such as temperature and vapor pressure deficit. In the past, information about soil moisture at these sites was obtained by laboratory analysis of soil samples or from daily to biweekly measurements taken using in-situ soil moisture probes. These methods have drawbacks, namely low temporal resolution and/or high labor requirements. However, sites within the global FLUXNET community and the AmeriFlux network of research sites in the Americas are being encouraged to collect continuous measurements of soil moisture, reportable in half-hour or hourly increments that correspond to energy and trace gas flux measurements. These types of measurements are well-suited for comparison to models that predict soil moisture dynamics at a single point.

FLUXNET provides a unique opportunity to examine ecological trends at a variety of sites, allowing analysis to be performed across functional types and climates. The climate gradient and range of vegetation seen by the flux network is wide. Several

recent, multi-site studies have been conducted that use the network to investigate broader topics, such as bud-break timing [*Baldocchi et al.*, 2005] and soil-respiration [*Hibbard et al.*, 2005]. AmeriFlux sites have been collecting soil moisture data for several years; however, no studies have yet examined soil moisture dynamics across a range of sites.

In this study, we present an analysis of soil moisture dynamics at four AmeriFlux sites in the continental United States. We use an ecohydrological model [*Laio et al.*, 2001] to find a probabilistic description of soil moisture dynamics at each site. We detail several methods for parameter estimation and a technique for calibrating the model to match the measured data. We then incorporate predictions of future precipitation patterns and evapotranspiration into the calibrated model to examine the shifts in the soil water balance that may occur due to global climate change.

2.2 Description of Sites

Four sites with a range of climate, vegetation, and soil type were selected for analysis. Only sites that listed soil type and collected half-hourly soil moisture data for at least two years were included. While half-hourly soil moisture is listed as a core AmeriFlux measurement, the majority of AmeriFlux sites do not measure and/or report soil moisture values at this temporal resolution. Although many sites collect it on a weekly or biweekly basis, shorter measurement intervals are necessary to fully capture the response to precipitation events and the accompanying wetting and drying cycles.

Data for each site was obtained from the AmeriFlux network of ecosystem observation towers [*AmeriFlux*, 2005]. Table 2.1 lists key characteristics for each site. The following data were included in the analysis: rainfall events and net radiation for

each year as gauged at the AmeriFlux station, soil type and grain size distribution as listed in AmeriFlux site information, and half-hourly soil moisture measurements.

The Tonzi and Vaira Ranch sites are located near Ione, CA, in the lower Sierra Nevada Foothills [*Baldocchi et al.*, 2004]. Tonzi is an oak savanna woodland while Vaira is an annual C3 grassland. The sites are located within 2 km of each other and share a similar Mediterranean climate, with a mean annual temperature of 16.6 °C and mean annual precipitation of around 560 mm y⁻¹ [*Baldocchi et al.*, 2004]. These two stations are similar enough climatically to be regarded as one study site, but are distinguished here due to the difference in their vegetation. The Walker Branch watershed site is a mixed deciduous forest located near Oak Ridge, TN. It has a temperate climate with mean annual precipitation of 1333 mm and an average temperature of 14.4 °C [*Wilson et al.*, 2001]. The Metolius site is an intermediate age ponderosa pine forest located in the eastern Cascade Mountains near Sisters, OR. It has a temperate climate, with a mean annual precipitation of approximately 360 mm y⁻¹ and a mean annual temperature of 7 to 8 °C [*Schwarz et al.*, 2004]. It is the only one of the four sites that receives a substantial amount of snow, which affects soil infiltration patterns during the winter. Precipitation data is collected at all sites using a tipping bucket, which is adapted to measure snowfall at Metolius.

Each site has different seasonal patterns (Table 2.1). At Walker Branch, the trees are active during the spring and summer, typical of deciduous forests. The Vaira Ranch primarily supports grasses, which are active during the wet, winter months of its Mediterranean climate. In addition to these grasses, Tonzi Ranch supports trees, active

Table 2.1: Site Characteristics

Site	Tonzi	Vaira	Metolius	Walker Branch
Location	Ione, CA	Ione, CA	Metolius, OR	Oak Ridge, TN
Vegetation Type	Oak Savanna	Grazed grassland	Coniferous forest	Mixed deciduous forest
Climate	Mediterranean	Mediterranean	Temperate	Temperate
Soil Type	Extremely rocky silt loam	Very rocky silt loam	Sandy loam	Silty loam
Precipitation (mm)	560	560	360	1330
Growing Season	Late October to mid May for grasses and March to October for trees	Late October to mid May	Year round	Mid March to early November
Maximum LAI	0.6	2.4	3.62	6
Average Annual NDVI	0.52	0.59	0.65	0.64
NDVI Range	0.35 – 0.79	0.46 – 0.81	0.23 – 0.84	0.35 – 0.88
Years	2002 to 2004	2001 to 2003	2002 to 2004	2003 to 2004

LAI, Leaf area index, in $m^2 m^{-2}$; NDVI, Normalized difference vegetation index. Site data as reported on the Ameriflux webpage [AmeriFlux, 2005].

between March and October. As a result, Tonzi always has actively transpiring vegetation. The Metolius site is in a semi-arid region with typical summer drought. The trees at Metolius are active year-round, however, seasonal differences in temperature, radiation, and vapor pressure deficit significantly reduce transpiration in the winter.

2.3 Methods

2.3.1 Data Collection

This study used data from each site as reported to and distributed by the AmeriFlux network. Two to four complete years of data were available for each site, generally from 2001 to 2004. Volumetric soil water content is considered a core measurement for AmeriFlux sites, to be taken at a depth between 0 and 30 cm and reported at 30 minute intervals [*AmeriFlux*, 2005]. At the Tonzi, Vaira, and Walker Branch sites, continuous soil moisture measurements were collected using an array of impedance sensors (Theta Probe model ML2-X, Delta-T Devices). These were placed vertically at depths of 5, 20, and 50 cm for Tonzi; 5, 10, and 20 cm for Vaira; and 5, 10, 20, and 60 cm for Walker Branch. Biweekly measurements were also collected at Tonzi and Vaira using segmented, time-domain reflectometer (TDR) probes (MoisturePoint, model 917, Environmental Sensors Equipment Corp.) [*Baldocchi et al.*, 2004]. At Metolius, continuous measurements were taken at a depth of 0 to 30 cm using a time-domain reflectometer (Campbell CS615). Periodically, measurements were taken throughout the soil profile (10 cm, 30 cm, 50 cm, and 90 cm) using a capacitance probe (Sentek Sensor Technologies).

Each type of probe has a different mode of operation and installation technique. The Campbell TDRs are 30 cm long metal probes, installed either vertically, to obtain an integrated water content or horizontally to record water content at a specific depth. Theta Probes have several short sensing rods and measure water content at a point. In general, both derive water content data by measuring the dielectric constant of the porous media. Theta probes determine this from the impedance of the sensing rod array.

The Campbell TDRs determine it by propagating waves along the rods, which act as wave guides. Both types are more accurate when calibrated to a specific soil, $\pm 0.02 \text{ m}^3 \text{ m}^{-3}$ for both the Theta Probe [Miller and Gaskin, 1999] and the Campbell TDR [Campbell Scientific, 1996].

Soil samples were periodically collected near the location of the probes. The samples represented a range of wetness values and were obtained at several depths throughout the rooting zone. At Metolius, a calibration curve was developed that related the gravimetric water contents to the voltage response from the TDR probe. At Walker Branch, the manufacturer-provided calibration curve for mineral soil was used, and matched the samples with a random error of around 4%. At Vaira and Tonzi, the half-hourly water content values were compared to the biweekly TDR measurements throughout the site to develop the calibration curve.

2.3.2 Data Analysis

Two main methods of raw data analysis were used: soil moisture histograms and annual time series. The time series charted the course of the daily volumetric water content over several years (Figure 2.1). From these, trends in year-to-year variability, seasonal patterns, and soil moisture at various depths could be determined. For each site, a series of histograms were generated from the half-hourly degree of soil saturation. The data were grouped in several ways: all years, single years, growing season only, and year-round.

The distinction between volumetric water content and degree of soil saturation is often unclear in the literature, and both terms are used here to describe soil moisture. This treatment is necessary because the model formulates the problem in terms of degree

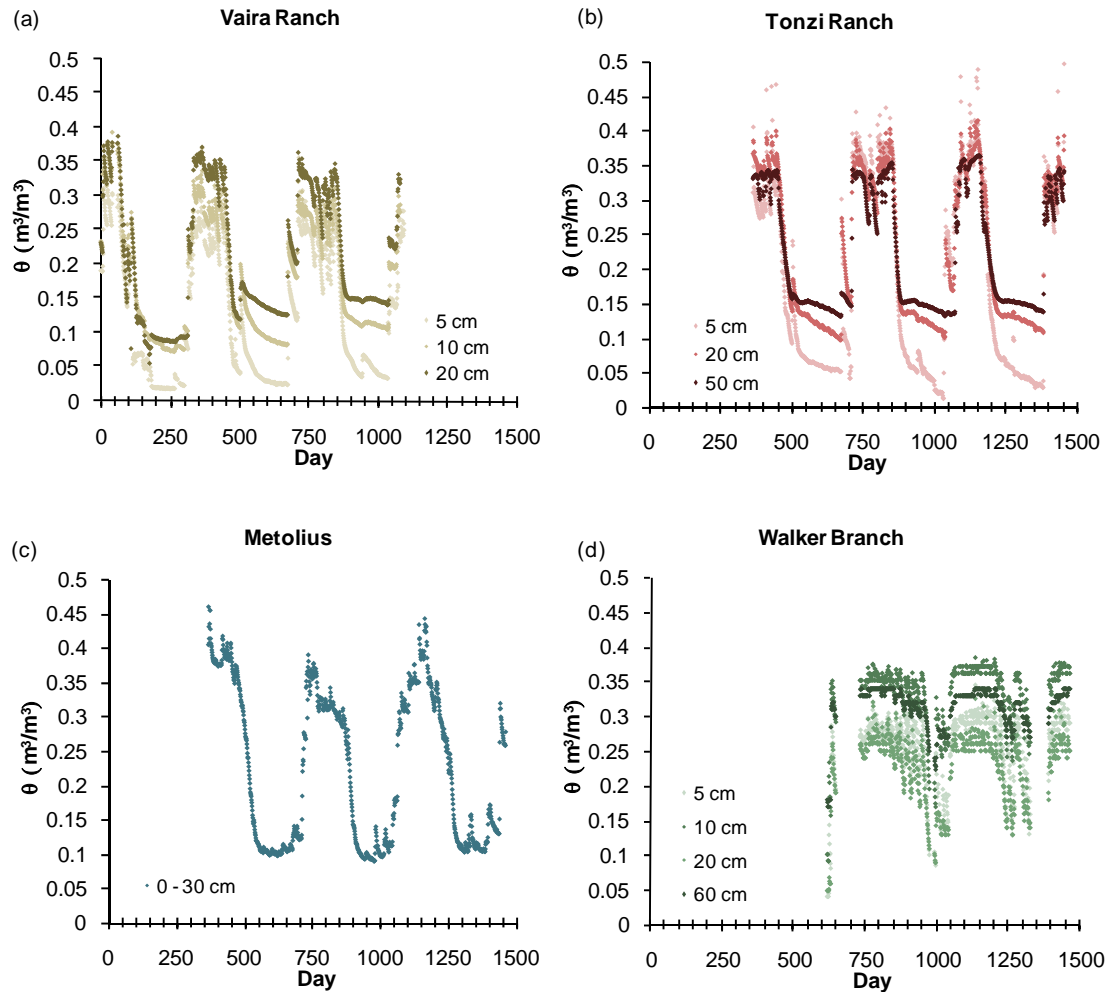


Figure 2.1: Average Water Content at Studied Sites
 Time series plots of average daily volumetric water content at each site. Vaira (a), Tonzi (b), and Metolius (c) show distinct seasonal patterns in soil moisture, with dry summers and wet winters. Soil moisture at Walker Branch (d) remains fairly steady throughout the year, due to the site's summer precipitation pattern.

of saturation while the AmeriFlux data is collected as volumetric water content.

Volumetric water content is defined as the volume of water in the soil divided by the total volume of the soil, V_w/V_t . Water content and saturation are easily related by the expression $\theta = nS$, where n is soil porosity (unitless), S is degree of saturation in $\text{m}^3 \text{m}^{-3}$, and θ is volumetric water content in $\text{m}^3 \text{m}^{-3}$. Degree of saturation can also be found by

dividing the volume of water by the volume of pore space V_w/V_p . In this case, the measured values were converted before creating the histograms.

When soil moisture measurements from multiple depths were available, histograms were generated for each depth. However, these did not individually capture the behavior over the entire rooting zone, and a method of finding depth-averaged soil moisture became necessary. Three methods of finding the average were compared: equal weighting, a zone weighting, and a root weighting.

The arithmetic, or equal weighted, average found the soil moisture as the sum of the measurements at all depths, for instance:

$$\theta_{equal} = \frac{\theta_{5cm} + \theta_{10cm} + \theta_{20cm}}{3} \quad (2.1)$$

The zone weighted depth-average attempted to divide the root zone into portions represented by each measurement. In the following example, the 5 cm probe was assumed to represent the soil between 0 and 7.5 cm; the 10 cm showed the water content between 7.5 and 15 cm; and the 20 cm probe represented the content between 15 and 30 cm.

$$\theta_{zone} = \frac{7.5 * \theta_{5cm} + 7.5 * \theta_{10cm} + 15 * \theta_{20cm}}{30} \quad (2.2)$$

Following Baldocchi et al. [Baldocchi et al., 2004], the root weighted, depth-averaged soil moisture ($m^3 m^{-3}$) was determined by:

$$\theta_{root} = \frac{\int_{Z_r}^0 (z)(dp(z)/dz)dz}{\int_{Z_r}^0 (dp(z)/dz)dz} \quad (2.3)$$

where z , depth, is positive downward and Z is the depth of the rooting zone. Here, $p(z) = 1 - b^z$, where b is a curve-fitting parameter. The b values used previously for Tonzi

and Vaira were 0.94 and 0.976, respectively [Baldocchi *et al.*, 2004]. Jackson *et al.* reported b as 0.966 for temperate deciduous forests [Jackson *et al.*, 1996], which was used for Walker Branch.

The depth-averaging process tempered the extreme high and low values that could be found at the surface, but which were not indicative of the overall moisture in the rooting zone. For Vaira, a site with relatively shallow soil, the weighting method did not significantly affect the histogram (Figure 2.2 a and c). However, the histograms at Walker Branch had different shapes depending on weighting technique (Figure 2.2 b and d). There, measurements taken simultaneously throughout the rooting zone frequently differ by $0.10 \text{ m}^3 \text{ m}^{-3}$.

Estimating the average value in the soil profile was more difficult at Metolius, where hourly measurements were limited to the upper 30 cm of the soil profile. Using the periodic Sentek FDR measurements, average soil profiles were generated for the wet, dry, and transitional periods using linear regression. The linear equations were then transformed so that given a half-hourly measurement between 0 and 30 cm, they could be used to estimate the water content at points throughout the rooting zone. The equations were then integrated using the formula described above, yielding an estimated average water content over the rooting zone.

2.3.3 Model Description

The model used in this research generates a probability density function (pdf) for steady-state soil moisture conditions at a point. It was originally developed by Rodriguez-Iturbe and colleagues in 1999 [Rodriguez-Iturbe *et al.*, 1999] and has been further described and modified in a series of papers by Laio, Porporato, Ridolfi, and Rodriguez-

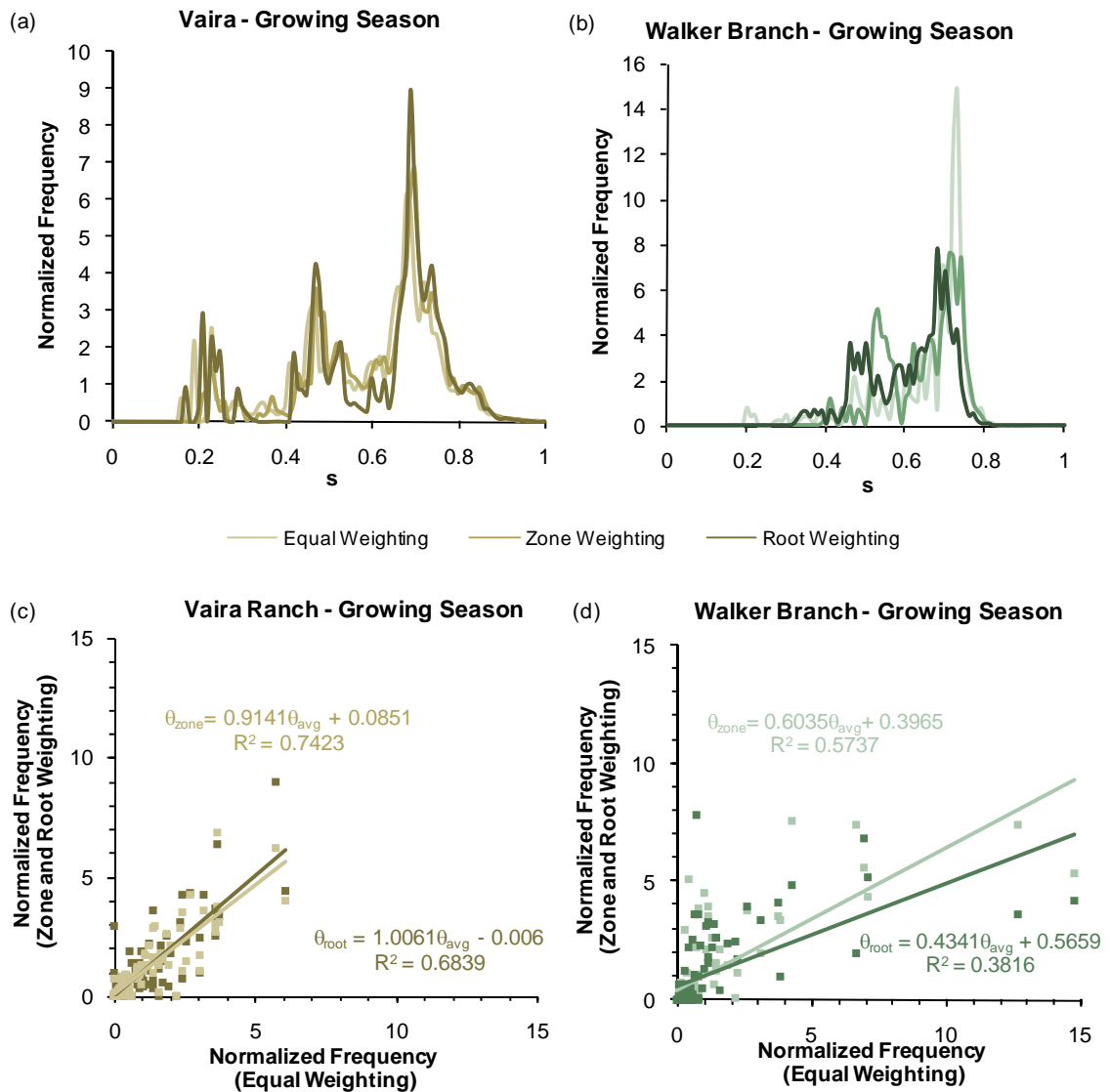


Figure 2.2: Soil Moisture Depth-averaging Methods

At Vaira Ranch, the weighting method does not make a qualitative (a) or quantitative (c) difference in the soil moisture histogram. However, at Walker Branch, the three methods deviate considerably, as shown in the plot of the histograms (b) and in the plot of comparing equal weighting to zone and root weighting (d).

Iturbe in 2001 [Laio *et al.*, 2001]. The model provides a realistic, quantitative description of the temporal dynamics of the soil moisture, while making the simplifications necessary to find an analytical solution. It has previously been shown to compare well with field data for sites with warm, wet growing seasons and dry,

temperate winters. This section will attempt to provide the reader with a brief overview of the model. For more detailed information, the authors recommend the references mentioned above as well as the book *Ecohydrology of Water-Controlled Ecosystems: Soil Moisture and Plant Dynamics* [Rodríguez-Iturbe and Porporato, 2004].

The foundation of the soil moisture dynamics model is the water balance at a point. This is given by the equation:

$$nZ_r \frac{ds(t)}{dt} = R(t) - I(t) - Q[s(t), t] - E[s(t)] - Lk[s(t)] \quad (2.4)$$

where n is the soil porosity, Z_r is the rooting depth, R is the rainfall rate, I is the amount of rainfall lost to canopy interception, Q is the runoff rate, E is the evapotranspiration rate, and L_k is the leakage. The (t) symbol is used to signify that the rate or amount is a function of time, while $s(t)$ indicates that it is a function of the soil moisture at a given time. The first three terms (R, I, Q) represent the amount of infiltration into the rooting zone, while the last two terms (E, L_k) define the amount of water lost from it. The sum of evapotranspiration and leakage forms the loss function, denoted by χ and shown graphically in Figure 2.3.

In this model, four points are critical to determining the shape of the loss function: s_h, s_w, s^* , and s_{fc} . These represent the degree of soil saturation at the hygroscopic point, the vegetation wilting point, the vegetation stress point, and the soil field capacity, respectively. The first three correspond to a matric potential (Ψ) in the soil. The hygroscopic point for soils, Ψ_h occurs at -10 MPa. The matric potential at the wilting Ψ_w and stress points Ψ_s are dependent on vegetation type.

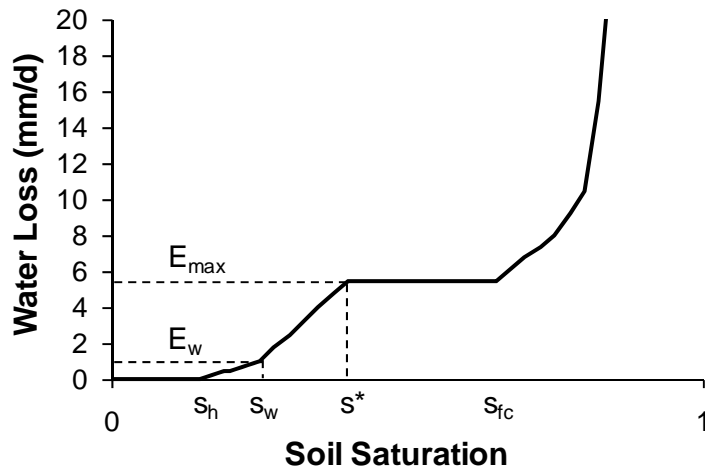


Figure 2.3: Soil Water Loss Function for Water-stressed Environments

Below the wilting point, all loss is determined by evaporation from soil. Between the wilting point and the plant stress point, additional loss occurs due to plant transpiration. Above the field content, soil is losing water at a rate defined by its hydraulic conductivity. (After Laio et al. 2001.)

Wilting generally occurs at around -1.5 MPa for grasses and crops, but can reach up to -5 MPa for trees and plants in semi-arid environments. Little data is available on the stress point, but the value -0.03 MPa is recommended by the developers of the model.

A water retention curve can be used to determine the values of these points in a specific soil, as shown in Figure 2.4. In this model, s_{fc} is “operationally defined as the value of soil moisture at which the hydraulic conductivity $K_s \dots$ becomes negligible (10 %) compared to the maximum daily evapotranspiration losses, $E_{max} \dots$ [Rodríguez-Iturbe and Porporato, 2004]” Field capacity can also be determined by examining TDR measurements to find the steady-state soil moisture after a wetting event, a somewhat subjective practice, or by using a given pressure, such as -0.01 MPa [Hillel, 1998].

In the soil moisture dynamics model, rainfall is treated as a Poisson process, with a rate of arrival equal to λ , and $1/\lambda$ equal to the mean time, in days, between rainfall

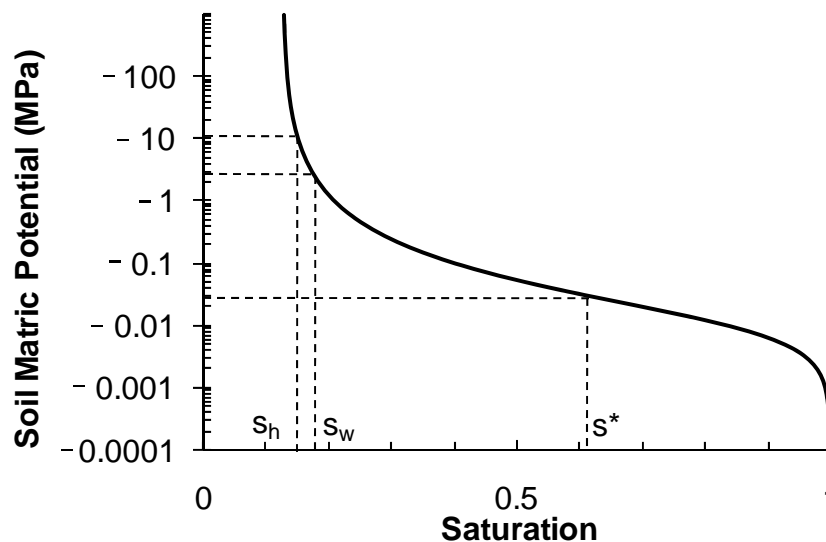


Figure 2.4: Water Retention Curve for Silt Loam

This curve was used to estimate the soil parameters for the model. The matric potentials anticipated at the hygroscopic, wilting, and stress points are known, and from the curve, the associated degree of saturation is found.

events. The amount of rainfall occurring during an event (α) is described by an exponential probability density function. Interception capacity (Δ) describes the amount of rainfall that can accumulate on vegetation during a rainfall event; rainfall above this threshold amount reaches the ground. It is included in the model as a modifier to α .
Runoff occurs once the soil is completely saturated ($S = 1$).

Because of the stochastic nature of rainfall, the soil water balance can only be described in a probabilistic manner. In this framework, the soil's degree of saturation over a given period of time can be modeled as a probability density function (pdf). The derivation of the equation is beyond the scope of this overview, although it can be found in the references cited earlier. In this model, $p(s)$ is the steady state pdf of soil moisture, which can be found using the equations below:

$$p(s) = \begin{cases} \frac{C}{\eta_w} \left(\frac{s - s_h}{s_w - s_h} \right)^{\frac{\lambda'(s_w - s_h)}{\eta_w} - 1} e^{-\gamma s} & \text{if } s_h < s \leq s_w \\ \frac{C}{\eta_w} \left[1 + \left(\frac{\eta}{\eta_w} - 1 \right) \left(\frac{s - s_w}{s^* - s_w} \right) \right]^{\frac{\lambda'(s^* - s_w)}{\eta - \eta_w} - 1} e^{-\gamma s} & \text{if } s_w < s \leq s^* \\ \frac{C}{\eta} e^{-\gamma s + \frac{\lambda'(s - s^*)}{\eta}} \left(\frac{\eta}{\eta_w} \right)^{\frac{\lambda'(s^* - s_w)}{\eta - \eta_w}} & \text{if } s^* < s \leq s_{fc} \\ \frac{C}{\eta} e^{-(\beta + \gamma)s + \beta s_{fc}} \left(\frac{\eta e^{\beta s}}{(\eta - m)e^{\beta s_{fc}} + m2e^{\beta s}} \right)^{\frac{\lambda'}{\beta(\eta - m)} + 1} \left(\frac{\eta}{\eta_w} \right)^{\frac{\lambda'(s^* - s_w)}{\eta - \eta_w}} e^{\frac{\lambda'(s_{fc} - s^*)}{\eta}} & \text{if } s_{fc} < s \leq 1 \end{cases} \quad (2.5)$$

where

$$\eta_w = \frac{E_w}{nZ_r} \quad (2.6)$$

$$\eta = \frac{E_{max}}{nZ_r} \quad (2.7)$$

$$m = \frac{K_s}{nZ_r [e^{\beta(1 - s_{fc})} - 1]} \quad (2.8)$$

$$\beta \sim \frac{\ln\left(\frac{0.1E_{max}}{K_s}\right)}{\ln(s_{fc})} \quad (2.9)$$

$$\gamma = \frac{nZ_r}{\alpha} \quad (2.10)$$

$$\lambda' = \lambda e^{-\frac{\Delta}{\alpha}} \quad (2.11)$$

In these equations, C is an integration constant. Although it has an analytical solution, the value of C can be found by normalizing $p(s)$ so that:

$$\int_{s_h}^1 p(s) ds = 1. \quad (2.12)$$

2.3.4 Model Application and Modifications

Laio et al. [Laio et al., 2001] cautioned that two conditions need to be fulfilled to apply the steady state results: the climate must be characterized by time invariant

parameters throughout the growing season, and the degree of saturation at the start of the growing season should not be very different than the mean steady state condition. The first requirement is met only for the Walker Branch and Vaira sites, which have relatively stable climates during their growing seasons. The year-round growing seasons at Tonzi and Metolius complicate the modeling procedure. The second requirement suggests that soil moisture storage is occurring during wetter periods not in phase with the growing season. However, the soil moisture plots for Tonzi and Vaira suggest that soil water stored during winter periods does not provide a significant amount of moisture during the dry summer periods; the drop in soil moisture is rapid (less than 25 days) and dramatic (around 50%). If significant amounts of storage were occurring, the soil moisture depletion would not be as rapid or as large. At Metolius, the decline is slower, occurring over around 50 days, but no less intense at around 70%. Storage or tapping of deep water sources could be a significant component at this site during days 100 to 175.

Laio et al. [Laio et al., 2002] also investigated seasonal variations in potential evapotranspiration and its relationship to mean soil moisture. They concluded that delays in the response of the mean soil moisture to rainfall and evapotranspiration forcings could limit the validity of the steady state solution, especially at sites with deep rooting zones and moderate rainfall. With the exception of Walker Branch, the sites experience low to moderate rainfall, but they do not have active soil depths greater than 1.1 meters.

To adapt the model for application at Metolius and Tonzi sites, we developed a simple weighting method. For example, at Tonzi, the year was divided into two parts based on the wet and dry seasons. The wet season corresponded to the winter when only

grass was active, and the early spring when the trees began to bud. The dry season occurred during summer months when only the trees were active. The model was applied to find two different pdfs using a separate set of parameters for each one. A composite pdf was then created by weighting the individual pdfs:

$$p(s) = f_{wet}P_{wet}(s) + f_{dry}p_{dry}(s) \quad (2.13)$$

We will refer to this as the quasi-steady-state model.

A two-season division was also necessary for Metolius: one season for low potential evaporation during the winter and another for high potential evaporation during the summer. Rainfall parameters, once adjusted for the timing of the snowmelt, were similar for both seasons. To incorporate the effects of snow at the site, the timing of the snowmelt was determined by tracking the soil temperature. Sudden increases in the soil temperature indicated a snowmelt event, which was recorded as a “rainfall” event. This change increased the amount of precipitation per event and the time between events, much as a summer drought would.

2.3.5 Model Parameter Estimation

The soil moisture dynamics model uses multiple parameters to estimate a pdf of soil moisture at a given site. Two parameters, average time between rainfall events (λ) and average amount of rainfall per event (α), were calculated directly using the precipitation data reported to AmeriFlux (Table 2.2). At sites with distinctive wet and dry seasons, separate values were calculated. Interception capacity (Δ) was estimated using data on similar species given by Breuer et al. [Breuer et al., 2003]. The soil parameters ($K_s, s_h, s_w, s^*, s_{fc}, n$) were estimated using water retention curves, as described in Section 2.3.3.

Table 2.2: Precipitation Patterns

Site		Precipitation (mm)	α_1 (mm)	α_2 (mm)	λ_1 (d ⁻¹)	λ_2 (d ⁻¹)
Tonzi	Average	556	9.17	6.59	0.29	0.04
	2002	496	9.15	9.46	0.27	0.022
	2003	616	9.06	3.87	0.35	0.039
	2004	518	9.28	6.42	0.25	0.061
Vaira	Average	441	7.16	-	0.29	-
	2001	389	6.97	-	0.29	-
	2002	494	8.74	-	0.25	-
	2003	439	5.77	-	0.34	-
Metolius	Average	311	8.33	4.72	0.13	0.17
	2002	351	8.24	7.83	0.11	0.13
	2003	306	10.59	3.98	0.12	0.16
	2004	278	6.17	2.36	0.17	0.22
Walker Branch	Average	1258	7.73	-	0.38	-
	2003	922	6.92	-	0.37	-
	2004	1594	8.53	-	0.38	-

The computer program ROSETTA [Schaap *et al.*, 2001] was used to generate the water retention curves (WRCs). ROSETTA predicts the parameters needed to create the WRC for a soil (including n and K_s) using a database of soil particle size distributions. These parameters can then be used in a equation created by Mualem [1976] that describes the volumetric water content as a function of soil matric potential ($\theta = f(\Psi)$). Rosetta is an appropriate choice for predicting the function parameters at these sites because it was developed using soils from temperate to subtropical climates in North

America and Europe and is heavily biased towards soils with high sand, moderate silt, and low clay contents [Schaap *et al.*, 2001].

Using a function instead of direct measurements to create the WRCs was advantageous in this case, because it allowed for the demonstration of a more general approach, which can be applied to other sites. The problems related to direct measurements of water retention (difficulty, expense, and experimental limitations) can be avoided using these estimates [Schaap *et al.*, 2001]. For the Tonzi, Vaira, and Walker Branch soils, laboratory measurements of the matric potential at various water contents were also collected using the WP4 Dewpoint Potentiometer (Decagon Devices) following the manufacturer's recommended procedure [Decagon Devices, 2005] (see Section 3.2). The measurements and the WRCs compared favorably for most water content values, however, the laboratory tests were unable to duplicate very low and very high pressures, so these portions of the WRCs could not be confirmed.

Critical soil moisture points for each site were identified using the soil water retention curves. The soil hygroscopic point (s_h), also known as the residual saturation, was generated as a parameter from Rosetta and is also visible as the inflection point of the WRC. The remaining critical points are more difficult to identify, primarily because they are plant and climate based. Laio *et al.* [Laio *et al.*, 2001] indicate that most vegetation in water-controlled ecosystems begins to experience water stress at a soil matric potential of -0.03 MPa and wilt at -3.0 MPa, although this can be highly variable. This variability is visible at the Tonzi site, where the wilting point of the seasonal grasses was found to be around -2.0 MPa while the nearby trees could continue transpiring below -4.0 MPa [Baldocchi *et al.*, 2004]. At Metolius, ponderosa pine begin

Table 2.3: Soil Characteristics and Critical Soil Moisture Points

Site	Sand	Silt	Clay	K_s	n	s_h	s_w	s^*	s_{fc}
Tonzi	43	43	43	200	0.39	0.147 - 0.156	0.159- 0.200	0.488- 0.758	0.59- 0.97
Vaira	30	57	13	278	0.42	0.142- 0.148	0.157- 0.179	0.585- 0.836	0.53- 0.93
Metolius	62	28	10	387	0.45	0.142- 0.146	0.160- 0.182	0.456- 0.575	0.59- 0.99
Walker Branch	28	60	12	322	0.42	0.136- 0.145	0.151- 0.170	0.589- 0.842	0.51- 0.93

K_s , saturated hydraulic conductivity; n , porosity; s_h , soil hygroscopic point; s_w , wilting point; s^* , stress point; s_{fc} , soil field capacity

to show water stress at a pre-dawn leaf water potential of -0.5 MPa, and tree transpiration declined to 0.3 mm d⁻¹ below -1.6 MPa [Irvine *et al.*, 2004].

In consideration of the uncertainty associated with critical point predictions, a range for each point was generated (Table 2.3). The range incorporated both the uncertainty in the WRC prediction and in the appropriate soil pressure head. Ranges for the wilting point water content corresponded to a pressure head of -4 MPa to -2 MPa. The stress point range corresponded to pressures of -0.04 MPa to -0.02 MPa. Field capacity ranges were determined by using field measurements after rain events and by finding the water content corresponding to -0.01 MPa and to a hydraulic conductivity of 0.45 mm d⁻¹ (around 10% of an assumed E_{max}). Values for the hygroscopic and wilting points showed the smallest ranges, while the stress point and field capacity have much more variability.

The remaining parameters, E_{max} and E_w , were more difficult to estimate.

Evaporation from soil (E_w) depends on a variety of factors, including atmospheric

conditions, depth to groundwater water surface, soil cover, and soil texture [Hillel, 1998]. Maximum evapotranspiration E_{max} is the daily loss of water through both soil evaporation and plant transpiration, assumed to be constant between s^* and $s = 1$ and decreasing linearly between s^* and s_w .

To estimate the atmospheric forcing on transpiration, the half-hourly value of E_{max} was calculated using the Priestly-Taylor equation [Priestly and Taylor, 1972] as follows:

$$E_{max} = 1.26 \frac{e'_s}{(e'_s + g)L} (R_n - G) \quad (2.14)$$

where g is the psychrometric constant and L is the latent heat of water. The terms G and R_n are the half-hourly net radiation and the ground heat flux measured using each site's flux tower. The saturation vapor pressure derivative with respect to temperature, e'_s , is found using the equation:

$$e'_s = \frac{2576.9 \exp\left(\frac{17.27 * T_a}{237.3 + T_a}\right)}{(240.97 + T_a)^2} \quad (2.15)$$

where T_a is the air temperature in °C. To find the daily value for E_{max} , the half-hourly values were summed.

It should also be noted that E_{max} is synonymous with the term potential or evapotranspiration (E_{pot}), commonly used in the hydrology literature, which is equal to the equilibrium evapotranspiration multiplied by the Priestly-Taylor coefficient, 1.26 in Eq (2.14). Unlike other models of evapotranspiration such as the Penman-Monteith equation [Monteith, 1965], stomatal conductance is not included in this estimate because it pertains only to the atmospheric drivers.

Table 2.4: Mean Potential and Actual Evapotranspiration

Site	Season	E_{pot} (mm d ⁻¹)	E_{act} (mm d ⁻¹)	E_{inv} (mm d ⁻¹)
Tonzi	Wet Season	1.22	0.76	1.8
	Dry Season	3.59	0.79	1.9
Vaira	Growing	1.26	0.97	1.0
	Non-growing	2.25	0.44	-
Metolius	Summer	4.35	1.69	3.2
	Winter	0.82	0.76	1.20
Walker Branch	Growing	4.88	2.41	2.4
	Non-growing	1.75	0.55	-

E_{pot} , potential evapotranspiration; E_{act} , actual evapotranspiration; E_{inv} , evapotranspiration from model inversion.

The evapotranspiration predicted by the Priestly-Taylor equation compares well with pan evapotranspiration [Xu *et al.*, 2004] and evapotranspiration only over certain conditions, particularly rangeland [Stannard, 1993] and crops [Davies and Allen, 1973]. Correlation coefficients ranging from $r^2 = 0.79$ to 0.90 were reported in these studies. However, the equation did not perform as well in studies of deciduous [Wilson and Baldocchi, 2000] and coniferous forests [Shuttleworth and Calder, 1979], where values for the leading term in Equation (2.14) were found to be between 0.72 and 1.0, lower than the standard 1.26.

The daily actual evapotranspiration (E_{act}), measured at each site using the flux tower, was compared to the potential evapotranspiration. At each site, the data were binned into appropriate time intervals, and the mean E_{pot} and E_{act} were found for each bin (Table 2.4). By comparing these values, we can determine if the evapotranspiration

at a site is limited by the atmospheric demand ($E_{\text{pot}} \leq E_{\text{act}}$) or by the availability of water to the vegetation ($E_{\text{pot}} > E_{\text{act}}$) [Baldocchi *et al.*, 2004]. Based on this criterion, all sites are water-limited throughout the year. The values found in this study are consistent with the year-round, average evaporation values previously cited in the literature: 1.6 mm d⁻¹ for Walker Branch [Wilson and Baldocchi, 2000], 0.81 mm d⁻¹ for Vaira, 1.0 mm d⁻¹ for Tonzi [Baldocchi *et al.*, 2004], and 0.77 mm d⁻¹ at Metolius [Irvine *et al.*, 2004].

The accuracy of E_{act} depends on the error associated with the measurements of latent heat flux (LE_{act}) collected at the micrometeorological towers. Anthoni *et al.* [Anthoni *et al.*, 1999] estimated errors in the latent heat flux to be $\sim \pm 15\%$ at a ponderosa pine site in Metolius, OR very similar to the one studied here. At Tonzi and Vaira, an annual bias error of 6%, or 0.06 mm d⁻¹, was estimated for latent heat flux [Baldocchi *et al.*, 2004]. When the evapotranspiration measurements collected by the tower at Walker Branch were compared to the values obtained using the catchment water balance, the mean annual difference between the two was 60 mm y⁻¹, approximately 10% [Wilson *et al.*, 2001].

2.3.6 Model Testing and Calibration

The model generated pdfs were compared with the measured histogram. The histograms were created using the root-weighted, depth-averaging technique (Section 2.3.2) in order to be representative of the entire root zone. Although the model cannot capture the systems behavior exactly, due to random noise, it should correctly depict the general shape of the histogram, capturing both the location (degree of saturation) and height (normalized frequency) of the peaks. In all cases, the model results were qualitatively different from the measured results in these respects. This difference was

attributed to poor initial estimates for one or more parameter values. A method for calibrating the model was needed.

The most uncertain parameters were assumed to be those that were difficult to measure directly and that had either a wide range of possible values (s^* , s_{fc} , Δ) or had to be estimated using methods with unknown accuracy (E_{\max} , E_w). Model calibration focused on determining the values of these parameters that best fit the actual data.

Model inversion is typically used to find values for parameters that cannot be easily measured, have a high degree of uncertainty associated with their measurement, or for which measurements are not available. Because the model is computationally inexpensive and the parameter space was relatively small, sophisticated inversion techniques were not necessary. Instead, a direct search approach was used. The range of each parameter was broken into equal increments; a model parameter grid was generated from all possible parameter combinations.

The model was run for each parameter set, and a least squared objective function (J) was used to identify the optimal parameter set:

$$J = \sum_{s=0}^1 (p_{modeled}(s) - p_{measured}(s))^2 \quad (2.16)$$

where $p_{modeled}$ is the pdf generated by the model and $p_{measured}$ is the normalized histogram.

The best-fitting parameter set is that which generates the smallest value of the objective function (J_{\min}). While this method would be inadvisable for a model with a larger parameter space or higher computational requirements, it has the advantage of being easy to conceptually visualize and implement. Using the least squared method

makes several assumptions about the data, namely that the measurement errors are normally distributed random variables. In all cases, when the new parameter sets (those associated with J_{\min}) were used, the modeled results more closely matched the measured data.

Using inversion, there is a danger of over-fitting the model. By fitting the parameters with limited data sets, there is a chance that the model will only be specific to those years and will not make useful predictions of future behavior. Using multiple years of data that span a large range of conditions minimizes this risk. Only a few years of hourly observations (none with extreme weather) were available for this analysis.

2.3.7 Forward Predictions Using the Soil Moisture Dynamics Model

Climate change is anticipated to significantly affect precipitation patterns in North America. As a result, vegetation distribution is likely to change in the future, although conflicting scenarios have been presented in the literature. Using two dynamic global vegetation models, Bachelet et al. [2003] forecasted the expansion of forests in the Pacific Northwest and the replacement of savannas by forests in north-central California. Based on a regional climate model, Kueppers et al. [2005] predicted that the range of California's blue oaks will shrink by up to 59% and shift northward due to 24.5 mm decrease in April through August precipitation. Clearly, the amount and timing of future precipitation will be a significant determinant of vegetation distribution.

To determine how vegetation at the sites studied would respond to changing rainfall and precipitation regimes, the soil moisture dynamics model was used. Detailed temperature and precipitation predictions from a regional climate model were available for the Sierra Nevada foothills region of California, near the location of Tonzi and Vaira

Ranches [Kueppers *et al.*, 2005]. Using the predicted daily precipitation totals for the years 2000 to 2100, new rainfall parameters (α and λ) were obtained for the two sites by calculating the five year averages for three periods during the time span: early, middle, and late 21st century. The new parameters for the late 21st century indicated decreased rainfall frequency for the spring and summer months, with precipitation event intensity increasing in the spring and falling to nearly half in the summer. Winter parameter values were relatively constant.

Predicting the values of E_{\max} and E_w under altered climatic conditions was more difficult. In Equation (2.14), E_{\max} is a function of temperature and available energy ($R_{\text{net}} - G$). Assuming that average values of R_{net} and G remain constant and only T_a increases, E_{\max} will increase by approximately 3% by mid-century and 7% by late-century at Tonzi and Vaira. However, it cannot necessarily be assumed that the net radiation will remain near its current level. Solar radiation reaching the earth's surface may be altered due to changes in cloud cover [Arking, 1991] or atmospheric aerosol concentrations [Mitchell and Johns, 1997], and warming surface temperatures can lead to reduced R_{net} .

A sensitivity analysis of Equation (2.14) shows that a 5 % decrease in $R_{\text{net}} - G$ negates the effects of increased temperature on E_{\max} . A 5% increase in $R_{\text{net}} - G$ produces an 8% mid-century and a 12% late century increase in E_{\max} . Assuming that precipitation and net radiation were related by cloud cover, Kumagai *et al.* [Kumagai *et al.*, 2004] fitted an exponential curve to data from a Bornean tropical rain forest, and used it to predict R_n from the predictions of future precipitation patterns at the site. This method was applied to find an appropriate exponential relationship for each site (Tonzi Summer: $R_n = 143.1e^{-0.163P}$, Tonzi Winter: $R_n = 69.5e^{-0.77P}$, Vaira: $R_n = 49.0e^{-0.23P}$, Metolius

Winter: $R_n = 35.7e^{-0.13P}$, Metolius Summer: $R_n = 152.4e^{-0.15P}$, Walker Branch: $R_n = 117.4e^{-0.016P}$). Based on these curves, Tonzi and Vaira were predicted to experience a 4% increase in year-round E_{\max} by mid-century, and a 10% late century increase. However, due to the vastly different nature of these sites and the rain forest, the relationship may not hold.

Although detailed climate predictions were not available for the other sites, recent global climate models provided generalized predictions for Oregon and Tennessee. By 2090, a 20% increase in summer precipitation [Burkett *et al.*, 2001] and a 1.3 to 6.5 °C increase in maximum summer temperature is anticipated in the southeastern U.S. Combined, these result in a 3 to 7% increase in E_{\max} .

In the Pacific Northwest, winter precipitation is expected to increase while summer precipitation decreases [Parson *et al.*, 2001]. Average temperatures are anticipated to increase by 4.1 to 4.6 °C in the summer and 4.7 to 5.9 °C in the winter. Nolin and Daly [Nolin and Daly, 2006] showed that warming could change the snowfall accumulation patterns in regions of the Pacific Northwest, including the Metolius area. Precipitation would be more likely to fall as rain, rather than snow, reducing the mean time between precipitation events during the winter, as represented by the parameter $1/\lambda_{\text{winter}}$. To model these changes, the precipitation parameters for each site were changed by 10 and 20%, in the appropriate direction. These changes result in an 11 to 20% winter increase in E_{\max} , and an 11 to 14% summer increase.

2.4 Discussion

2.4.1 *Water Content Time Series and Histograms*

The three sites that had distinctive dry periods in the present climate also demonstrated a distinctive drop in water content at the beginning of the dry season. At the Northern California sites, Tonzi and Vaira, this initially occurred around day 150 and continued until approximately day 300. This pattern indicates that the soil at these sites does not store any appreciable amount of water and reaches a new equilibrium quickly after a change in rainfall regimen. A similar pattern occurred during summer at Metolius, however, the drop in content was less abrupt. The Walker Branch site showed soil moisture that was fairly constant year round, consistent with the more regular rainfall pattern observed.

The water content stress points, as determined by the water retention curves, were compared to the plots of soil moisture (Figure 2.1). These plots indicated that the trees at Tonzi and Metolius spent a substantial portion of the growing season under water stress. At the Walker Branch site, the findings were slightly more complex, since more information about the soil profile was available. Generally, the soil moisture hovered around the stress point, even though the site received over twice the amount of rainfall of Tonzi and around four times that of Metolius. The forest at Walker Branch is denser, with a leaf area index of 6, as compared to 2 and 3 for the other sites. This could indicate that the trees at each site have adapted to the available soil water. Clearly, Walker Branch can support denser vegetation because of more available moisture. This has caused more growth, but not so much that the trees are overly stressed. It is also important to note that at three of the sites, the soil water content never dropped below the

wilting point, except in the surface soil layers. Once soil moisture falls below the wilting point at Vaira, the grass senesces, preventing additional transpiration from occurring. *Metolius* is clearly water stressed during the summer; however, its leaf area index and the vegetation's water use do not exceed the water delivering capacity of its environment, which would be evidenced by a reduction of the soil water beyond the wilting point.

Some evidence points to tapping of deep water sources by the trees at the Tonzi site. During the summer months, soil moisture values can drop below the theoretical wilting point for the trees, however, they continue to transpire, albeit at a highly reduced rate. There are two possible explanations: either the trees can endure higher soil matric potential values than previously considered, or they are using another water source not measured by the soil moisture probes. The first explanation is less likely, because as the soil approaches the hygroscopic point, soil matric potential increases exponentially. A decrease in a degree of saturation by 0.01 (from 0.16 to 0.15), can cause the matric potential to double (from -5 MPa to -10 MPa). The second explanation is also supported by the work of Lewis and Burgy [*Lewis and Burgy, 1964*] who showed that several oak species, including blue oaks, could extract groundwater from fractured rocks at depths of up to 24 m. Although roots extend significantly past 60 cm at the Tonzi site, it is not possible to measure soil moisture past this depth, due to the high gravel content of the soil.

Water content patterns also revealed the importance of measuring water content throughout the root zone (Figure 2.5). Many sites collected measurements only in the top portion of the root zone (<20 cm). However, on average, these surface water

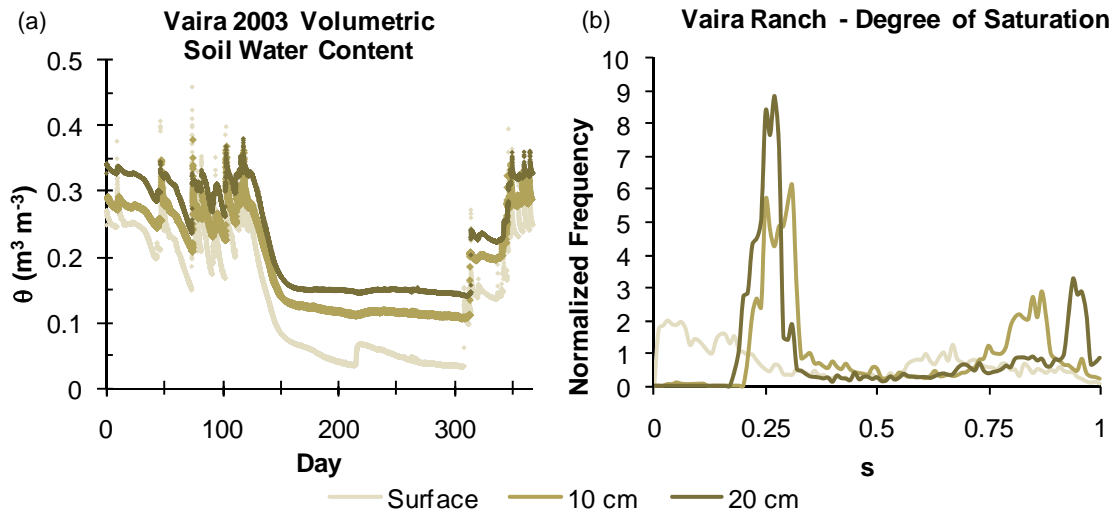


Figure 2.5: Soil Moisture as a Function of Depth

Example of soil moisture time series and histograms at varying depths at same site. During the summer months, the difference in volumetric water content can be up to $0.1 \text{ m}^3 \text{ m}^{-3}$ (a), resulting in substantially different histograms for each depth (b).

contents were significantly less than those taken deeper in the root zone. At Walker Branch, the surface measurement was 20% less than the measurement at 60 cm. At the more arid sites, the difference was more significant with the 5 cm measurement an average of 23% less than that at 50 cm at Tonzi and 45% less than that at 20 cm measurement at Vaira. At Metolius, a similar comparison using the periodic full root zone data indicated that the measurements collected at 10 cm depth were, on average, 37% less than those collected at 90 cm.

The sites with clear dry seasons (Tonzi, Vaira, and Metolius) have strongly bimodal distributions of half-hourly, depth averaged soil water content (Figure 2.6). Although Walker Branch did not have a clear dry season, it also showed a bimodal distribution, due to some summer dry periods. For the sites that recorded soil moisture at several depths (Tonzi, Vaira, and Walker Branch), the year-to-year variations

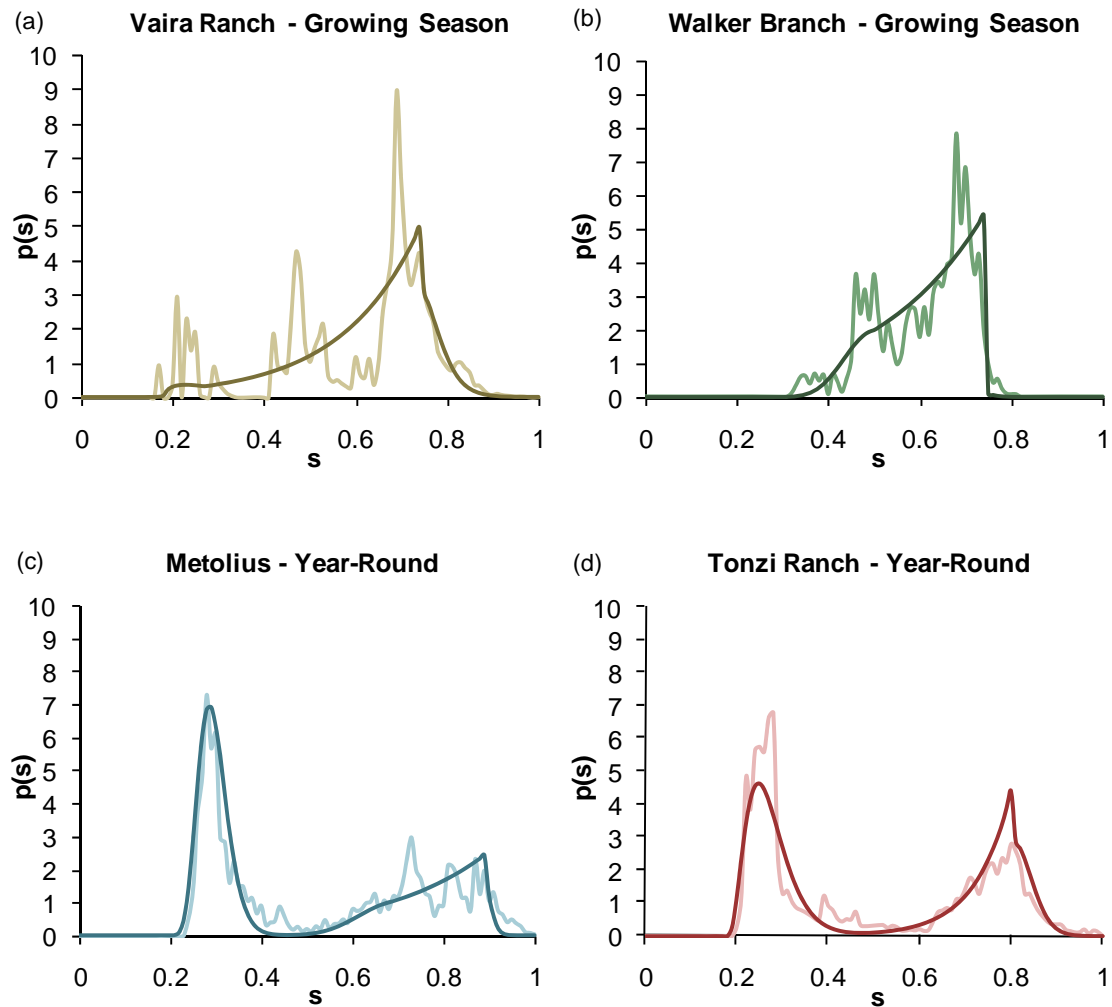


Figure 2.6: Measured versus Modeled Histograms

A comparison of measured, depth-averaged data displayed as histograms (gray) and calibrated model results as pdfs (black). The measured and modeled results show good agreement in overall shape, but the model cannot capture all of the variation, even with adjustments for seasonality. These problems are likely due to the model's inability to capture growing season dynamics; it is clear from the data that the model's steady state assumptions are still being violated.

appeared to vary less with increasing depth. Walker Branch and Vaira have limited growing seasons, from days 111-311 and days 304-110 respectively. When non-growing season data was excluded (Figure 2.6), the Vaira histogram shifted toward

higher soil moisture levels, while the Walker Branch peak shifted toward higher soil moisture levels and increased in variance.

Histograms such as these may be useful in plant physiology models that predict the carbon and water fluxes at a site. Including soil moisture as a stochastic variable could lead to more probabilistic predictions of these fluxes, perhaps through the use of Monte Carlo methods. The stochastic soil moisture approach could be a useful compromise between vegetation models which neglect soil moisture constraints on plant processes and fully-coupled models which, at great computational expense, describe flow throughout the soil-plant-atmosphere continuum.

2.4.2 Hydraulic Redistribution

Hydraulic redistribution occurs when plant roots passively move water through the rooting zone along gradients of high to low matric potential [Meinzer *et al.*, 2004]. Generally, water flows upward through the roots from deep, wet layers of soil and is released into the shallow, dry soil layers; however, downward and lateral flow can also be induced. In field studies, hydraulic redistribution may be confused with other mechanisms of soil water transport, such as capillary rise, which take place without the influence of vegetation.

To test for hydraulic redistribution, the diurnal patterns of water content were examined. The following temperature correction equation was used on the CS615 readings at Metolius [Campbell Scientific, 1996]:

$$\theta_{\text{corrected}} = \theta - (T_s - 20) * (-0.000346 + 0.019\theta - 0.045\theta^2) \quad (2.17)$$

where T_s is the soil temperature. The Theta probes have not been shown to have a temperature dependency [Delta T Devices, 1999], so no correction was applied. During

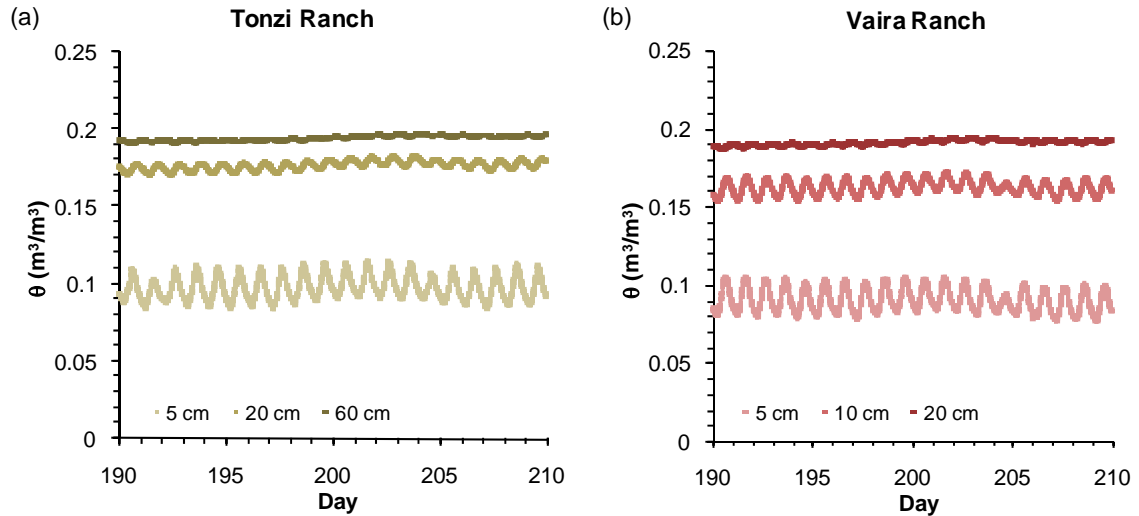


Figure 2.7: Diurnal Fluctuations in Soil Moisture
 Temperature corrected diurnal fluctuations in soil moisture at the Tonzi (a) and Vaira Ranch (b) sites. The volumetric water content increases slightly during the nighttime hours.

the summer periods when no rain occurs at Tonzi, the soil moisture at 20 cm experiences daily fluctuations in θ of around 0.002, with the peak occurring at 2200 hours and the minimum occurring at 1000 hours (Figure 2.7a). While this small increase seems unlikely to influence transpiration, it could, when integrated over the length of the rooting zone, provide for 1.2 mm d^{-1} . Soil moisture at the surface has daily fluctuations of around 0.005, with a peak at 1530 hours and a minimum at 0430 hours. A similar pattern occurs at the Metolius site; during the summer, the daily peak occurs around 0630 and the minimum occurs around 1200 hours. The difference was more pronounced, around $\theta = 0.014$. The analysis could not be performed at Walker Branch because water content was reported to two significant figures, not sufficient to detect changes of this magnitude.

These diurnal fluctuations were similar to those observed by Meinzer et al. [2004] in a study of several tropical savannas and temperate coniferous forests. They observed that hydraulic redistribution was possible once soil matric potential fell below approximately -0.2 to -0.4 MPa, which is roughly equivalent to $\theta \leq 0.15$ at these sites.

Some evidence against hydraulic redistribution remains. A similar, although smaller, diurnal pattern (Figure 2.7b) occurred at Vaira even after the grass had senesced, leading to the conclusion that a water transport mechanism other than hydraulic redistribution was acting, possibly upward water vapor flux (capillary rise) during the day followed by condensation at night. Based on this observation, soil moisture and matric potential measurements alone are not sufficient to demonstrate hydraulic redistribution; studies attempting to do so should include other evidence, such as isotopic tracer results or root sap flow measurements.

2.4.3 Inverse Soil Texture Effect

The inverse soil texture theory states that in dry climates, the most developed vegetation can be found on sandy soils, while in wet climates, it can be found in finer soils [Noy-Meir, 1973]. Based on the principle of water conservation, it asserts that the most suitable soil for a climate is one that loses the least water through evaporation or leakage. In dry climates (less than 500 mm y^{-1}), loss to evaporation from upper soil layers is higher [Hillel, 1998]; soils that lose the least to evaporation, such as sands, have an advantage in supporting vegetation. In wetter climates, loss to leakage is the higher than loss to evaporation and sandy soil becomes a disadvantage. Thus clays, which slow leakage, support denser vegetation in wetter environments. These properties are related to the shapes of the water retention curves for each type of soil.

This effect is prominent when considering the Northern California sites. Although the two have very similar climates, Vaira supports less vegetation than Tonzi. Their soils have the same clay content, but Tonzi has a 13% higher sand content. Metolius, which supports a pine forest, receives even less rainfall, however, its sand content is at 62%, over 30% higher than Vaira, which supports only grass. Walker Branch, which supports an oak forest, has a soil grain distribution very similar to Vaira's, an advantage in wetter climates. This evidence supports assertions made by Fernandez-Illescas et al. [2001], which used the soil moisture dynamics model (Section 2.3.3) to examine species coexistence at a water stressed site in Texas.

2.4.4 Probability Density Functions

The final pdfs and their corresponding histograms are shown in Figure 2.6. The best model fit was found for the Metolius site, with a minimum objective function value (J_{\min}) equal to 30. Good fits were also found for Vaira Ranch ($J_{\min} = 89$), Tonzi Ranch ($J_{\min} = 59$), and Walker Branch Watershed ($J_{\min} = 46$). This result may be related to the rooting depth at each site; Metolius had the deepest roots and the best fit while Vaira had the shallowest roots and worst fit. The shallow rooting depth causes greater susceptibility to rainfall pulses and more frequently changing water contents, making the data at Vaira noisier. However, the difference in performance was not great, and the modeled pdfs captured the correct shape and location of the peaks. Even though Metolius and Tonzi are not ideal sites to model, the modifications mentioned in Section 2.3.4, coupled with careful model calibration, appear successful.

Accurate parameter value estimation was critical to the accuracy of the model. Model calibration procedures increased model accuracy, decreasing the objective

Table 2.5: Degree of Saturation at Stress Point

Site	s^*	Soil Matric Potential (MPa)
Vaira	0.3	-0.3
Tonzi Grass and Trees	0.3	-0.2
Walker Branch	0.56	-0.06
Metolius	0.68	-0.009
Tonzi – Trees Only	0.85	-0.009

s^* , stress point

function by over 80%, in some cases. The most sensitive parameters were also the most difficult to determine with accuracy, E_{\max} and s^* . Calibration showed that the originally estimated values of E_{\max} did not necessarily produce a good fit between the data and the model. The calibrated E_{\max} values (E_{inv}) were up to 50% different from the estimates (Table 2.4). Calibration results for interception capacity, Δ , ranged from 0.3 to 2.5 mm, roughly corresponding to ranges given by Breuer et al. [2003] for species similar to the ones at these sites.

The stress points found through model calibration (Table 2.5) did not correspond to the matric potentials suggested by the literature. For Ψ_{s^*} , -0.03 MPa is too negative for trees acclimated to semi-arid conditions and too positive for those acclimated to wet conditions. For grasses at Vaira, the matric potential at the stress point was around -0.25 MPa, much more negative than originally presumed.

At Tonzi, the value of E_{inv} was much less than predicted during the winter. Several possible explanations exist for the difference: the equation used to predict E_{\max} was in error, the root zone was being kept moister by some water source besides

precipitation (e.g. hydraulic redistribution), or the trees were tapping water below the lowest measurement location. To explore the question, the uncertain parameters in the model were set to reasonable values ($E_{\max} = 3.5$, $s^* = 0.65$, and $\Delta = 1.4$) while the precipitation values were altered. The pdf matched the histogram when $\alpha \approx 0.05 \text{ d}^{-1}$ and $\lambda \approx 11 \text{ mm}$, double the measured value. Additionally, the average evapotranspiration measured during the dry season is 141 mm, more than double the average precipitation, 45 mm. The rooting zone is remaining wetter than anticipated based on the precipitation. Some process that prevents the water in the rooting zone from being depleted through transpiration must be occurring, either tapping of deep water sources, hydraulic redistribution, or capillary rise. As a result, the best-fitting E_{\max} values are low, not reflecting the effects of the additional water.

2.4.5 Soil Moisture Under Climate Change Scenarios

The predictive soil moisture pdfs (Figure 2.8) were evaluated to determine how climate change could potentially increase plant stress. The classification scheme proposed by Porporato et al. [2004] divides the water balance at a site into “dry”, “intermediate-stressed”, “intermediate-unstressed”, and “wet” categories based on the shape of its pdf. The predicted precipitation changes should have little impact at the Walker Branch site, which moves from the “intermediate-unstressed” to the “wet” category. The grasses at the Vaira Ranch site were placed in the “intermediate-unstressed” category for both current and future scenarios. While the site is semi-arid, the grasses die once the soil water content falls below a certain level for a sufficient duration, so their growing season does not include the drier summer months. The

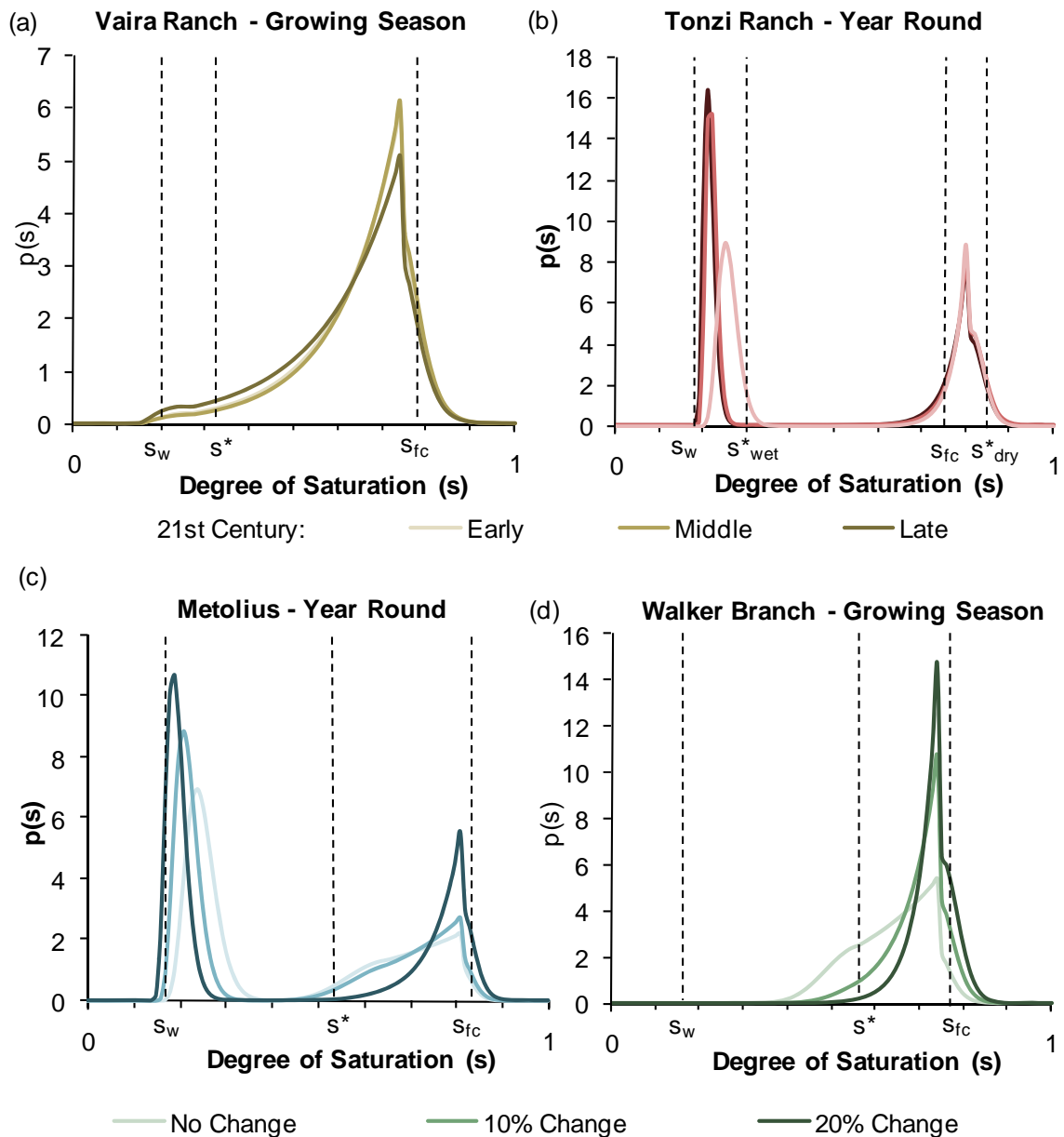


Figure 2.8: Soil Moisture Distributions Under Climate Change

A comparison of pdfs predicting results of alterations in precipitation patterns and evapotranspiration levels due to climate change. The results for Vaira (a) and Tonzi (b) are based on data from a regional climate model. The results from Metolius (c) and Walker Branch (d) are based on regional projections from global climate models and represent a 10% and 20% change in precipitation model parameters and the corresponding change in evapotranspiration.

increased precipitation during the winter and spring months may prolong the growing season of the grasses or cause the dominant species to change [Knapp *et al.*, 2002].

The results from Tonzi and Metolius are harder to classify using this system, since they are bimodal. Currently, both sites fall under the “intermediate-stressed” category in the summer. During the winter, Metolius is “intermediate-unstressed” and Tonzi is “wet”. In future scenarios, Metolius becomes more seasonally extreme, “dry” in the summer and “wet” in the winter. Tonzi becomes extremely “dry” in the summer and stays “wet” in the winter. The trees at these sites will likely not survive the very dry summers unless they are able to access deeper water resources through root tapping and hydraulic redistribution [Kueppers *et al.*, 2005].

Timing of precipitation appears to be the defining factor determining how the soil moisture dynamics at a site will be altered due to climate change. Kumagai *et al.* [2004] addressed the issue of soil moisture dynamics and climate change in a tropical rainforest, concluding that at their site, the pdf of soil moisture was not extremely sensitive to the predicted changes in precipitation. Their results are similar to those for Vaira and Walker Branch, where precipitation during the growing season increased, while year-round precipitation remained the same or decreased. Alternately, Porporato *et al.* [Porporato *et al.*, 2004] showed dramatic changes in the pdf representing a grassland when the frequency but not the total amount of precipitation was altered. These changes are similar to those at Tonzi and Metolius, where predictions indicate increased annual precipitation, but more time between summer rainfall events.

2.5 Conclusions

We applied a probabilistic model from the ecohydrological literature [*Laio et al.*, 2001; *Rodríguez-Iturbe and Porporato*, 2004] to describe and predict the behavior of soil moisture dynamics at four different AmeriFlux sites with a range of soil textures, plant types, and climate. Several techniques for analyzing AmeriFlux soil moisture data and incorporating it into the model were presented, including depth-averaging methods and parameter value estimation. Using a simple inversion method for model calibration, the “best-fitting” parameter values for each site were found. Based on the calibrated parameters and estimates of future precipitation and evapotranspiration, the model was used to predict changes in the soil moisture regime due to climate change.

This study suggests that for AmeriFlux sites where soil moisture dynamics are critical to vegetation response, extra care should be taken when collecting soil moisture data. The AmeriFlux network is currently planning to upgrade soil moisture measurements such that moisture profiles are measured with automated capacitance probes (daily measurements) to as deep as possible to characterize the soil profile throughout the rooting zone of the dominant species. When this is implemented, it will improve our ability to characterize and model soil water transport.

The steady-state probabilistic model of soil moisture dynamics [*Laio et al.*, 2001] can be used successfully under a variety of site conditions, if appropriate modifications are made. Sites with year-round growing seasons should be divided into several segments corresponding to the dominant species phenology or hydraulic regime, and the results for each weighted to form a year-round pdf. Each time segment should have different evaporation and precipitation parameter values. In cases where different plant

types at a site have alternate growing seasons, changes to the soil stress points, rooting depth, and interception capacity may also be appropriate. Parameterization should be done carefully; parameter values should be taken, to the extent possible, from data measured at the site. When parameter values are highly uncertain, a simple inverse modeling technique may be used to determine them with greater confidence. Because seasonality is very important with respect to evaporative potential, the model uses an average taken over a season (winter or summer) when generating soil moisture probability density functions (pdfs). However, assuming a constant evaporative potential may be a significant source of error. The discrepancy between the estimated and calibrated values of E_{\max} may be due to this assumption or may be caused by the error inherent in predicting E_{\max} from an empirical equation. It may also be due to vegetation using deeper sources of water than those measured.

Using inversion to calibrate the model had the advantage of obtaining effective, or integrated, parameters over the entire rooting depth. The stress points determined from model inversion were not consistent with previous expectations. The matric potential at the estimated stress point for grasses was less negative than that for trees, indicating that transpiration from grass would begin to decline at higher soil moisture values. The model calibration results for both Tonzi and Vaira Ranches indicate that this might not be an accurate assumption. For grasses, stress began at -0.2 MPa; for trees, it began at -0.009 MPa. One explanation for this behavior could be that trees regulate transpiration more efficiently. A higher stress point indicates that water conservation begins to occur earlier, increasing the range of soil moisture values between the stress point and wilting point. Grasses have a smaller range, and therefore use water less

efficiently. An alternate explanation is that a process such as hydraulic redistribution or capillary rise is keeping the rooting zone wetter than the precipitation data would indicate, or that the trees are able to access deep sources of water.

Comparing the results for the trees at Tonzi to the inversion results for Walker Branch and Metolius, this trend was also apparent. Vegetation at Walker Branch typically experiences the least water stress and has a stress point at -0.064 MPa. Metolius and Tonzi experience more stress and have less negative stress points, indicating much larger ranges between stress and wilting points. Again, trees that begin decreasing transpiration at higher water contents will make more efficient use of available water. On the plot of evaporation as a function of degree of saturation (as in Figure 2.3), the slope of the line between the wilting point and stress point will be steepest for grasses, will decrease for non-drought tolerant trees, and will be the flattest for trees adapted to water stress. These results support the conclusion that the matric potential at the stress point may be highly variable by plant type and that the suggested value of $\Psi_{s^*} = -0.03$ MPa is not appropriate for many sites.

Climate models predict that precipitation patterns at these sites will be altered as the earth warms. While only minor alterations in the soil moisture dynamics were predicted at the Walker Branch and Vaira sites, climate change is predicted to have a much more substantial impact at Tonzi and Metolius. Although average annual precipitation may remain relatively constant or increase, changes in the frequency and timing of this precipitation could increase the stress on the trees at these sites. The question remains: when vegetation at a site experiences near constant, severe stress, will the ecosystem quickly or gradually adapt through changing vegetation type?

The stress points and corresponding soil matric potentials are important, and relatively unknown, factors needed to determine how vegetation responds to a changing climate. Further studies to determine these values based on field observations should be performed to confirm these preliminary findings, and the analysis should be extended to other sites. Additional research into the relationship between increased time spent under water stress and changes in species type may also be appropriate.

Finally, the question of uptake from sources outside of the soil zone should be thoroughly explored. The soil moisture dynamics models used in this chapter are based on a water balance that precludes the possibility of groundwater uptake. However, previous researchers have speculated that this is not the case for at least one of the sites, Tonzi Ranch. The blue oaks there potentially have very deep rooting systems, and if they can use groundwater for transpiration, it could account for the inconsistencies noted earlier. This possibility is directly addressed in Chapter 4: Groundwater Uptake in a Semi-Arid Oak Savanna.

Chapter 3: Hydrogeological Characterization of Tonzi Ranch

3.1 Introduction

As shown in the previous chapter, the properties of subsurface materials have a large influence on the water balance at a site, affecting the ecosystem in numerous ways. The next three chapters narrow our focus to one particular ecosystem, a semi-arid oak savanna at the Tonzi Ranch field site. In order to better understand the site, a detailed investigation of its subsurface materials and processes was conducted. The purpose of this chapter is to review the literature on the geology, geochemistry, and hydrogeology of the site and to provide more extensive data on the spatial distribution of soil properties and the location and movement of groundwater. These data sets are used in Chapters 4 and 5 and will be useful to future models of biogeochemical cycling and water flow through the groundwater-soil-plant-atmosphere continuum (GSPAC).

Geographically, the Tonzi Ranch site is located in the western foothills of the Sierra Nevada, near Ione, CA in Amador County. It sits at a latitude of 38.4311° N and 120.966° W (UTM 10S 677524.4 4255603.9) in the Irish Hill Quadrangle. The site is underlain by approximately 60 cm of very rocky loam followed by a 5 to 10-meter saprolite zone, and then competent, but fractured, greenstone and slate bedrock to an unknown depth. Section 3.2 describes the thin soil layer in detail, while Section 3.3 delves deeper into the subsurface to explore its parent geologic material. Section 3.4 concludes the chapter with a discussion of the movement of water through the deep, fractured bedrock.

3.2 Soils

The soil at Tonzi Ranch belongs to the Auburn soil series [*Sketchley*, 1965], which formed from the weathering of the parent material, a metavolcanic rock. The series typically consists of less than 1 m of silty loam soil, followed by fragments of weather rock, and finally soil bedrock. Up to 25 percent of the soil mass can be gravel to cobblestone sized rock fragments. Auburn series soils are commonly found on rangelands and oak savannas.

Preliminary soil property analysis at the site (Table 3.1) was performed by Kiang [2002] for selected locations both under the tree canopy and in the open space. The under-canopy samples contained approximately 11% more clay and silt, and were slightly less dense. As part of this research project, fifty spatially distributed surface soil texture samples were collected and analyzed by the DANR lab at the University of California-Davis. ArcView GIS and spatial interpolation (ordinary kriging) were used to create a series of soil texture (Figure 3.1), porosity (n), and bulk density (ρ_b) (Figure 3.2) maps. Porosity was estimated using the equation [*Hillel*, 1998]:

$$n = 1 - \frac{\rho_b}{2.56} \quad (3.1)$$

Table 3.2 summarizes the results of the distributed, open space soil sampling. The area soil survey classifies the Auburn soil series as a silt loam; however, based on the range of sand, silt, and clay contents, all samples tested as either loam or sandy loam. The relationship between higher silt content and proximity to the canopy may be the source of the discrepancy; however, it is unknown where the samples in the soil survey

Table 3.1: Soil Properties at the Tonzi Ranch Site

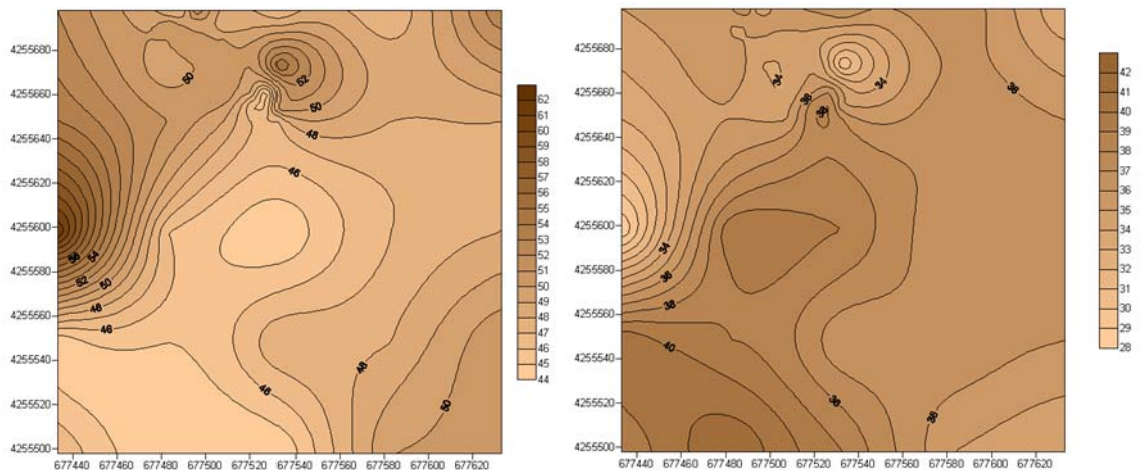
Location	Soil Texture	Bulk Density	Porosity
Under Canopy	38% sand, 45% silt, 18% clay	1.58 g cm ⁻³	0.4
Open Space	48% sand, 42% silt, 10% clay	1.64 g cm ⁻³	0.4

Data from [Kiang, 2002]

Table 3.2: Distributed Soil Texture and Density Measurements

	Sand [%]	Silt [%]	Clay [%]	Bulk Density [g cm ⁻³]	Porosity [-]
Average	49	36	15	1.48	0.44
Std. Dev.	3.2	2.4	1.3	0.162	0.061
Range	44 - 62	28 - 42	10 - 18	0.98 - 1.75	0.34 - 0.63

Soil texture analysis conducted at the DANR lab at the University of California – Davis

**Figure 3.1: Soil Texture at Tonzi Ranch**

Sand (left) and silt (right) content of soil at Tonzi Ranch. The eddy-covariance tower is located in the center of the maps. The sand content ranged from 44 to 62%, while the silt content was between 28 and 42%. At any given point, clay content is the difference of the two; it remained fairly constant in the samples, typically between 11 to 14%.

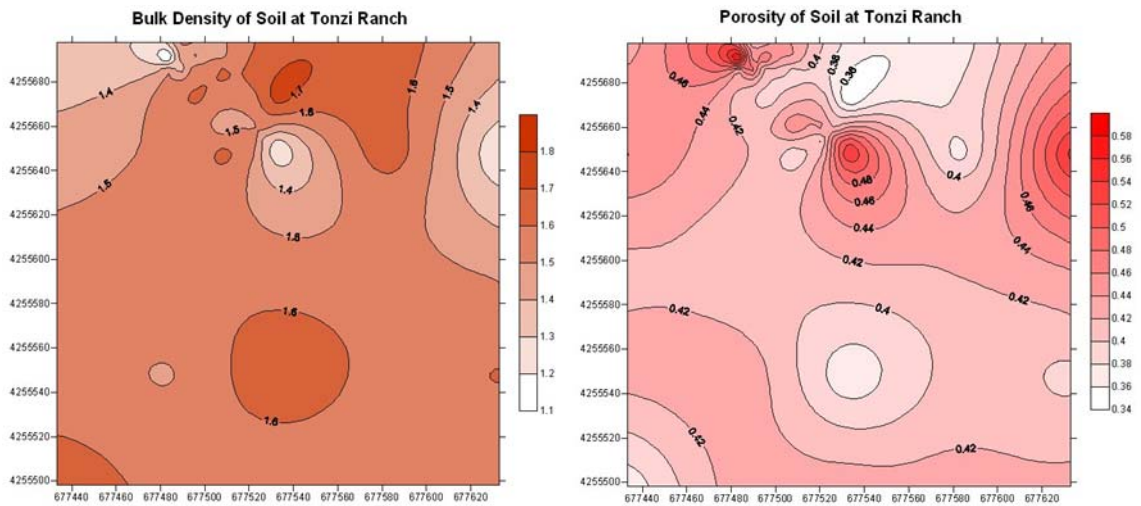


Figure 3.2: Bulk Soil Properties at Tonzi Ranch
Bulk density (left) was measured from oven dried samples of a known volume, and porosity was calculated as a function of density.

were collected. Porosity averaged 44%; this value is consistent with the volumetric water content measured after large precipitation events using soil moisture probes.

The water retention properties of the soil were measured using a dewpoint potentiometer (model WP4, Decagon Instruments). The instrument measures relative humidity in a chamber above a sample and converts it to a water potential representing the soil matric potential. (For more discussion on the relationship between water potential and relative humidity, see Section 4.4.2.) By measuring the potential above soil samples of known volumetric water content or soil saturation, a water retention curve is generated (Figure 3.3). Based on the manufacturer's recommendations [Decagon Devices, 2005], sample preparation consisted of the following steps: grinding soil to a uniform consistency, adding a known volume of water to a known weight of soil, sealing the sample and allowing it to equilibrate overnight, and bringing the sample

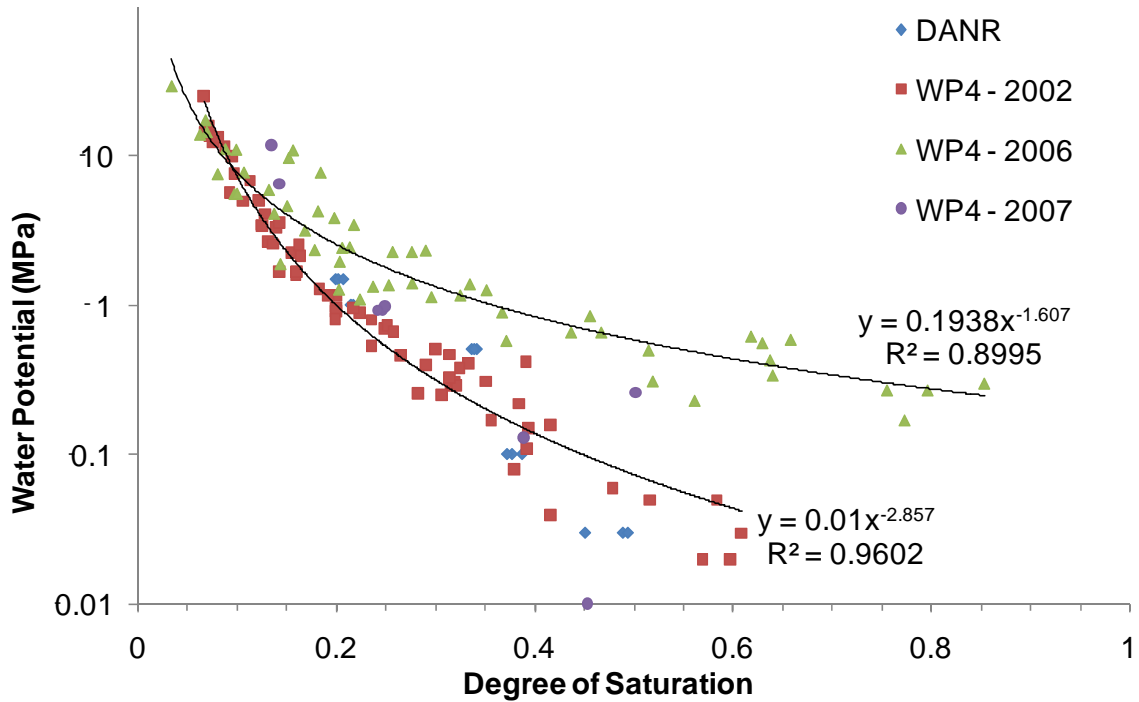


Figure 3.3: Water Retention Curve for Tonzi Ranch Soils

The water retention curve for soils at Tonzi Ranch, generated by the WP4 potentiometer (indicated by WP4-year) and the pressure plate method (indicated by DANR).

to the ambient temperature of the instrument. Care was taken to keep the instrument itself at a steady temperature, as rapid temperature fluctuations during sampling can cause erroneous readings. A 1 °C difference between the sample temperature and chamber air temperature can lead to an error of up to 8 MPa in the water potential, according to the governing equation [Decagon Devices, 2005]:

$$\Psi = \frac{RT}{MW} \ln \frac{p}{p_o} \quad (3.2)$$

where Ψ is the water potential, R is the ideal gas constant, T is the temperature, MW is the molecular weight of water, p is the partial pressure of water vapor, and p_o is the saturation vapor pressure. Additionally, the instrument was calibrated frequently, using a potassium chloride solution.

Liukang Xu generated an initial water retention curve for the site's soil [Baldocchi *et al.*, 2004]. In Figure 3.3, the data labeled WP4 – 2002 represents Xu's work, while the others were collected specifically for this study. The data set from 2006 significantly differs from the initial data; two possible reasons should be noted. First, the sample preparation technique was altered to see the influence of using an intact sample rather than a ground one, as grinding destroys natural macropores present in the sample. Second, it was much later discovered that the calibration solution was expired. Either of these factors could have caused the discrepancy, although only the former suggests that the true values are different. Repeat testing, using both new calibration standards and the soil grinding method (labeled WP4 – 2007), supported the initial results.

To confirm the curve in the presence of this uncertainty, twelve soil samples were sent to the DANR soil testing facility at the University of California – Davis, where the pressure plate method could be used [Klute, 1986]. Six samples were ground while the remaining six were left intact. Both methods produced similar results; the curves generated by the DANR analysis roughly corresponded to the 2002 and 2007 measurements (Figure 3.3). An exponential curve was fitted to the combined 2002, 2007, and DANR data, creating the following relationship:

$$\Psi_{\text{soil}} = 0.01 S^{-2.857} \quad (3.3)$$

where S is the soil saturation and Ψ_{soil} is the matric potential of the soil.

Using these soil properties, and data from the computer program ROSETTA [Schaap *et al.*, 2001], a curve was also generated showing soil hydraulic conductivity (Figure 3.4) as a function of soil volumetric water content (θ). The program itself

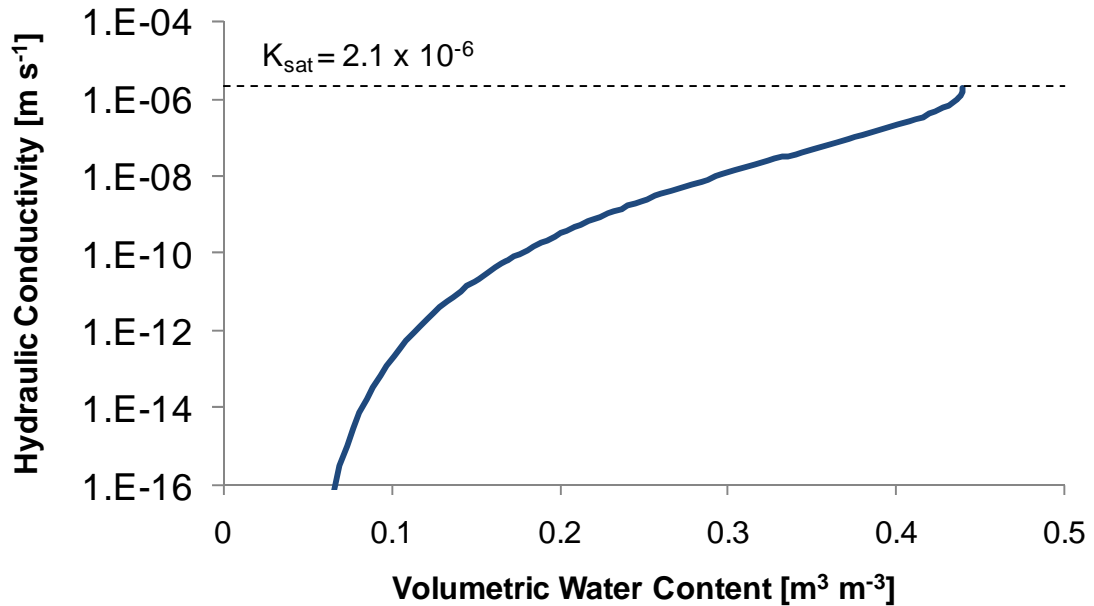


Figure 3.4: Soil Hydraulic Conductivity Curve
 Hydraulic conductivity as a function of volumetric water content, for Tonzi Ranch soils. The parameters governing the curve were estimated using the computer program ROSETTA.

predicts parameter values for the van Genuchten-Mualem equation, described in more detail in Section 6.2.3.1. As the residual saturation and porosity had been measured at the site, the only two unknown parameters in the equation are the unitless fitting parameter n , estimated to be 1.46, and the matching point at saturation, K_o , estimated at $6.6 \times 10^{-7} \text{ m s}^{-1}$. The resulting saturated hydraulic conductivity (K_{sat}) was $2.1 \times 10^{-6} \text{ m s}^{-1}$.

3.3 Geology and Geochemistry

Initial geologic surveys of the area reported the potential presence of three types of rock around the site: unaltered diabase and porphyrite, amphibolite schist altered from the diabase, and Mariposa Slate [Turner, 1894]. In the subsequent geologic mapping of the Sacramento area, this description was revised to Jurassic-Triassic Metavolcanics

(JRv) and Upper Jurassic metamorphosed marine sediments (Ju) [*Strand and Koenig, 1965*]. More detailed geological investigations of the area classified the metavolcanic formation with the somewhat generic descriptor of “greenstone”, usually used to indicate altered, mafic volcanic rock. In this location, the greenstone is known as the Gopher Ridge formation, which consists of weakly metamorphosed volcanics, mainly pyroclastic rocks interbedded with andesitic and basaltic lava [*Clark, 1964*]. The formation dates to the late Middle to early Late Jurassic Period and may have a thickness of up to 4600 m. The slate belongs to the Salt Spring formation, of the Late Jurassic Period [*Clark, 1964*], and originally consisted of fine-grained sediments overlying the volcanic rocks. During later uplift activity, these layers were folded, faulted, and metamorphosed, resulting in repeated bands of slate and greenstone (Figure 3.5).

Surface expression of the Salt Spring slate occurs near the entrance to the site, while Gopher Ridge volcanics outcrop in multiple locations throughout. Both formations consistently trend north-northwest and are extensively fractured. These fractures have a 320 to 330° strike and a deep 55 to 70° SW dip. The exposed slate exhibits a characteristic “tombstone” appearance (Figure 3.6).

Both formations belong to the “western block”, the area bounded by the Bear Mountains fault zone to the east and the young alluvial cover of the Central Valley to the west. Two very similar formations lie across the fault zone: the Mariposa Slate and the Logtown Ridge Volcanics. These formations were likely deposited at the same times and by the same mechanisms as the greenstone and slate formations on the Tonzi site; however, geologic evidence directly linking the groups is sparse, according to the

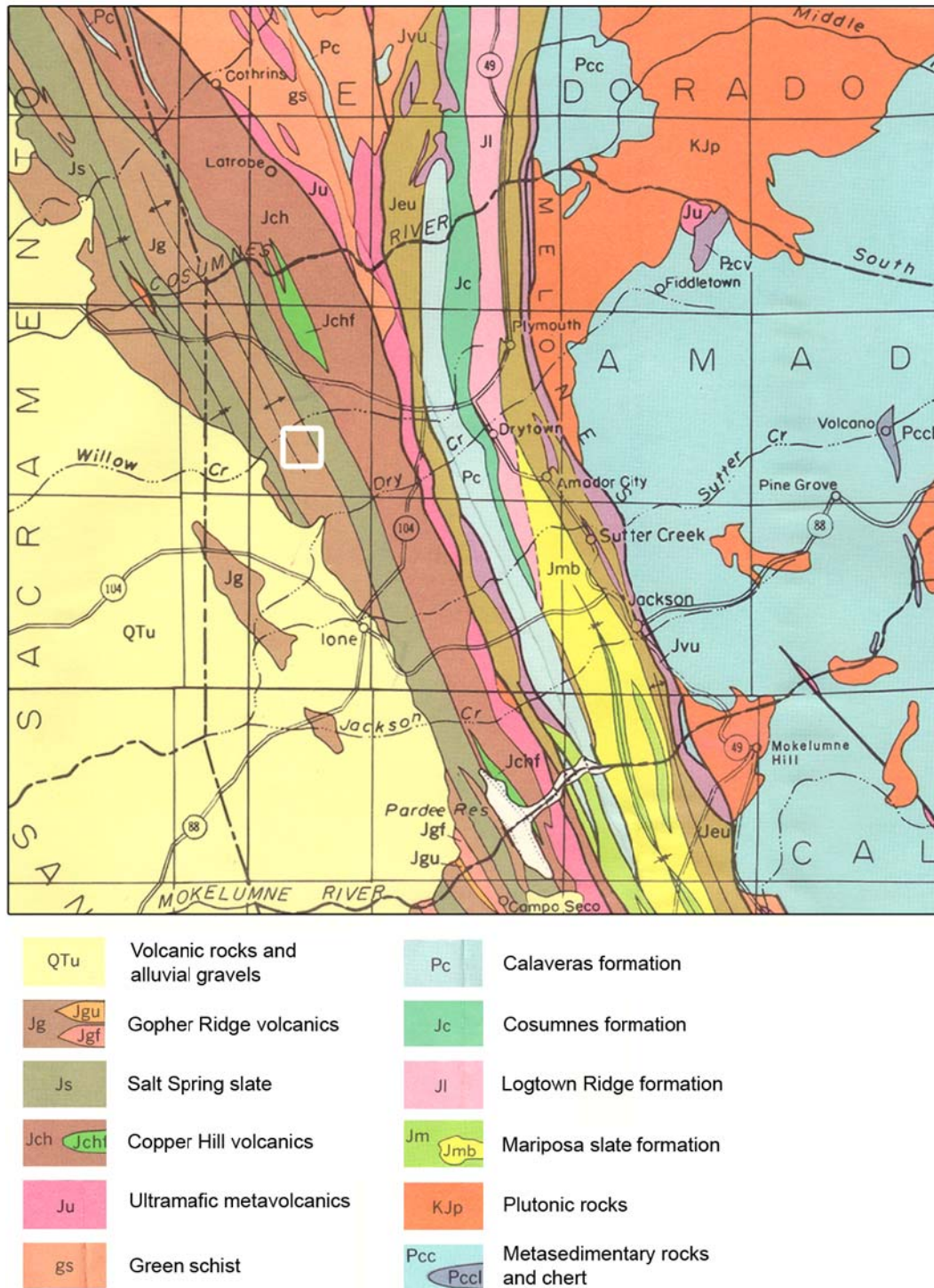


Figure 3.5: Geologic Map of the Tonzi Ranch Area
 Selected portion of the “Geologic Map of the Western Sierra Nevada between the Merced and Cosumnes Rivers, California” [Clark, 1964]. The approximate area of the site is shown in the white outline. With the exception of the alluvium in the Central Valley, all formations shown are metamorphic or plutonic in nature.



Figure 3.6: Rock Outcrops at Tonzi Ranch
Left: Salt Spring Slate near the entrance of the site. Right: Gopher Ridge Volcanics (greenstone) closer to the tower. Both the slate and the greenstone outcrops are highly fractured, and these fractures trend north-northwest with a 320 to 330° strike and a 55 to 70° SW dip.

literature [Clark, 1964; Duffield and Sharp, 1975]. Chapman et al. [1975] offer this description, matched well by conditions on site:

Rocks of the Amador Group generally have a moderate-to-steep dip and crop out in long northwest-trending belts separated by bands of slate of the Mariposa Formation. The prominent ridge north of Jackson Valley and west of Ione is composed of greenstone of the Logtown Ridge Formation. The Amador Group is believed to be late Middle and early Late Jurassic [Taliaferro, 1943]. In this area, it is in sharp conformable contact with the overlying Mariposa Formation [Chapman et al., 1975].

The relationship between the groups is only consequential in that geochemical data exists for the more thoroughly studied Logtown Ridge and Mariposa formations. A geochemical analysis of the greenstone samples from the Logtown Ridge formation are shown in Table 3.3 and indicates that the material is mafic, i.e., it is a silicate rock high in iron and magnesium. The iron contained in the rocks creates a distinctive color change from green to dark orange as the rocks weather into soil.

Nutrients, particularly nitrogen, are also important geochemical considerations at forest and woody sites. Holloway and Dahlgren [1999] reported that geologic nitrogen provided a significant portion of the total nitrogen found in soils in certain regions of the

Table 3.3: Geochemical Analysis of Greenstone

Chemical	Range [%]
SiO ₂	48.7 – 55.5
Al ₂ O ₃	14.6 – 17.9
Fe ₂ O ₃	0.5 – 3.2
FeO	5.2 – 9.9
MgO	2.9 – 11.8
CaO	5.7 – 11.6
Na ₂ O	2.1 – 3.8
K ₂ O	0.9 – 2.8
TiO ₂	0.6 – 1.7
P ₂ O ₅	0.2 – 0.5
MnO	0.1 – 0.2
CO ₂	0.1 – 1.9

Data from [Duffield and Sharp, 1975]

Sierra Nevada foothills. The weathering of parent rock materials created soils rich in nitrogen; the Logtown Ridge greenstone formed soils belonging to the Auburn Series, and the Mariposa slate formed soils of the Exchequer series. During weathering, the greenstone and the slate respectively released 2350 and 2570 kg N ha⁻¹, representing between 30 to 50% of the soil nitrogen currently present [Holloway and Dahlgren, 1999]. In addition to affecting the water quality of the Cosumnes and Mokelumne watersheds, this geologic nitrogen could have a large impact on the biogeochemical cycling in ecosystems like that at Tonzi Ranch. The easily available nitrogen may contribute to the success of oak savannas in the foothills.

3.4 Hydrogeology

An area soil survey estimated the saturated hydraulic conductivity in near surface rocks to be 0 to $1.4 \times 10^{-6} \text{ m s}^{-1}$ [Sketchley, 1965]. In other, fractured igneous and metamorphic rock formations, hydraulic conductivity has been measured at 1×10^{-13} to $3 \times 10^{-4} \text{ m s}^{-1}$ [Domenico and Schwartz, 1998; Singhal and Gupta, 1999]. Literature estimates of secondary porosity in fractured, crystalline rock range from 2 to 5% [Fetter, 2001] and from 0 to 10% [Domenico and Schwartz, 1998].

Few hydrogeological investigations have been conducted in Amador County, partly due to the scarcity of groundwater resources in the dominantly crystalline subsurface. Most wells are drilled for individual domestic and irrigation purposes; municipal water, where distributed, is derived primarily from surface water resources. The California Department of Water Resources “Mountain Counties Water Management Studies: Amador County” provides data on the water resources of the area, particularly how it will respond to future population growth [Chima, 1990]. An appendix to the report specifically addresses groundwater, distinguishing between areas of the county underlain by “hard rock” from those above alluvium. After examining a randomly sampled fraction of the county drilling permits issued from 1949 to 1990, Chima observed that most wells are drilled into fractured metamorphic rock and of these wells, most had a yield under 10 gallons per minute (0.01 L s^{-1}).

In 1977 and 1989, the land-owner installed two wells at the Tonzi Ranch site, for irrigation and domestic use. Three monitoring wells followed; these were installed in 2006 as part of this research project, designed to better characterize groundwater and aquifer properties near the study site itself. All wells, drilled by the Briski Well Drilling

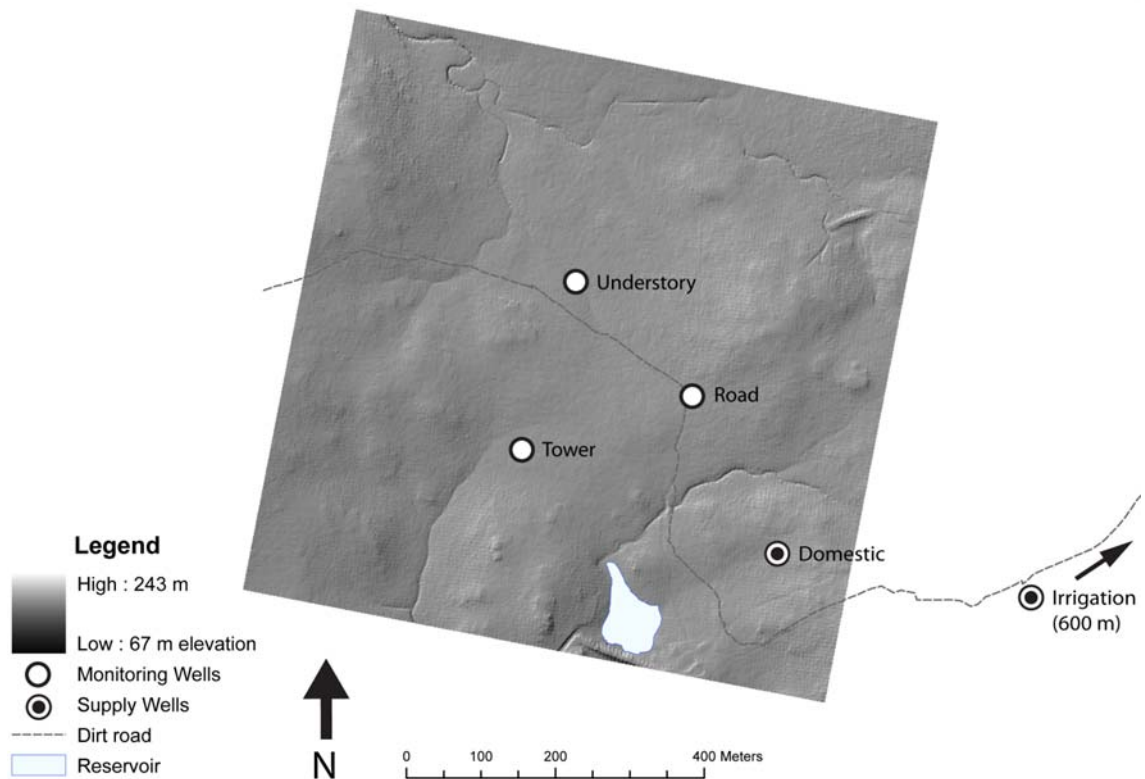


Figure 3.7: Well Locations and Hydrologic Features
 Two water supply wells, labeled Domestic and Irrigation, were initially present on the property, and three monitoring wells, labeled Understory, Road, and Tower, were installed for purposes of this study.

Company of San Andreas California, were placed using the air rotary drilling method. Figure 3.7 shows the location of the wells with respect to site features such as the dirt road, retention pond, and ephemeral streams.

Drilling logs indicate that the bedrock encountered consisted primarily of “hard greenstone” with frequent fracturing and sporadic quartz veins (Figure 3.8). Depth to “first water” ranged from 10.7 to 24.4 m and final static water level rose to between 9.1 to 13.7 m. In the three observation wells, depth to first water and static water level were equal, suggesting an unconfined aquifer. Brief air injection pumping tests estimated

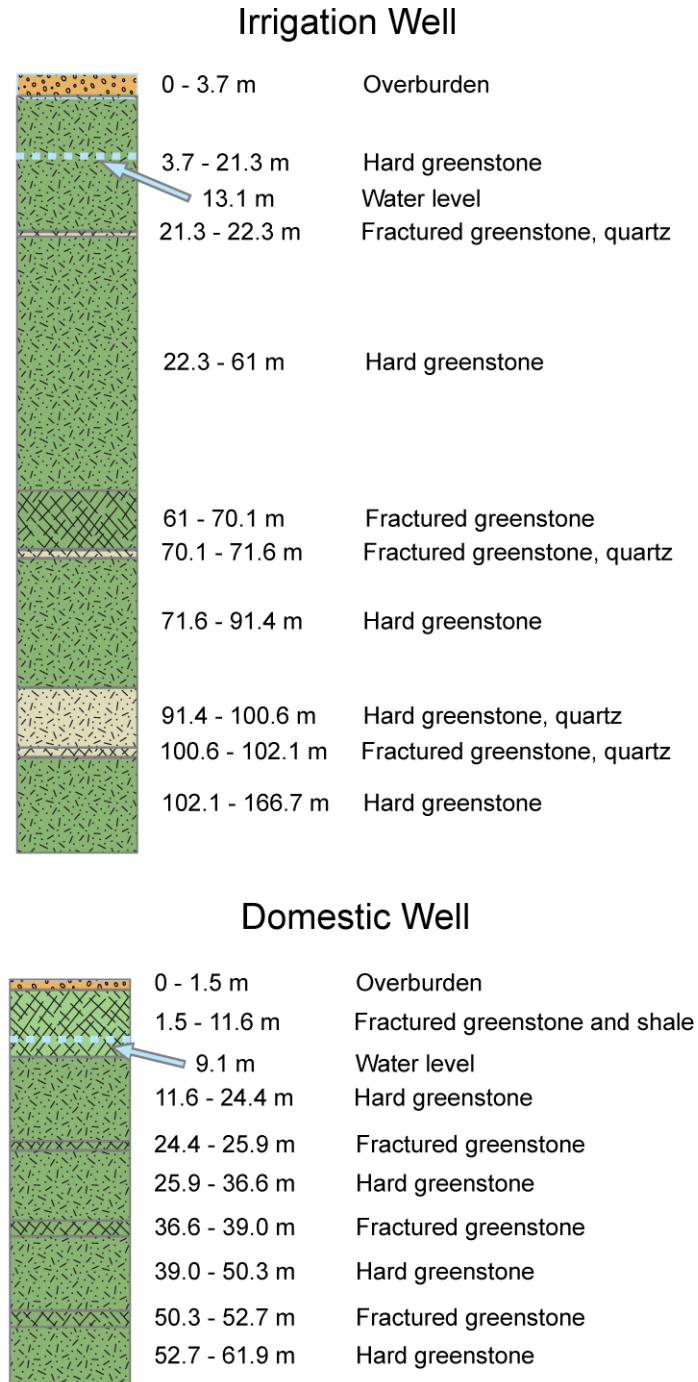
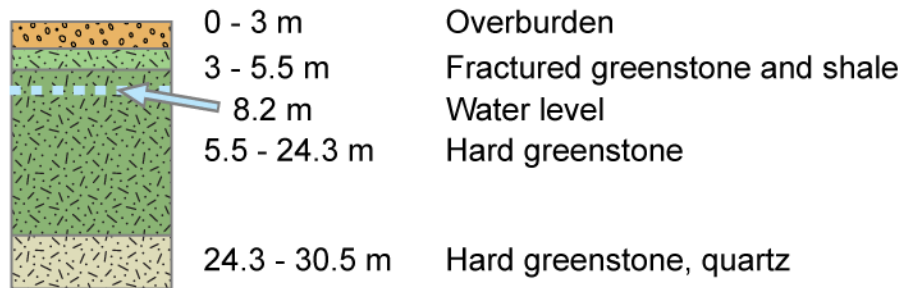


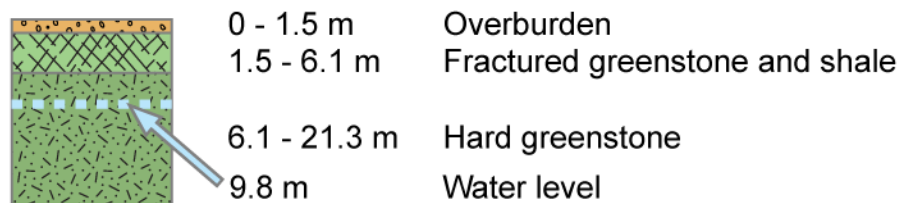
Figure 3.8: Profiles from Supply Wells

Hydrogeological columns reconstructed from drilling logs for irrigation (top) and domestic supply (bottom) wells completed on the property prior to the investigation. The wells are located approximately 950 m and 350 m, respectively, from the tower [Briski, 1977; 1989].

Understory Well



Tower Well



Road Well

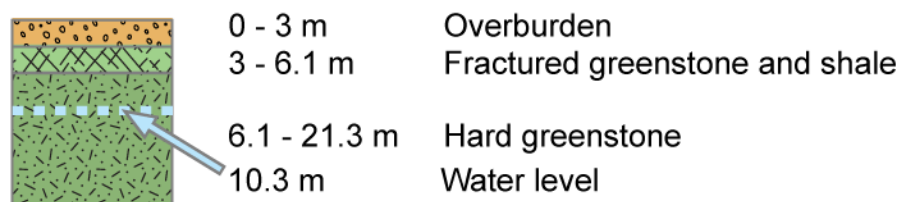


Figure 3.9: Profiles from Monitoring Wells
 Hydrogeological columns for the Understory Well (top), Tower Well (middle), and Road Well (bottom), which were drilled during the investigation. The three wells form a triangle centered on the tower and are all located within 150 m of it. For a map of the well locations, see Figure 3.7.

well yields from 6×10^{-2} to $3 \times 10^{-4} \text{ L s}^{-1}$, consistent with observations from the literature [Chima, 1990]. Table 3.4 summarizes the permitting records for each well.

Three slug tests were conducted on each of the wells, and the resulting data sets were analyzed using the Dagan method [1978] for wells screened across the water table,

Table 3.4: Tonzi Ranch Well Completion Data

Well	Date of Completion	Total Depth [m]	Casing Depth [m]	Depth to First Water [m]	Static Water Level [m]	Estimated Yield [L s ⁻¹]
Irrigation	9/22/1977	117	6.1	21.3	13.1	2.6 x 10 ⁻³
Domestic	8/25/1989	61.9	12.2	24.4	9.14	6.3 x 10 ⁻²
Understory	11/10/2006	30.5	9.14	12.2	12.2	1.3 x 10 ⁻³
Tower	11/15/2006	21.3	9.14	13.7	13.7	1.1 x 10 ⁻³
Road	11/16/2006	21.3	9.14	10.7	10.7	2.6 x 10 ⁻⁴

as described by Butler [1997]. For each test, 6.9 L of water were removed from the well, creating a water level drop of approximately 0.38 m within the 15.24 cm diameter well bore. After slug removal, the depth to the water table was measured as the water level inside the well recovered. For the understory well, depth was collected both manually, using a tape style water level meter, and automatically, using a pressure transducer. The two methods produced comparable results, allowing for only manual measurements in the other two wells. To produce values that were intercomparable, the measured depths were converted to represent changes in head ($H(t)$), with a head of -0.38 m representing the initial drawdown (H_0) and a head of 0 m indicating complete recovery. The time series of heads for each test are shown in Figure 3.10.

Figure 3.11 shows plots of the normalized head as a function of time. For a fully penetrating well, the head is typically normalized using the formula:

$$H'(t) = \frac{H(t)}{H_0 \left(\frac{2b - H(t)}{2b - H_0} \right)} \quad (3.4)$$

where b is the effective well screen length, or the total depth of the well minus the depth

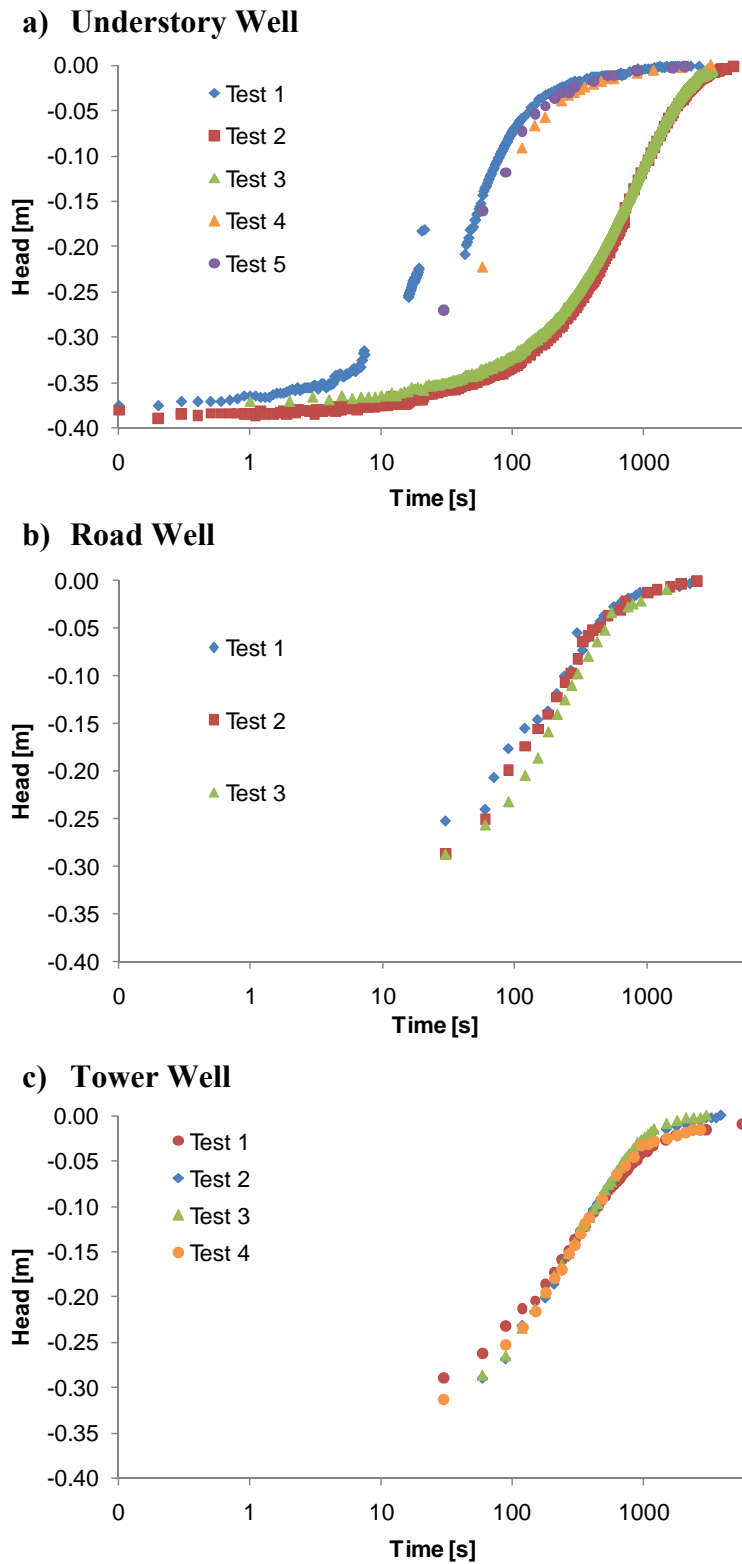


Figure 3.10: Drawdown and Recovery during Slug Tests
Groundwater level drawdown as a function of time since slug removal for the (a) Understory Well, (b) Road Well, and (c) Tower Well.

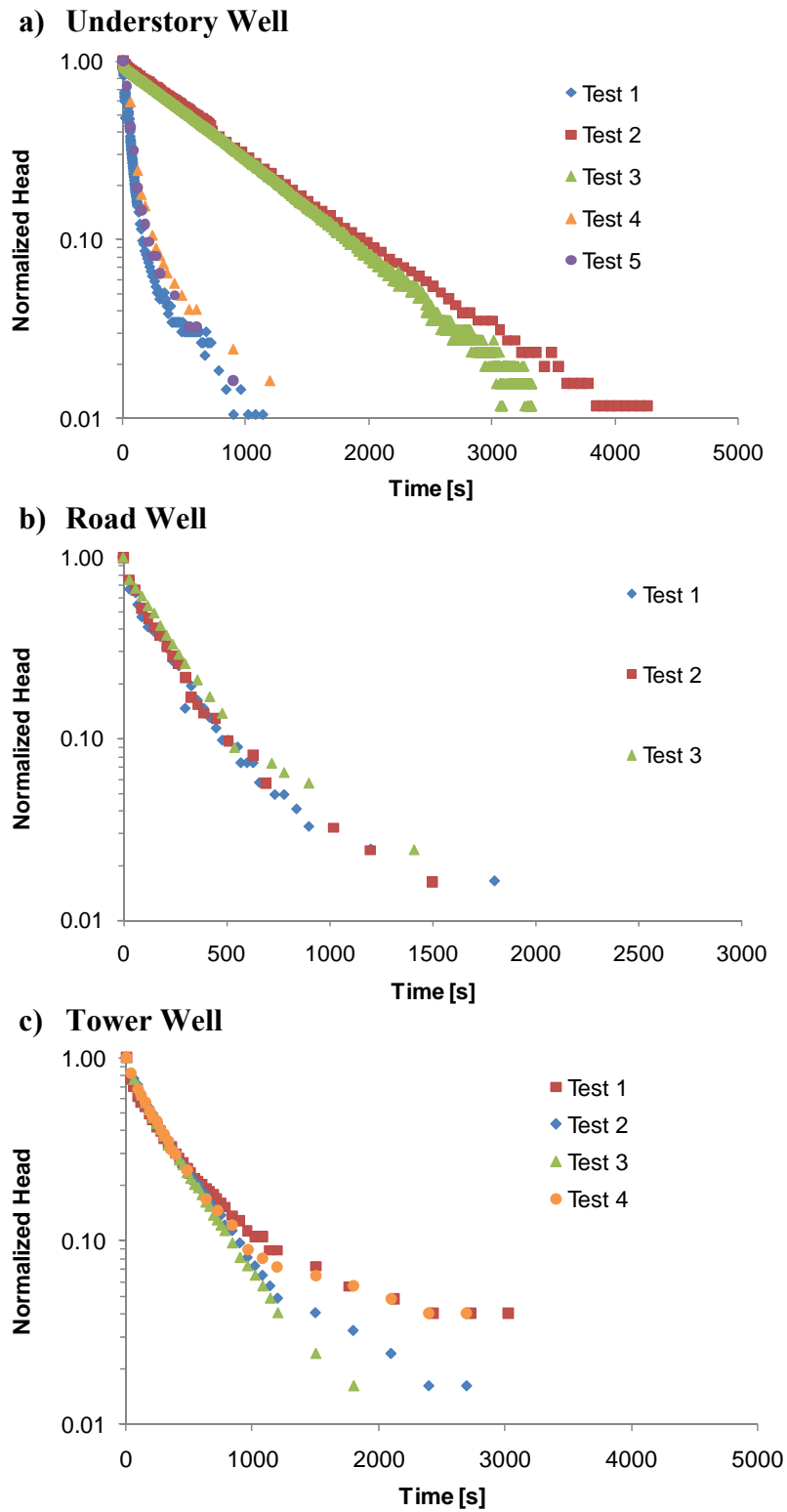


Figure 3.11: Normalized Head during Slug Tests
 Normalized head as a function of time since slug removal for (a) Understory Well, (b) Road Well, and (c) Tower Well. See text for an explanation of the normalization procedure.

to the water table. The length of b is approximately 21 m in the Understory Well and 12 m in the Road and Tower Wells. Since $H_0 \ll b$, the equation reduces to:

$$H'(t) = \frac{H(t)}{H_0} \quad (3.5)$$

The \log_{10} of the normalized head is then plotted as a function of time. A line is fitted to the early, linear portion of the measurements, and its slope (s) is determined. The basic lag-time, T_0 , was found using the equation $T_0 = 1/s$. Figure 3.11 shows plots of the normalized head as a function of time for each of the slug tests.

Hydraulic conductivity is then calculated using the equation:

$$K_c = \frac{r_c^2(1/P)}{2bT_0} \quad (3.6)$$

where the remaining terms r_c and P represent the effective radius of the casing and a dimensionless flow parameter. The effective radius in a well without a filter pack is ideally the same as the nominal radius, in this case 7.62 cm. By comparing the actual initial drawdown to the drawdown anticipated based on the volume removed, this equivalency can be confirmed. Here, the initial drawdown could only be measured in the Understory Well, using the pressure transducer; in all tests, it equaled the expected drawdown, 0.38 m. It was assumed that the remaining wells would exhibit the same behavior.

The dimensionless flow parameter P originates in Dagan's semianalytical solution to the flow problem [1978] and allows for the consideration of formation anisotropy. It is calculated using the formula:

$$P = 0.216(1 + 20\psi) \quad (3.7)$$

Table 3.5: Hydraulic Conductivity

	Test 1	Test 2	Test 3	Test 4	Test 5
Understory Well	7.1×10^{-6}	6.3×10^{-7}	7.1×10^{-7}	3.5×10^{-6}	5.0×10^{-6}
Road Well	4.4×10^{-6}	4.3×10^{-6}	4.6×10^{-6}	-	-
Tower Well	2.2×10^{-6}	2.5×10^{-6}	2.6×10^{-6}	2.4×10^{-6}	-

Hydraulic conductivity, [m s⁻¹]

where ψ is a function of the vertical to radial anisotropy ratio (K_z/K_r), the effective well length b , and the well radius r_w :

$$\psi = \frac{r_w \sqrt{K_z/K_r}}{b} \quad (3.8)$$

As is typically done, K_z/K_r was assumed to be equal to one.

The computed hydraulic conductivities are shown in Table 3.5. All values range from 10^{-6} to 10^{-7} m s⁻¹, in the high range of the literature values previously discussed. Hydraulic conductivity (K) measured 4.3 to 4.6×10^{-6} m s⁻¹ in the Road Well, and 2.1 to 2.6×10^{-6} m s⁻¹ in the Tower Well. The differences between repetitions were 9% and 20%, respectively - acceptable measurement error for a slug test. For the Understory Well, the K values were over an order of magnitude different during tests conducted at different times during the year.

The most likely explanation for the large difference is that the hydraulic conductivity near the Understory Well is vertically anisotropic, particularly that it increases with depth. In theory, in a slug test in an unconfined aquifer, the water is extracted from the upper portion of the water column in the well, and the water flowing

Table 3.6: Slug Test Results in Understory Well

Test	Date	Depth to Water [m]	Hydraulic Conductivity [m s⁻¹]
1	8/20/2008	8.89	7.1×10^{-6}
4	2/27/2009	9.18	3.5×10^{-6}
5	2/27/2009	9.18	5.0×10^{-6}
2	12/06/2008	9.62	6.3×10^{-7}
3	1/14/2009	9.71	7.1×10^{-7}

back into the well comes primarily from the area right under the water table. This means that they are sensitive to the depth of water in the well. Tests 1, 4, and 5 were conducted when the depth to groundwater was between 8.9 and 9.2 m, while Tests 2 and 3 were performed at depths of 9.6 to 9.7 m (Table 3.6). A plot of hydraulic conductivity as a function of depth to water table reveals that K does increase with depth, at a rate of $8 \times 10^{-6} \text{ m s}^{-1}$ per meter (Figure 3.12). While there is nothing in the well logs to suggest why this may be true for one well and not the other two, it is likely that the degree of fracturing is inconsistent over the depth of all of the wells, but is only apparent in one. This finding highlights the subsurface heterogeneity and the importance of testing in multiple wells.

3.5 Summary

In summary, the characteristics of the soils and subsurface hydrology at the Tonzi Ranch site are heavily influenced by the fractured, metavolcanic rock that underlies it. This rock weathers into a thin layer of loamy, nitrogen rich soils, which

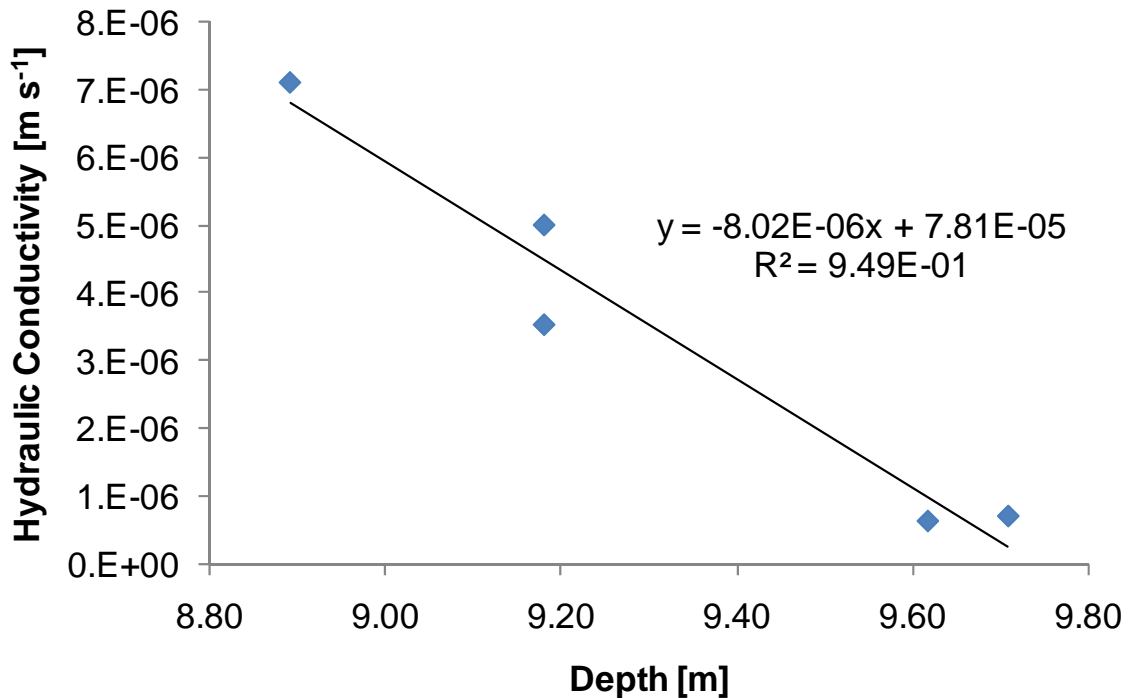


Figure 3.12: Understory Well Hydraulic Conductivity as a Function of Depth

As the water table declines in the Understory Well, the saturated hydraulic conductivity (K) is reduced. A one meter change in depth to water table produced a K value an order of magnitude lower.

support the oak savanna. As the depth from the surface increases, the soils transition into a saprolite layer composed of clay, gravel, and cobblestones. This saprolite is followed by highly fractured metavolcanic greenstone interbedded with weakly metamorphosed sedimentary rock. The fractures in this bedrock likely decrease with depth, reducing the secondary porosity, and thus the hydraulic conductivity, to near zero.

Water storage occurs primarily in the pores of the soil and in the fractures of the bedrock, and these reservoirs supply all of the herbaceous and woody vegetation with the water required for transpiration. The timing of this water use and storage is key to understanding the site's ecohydrology. Here, transpiration demand is out-of-sync with precipitation; the water stored during the wet season is critical to sustaining plants during

the dry season. The next chapter presents an analysis of the relative importance of the ephemeral and shallow soil stores and the deep and more permanent groundwater reserves.

Chapter 4: Groundwater Uptake in a Semi-Arid Oak Savanna

4.1 Introduction

California's oak savanna ecosystems may be subject to increased water stress as climate change fundamentally alters hydrological patterns in the region [Kueppers *et al.*, 2005]. Previous studies of these water-limited ecosystems have focused on soil moisture as a regulator of transpiration [Baldocchi *et al.*, 2004; Chen *et al.*, 2008; Miller *et al.*, 2007], but have not yet addressed the role of groundwater in the system's overall water budget, leading to a potentially incomplete understanding of water use. In this paper, we explore the uptake of groundwater resources by woody vegetation in one such ecosystem and discuss its ecohydrological implications.

Current research into phreatophytic, or groundwater dependent, vegetation has focused on uptake from shallow aquifers associated with riparian zones [Butler *et al.*, 2007; Lamontagne *et al.*, 2005; Lautz, 2008; Loheide, 2008; Scott *et al.*, 2008b] and humidland systems [Rodríguez-Iturbe *et al.*, 2007; Rodríguez-Iturbe *et al.*, 2008], while groundwater has been largely considered "out-of-reach" for many semi-arid ecosystems. However, several studies have demonstrated that woody vegetation in dryland areas can tap groundwater 7 m or more below the land surface [Burgess *et al.*, 2001b; Jewett *et al.*, 2004; McElrone *et al.*, 2003; Scott *et al.*, 2004]. A tracer study conducted on a California oak ecosystem demonstrated that blue oaks (*Quercus douglasii*) penetrate through up to 24 m of fractured rock in order to access groundwater [Lewis and Burgy, 1964]. Canadell *et al.* [1996] noted that sclerophyllous trees had a mean maximum

rooting depth of 12.6 ± 3.4 m; this type of vegetation consists mostly of *Eucalyptus* and *Quercus* species found in Mediterranean areas.

Determining if, and to what extent, an ecosystem is groundwater dependent can be difficult. Eamus et al. [2006a] suggest that an ecosystem may be reliant on the subsurface presence of groundwater if it meets one or more of the following criteria:

1. The rooting depth of the vegetation is at or below the water table or its capillary fringe.
2. The vegetation, or a portion of it, continues fixing carbon during extended dry periods.
3. Within areas of similar rainfall inputs, some ecosystems show large changes in leaf area index while others do not.
4. Daily changes in groundwater depth are observed which are not due to lateral flows, percolation to depth, or atmospheric pressure changes.
5. The annual rate of transpiration is larger than the rate of water entering the area, i.e. sum of the precipitation and run-on rates.
6. Significant surface expressions of groundwater exist, and the vegetation associated with these expressions is substantially different from other nearby vegetation.

A large spectrum of reliance on groundwater may be present, but individual ecosystems or species are typically further distinguished as having either obligate or facultative dependencies [Eamus et al., 2006a]. Naumburg et al. [2005] note that when groundwater becomes inaccessible “the fate of...drought-stress-tolerant species [*xeric*

phreatophytes] may range from minor biomass losses to significant diebacks.” Making this distinction is difficult, however, since it may require long periods of observation.

Multiple techniques can more readily reveal the use of groundwater by woody vegetation [O'Grady *et al.*, 2006], although the precision and conclusiveness of these methods vary. Studies using direct hydrological measurements to quantify the use of groundwater by vegetation have noted seasonally dependent uptake composing between 20 and 50% of total evapotranspiration by *Juniperus ashei* and *Quercus fusiformis* trees [McElrone *et al.*, 2003]; 14 to 70% in a semi-arid shrubland system [Scott *et al.*, 2008a]; and 9% in old-growth coniferous forests [Warren *et al.*, 2006]. Stable oxygen and hydrogen isotope methods [Dawson *et al.*, 2002] can also yield information on the relative use of water sources. An estimate of the proportion of groundwater used by a plant can be found by comparing the groundwater's isotope fractionation to that of the plant's xylem water and of the surrounding surface or soil water [Cramer *et al.*, 1999; Dawson, 1993; Snyder and Williams, 2000]. Predawn leaf water potentials that are less negative than soil water potentials can serve as a crude indicator that plant roots are currently exposed to groundwater [Eamus *et al.*, 2006b], although several plant water use processes conflate the issue, particularly nighttime transpiration and refilling of internal water storage [Bucci *et al.*, 2004; Donovan *et al.*, 1999].

Groundwater use by vegetation has substantial implications for the management of water resources, the response of ecosystems to climate change, and the modeling of ecosystem water use. Over-pumping of aquifers or decreased rainfall due to climate change could potentially initiate a positive, or amplifying, feedback loop leading to more arid landscapes; by lowering the water table and preventing vegetation access, these

events can reduce transpiration which in turn reduces precipitation. Modeling these systems and their responses to drought can be difficult since established ecohydrology and ecophysiology models do not yet address the problem. Uptake from below the soil zone affects the water balance at a point, altering the popular stochastic formulation of the problem [Rodríguez-Iturbe and Porporato, 2004] by adding an additional and potentially non-steady-state term. Ecophysiological canopy models, such as CANOAK [Baldocchi *et al.*, 2002], need to accurately represent leaf water stress and its effect on stomatal conductance to predict water vapor and carbon dioxide fluxes.

In order to address the question of groundwater uptake in a water-controlled ecosystem, the objectives of this research are: 1) To integrate three measurement strategies for quantifying groundwater uptake - water balance closure at the stand level, water balance closure at the tree level, and diurnal water table fluctuations; 2) To use indirect lines of evidence for groundwater uptake, including water potential measurements and oxygen isotope ratios, to support our conclusions about if and when uptake is occurring; 3) To estimate the measurement error associated with each direct and indirect method and to suggest ways this error may be minimized; and 4) To discuss challenges associated with quantification of groundwater uptake, particularly the problems of measuring “storage” in vegetative and soil reservoirs.

Specifically, we ask the following questions: What percentage of transpired water comes from deep groundwater sources? Does this vary over time? What driving force (hydraulic gradient) is necessary to move water from the aquifer to the top of the canopy? Do our water potential measurements indicate whether this force is present and when? How fast will water move under this gradient and will this affect the time-scale

over which we need to quantify hydrologic fluxes? Do indirect measurements, such as isotope fractionation and water potential data, corroborate the conclusions supported by direct hydrological measurements?

We hypothesize that mature oaks have a seasonal, yet obligate, dependency on groundwater for their survival during the dry summer months, and that the percentage of transpired water from groundwater is non-zero during the spring months and increases during times of soil water scarcity. Water potential levels reached in the leaves will create a hydraulic gradient sufficient to transport water the 20 m between the groundwater table and the top of the canopy, and these potentials will suggest the percentage of roots tapping deep water sources. The multiple direct methods will obtain results that are consistent on the timing of uptake, although magnitude of uptake may vary due to differences in sampling scale.

4.2 Data Collection

4.2.1 Site Description

The site, Tonzi Ranch, is an oak savanna located in the western Sierra Nevada foothills near Ione, CA (Latitude: 38.4311°N, longitude: 120.966°W, altitude 177 m). The site is a member of AmeriFlux and Fluxnet micrometeorological observation networks, and half-hourly water vapor flux, soil moisture, and precipitation measurements have been collected near-continuously since Spring 2001. In this research, we confine our study period to January 2007 through December 2008 and define our study area as the 40,000 m² surrounding the site's eddy-covariance flux tower.

In this oak savanna ecosystem, trees cover approximately 40% of the landscape in the study area [Baldocchi *et al.*, 2004]; they are predominately blue oaks (*Quercus douglasii*) with occasional grey pines (*Pinus sabiniana*). The mean height of the canopy is 7.1 m, with approximately 194 stems per hectare, a mean diameter at breast height of 0.199 m, and a basal area of 18 m² ha⁻¹ [Baldocchi *et al.*, 2004]. The understory cover consists primarily of non-native herbs and grasses, with approximately 31% false brome (*Brachypodium distachyon*), 15% soft brome (*Bromus hordeaceus*), 7% redstem filaree (*Erodium cicutarium*), 5% smooth cat's ear (*Hypochaeris glabra*), 12% other unidentified grasses, 16% oak litter, 8% other litter, and 6% bare ground (Wenk, 2008, unpublished data).

The site's hydroclimate is Mediterranean and semi-arid, receiving 370 to 780 mm of rain per year and losing between 350 and 485 mm of this to evapotranspiration. Most rainfall occurs during the cool wet season (November to April), with almost no precipitation occurring during the hot dry season (May to October). During the study period (2007 to 2008), no surface water features were observed near the tower; however, during extremely wet years, ephemeral streams can occur. These, as well as precipitation, feed a small, man-made reservoir approximately 500 m from the tower. These hydrological features can be seen on a relief map of the site (Figure 4.1).

The site's hydrogeology is typical of the Sierra Nevada foothills [Duffield and Sharp, 1975]. It has a thin layer of surface soil, 60 to 100 cm, which is classified as silt loam to rocky silt loam [Sketchley, 1965]. Approximately four to eight meters of saprolite (weathered rock) follows until reaching the bedrock, which consists of fractured, metamorphosed volcanic rocks (greenstone) and sedimentary rocks (slate) of

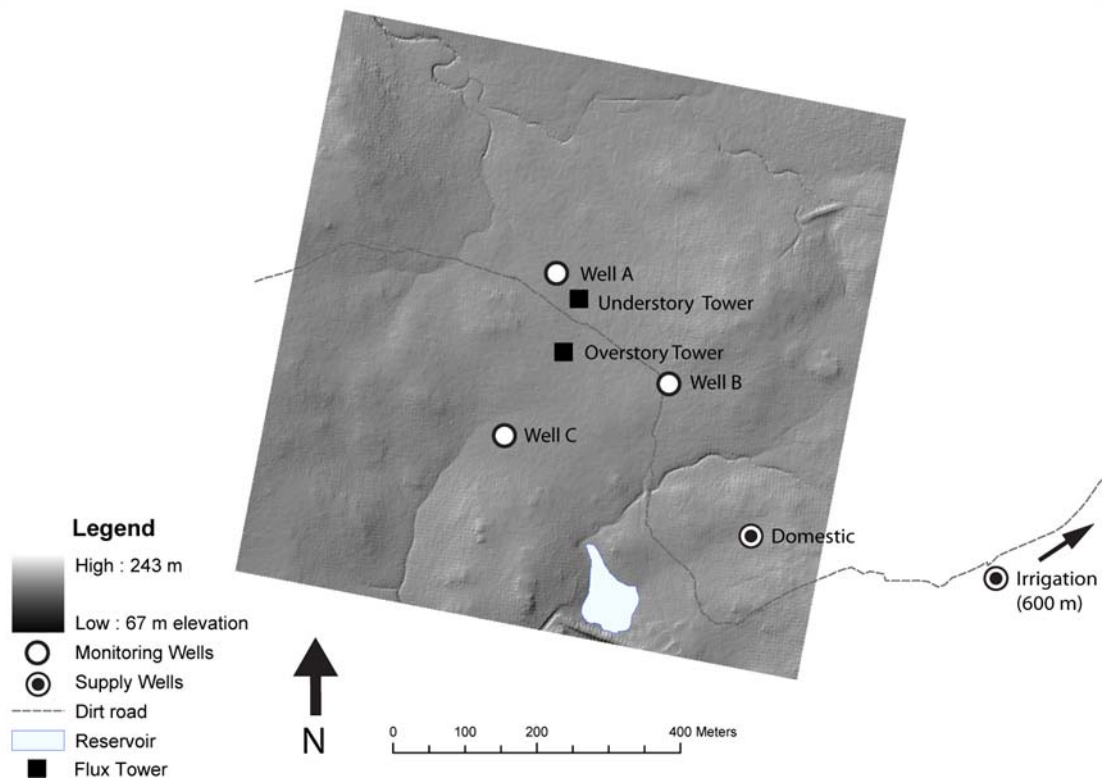


Figure 4.1: Tonzi Ranch Site Map

Relief map showing the location of hydrological features, monitoring and supply wells, and the eddy-covariance towers.

the Jurassic period. The depth to groundwater ranges between 7 to 12 m below ground surface, and the groundwater is contained within a fractured rock “aquifer”. Preliminary pumping tests estimate a maximum groundwater yield between 0.015 to 0.063 L s^{-1} (0.25 and 1 gpm), making the area unsuitable for groundwater extraction for domestic or agricultural use. Slug tests indicate a saturated hydraulic conductivity of 6×10^{-7} to $3 \times 10^{-6} \text{ m s}^{-1}$ (see Section 3.4).

4.2.2 Hydrological Measurements

A suite of hydrological measurements have been collected at the site, in order to characterize the flows of water into and out of the study area and its water storage.

Figure 4.1 shows a map of the site and instrument locations. All measurements are obtained every half-hour, unless otherwise noted. Precipitation was measured using a tipping bucket range gauge (Texas Electronics, TE 5252 mm), air pressure was measured with a capacitance barometer (model PTB101B, Vaisala, Helsinki, Finland), and air temperature and relative humidity were measured with a platinum resistance thermometer and a solid-state humicap (model HMP-45A, Vaisala, Helsinki, Finland), shielded from the sun and aspirated.

The eddy-covariance method [*Baldocchi, 2003*] was used to measure latent heat flux (and by proxy, evapotranspiration). As part of the method, wind velocity fluctuations were measured with a three-dimensional ultra-sonic anemometer (Windmaster Pro, Gill Instruments, Lymington, UK), and water vapor density was measured using an open-path infrared absorption gas analyzer (model LI-7500, LICOR, Lincoln, NE). Two eddy-covariance towers are present at the site – an overstory tower located at 23 m above ground (16 m above the canopy) and an understory tower located at 2 m above the ground surface. The combination of towers allows total stand tree transpiration to be calculated by taking the difference in latent heat flux from the understory (representing the evaporation from the soil and the grasses) and the flux from the overstory (representing the total stand flux). During the summer, understory evapotranspiration is near zero; the winter annual grasses and herbs have died and the surface soil is near its hygroscopic point.

To measure individual tree transpiration and soil environment, a network of nine “sap flow stations” were located across the site. Each station measured the sap velocity at four points within one tree, using the heat ratio method [*Burgess et al., 2001a*]. Each

station was also equipped with five ECH₂O EC-5 soil moisture sensors (Decagon, Pullman, WA), three located immediately adjacent to the tree at depths of 5, 20, and 50 cm, one at the tree's drip-line at a depth of 20 cm, and one at the nearest canopy opening at a depth of 20 cm. One station was also equipped with two gypsum blocks (Model 227, Delmhorst, Towaco, NJ) to measure soil water potential at a depth of 20 cm. During 2008, tree diameter was also recorded on a biweekly basis using manual band dendrometers (Series 5 Low Tension, Agricultural Electronics Corporation, Tucson, Arizona). To complement these measurements, midday and predawn leaf water potentials were measured in three of these trees, every 10 to 14 days during the growing season, using a portable plant water status console (Model 3005, Soil Moisture Corp, Santa Barbara, CA).

Biweekly measurements of depth to groundwater have been manually recorded in three observation wells since their installation in Fall 2006, with automated half-hourly measurements collected in one well. Manual measurements were made with a water level indicator tape (Model 101, Solinst, Georgetown, CA), while a cable vented pressure transducer and datalogger was used for the continuous measurements (Model WL16U-15, Global Water Instrumentation, Gold River, CA). Biweekly groundwater gradient was calculated from these measurements.

Soil, stem, and groundwater samples were collected for ¹⁸O stable isotope analysis during August 2008, and rain and pond water was sampled during the following wet season, in April 2009. A total of 15 soil samples were obtained using a hand auger: three depths (5 - 15 cm, 15 - 30 cm, and 30 - 50 cm) at five points located near the sap flow stations. Three, 4 cm long stem samples were collected from each sap flow tree,

culled from randomly selected branches at a height of approximately 2 m. Groundwater samples were obtained from each well using a stainless-steel, submersible pump placed approximately 0.5 m below the water surface. Prior to collection, each well was purged by extracting three well volumes; this procedure was necessary in order to ensure that water was obtained directly from the formation itself and not the well bore. All samples were placed in plastic-capped glass vials, sealed with parafilm to prevent evaporation, and stored at -20°C until analysis. Water was extracted from the soil and stem samples using the cryogenic vacuum distillation-extraction method [Ehleringer and Osmond, 1989; West *et al.*, 2006]. To prepare for analysis, 200 μL of each sample was pipetted into a 10 mL Exetainer which was then purged with 0.2% carbon dioxide in helium and allowed to come to equilibrium at room temperature for 48 hours. The ^{18}O in the CO_2 was then measured using a Thermo Delta Plus XL mass spectrometer with a Thermo Gas Bench II [Center for Stable Isotope Biogeochemistry, 2009]. Samples were run against BSMOW and multiple other controls, and values were reported as the ratio oxygen-18 /oxygen-16 relative to the VSMOW standard ($\delta^{18}\text{O}$, ‰).

4.3 Data Analysis

In this work, we compare three methods for estimating groundwater use from direct hydrological measurements. The first method uses diurnal fluctuations in depth to groundwater to isolate the daily change in groundwater (driven by vegetative uptake) from the overall, seasonal trends in the water table level. The second is the flux-tower water budget closure method. This method takes measurements of canopy evapotranspiration and site precipitation using established micrometeorological

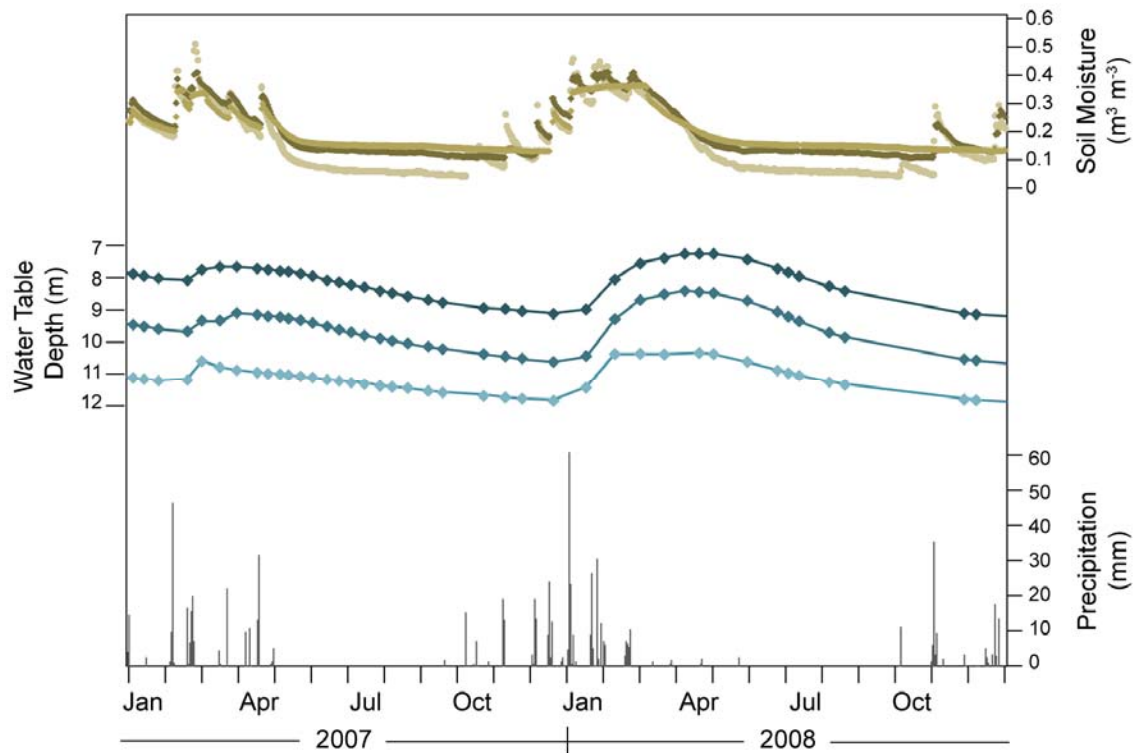


Figure 4.2: Temporal Patterns of Water Flux and Storage
Groundwater table elevations during the study period, with daily precipitation and soil moisture values. The wells are located in a triangular pattern, centered on the flux tower. Soil moisture sensors are buried within 10 m of the tower.

techniques and calculates the groundwater uptake that must occur based on the deficit between incoming, outgoing, and stored water in the system. The third method uses the same water budget principles as the first, except that it is confined to a much smaller region immediately around a single tree. Instead of using eddy-covariance data, this method uses measurements of sap flow to determine transpiration.

4.3.1 Uptake from Groundwater Measurements

We have measured the groundwater levels in all wells on a biweekly basis since December 2006 (Figure 4.2). Continuous measurements have been collected on a half-hour cycle in the “Understory Well” since May 2007. To calculate the daily vegetative

groundwater uptake (U), we use the method developed by White [1932] and later refined [Butler *et al.*, 2007; Vincke and Thiry, 2008]:

$$U = S_y[R + D] \quad (4.1)$$

where S_y is the specific yield of the aquifer and is dimensionless; R is the rate of aquifer recharge, in m d^{-1} , calculated from the slope of the water table between 10 pm that night and 7 am the next morning, when evapotranspiration is at a minimum; and D is the daily drawdown, in m d^{-1} . The drawdown is the change in groundwater head over the span of a day, which is found by computing the difference between the peak head on the initial day, H_1 , and the peak head on the subsequent day, H_2 , so that $D = (H_1 - H_2)/(1 \text{ day})$.

Loheide *et al.* [2005] discuss the major assumptions made with this method:

- (1) Diurnal water table fluctuations are a product of plant water use.
- (2) Groundwater consumption by plants is negligible between midnight and 4 A.M.
- (3) A constant rate of flow into the near-well region occurs over the entire day; that is, impacts of recharge events, cyclic pumping, etc. are assumed negligible.
- (4) A representative value of specific yield can be determined.

To address the validity of these assumptions for the Tonzi site, we note that first, we have carefully checked and eliminated other possible sources of diurnal fluctuations.

The main sources of such fluctuations are tides from nearby water bodies, groundwater extraction, changes in atmospheric pressure, and changes in temperature [Freeze and Cherry, 1979]. The first two causes can be eliminated, as there are no large water bodies in the vicinity, and the only nearby groundwater pumping is minimal (<1 gpm) and takes place in the landowner's personal well, over 200 m away (Figure 4.1). These effects would also create a year-round signal, which is not observed in the data. To reduce the potential for atmospheric pressure effects on the measurements, a vented pressure

transducer was used. Pressure effects directly on the water table were not likely, since the aquifer is unconfined (see Section 3.4). To eliminate any further uncertainty, we tested for correlations between the changes in groundwater depth and the changes in temperature or pressure, as measured by the nearby meteorological equipment; no correlations were found, even when potential time lag effects were taken into account.

The second assumption, that no tree uptake is occurring overnight, is more problematic. Previous studies have shown that trees at the site continue to transpire during the nighttime [Fisher *et al.*, 2007], as indicated by positive sap flows during the night. These flows continue to be observed (see Chapter 5), and amount to approximately 10 to 20% of daytime values (Figure 5.6). The apparent violation of this assumption could lead to the under-prediction of R , the aquifer recharge term in Equation (4.1), reducing the daily value of ET_G when overnight transpiration is occurring.

As suggested by the third assumption, in shallow aquifers, this analysis must be confined to days when no precipitation occurs, as it can interfere with the signal. This consideration is minimal at the Tonzi Ranch, due to its long dry summers. Additionally, since the aquifer is over 8 m below the ground surface, when precipitation events do happen, they are only rarely seen in the fluctuations.

Specific yield, the sole parameter in Equation (4.1), represents the volume of water released from the aquifer per total rock volume. In this context, it can be understood as the ratio of plant uptake to the measured fluctuation. For instance, if storativity is 0.10, and a groundwater fluctuation of 2 cm is observed over the course of a day, then the calculated groundwater uptake would be 2 mm d^{-1} . In an unconfined

aquifer, such as this one, specific yield and storativity are typically equivalent and are roughly equal to the porosity of the material [Domenico and Schwartz, 1998]. Literature estimates of total porosity in fractured, crystalline rock range from 0 to 0.10 [Domenico and Schwartz, 1998; Freeze and Cherry, 1979]. In other rocks with significant secondary porosity, such as shale and limestone, specific yield is found to be between 0.005 to 0.05 [Driscoll, 1986]. As of this writing, pumping tests designed to measure specific yield are in the planning stages, and should be complete by mid-summer 2009.

4.3.2 Stand-level Uptake from Water Balance Closure

To estimate the stand-level uptake, a water budget is formed by specifying a control volume centered on the flux tower, creating a 200 m by 200 m square area which extends vertically from the soil/rock interface to the top of the flux tower (Figure 4.3).

In this control volume, the water budget can be defined as:

$$G_w + P - E = \frac{h_t}{\rho_w} \frac{\partial \rho_v}{\partial t} + z \frac{\partial \theta}{\partial t} + \frac{V_b}{A} \frac{\partial m_c}{\partial t} \quad (4.2)$$

where the fluxes, shown on the left-hand side of the equation, are: G_w , the net groundwater source or sink (m d^{-1}); P , the precipitation (m d^{-1}); and E , the stand evapotranspiration (m d^{-1}). On the right-hand side of the equation, the system storage terms are represented by the constants: h_t , the height of the eddy-covariance tower (23 m); ρ_w , the density of water (996 kg m^{-3}); z , the soil depth (0.6 m); A , the area of stand ($4.0 \times 10^4 \text{ m}^2$); and V_b , the volume of woody biomass (estimated as 61 m^3). The following system variables are included: ρ_v , the density of water vapor in atmosphere [g m^{-3}] ($18.01 \text{ g mol}^{-1} * \rho_v \text{ mol m}^{-3}$); θ , the soil moisture content [$\text{m}^3 \text{ m}^{-3}$]; m_c , the moisture content of woody biomass [$\text{m}^3 \text{ m}^{-3}$]; and t , the time [d]. This equation assumes

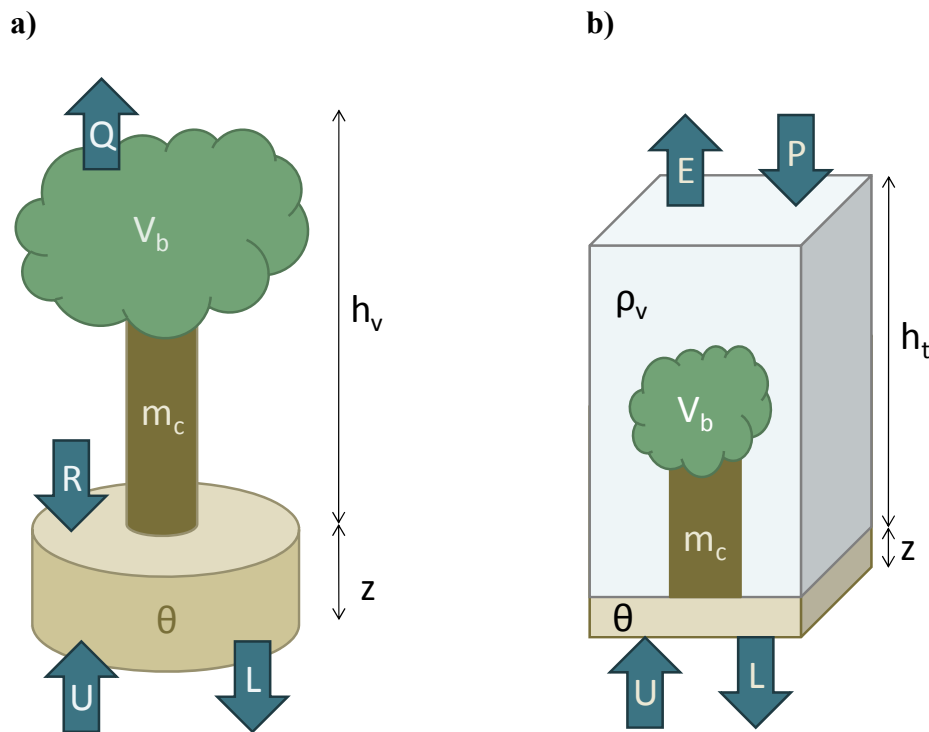


Figure 4.3: Water Balance at the Stand and Tree level

The water balance at the stand level (a) is centered around a control volume with the eddy-covariance system at the top boundary and the deepest soil moisture probe at the bottom boundary. The tree level water balance (b) takes the tree itself and the soil around it as the control volume, with the top of the tree canopy as one boundary and the deepest soil moisture probe as the other.

that no net lateral movement of water occurs, i.e. ΔQ_r , ΔQ_v , and ΔQ_s (lateral flow rates of runoff, water vapor in atmosphere, and soil water) are equal to zero. In practice, the last term in the equation, representing the change in stem water storage, is much smaller than the others, and can be neglected, as it is within the measurement errors of the other terms.

Here, the net groundwater flux represents the value of deep water uptake by vegetation minus leakage from the soil layer ($U-L$), which cannot be segregated based on the stand- or tree-level data alone. While this is a major drawback to the method, the net groundwater uptake can still be an informative measure, particularly during the long

summer dry season when soil is far below its field capacity, making leakage nonexistent. It also provides a measure of monthly groundwater recharge, a quantity useful for water resources planning.

4.3.3 Tree-level Uptake from Water Balance Closure

In this method, we focus on eight individual trees, defining each tree's rooting zone and trunk as the control volume (Figure 4.3). This control volume is defined differently than at the tower level because we are measuring water loss directly from the tree, and not over a distributed area. The equation for the water balance in this control volume is given as:

$$G_w + R - \frac{Q_{sap}}{A_r} = z \frac{\partial \theta}{\partial t} + \frac{V_b}{A_r} \frac{\partial m_c}{\partial t} \quad (4.3)$$

where the fluxes on the left-hand side are: G_w , the net groundwater source or sink (m d^{-1}); R , precipitation after interception per event has been subtracted (m d^{-1}); Q_{sap} , the sap flow rate of a given tree ($\text{m}^3 \text{d}^{-1}$); and A_r , the rooting zone area (m^2) around that tree. The system storage terms, on the right-hand side, are given by the constants z , the soil depth (0.6 m), and V_b , the volume of woody biomass in tree, and by the variables θ , the soil moisture content [$\text{m}^3 \text{m}^{-3}$]; m_c , the moisture content of woody biomass [$\text{m}^3 \text{m}^{-3}$], and t , the time [d]. As with the stand water balance, the biomass water storage term can be neglected in the calculations.

The lateral extent of the rooting zone is subject to uncertainty and is difficult to determine without destructive testing. Here, we assume that the spatial extents of the root zone are limited on the lower bounds by the size of the canopy and on the upper bounds by the spacing between trees. Tang and Baldocchi's work on tree root

respiration supports the former assumption, showing that soil CO₂ efflux drops exponentially as the distance from the tree stem increases, and stabilizes as the outer extent of the canopy is reached [Tang and Baldocchi, 2005]. Alternately, if the trees are “optimally” spaced [Eagleson, 1982], then it is reasonable to assume that the root zone for each tree should extend until it reaches the root zone of its neighboring trees. Since we know that the trees cover approximately 40% of the landscape, we can deduce that $A_r \leq A_c/0.4$, where A_c is the canopy area of a tree and A_r is the root zone area, allowing for the calculation of a range of possible uptake values.

In both water balance formulations, the time-step used for calculations is an important consideration. Clearly, half-hourly values are the smallest meaningful time-step, as the data is collected at this interval. However, some argue that soil moisture itself is only meaningful on a daily time-step or that water balances should only be conducted at monthly or yearly intervals. In light of this, we have chosen a compromise: calculations are performed using the smallest time interval available, but results are reported in no less than daily or monthly intervals.

4.3.4 Water Potential Data

The water in the tree xylem moves at a maximum velocity of 30 cm h⁻¹, as indicated by the sap flow data from a 30 cm diameter tree. This means it would take approximately 2.4 days for water extracted from the water table to travel the 17.1 m to the top of the average tree. If a tree is transpiring for approximately 50% of the day, it will take a total 5 days for extracted groundwater to be transpired. This is only relevant for tracer or biochemical studies, since the extraction rate at a given point in time is only a function of the hydraulic gradient between the groundwater and the hydraulic

resistance. Changes in pressure should quickly transmit through the system, even if the water itself does not.

Assuming that the Dixon cohesion-tension theory of sap water ascent is correct [Dixon and Joly, 1894; Tyree, 1997], the water potential measured in the leaves must be sufficiently negative to overcome both the gravitational potential caused by the change in height from the roots to the leaves and the matric potential associated with soil hygroscopic forces. By comparing the water potential measured in the leaves to the potential needed to obtain water from various sources, we can theoretically determine which water sources would be favored thermodynamically. For example, if soil matric potential at a depth of 50 cm is -2 MPa, then it will require at least a leaf water potential of -2.8 MPa to use this water: -2 MPa for roots to extract water from the soil, -0.1 MPa to move the water against a 10.5 m gravitation head from the soil to the leaf, and another -0.8 MPa to overcome the frictional resistance of water flowing against the xylem walls. Alternately, if groundwater is to be used, a gravitational head and frictional resistance over approximately 17 m needs to be overcome, requiring a driving pressure of approximately -1.4 MPa. In this case, extracting groundwater would be more energetically favorable than extracting soil moisture. However, this argument is only valid if a sufficient number of roots are present at the depth required; the necessary plant hydraulic architecture must be present in order to take advantage of groundwater resources.

In order to directly compare groundwater, soil, and leaf water potential measurements, we have adjusted all values to account for gravitational and frictional resistance, using the following equation:

$$\Psi_{i,T} = \Psi_i - \Delta P_x \quad (4.4)$$

Here, $\Psi_{i,T}$ is the total adjusted potential at a measured location, in MPa; Ψ_i is the direct pressure measurement, for example, soil matric potential, in MPa; and ΔP_x is the maximum theoretical change in pressure associated with overcoming gravity and the frictional resistance of the stem in order to reach a leaf at 3 m above the ground. It is calculated using an appropriately modified version of Darcy's Law:

$$\Delta P_x = \rho_w z \left(\frac{q_{max}}{K_s} + g 10^{-6} \right) \quad (4.5)$$

where ρ_w is the density of water, 999 kg m³; z is the length of the stem segment from the measurement point to the leaf height, in m; q_{max} is the maximum rate of sap ascent in the xylem measured by the sap flow sensors, 30 cm h⁻¹ or 8.3 x 10⁻⁵ m s⁻¹; K_s is the hydraulic conductivity of the stem, 1.10 kg s⁻¹ m⁻¹ MPa⁻¹ for deciduous *Quercus* trees [Cavender-Bares and Holbrook, 2001]; g is the gravitational acceleration constant, 9.81 m s⁻²; and 10⁻⁶ converts from Pa to MPa. These figures indicate that a maximum of 0.075 MPa of resistance must be overcome per meter of xylem for friction and 0.0098 MPa per meter of elevation change for gravity.

The groundwater table is, by definition, the location where soil or rock matric potential (Ψ_{matric}) equals zero. Volumetric soil water content measurements (θ) were converted to water potentials, using the following water retention curve developed after extensive laboratory testing, as discussed in Section 3.2 (Figure 3.3):

$$\Psi_{soil} = 0.1 \left(\frac{\theta}{0.44} \right)^{-2.8753} \quad (4.6)$$

The atmospheric water potential (Ψ_{atmos}) was calculated based on the relative humidity measured at the site:

$$\Psi_{atmos} = RT \ln \left(\frac{e}{e^o} \right) \quad (4.7)$$

where R is the gas constant, 8.31 J g^{-1} ; T is the air temperature in Kelvin; e is the water vapor pressure; e^o is the saturation water vapor pressure at temperature T ; e/e^o is the fractional relative humidity; and the resulting value is in MPa.

4.3.5 Stable Isotope Analysis

Stable isotopes can act as tracers for water movement and have, in the past, been successfully used to determine the source of water for any given tree [Dawson, 1996]. By comparing the oxygen or hydrogen stable isotope ratios in xylem water to those in soil water and groundwater, the source of plant water often becomes apparent. For instance, if the $\delta^{18}\text{O}$ ratios are -4‰ in the stem, -8‰ in groundwater, and -4.5 to -3.5‰ in soil, the plants must be solely using soil water. However, if the stem ratio in this example is instead -6‰, then the plant must be using a mix of groundwater and soil moisture.

Using a two end-member mixing model, we can then estimate the proportion of water coming from groundwater versus soil moisture:

$$\delta^{18}\text{O}_{stem} = a\delta^{18}\text{O}_{soil} + b\delta^{18}\text{O}_{groundwater} \quad (4.8)$$

where $\delta^{18}\text{O}$ is the oxygen isotope ratio and a and b are the proportions of stem water coming from the soil and the groundwater. These fractions must sum to unity ($a + b = 1$). In order to use the two-member model, the soil water oxygen isotope measurements needed to be weighted by the soil water potentials on the day of sampling. Based on the soil and leaf water potential data, we could, in most cases, exclude uptake from the top regions of soil, leaving the deeper soil (20 – 50 cm) and groundwater as the only

possible sources of plant stem water. The two values for soil, collected under each of the eight test trees, were weighted by water potential to obtain a $\delta^{18}\text{O}_{\text{soil}}$ value to use in the model.

Similar samples of xylem sap were collected by the Dawson group in 2006 [Mambelli, 2008] and analyzed to determine how their oxygen isotope ratios ($\delta^{18}\text{O}$) changed over the course of the dry season. Little variation ($<0.2\%$) was noted between Days 157, 186, and 229; all samples measured approximately -8% . The final sampling event, which occurred on Day 284, showed that the ratio had increased to between -6 and -7% . This change was mostly likely due to a rain event on Day 278 that altered the composition and quantity of soil moisture. Because of this seasonal stability, we elected to collect an intensive set of samples at one point in the late summer (Day 232), before the rains started.

4.4 Results and Discussion

4.4.1 Groundwater Uptake from Hydrological Measurements

Using the stand-scale water balance, we calculated that during the years 2005 to 2008, between 0 to 370 mm of water was lost per year through run-off or recharge to the underlying groundwater (Figure 4.4). This large variation relates directly to variation in precipitation received, rather than in changes evapotranspiration or soil storage. The wet years (2005, 2006) received upwards of 700 mm of precipitation each, over 50% of which (450 mm) was returned to the atmosphere through evapotranspiration from the soil and the vegetation. In the dry years (2007, 2008), precipitation dropped significantly, to less than 400 mm. Evapotranspiration, however, was not reduced

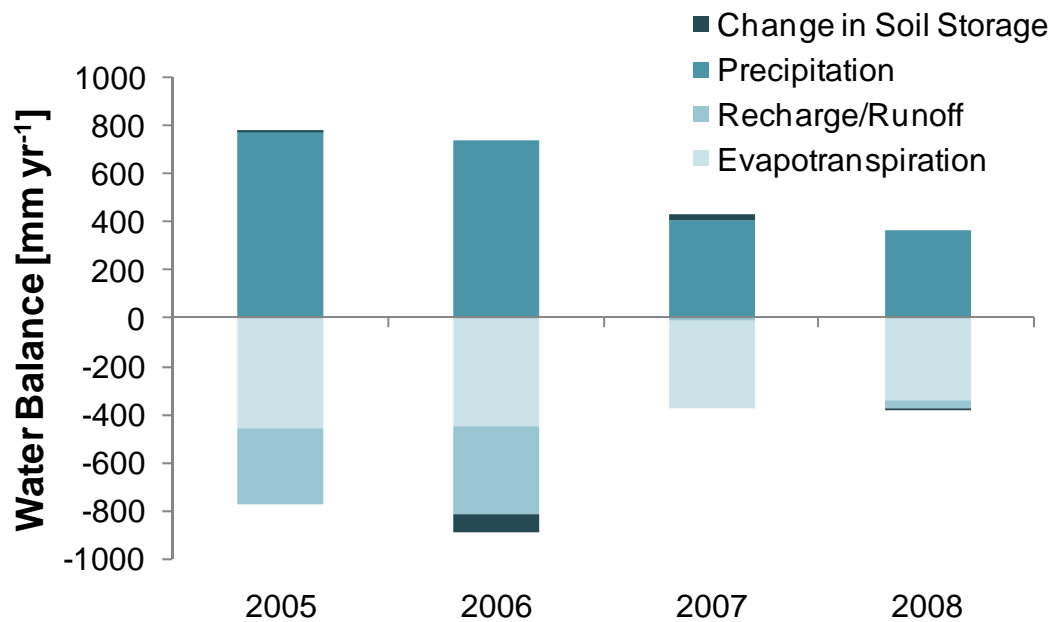


Figure 4.4: Annual Variation in Water Balance

correspondingly; in 2008, it dropped to 350 mm per year, more than 95% of precipitation. A dramatic change in the recharge and runoff accounted for the difference.

Looking more closely at ET, we find that its variability is related to grass and soil evapotranspiration, rather than tree transpiration. In 2005, a wet year, the yearly total tree ET was 184 mm while the grass and soil ET was 272 mm. During 2007, a dry year, grass and soil ET dropped dramatically to 130 mm, while tree ET increased, to 250 mm. This suggests that trees are less susceptible to interannual variations in precipitation than grasses, hinting that they can access stored water sources that are deeper than soil moisture.

At this time scale, though, groundwater uptake by woody vegetation is not apparent. Because of the Mediterranean type, bimodal distribution of precipitation at the

site, the oak active season (April – October) is out-of-phase with the bulk of the rainy season (November – May). This forces the trees to rely on stores of water built up over the wet winter. At the beginning of the dry season, the trees quickly deplete the soil moisture reserves (Figure 4.2), but continue to transpire, albeit at very reduced rates. During the summer, soil moisture stays at a more or less constant rate, near 10% for most soil layers. While the soil moisture does decrease very slightly over the dry season, it does not appear that a sufficient volume of water is removed to account for the levels of water transpired. This pattern is contrasted with that of the groundwater levels (Figure 4.2), which decrease steadily throughout the summer.

Breaking the stand-scale water balance into monthly segments (Figure 4.5), we see this same pattern again; recharge of the aquifer is occurring during the wet months, and uptake by the oaks is occurring during the dry ones. Over the course of the year, transpiration is highest when both the trees and grasses are active in March, April, and May, reaching a maximum of 80 to 100 mm per month. After soil moisture is reduced and the grasses senesce, rates of transpiration decrease. They are around 30 mm per month in June and decrease to 6 mm per month in August and September. However, this period is when groundwater uptake occurs. It begins in May or June, depending on the date of last precipitation, and lasts until September or October, when the rainy season starts. According to the water balance data, uptake from groundwater can amount to almost 90% of the total evapotranspiration during these months. As the wet season begins, the trees senesce and grasses are again active. From November to February, grasses are transpiring at a rate that, as previously stated, is highly dependent on that year's precipitation. Loss of moisture from the soil, or leakage, occurs, recharging the

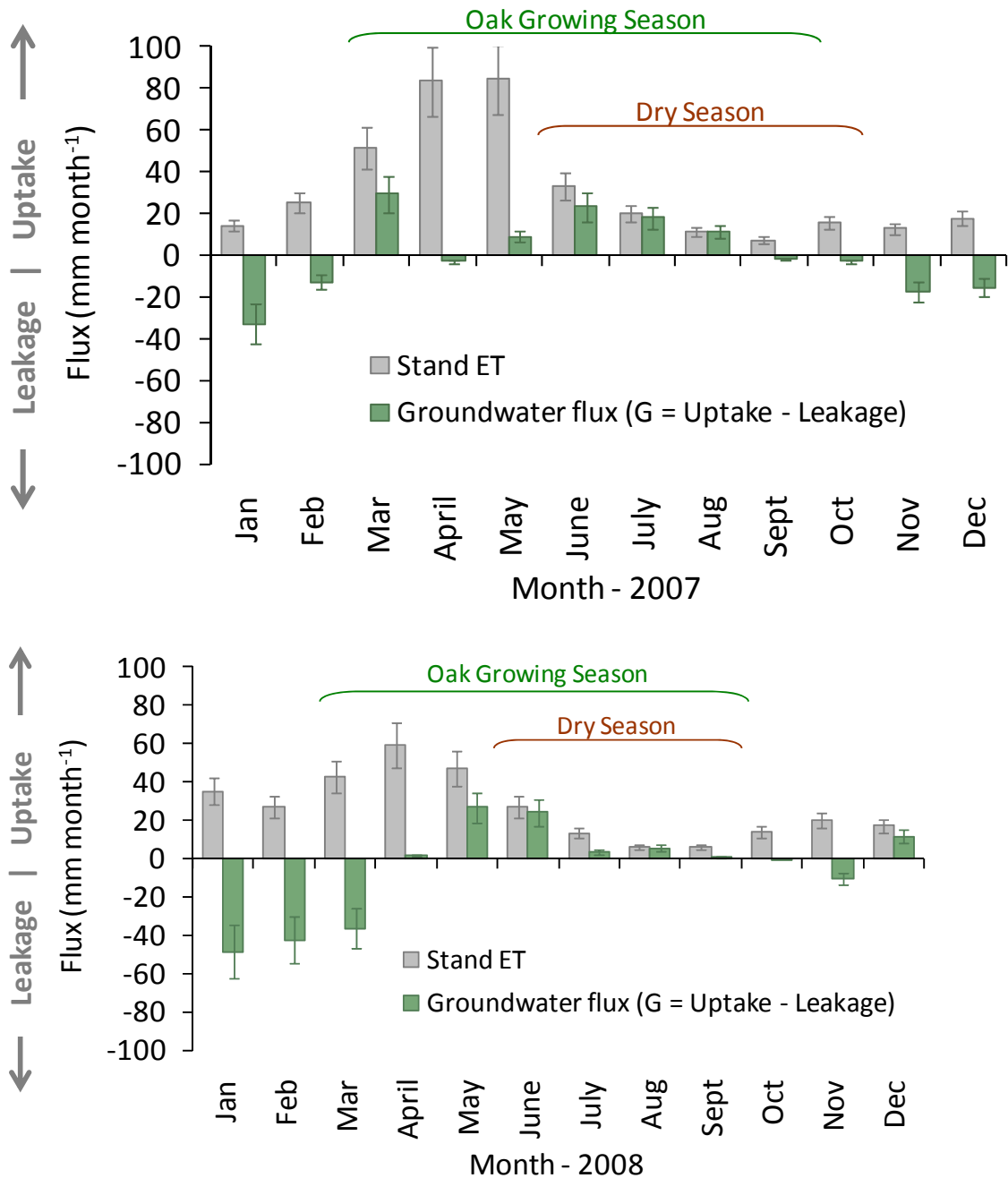


Figure 4.5: Groundwater Uptake from Stand Water Balance
Monthly groundwater uptake calculated using stand water balance for (a) 2007 and b) 2008. Positive fluxes indicate that uptake is occurring; not enough soil moisture is removed to account for all stand transpiration. Negative fluxes indicate leakage from the soil, i.e. water is traveling out of the 60 cm soil column and recharging the groundwater.

underlying, deep stores of water at rates between 30 and 100 mm per month. These numbers are uncertain, however, in wet years, when run-off may occur. Little or no runoff after rain events was observed during 2007 and 2008, the dry years.

Year-to-year, this recharge, as compared to evapotranspiration, is highly variable and depends on precipitation. Uptake from groundwater, though, is more consistent. Figure 4.6 shows the percentage of ET that comes from groundwater uptake, denoted as $ET_G/ET*100\%$. During the wet months, variability is high and the percentage is typically negative, indicating leakage. As the summer dry months progress, the range decreases. In June, the proportion of ET from groundwater uptake is 40 to 90%, while it is 75 to 97% in August, when soil moisture resources are only rarely present.

Using the stand water balance data is not without difficulties. First, and foremost, its sensitivity to “leakage events” prevents the calculation of the true uptake rate; only the net flux to and from groundwater can be calculated: $G_w = U - L$. For four months of the year, when it is not raining, this value closely estimates uptake. Uptake could be occurring outside of this time span, but it would not be detected by this method. Second, the tower latent heat flux and the soil moisture measurements are subject to error: 1% for the Delta-T probes themselves [Delta T Devices, 1999] and up to 25% for the eddy-covariance system [Wilson *et al.*, 2002]. These error values are reflected on the monthly stand water balance charts (Figure 4.5).

With the soil moisture probes, there is the added difficulty of capturing spatial representativeness. To account for horizontal variability, an average of the tower probe and all of the sap flow station probes was used. Finding a representative soil moisture value that described the changes with depth was more complicated. A root weighted

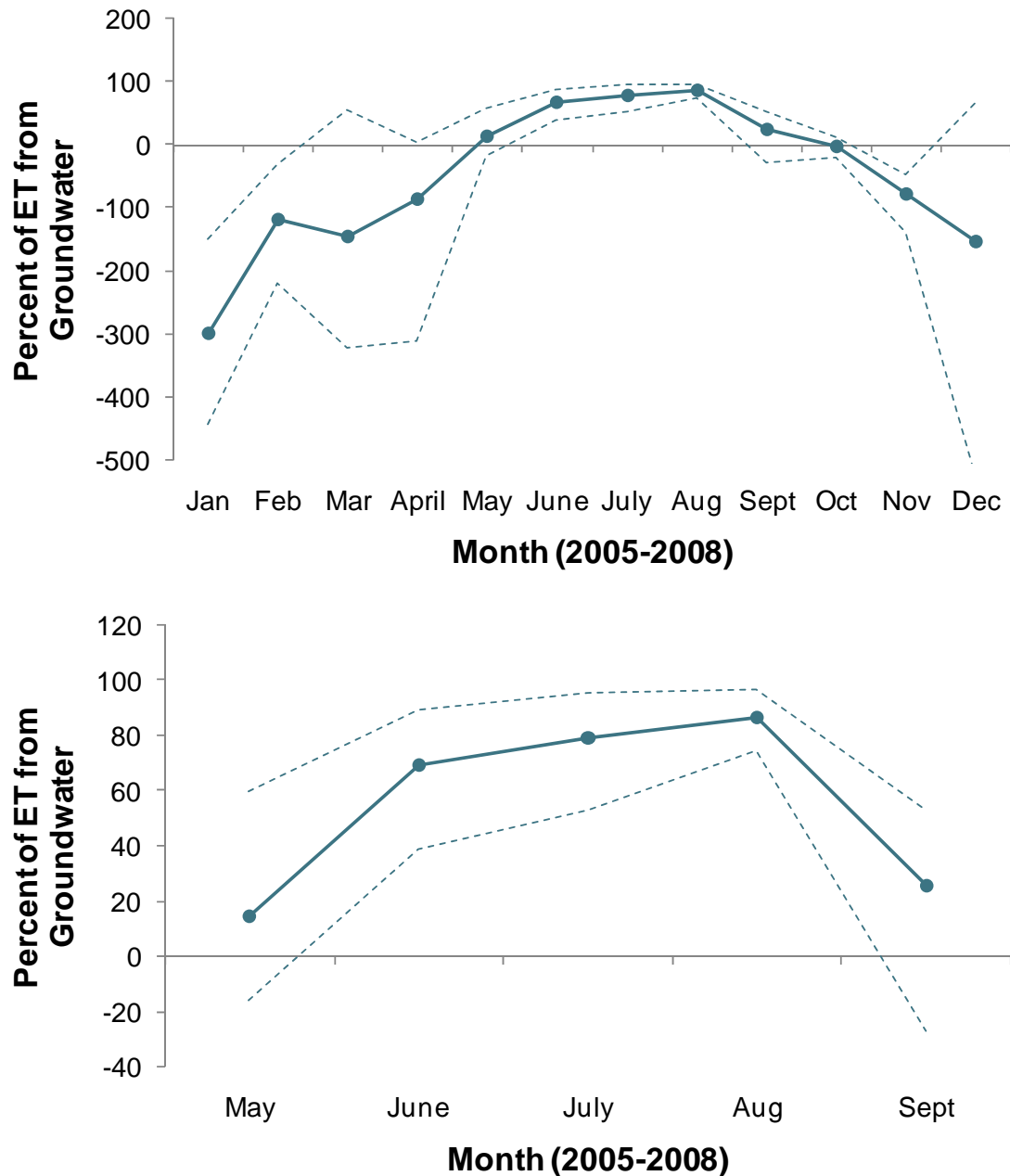


Figure 4.6: Annual Variation in Percentage of ET from Groundwater Uptake

This percentage represents the ratio of groundwater uptake rates by woody vegetation to the overall tower evapotranspiration ($ET_G/ET*100\%$). Positive values indicate that uptake is occurring, while negative values denote leakage from the soil zone. The percent of ET from groundwater has high annual variability; for instance, it ranges from 55 to 95% during the month of July. However, despite being such a large fraction of ET, the actual value of ET_G is widely variable and can be very small during these months. For 2005 to 2008, it was between 3.7 and 40 mm per month in July and August.

averaging method was used [Miller *et al.*, 2007], but given that there were only three depths measured, there is considerable uncertainty in the soil moisture portion of the tower water balance.

While the stand level water balance allows for an analysis of multiple years using existing data, more direct measures are necessary to capture the patterns of year round uptake. In this regard, the analysis of the groundwater data is very useful. Diurnal fluctuations in the depth to the groundwater table are indeed observed during the oak active season (Figure 4.7, top) and disappear when senescence of the oaks is complete (Figure 4.7, bottom). The pattern of the daily fluctuations strongly supports oak groundwater uptake; the depth to the water table increases during the daylight hours, when the trees are transpiring, and decreases during the nighttime, indicating recharge of the aquifer. The patterns are similar to those that have been noted in other dryland or riparian ecosystems [Bauer *et al.*, 2004; Loheide, 2008; 2008; 1932].

To see how these fluctuations translate into uptake rates, Equation (4.2) was applied to data from seven days in July 2007 (Figure 4.7). Using this method, we find that groundwater uptake (ET_g) was between 0.25 and 0.45 mm d⁻¹ during this period, given an estimated specific yield (S_y) of 0.04 for fractured metamorphic rock (see section 2.3.3). The eddy-covariance system measured total daily evapotranspiration at 0.7 to 1.0 mm d⁻¹, indicating that approximately 42% of transpired water comes from deep sources (Table 4.2). Day-to-day variability in this uptake was somewhat high; the ET_g rate and the ET_g/ET ratio had standard deviations of 0.07 mm d⁻¹ and 12%, these variables have such different magnitudes and units, with maximums of 5 kPa and

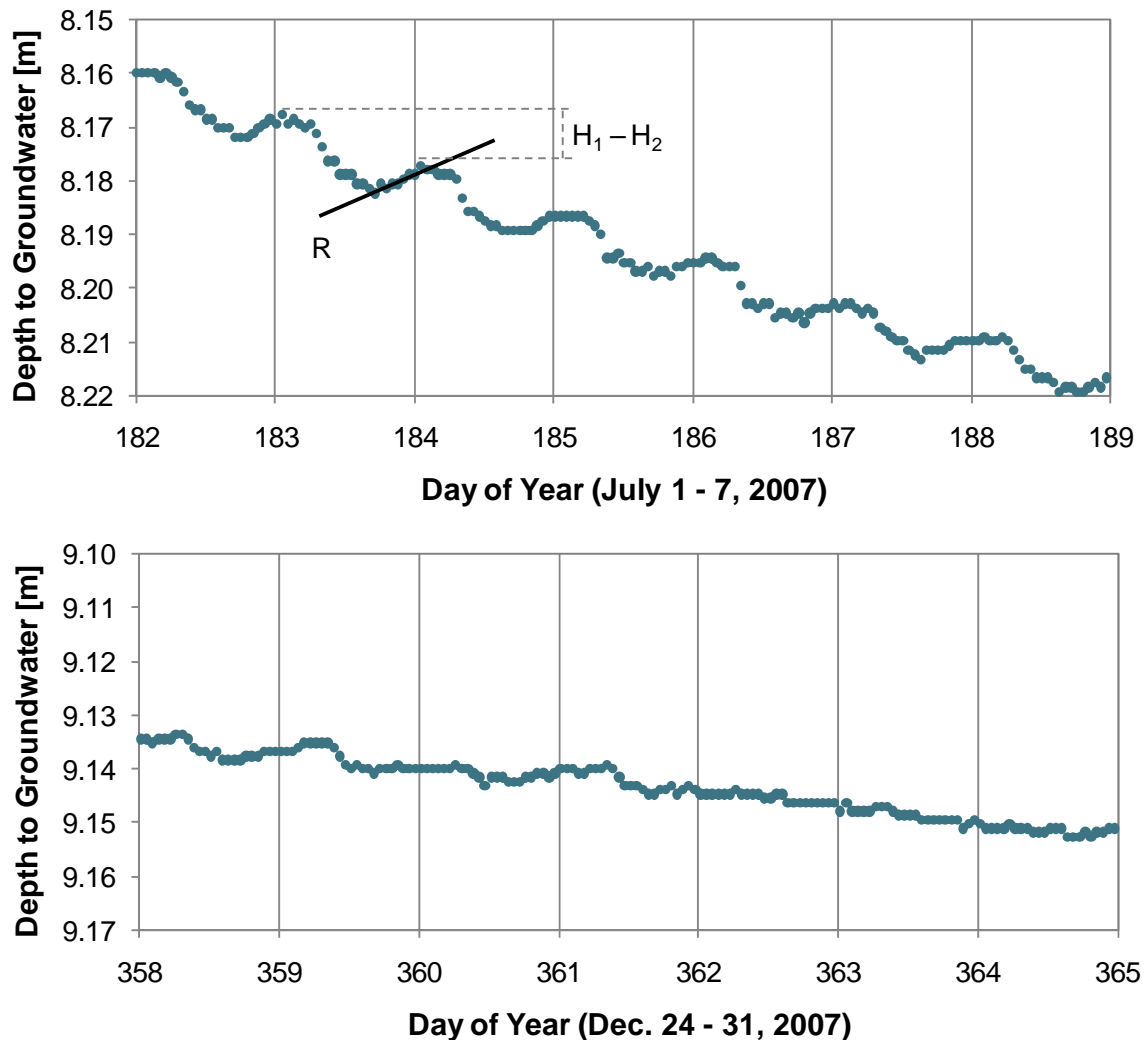


Figure 4.7: Diurnal Groundwater Fluctuations

Change in groundwater table fluctuations during oak active season (top) and senescent season (bottom). Fluctuations are largest during the summer months when uptake is occurring and lowest during the winter months when recharge and uptake are both low. Groundwater fluctuations are a more direct measurement of uptake than the water balance, which is sensitive to individual precipitation/leakage events. In addition to the fluctuations, the relatively rapid decline of the water table in the summer months (0.007 mm d^{-1}) supports groundwater uptake by plants. After transpiration has ceased, the decline is reduced to 0.002 mm d^{-1} , which likely represents the baseline groundwater flow under a regional gradient.

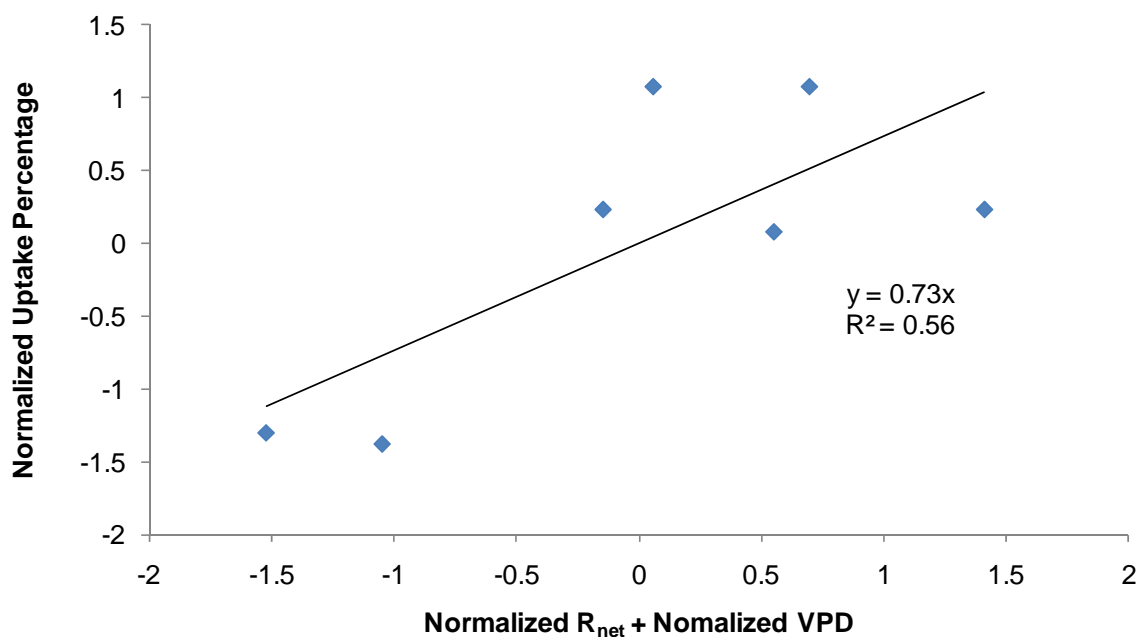


Figure 4.8: Correlation between Groundwater Uptake and Meteorological Variables Both the daily groundwater uptake percentage (ET_g/ET), shown here, and the groundwater uptake rate appear to be positively correlated with net radiation (R_{net} in $W\ m^{-2}$) and vapor pressure deficit (VPD in kPa). Because these variables have much different magnitudes, they must be standardized before a generalized linear model is applied.

Table 4.1: Daily Uptake from Groundwater Fluctuations for July 2007

DOY	ET_g	ET	$ET_g/ET(\%)$	VPD (kPa)	R_{net} ($W\ m^2$)
182	0.27	0.99	27	1.81	189
183	0.37	0.79	47	2.15	194
184	0.45	0.78	58	2.37	197
185	0.36	0.77	47	3.24	196
186	0.33	0.74	45	4.16	187
187	0.25	0.98	26	3.03	185
188	0.39	0.66	58	1.38	199
Total	2.43	5.72	42	-	-

800 W m⁻², respectively, all data were normalized using the equation: $\hat{x} = (x - \mu_x)/\sigma_x$. Using a generalized linear model for regression, we find that $ET_g/ET = 0.76$ (Rnet+VPD) with a correlation coefficient of 0.60 (Figure 4.8). Clearly, plant physiological processes, such as stomatal control, are at work here, which may be fruitful to explore in the future, given additional datasets.

Looking at these daily uptake rates during 2007 and 2008 (Figure 4.9a), we see similar day-to-day variability. However, compared to the stand evapotranspiration rates, groundwater uptake is fairly steady throughout the growing season, at about 0.25 to 0.4 mm d⁻¹. This trend suggests that there is a baseline uptake level which fluctuates slightly based on atmospheric conditions. It is also not as susceptible to precipitation events, the problem noted with the stand scale water balance. Shown in green on Figure 4.9, the tower derived uptake value frequently goes negative in the wet months. This problem does not plague the fluctuation derived values, shown in blue, with the exception of several days in January of 2008 when large rain events occurred. These events caused the summed flux for the month to also be negative (Figure 4.9).

Looking at the monthly sums in Figure 4.9, we find that groundwater uptake occurs for a wider span of the year than suggested by the water balance data. This uptake starts in April, rather than May, and continues until the beginning of December. Rates from April through July are fairly consistent, around 16 mm d⁻¹, and drop slightly in August. Groundwater uptake continues to occur until mid-December, much longer than previously assumed. This late-season uptake may be due to the activity of

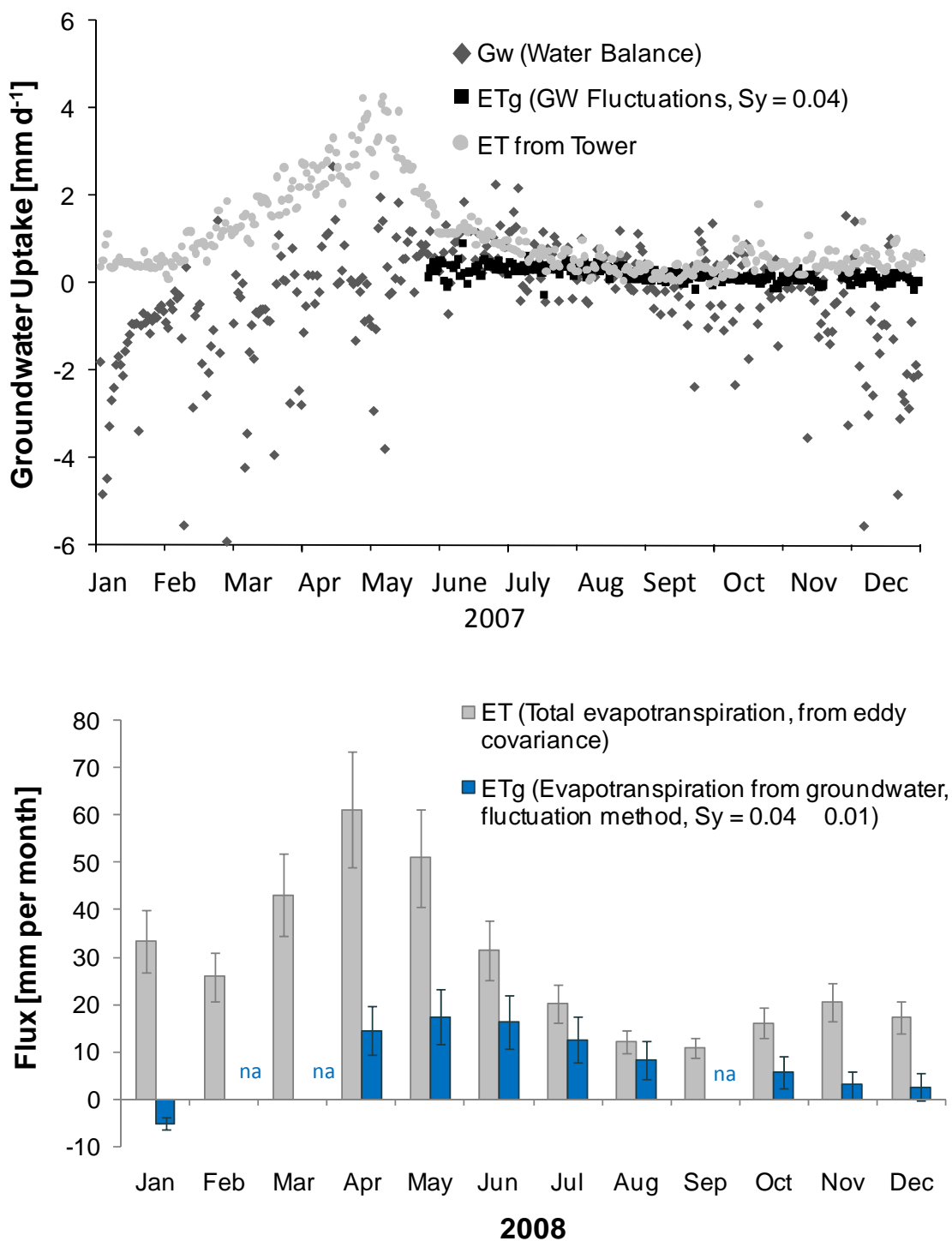


Figure 4.9: Daily and Monthly Groundwater Uptake from Fluctuation Method
Top: Groundwater uptake occurs longer than previously suspected, continuing into December when only a small fraction of trees are still active. Bottom: Its measurement is

subject to error due to estimation of the specific yield. Neither method is error free, however. The water balance method produces occasionally erroneous values in G_w at the daily scale. Large peaks in rainy season groundwater uptake are typically balanced out by equally large negative values the following day. This effect is likely due to the soil moisture wetting fronts associated with precipitation events, and the inability of the method to adequately account for them. This is one of the major drawbacks to the water balance method that is eliminated by the groundwater fluctuation method.

individuals that are still transpiring after the majority of trees have lost their leaves, or due to groundwater use by the evergreen grey pines at the site. As with the eddy-covariance data, these measurements are subject to some uncertainty. Two errors influence the uptake rates from the fluctuation method: uncertainty in both the specific yield parameter and in the pressure transducer measurements themselves. We estimate specific yield to be 0.4 ± 0.1 , a 25% error range. In addition, the pressure transducer has a resolution of 0.076 mm. When combined, these results are subject to an uncertainty between 3 and 6 mm per month, as shown on Figure 4.9. These groundwater uptake values compare poorly to those calculated using the tower scale water balance (Table 4.2). This difference is likely due to the uncertainty in both methods, since their error ranges nearly always overlap. The lower values for the fluctuation method may also reflect the violation of the no nighttime groundwater uptake assumption discussed earlier.

Looking at the late-fall, early-winter transpiration issue, we note that at the site, tree senescence typically occurs at the end of September. The fluctuation method indicates, however, that uptake was still occurring in early December 2008. What explains this discrepancy? The date for senescence is typically selected when a certain percentage of trees have lost their leaves for the winter. However, through careful

Table 4.2: Comparison of Groundwater Uptake Method

Year	Month	From Tower [mm month⁻¹]	From Fluctuations [mm month⁻¹]
2007	June	23 ± 6.7	11 ± 4.5
	July	18 ± 5.2	11 ± 4.2
	August	11 ± 3.2	9.2 ± 3.1
2008	May	27 ± 7.8	17 ± 5.8
	June	24 ± 7.0	16 ± 5.5
	July	3.7 ± 1.1	13 ± 4.9
	August	5.6 ± 1.6	8.3 ± 4.0

observation in 2008, we noted that leaf-fall for select, individual trees can be much later. Some groundwater uptake may also be occurring by the evergreen grey pines at the site, but it is impossible to differentiate the two using these methods.

Here, the individual tree water balance data can provide some useful perspective. Unfortunately, year-round water balances cannot be calculated from the data, due to too many gaps in the data collection. However, Figure 4.10 shows a selected portion of the 2007 record for two trees in average soil environments: one large, 46 cm diameter oak and one medium, 31 cm diameter oak. We find that for the smaller tree, the daily groundwater uptake ranged from 15 to 45 mm per month, peaking in June and July and ending in September. The larger tree had slightly lower rates, around 20 mm per month, but uptake continued further into the fall. The plot shows leakage around the larger tree in October, but it does not rule out uptake, since rain events likely masked any uptake

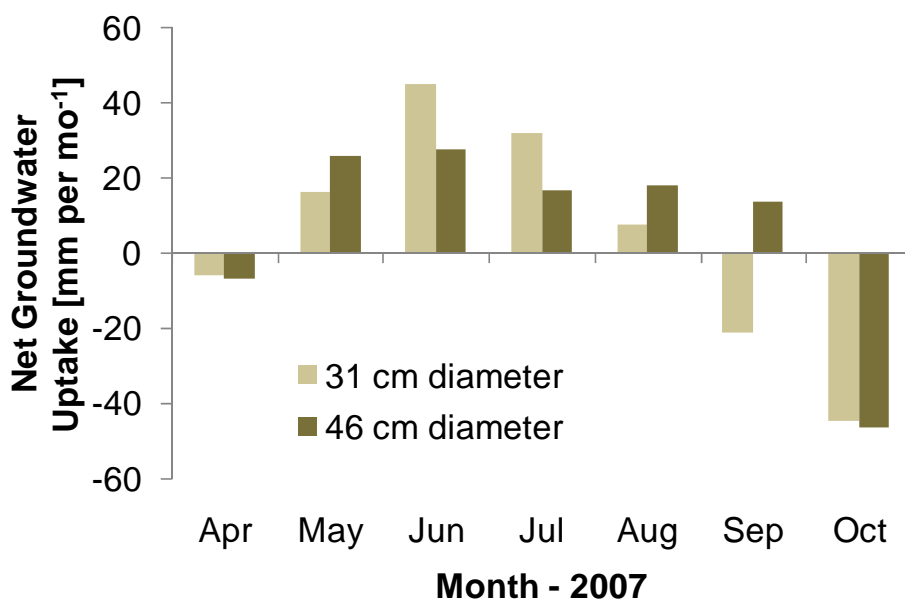


Figure 4.10: Groundwater Uptake from Tree Level Water Balance
 Monthly groundwater uptake at the tree level during 2007. The uptake was calculated using $A_r = A_c/0.4$.

that was occurring. This longer uptake period is consistent with the groundwater fluctuation data.

The tree scale water balances are potentially subject to more error than the other methods, but this error is more difficult to quantify. Sap flow sensors are notoriously problematic to upscale to a tree level flow rate (see Sections 5.1 and 5.3.4). Depending on the accuracy of the parameters used in the upscaling process, error rates can be up to 60% [Bleby *et al.*, 2004]. For our sensors, the calibration process is known to have a 4% error rate when calculating sap velocity from heat pulse velocity [Chen *et al.*, In preparation]. This corrects for errors in probe spacing, which can cause overestimations of 30-50%, but does not correct the radial velocity profile within a tree. The estimation of sapwood area can also contribute to the under- or over-prediction of flow rates. We find a correlation coefficient of 0.9 on the relationship we use to predict sapwood area

(Figure 5.4), implying some natural variability is present. Additionally, the same soil moisture considerations are present with the tree water balances: representativeness of the depth profile and accuracy of the sensors. In these water balances, the area of the rooting zone is also used in the calculation, and the estimates of rooting area vary by up to 85%.

While the tree water balances suggest some intriguing behavior, the high level of uncertainty indicates that they should be taken with caution. The pattern raises some interesting questions: Do larger trees show more groundwater uptake? Is there a “threshold diameter” below which no uptake occurs because the tree is too young or too small? Does leaf loss relate to the time at which the groundwater table drops below a tree’s rooting zone? Further study on the relationship between depth to groundwater table, tree diameter, sap flow, time of tree senescence, and perhaps even genetic variability is certainly justified, and could yield interesting results.

4.4.2 Evidence of Uptake in Water Potential

Water potential measurements can help determine if uptake is possible or even favorable from a “thermodynamic” perspective. Based on the mid-day water potential measurements, mid-day leaf water potential is sufficiently negative to induce groundwater uptake (Figure 4.11). For instance, in July of 2007, groundwater potential is around -0.8 MPa, while soil moisture potentials are at -1 and -12 MPa, both adjusted for the pressure loss associated with xylem transport (see Section 4.3.4). The driving pressure at the leaf surface is -3.4 MPa. This pressure is sufficient to extract and transport both groundwater and deep soil water to the leaf, although it takes less energy to use the groundwater. Shallow soil moisture cannot be extracted.

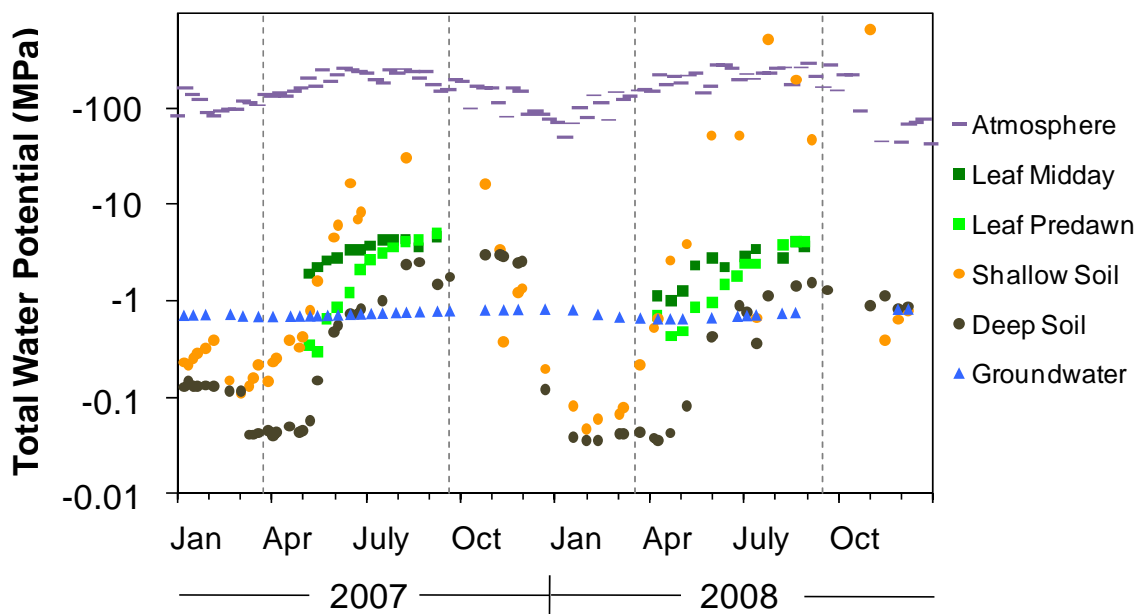


Figure 4.11: Water Potential Across the GSPA Continuum

Total adjusted water potential measured in the leaves, soil, and at the groundwater table. All measurements are adjusted to account for the frictional and gravitational resistance associated with moving sap water upward through the xylem (approximately 0.09 MPa per meter). The gray bars indicate the portion of the year when the majority of the blue oaks are active. Surface soil measurements were collected at a depth of 5 – 10 cm, while deep soil measurements occurred near the soil-rock interface, 50 – 60 cm below the surface.

Further, groundwater uptake is energetically favored over uptake from the shallow surface soil (<10 cm) during the entire dry season, from late March to late November, and over uptake from deep soil (40 to 50 cm) during the summer months, from late June to late November. These dates roughly correspond to the time when the water balance data indicate that a majority of transpiration comes from groundwater uptake, early June, and continues through the time when they indicate that uptake ends, early December. Regardless of the favorable energetics, uptake is only possible if the roots are sufficiently deep to reach the groundwater table.

The largest errors associated with this method relate to the conversion of soil moisture to water potential, since it is extremely difficult to measure such negative (<-10 MPa) soil matric pressure *in situ*. The water retention curve developed earlier was used to estimate the potential from the volumetric water content (see Section 3.2). These values correlate well ($r^2 = 0.96$), but do have some uncertainty. Pre-dawn and mid-day water potentials can be measured to a 0.1 MPa resolution, but these are subject to sample variability. Three leaves are collected from each tree, and three trees are sampled per event, in order to find representative values. A standard deviation of around 0.42 MPa in the nighttime and 0.27 MPa in the daytime is common.

4.4.3 Isotopic Signature of Soil Water versus Groundwater

The analysis of the soil, groundwater, and stem oxygen isotope ratios $\delta^{18}\text{O}$ in ‰ yielded inconclusive results. Groundwater was found to have an average ratio of -6.9 ‰, similar to samples of rain water and retention pond water (Table 4.3). The shallow and moderate soil samples were considerably less depleted, with an average of -0.07‰ for 5 cm samples and -4.1‰ for 20 cm samples. The deep, 50 cm soil samples were more depleted, at an average of -8.5‰. Stem samples measured between -5.7 and -8.8‰ and did not appear to be related to tree diameter. The analysis method has a margin of error of $\pm 0.2\%$.

While these values are reasonable and in-line with previous measurements, they present a problem: groundwater ratios are not sufficiently different from the deep soil ratios to allow for a distinction between the two. For most trees, three distinct mixing models are plausible. The stem value could be the result of uptake from just the 20 cm and 50 cm soil layers; it could be a mixture of the 20 cm layer and the groundwater; or it

Table 4.3: Oxygen Isotope Ratios ($\delta^{18}\text{O}$ in ‰) for Water in Ecosystem

Category	Average	High	Low
Blue Oak Tree	-7.11	-5.69	-8.75
Soil 5 cm	-0.07	1.82	-2.78
Soil 20 cm	-4.05	-1.84	-6.03
Soil 50 cm	-8.46	-7.12	-9.05
Groundwater	-6.93	-5.66	-7.66
Rain	-7.84	-5.01	-10.43
Pond Water	-6.44	-6.33	-6.57

Soil, groundwater, and tree samples were collected on August 20, 2008 (DOY 233); Rain and retention pond water samples were collected near the end of the following rainy season on April 7, 2009 (97)

could be a mixture of all three. Weighting the soil moisture by water potential does not clarify the issue. Depending on the root profile assumed, all three of the scenarios are possible. Stable isotope ratios do not confirm or deny the possibility of groundwater uptake by vegetation.

4.5 Conclusions

Woody vegetation in the California oak savanna uses a significant amount of groundwater during the late-spring and early summer months, as soil moisture reserves are depleted. Direct measurements of water table fluctuations provide the most reliable method for determining its quantity; these show uptake rates between 10 and 20 mm per month for late April to July and between 3 and 10 mm per month from August to early December. During the dry summer, these rates occasionally account for almost all of the evapotranspiration measured by the tower, but typically ET_g is around 60% of ET . This

conclusion is also supported by tree and stand water balances, which show similar groundwater uptake patterns in the dry season, but higher ET_g/ET ratios, upwards of 90%. These estimation techniques suffer from a variety of problems, primarily that they are sensitive to precipitation and leakage events and that they demand extremely accurate equipment.

The indirect methods offer varying levels of support. While stable isotope methods do not rule out groundwater uptake, they also cannot be used to definitively support it. On the other hand, water potential measurements strongly support these conclusions. Not only do they show that uptake is possible, they show that it is often energetically favorable over soil moisture extraction. Provided that they have sufficiently deep rooting systems, and that the cohesive theory of sap ascent is correct, oak trees at the site should be using groundwater for over half the year.

Based on these lines of evidence, we can conclude that the blue oaks are indeed obligate phreatophytes and not summer or drought deciduous. The ecosystem meets three of the six criterion suggested for determining groundwater dependence: sufficient rooting depths, fixing carbon during dry periods, and daily changes in groundwater level (Section 4.1). Additionally, a large percentage of water transpired in the summer comes from deep, long term stores rather than shallow, ephemeral sources.

Early circumstantial evidence suggests that as the water table declines in the dry season, certain trees begin to senesce while others continue to be active. Exploring this possibility is an important future step to understanding vegetation water use at this site and its response to future changes in the hydrologic regime. It may also provide clues to how tree rooting extents change with diameter, species, or stand location.

Chapter 5: Upscaling Transpiration from Sap Flow Measurements

5.1 Introduction

The development of the eddy-covariance method has revolutionized the measurement of water vapor fluxes across landscapes, allowing for the nearly continuous monitoring of plant transpiration in forest, agricultural, and grassland ecosystems. Its key advantage lies in its ability to collect in-situ, spatially integrated measurements of the trace-gas fluxes emanating from a plant canopy [Baldocchi, 2003]. Problems develop, however, when applying the method over complex terrain and in areas with insufficient fetch [Massman and Lee, 2002], which can limit its usefulness over mountains, riparian corridors, patchy landscapes, and experimental water-exclusion or carbon-enrichment sites.

Sap flow sensors represent an alternative method for measuring water vapor flux from woody vegetation. Developed over a half-century ago [Marshall, 1958], these instruments use heat pulses as tracers to follow the internal movement of xylem water. Given the sap flow rate within a tree and the water conducting area of the stem, we can calculate the total transpiration of an individual tree. With unlimited time and resources, an equivalent integrated flux from a forest canopy could theoretically be obtained by measuring all trees in a stand with sap flow sensors. But given limited resources and the logistical problems inherent in instrumenting an entire forest, how do we select the trees that we measure so that they are best representative of the integrated flux?

Sap flow rates, and thus plant transpiration, are known to scale allometrically with tree stem diameter at breast height (DBH) [Meinzer *et al.*, 2001], and

considerations of diameter alone are typically used to locate these sensors. However, this method does not lend itself to dry ecosystems with heterogeneous soil moisture. Plant transpiration in these systems is thought to be heavily dependent on soil moisture [Chen *et al.*, 2008; Rodríguez-Iturbe and Porporato, 2004; Williams and Albertson, 2004], thus failure to collect measurements along the spectrum of possible soil moisture conditions may lead to biased transpiration values. Dragoni *et al.* [2009] found that stem conductance and its derivative, sap velocity, was “strongly correlated to local soil water availability that arises from the presence of mild topography on relatively shallow soils.” Similar conclusions were drawn by other work [Granier, 1996; Martínez-Vilalta *et al.*, 2003], but Loranty *et al.* [2008], not detecting these correlations across moisture gradients, speculate that they may only be significant at sites where plants experience water stress.

While the details of upscaling vary across the literature, the process of translating sensor measurements to canopy transpiration has three general steps:

1. Convert the heat pulse velocity (v_h) to a sap velocity (v_s). In most sap flow methods, the sensors actually measure the travel time of a heat pulse, rather than a water movement rate, and this value must be converted using heat transfer equations.
2. Upscale from point measurements of sap velocity within the xylem, typically in units of length per time ($L T^{-1}$), to whole tree transpiration or volumetric flow rate (Q_{tree}), in $L^3 T^{-1}$. This step is almost always performed by multiplying the velocity times the area of conducting sapwood (A_{sap}).

3. Upscale from individual tree flow rate to a stand transpiration rate (q_{stand}), in L T^{-1} , which can then be compared to rates measured by other methods.

While accurately performing all of these steps is necessary, we choose to focus on the third step, the upscaling from individual tree to stand transpiration. A number of papers already address the first and second steps, and their associated difficulties, which we will briefly summarize here. First, the necessary coefficients describing the heat conducting properties of various woods must be found, and estimates of these parameters are available both in the papers developing the method [*Burgess et al.*, 2001a] and manuals for the forestry industry [*Panshin and De Zeeuw*, 1980]. However, they are all sensitive to stem moisture content, and thus must either be measured directly or inferred using inverse modeling [*Chen et al.*, In preparation]. Additionally, sap velocity is known to vary along the radial axis into the tree [*Eamus et al.*, 2006b], and the typical method of addressing this is to measure at two or three discrete locations and create an areal average sap velocity. Newer methods are being developed to quantify this variation, such as the ones presented by Caylor and Dragoni [2009], but these are not yet the standard in practice.

Although a variety of approaches to the third step have been reported in literature, the majority use biometric, tree centered properties to relate the tree sap flow rates from a group of measured trees to the transpiration rate of the entire stand [*Cermak et al.*, 2004]. Most research is aimed at generating and using allometric relationships between sap flow and stem density, leaf area, diameter, or sapwood area [*Kumagai et al.*, 2005; *Meinzer et al.*, 2001; *Vertessy et al.*, 1997; *West et al.*, 1999]. Remote sensing is often used to obtain this biometric data [*Chavarro-Rincon*, 2009; *Chen et al.*, 2006].

Even in the well-watered ecosystems, where these approaches have been tested, upscaling sap flow typically underestimates the transpiration rate derived using other means, by 30 to 50% [Oishi *et al.*, 2008]. One study, conducted by Wilson *et al.* [2001], reported much poorer upscaling results, with sap flow underestimating both eddy-covariance and water balance measurements by 50%. The discrepancy was attributed to the diversity of species in that ecosystem and the differences in their sap flow rates [Wullschleger *et al.*, 2001]. In their study of a semi-arid woodland in Australia, Hatton *et al.* [1995] report that upscaling errors of up to 44% are possible, although they ascribe a majority of this to problems scaling from heat pulses to tree transpiration. The resolution of the velocity sensor itself may also be a problem; Oishi *et al.* [2008] attribute upscaling problems to the difficulties in measuring low nighttime sap flow rates with Granier-type thermal dissipation probes. However, more favorable comparisons have been reported. For instance, Ford *et al.* [2007] compared stand transpiration rates derived from sap flow and water balance methods, in a pine plantation receiving 1978 mm of water per year. They observed a difference of 7 to 14% in the rates, noting that “accounting for variation in stand density and sapwood area was the most influential step in scaling to the landscape.”

This study focuses on upscaling sap flow in a semi-arid oak savanna in California. Previous sap flow research at this site had similar upscaling difficulties; daily tree transpiration found using the sap flow method was only 60% of the transpiration measured by the tower. Kiang [2002] noted that this was particularly problematic during the early summer, with peak daily sap flow rates equal to 1.4 mm d^{-1} and compared to 2.2 mm d^{-1} measured by the eddy-covariance system. The two values

converged during the dry season, to under 0.5 mm d^{-1} , and remained fairly consistent until leaf senescence. While the direct cause of these differences was never determined, Kiang proposed several explanations: poor characterization of the velocity in the outermost xylem vessels, neglect of seasonal changes in hydraulic capacitance or thermal diffusivity when calculating the velocity from the raw heat pulses, and evaporation of intercepted rainfall from tree leaf surfaces during the wet season. We hypothesize that problems occurring when attempting to upscale from individual tree transpiration measurements to canopy transpiration are instead a direct result of failure to consider variations in soil moisture and elevation in water-stressed areas.

In this work, we first present an alternative method for locating sap flow sensors that respects these water availability considerations and allows for direct, simple upscaling of fluxes. We then use it to construct a prototype network at a well-documented, semi-arid site, monitoring sap flow and soil moisture at eight carefully selected trees. We compare this dataset to the hourly and daily latent heat fluxes measured using the eddy-covariance method, and further refine this comparison by considering only the trees located within the footprint of the eddy-covariance system. Based on the results of this pilot study, we make recommendations for future upscaling work at semi-arid sites.

5.2 Methods

5.2.1 Site Description and Characterization

The site, Tonzi Ranch, is an oak savanna located in the western Sierra Nevada foothills near Ione, CA (Latitude: 38.4311°N , longitude: 120.966°W , altitude 177 m). It

is affiliated with the AmeriFlux and Fluxnet micrometeorological observation networks and has two eddy-covariance towers: an “overstory” tower located at 23 m above the ground surface and an “understory” tower at 1 m. Half-hourly water vapor flux, soil moisture, and precipitation measurements have been collected near-continuously since Spring 2001. The presence of the two towers allows us to isolate tree transpiration from the ground surface evaporation, by subtracting the understory flux from the overstory flux.

In this work, we confine our study to the 2008 growing season, focusing special attention on four, one-week periods: May 14 to 20, June 14 to 20, August 2 to 9, and September 6 to 12 (DOY 135-141, 166-172, 215-222, 250-256). Our study area is an 800 m by 800 m region surrounding the site’s eddy-covariance flux tower, a region slightly smaller than a MODIS pixel and corresponding to the available LIDAR data at the site. Trees cover around 40% of the landscape in this area; they are predominately blue oaks (*Quercus douglasii*) with occasional grey pines (*Pinus sabiniana*). The mean height of the canopy is 7.1 m, with approximately 194 stems per hectare, a mean diameter at breast height of 0.199 m, and a basal area of 18 m² ha⁻¹ [Baldocchi et al., 2004]. The understory cover consists primarily of non-native herbs and grasses. The site’s hydroclimate is Mediterranean and semi-arid, receiving approximately 550 mm of rain per year and losing between 295 and 427 mm of this to evapotranspiration [Baldocchi et al., 2004; Baldocchi and Xu, 2007]. Most rainfall occurs during the cool wet season (November to April), with almost no precipitation occurring during the hot dry season (May to October).

To characterize the soil properties at the site, fifty spatially distributed soil texture and moisture measurements were collected. Variograms were developed to characterize the spatial properties of the soil texture measurements. Most of the soil properties could be modeled using a spherical function, which replicates the small-scale variability found in the samples [Rubin, 2003]. The variograms for sand content had a range of 143 m, a nugget of 0.80 (%²), and sill of 16.5 (%²). Airborne LIDAR data, collected by Qi Chen [Chen *et al.*, 2006], describe the elevation, leaf area, height, and diameter (DBH) of each tree within the study area (Figure 5.1). Some spatial autocorrelation was found among the tree diameters, tree heights, and leaf areas, but only at very small lag distances (<10 m). Elevation, however, was highly autocorrelated, which is physically apparent in the site's gently sloping hills. Using ArcView GIS, the soil surface properties at each tree were determined: surface slope was calculated from the elevation, and soil sand content was determined by kriging the measured values.

5.2.2 Design of a Sap Flow Sensor Network

A network of eight “water flow measurement stations” was constructed at the Tonzi Ranch site (Figure 5.2). Each station collected half-hourly measurements of the “water storage and flow” in and around an individual tree. Five Decagon EC-5 probes were placed near the tree: three within 1 m of the stem, at depths of 5, 20, and 50 cm, one at the tree canopy's dripline at a depth of 20 cm, and one under the nearest opening in the canopy, also at a depth of 20 cm. Two sap flow sensors were placed into the tree stem, at 0.5 and 1.5 m from the ground surface. The sensors used the Heat Ratio Method [Burgess *et al.*, 2001a] to monitor the progress of a tracer heat pulse released within the xylem, from which a sap velocity can be calculated.

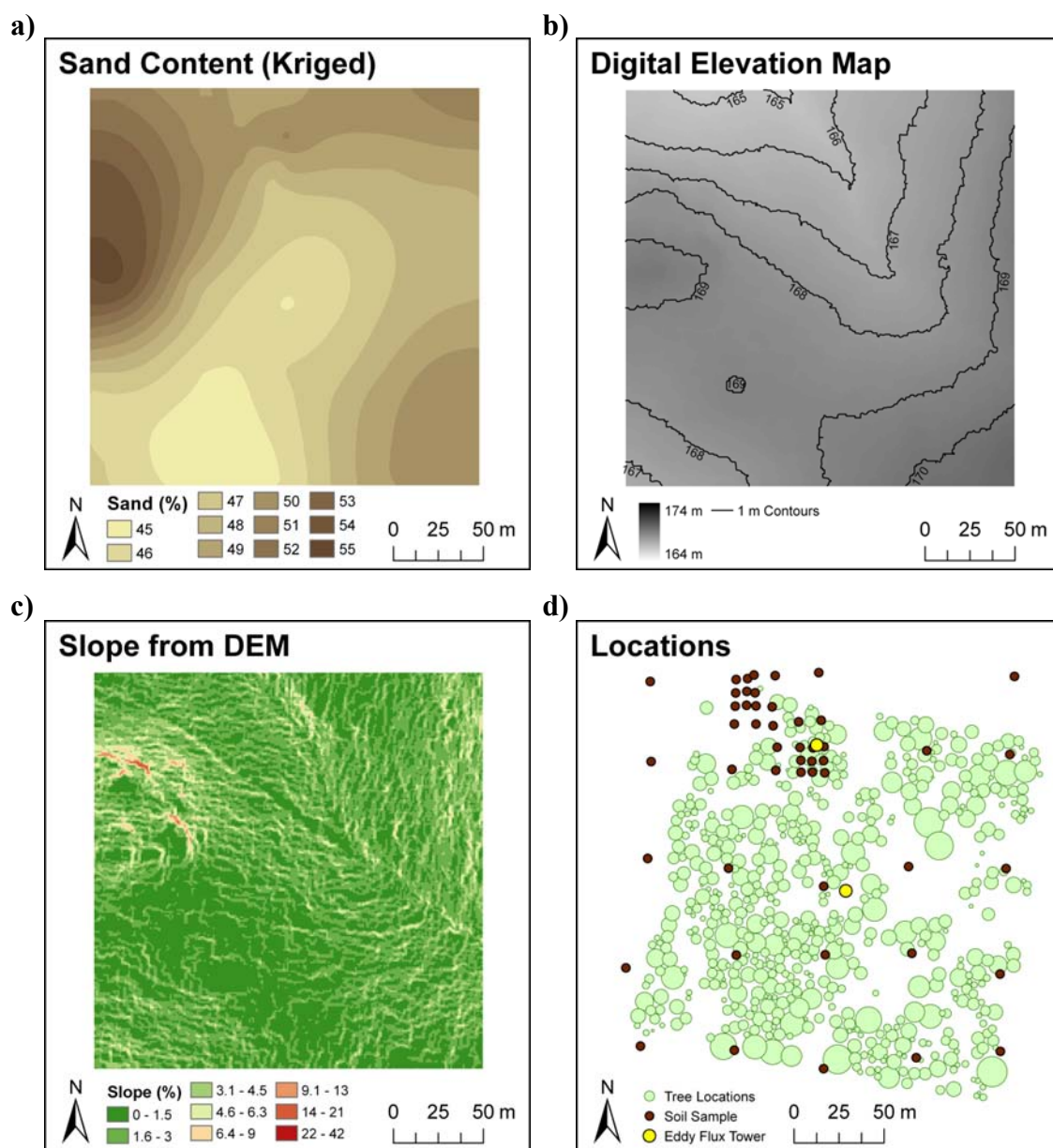


Figure 5.1: Site Characterization Maps
 Plots of (a) soil sand content from texture measurements and (b) elevation, (c) slope, and (d) tree diameter from airborne LIDAR data. The plots are shown for a 200 x 200 m patch around the tower, extracted from the larger, 800 x 800 m data set.

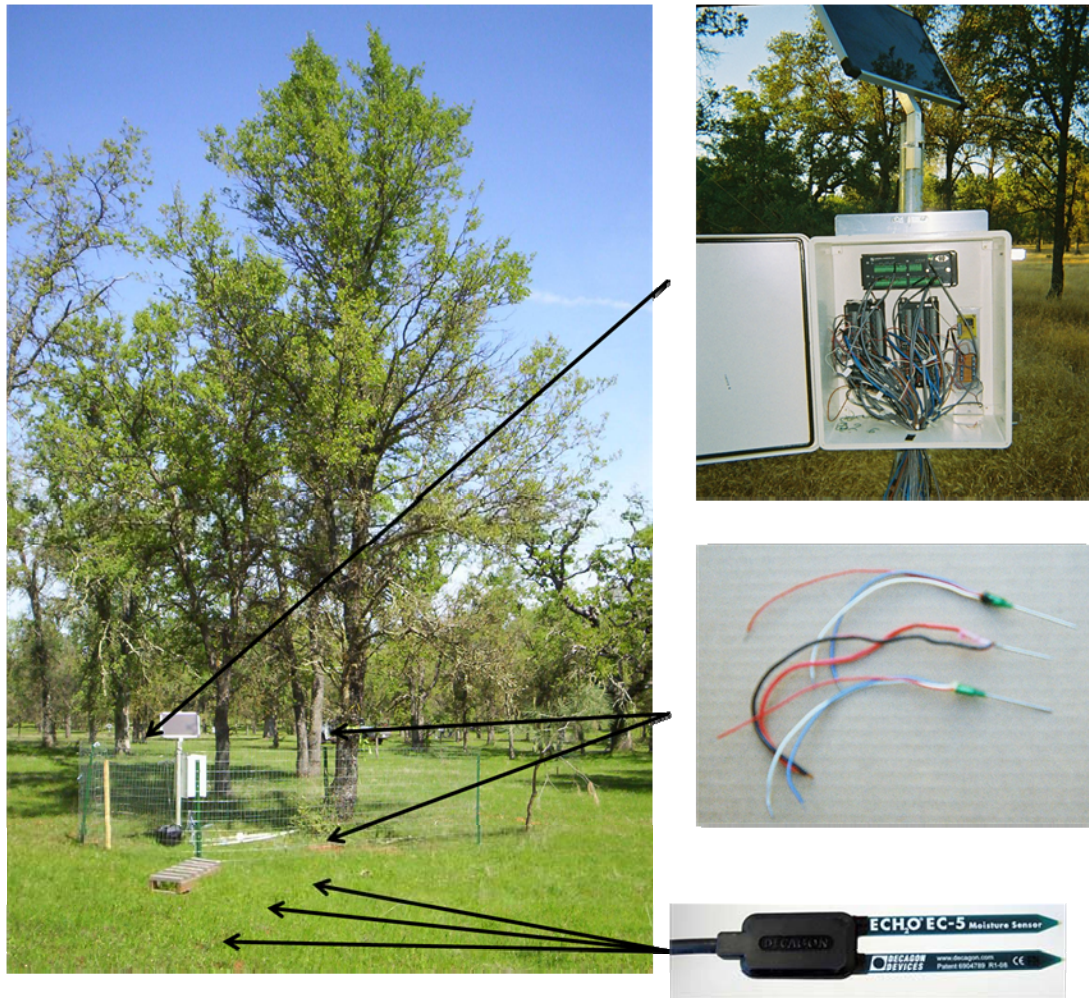


Figure 5.2: Sap Flow Monitoring Station

From left clockwise: Tree representing medium diameter, high soil moisture cluster; data logger and solar panel; a heat pulse ratio sapflow sensor consisting of two thermocouples and a heating element; and an EC-5 soil moisture sensor.

5.2.2.1 Network Design using Cluster Analysis

Cluster analysis is an artificial intelligence application that sorts objects into groupings based on their degree of similarity, without relying on preordained categories.

In particular, the cluster analysis algorithm Partitioning Around Medoids, or PAM, [Kaufman and Rousseeuw, 1990] iteratively searches for k such groupings among the

data. Each grouping, known as a *cluster*, is centered on a representative object, referred to as a *medoid*. The medoid is described by Kaufman and Rousseeuw as “that object of the cluster for which the average dissimilarity to all the objects of the cluster is minimal...These are objects that represent the various structural aspects of the set of objects being investigated...Not only can these objects provide a characterization of the cluster, but they can often be used for further work or research, especially when it is more economical or convenient to use a small set of k objects.”

Unlike hierarchical cluster analysis methods, partitioning methods such as PAM require the user to pre-specify the number of clusters. This feature can be considered both an asset and a liability. With field sampling programs such as this one, logistic constraints often limit the amount of equipment that can be deployed. For instance, we needed to limit the number of sap flow monitoring stations to eight, and therefore set $k = 8$. In the absence of such constraints, a hierarchical method may be a better choice, as it can aid in determining the optimal number of clusters needed to represent the structure of the data.

The cluster analysis and medoid selection was limited to a 200 m x 200 m region around the tower, as this was considered the area most influential on the eddy-covariance measurements. PAM, as implemented in the R statistical package [Maechler *et al.*, 2006; R Development Core Team, 2006], was used to segregate the trees into eight clusters based on tree diameter and the tree’s elevation, slope, and soil sand content. These values were standardized using the equation: $z = (x - \mu_x)/\sigma_x$. Within the program, a Euclidean dissimilarity matrix was used to quantify the difference between

each tree and every other tree. The equation for the Euclidean “distance” between each tree is [Kaufman and Rousseeuw, 1990]:

$$d(i, j) = \sqrt{\sum_1^n (x_{i,n} - x_{j,n})^2} \quad (5.1)$$

where i and j denote individual trees; n represents the number of properties used in the analysis; and x_n represents the standardized values of each of these properties for an individual tree. The Euclidean distance thus becomes a metric for identifying similar trees based on a selected set of characteristics. In this case, $n = 4$ properties—diameter, elevation, slope, and sand content.

Additionally, the standardized tree diameters were weighted, to ensure that the algorithm would not give greater preference to the three soil properties than it did to tree diameter. This resulted in a distance equation:

$$d(i, j) = \sqrt{(3x_{i,D} - 3x_{j,D})^2 + (x_{i,L} - x_{j,L})^2 + (x_{i,E} - x_{j,E})^2 + (x_{i,S} - x_{j,S})^2} \quad (5.2)$$

where D stands for diameter, L for slope, E for elevation, and S for sand content.

Alternatively, soil moisture content could have been used in the analysis. At the time of collection, during the rainy season, the soil was almost uniformly moist, making it an uninformative metric. Instead, we decided to use a surrogate for it (the combination of elevation, slope, and sand) that would be representative of its intrinsic water holding properties, particularly those that would be influential during the dry summer months. Section 5.3.1 discusses the performance of this surrogate measure based on the results.

Once a distance matrix was established, the trees were initially segregated into $k = 8$ random groups (clusters) and a medoid tree for each was randomly selected. An

Table 5.1: Results of Cluster Analysis

Cluster	Mean	1	2	3	4	5	6	7	8
DBH (cm)	26	30	45	31	22	15	10	30	18
Trees (num.)	-	97	56	94	83	71	80	42	52
Sapwood area (m ²)	-	5.1	5.3	4.6	2.5	1.3	0.6	2.4	1.1
Slope (%)	1.81	L	H	H	L	H	H	L	L
Elevation (m)	168.31	L	H	L	H	H	H	H	L
Sand (%)	47.8	L	H	H	L	H	H	L	L

L represents a medoid tree with a value lower than stand average, H represents higher than average.

average dissimilarity between the trees in a group and their medoid was calculated. The algorithm then iteratively and systematically alters these groupings and medoids, minimizing this average dissimilarity metric. Once the metric could not be improved by switching either the cluster membership of any tree or the medoid tree of any cluster, the classifications were established.

As an end result, each grouping, shown graphically in Figure 5.3, represents a different soil environment and diameter combination. Table 5.1 presents the results of the analysis, listing the diameter of each selected medoid tree (where the sap flow stations were located), the number of trees in the cluster, and the total sapwood area represented by the trees. It also shows how the soil properties of the cluster compare to the mean values for the site: 168.31 m for elevation, 47.8% for sand content, and 1.81% for slope.

Several potential misconceptions about this analysis should also be addressed.

First, PAM and partitioning cluster methods *are not* related to spatial statistics methods

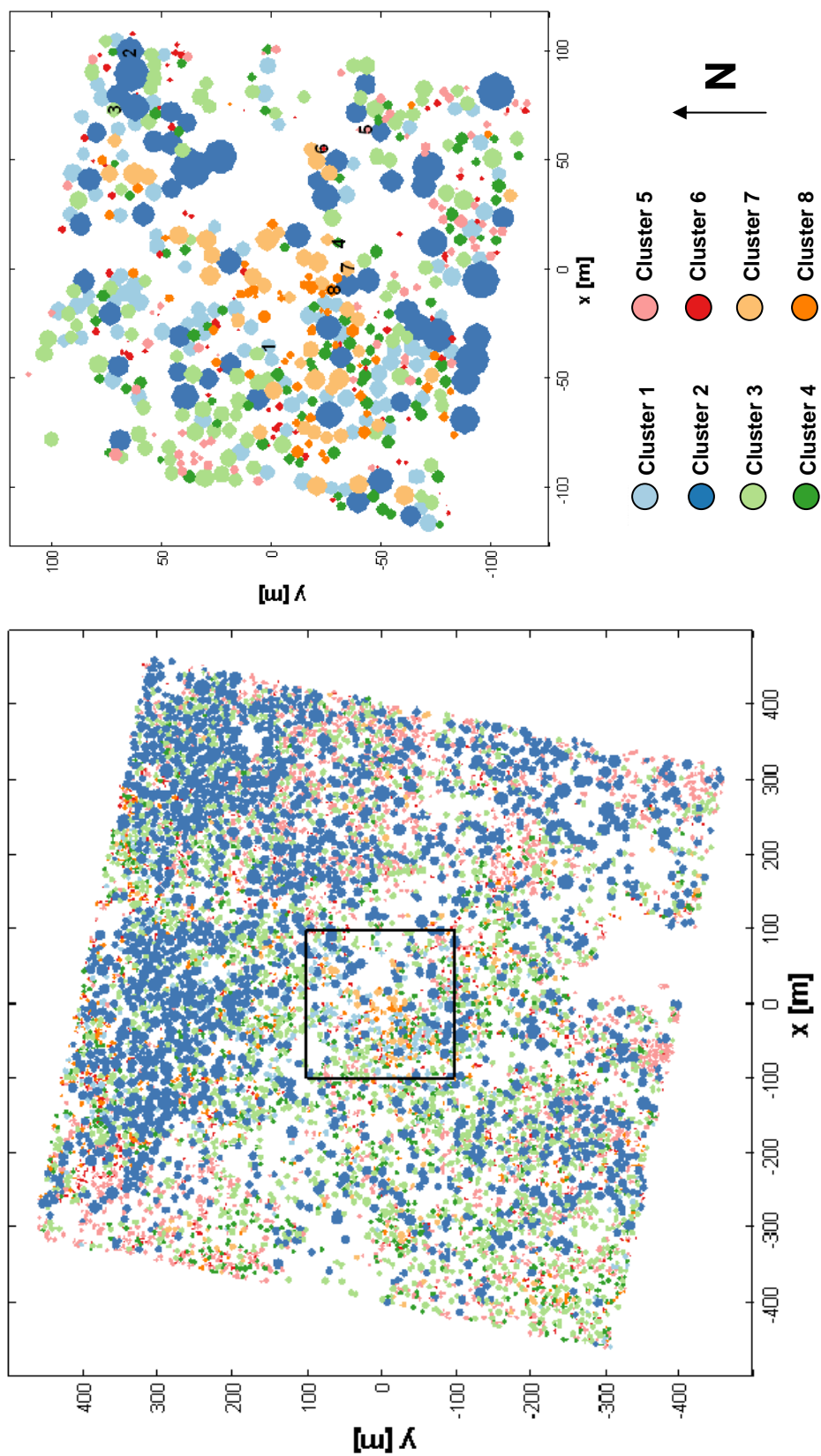


Figure 5.3: Maps of Tree Locations, Size, and Cluster Membership
Map of the cluster membership for each tree, with the 200 x 200 m study sub-area shown in the pullout. The representative, or medoid, tree for each cluster is denoted by the number, and these are the trees that were selected to host the sap flow stations. The eddy-covariance tower is located in the center of each plot, at coordinate (0,0).

such as the Ripley's K function, which is frequently used by the forestry community to determine if trees are distributed in a random, clumped, or regular pattern [Ripley, 1981]. Second, the Euclidian distance between two properties should not be confused with the physical distance between two trees. While it is a simple procedure to include the physical distance in the calculation (by using Cartesian coordinates as a property), it would have been inappropriate in this case and was not done.

5.2.2.2 Data Processing and Calibration

The raw heat pulse velocity (v_h , in cm hr^{-1}) is calculated using the equation:

$$v_h = B_0 + B_1 \frac{k}{x} \ln \frac{T_d}{T_u} \quad (5.3)$$

where x is the average value of x_d and x_u , the locations of the downstream and upstream temperature probes; T_d and T_u are average temperature rise over $60 \text{ sec} \leq t \leq 100 \text{ sec}$ measured by the probes; B_0 and B_1 are tree specific empirical calibration factors; and k is the average thermal diffusivity of the wood, $0.0033 \text{ cm}^2 \text{ s}^{-1}$. The parameters B_0 , B_1 , and k were inferred using inverse modeling techniques [Chen *et al.*, In preparation]. To be consistent with the previously published literature, this measurement is shown in units of cm hr^{-1} in this work; however, when used in further calculations, it is converted to m s^{-1} .

The heat pulse velocity must then be converted to sap velocity (V_s , in m s^{-1}) based on the heat retention properties of the wood [Burgess *et al.*, 2001a]:

$$V_s = V_h \beta \frac{\rho_b (C_w + m_c C_s)}{\rho_s C_s} \quad (5.4)$$

where ρ_s is the density of water, 996 kg m^{-3} ; C_w and C_s are wood and water specific heat capacities at $20 \text{ }^\circ\text{C}$, 1200 and $4182 \text{ J kg}^{-1} \text{ K}^{-1}$, respectively [Burgess *et al.*, 2001a]; β is a unitless wounding factor for blue oaks, 1.96 [Kiang, 2002]; and m_c is stem

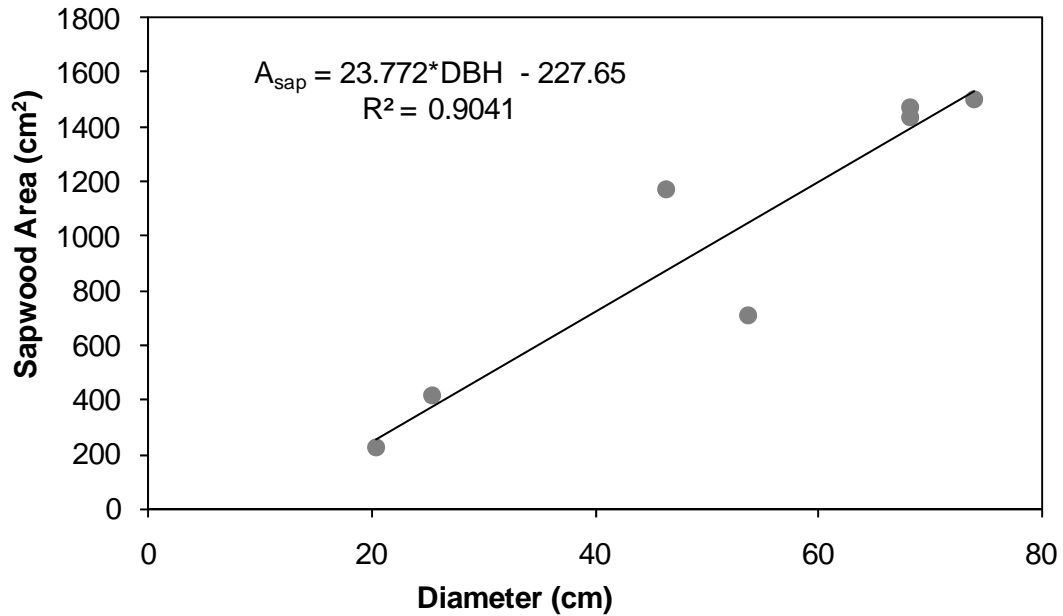


Figure 5.4: Sapwood Area
Sapwood area as a function of diameter, collected using trees felled by the landowner during the study period.

moisture content, estimated as 0.7. The basic density, ρ_b , of blue oak wood, was found by multiplying its specific gravity by the density of water; literature values found for a specific gravity range from 0.64 and 0.8928 [Sargent, 1885; Wilson *et al.*, 1987], making ρ_b between 1120 and 1556 kg m⁻³. A value of 1350 kg m⁻³ was used here.

After calculating the raw sap flow velocities, some signal processing is then necessary: spikes in the data are removed using a cutoff filter of three standard deviations; its baseline is shifted to correspond to the zero sap flow rates found during winter nighthtimes [Fisher, 2006]; and the gaps are filled. Finally, the tree volumetric flow rate (Q_{sap} , in m³ s⁻¹), otherwise known as the sap flow rate, was found using the equation:

$$Q_{sap} = (1 - \gamma)V_s A_{sap} \quad (5.5)$$

where A_{sap} is the sapwood cross-sectional area and γ is a ray cell factor representing the fraction of non-conducting area within the sapwood, 0.29 for blue oaks [Kiang, 2002]. The sapwood area and the DBH correspond in a roughly linear fashion (Figure 5.4); this relationship was used to estimate A_{sap} for each medoid tree.

Since sap velocity is, as previously noted, known to vary along the radial axis into the tree, the probes were constructed to measure at depths of 0.8 cm and 2.8 cm into the sapwood. Modifying Equation (5.5), we find an area weighted average of the velocities:

$$Q_{sap} = (1 - \gamma)(V_{s,1}A_1 + V_{s,2}A_2) \quad (5.6)$$

where $V_{s,1}$ and $V_{s,2}$ are the sap velocities measured at each depth into the wood; A_1 and A_2 are the areas represented by each velocity; and $A_{sap} = A_1 + A_2$.

5.2.3 Upscaling from Tree to Stand Transpiration

To upscale the sap velocities from the medoid tree measurements to a stand level flow rate (Q_{stand}), the following equation was used:

$$Q_{stand} = \sum_{j=1}^8 (1 - \gamma)(V_{s1,j}A_{1,j} + V_{s2,j}A_{2,j}) \quad (5.7)$$

where $A_{1,j}$ and $A_{2,j}$ are the total outer and inner sapwood areas in each cluster, over the entire study area (Table 5.1). To find a value for the stand transpiration (q_{stand}) that is comparable to the flux from eddy-covariance (E), the total stand volumetric flow rate must be normalized by the study area (A_{stand}):

$$q_{stand} = \frac{Q_{stand}}{A_{stand}} \quad (5.8)$$

where A_{stand} is 42,822 m² and q_{stand} is in m s⁻¹. This value will be referred to as the stand transpiration found using the ‘‘Sapwood Area’’ method.

An alternate approach considers the area of the stand measured by the eddy-covariance tower when computing the stand flux. Using a 2-D analytical solution along with the detailed canopy maps, we can determine which trees are in the tower’s ‘‘footprint’’ at a given point in time. This approach produces a flux that is potentially less representative of the landscape as a whole, but is more fairly compared to that measured by the eddy-covariance, or ‘‘tower’’, system.

The analytical solution used for this method was developed by Hsieh et al. [2000] and modified by Detto et al. [2006b]. It considers the turbulence properties of the atmospheric flows and is given by the equation:

$$f(x, y) = \left[\frac{1}{\sqrt{2\pi}\sigma_y} e^{-\frac{1}{2}\left(\frac{y}{\sigma_y}\right)^2} \right] \left[\frac{1}{k_v^2 x^2} D z_u^P |L|^{1-P} e^{\frac{D z_u^P |L|^{1-P}}{k_v^2 x}} \right] \quad (5.9)$$

where $f(x, y)$ is the source area function; x and y are Cartesian coordinates with the tower at (0,0); L is the Obukhov length, in m; k_v is the von Karman constant, 0.4; and D and P are constants with values for stable, unstable, and neutral atmospheric conditions.

The value of σ_y can be found from the equation:

$$\sigma_y = 0.3 z_0 \frac{\sigma_v}{u^*} \left(\frac{x}{z_0} \right)^{0.86} \quad (5.10)$$

where σ_v is the standard deviation of the lateral wind fluctuations, in m s⁻¹; u^* is the friction velocity, in m s⁻¹; and z_0 is the roughness length for momentum, 0.92 m [Kim et al., 2006]. The length scale z_u is related to z_0 and z_m , the measurement height (23 m):

$$z_u = z_m \left(\ln \left(\frac{z_m}{z_0} \right) - 1 + \frac{z_0}{z_m} \right) \quad (5.11)$$

In this formulation, slightly modified from Detto et al. [2006a], the source area function is discretized onto a uniform $M \times N$ grid:

$$q_{stand} = \sum_{k=1}^8 \frac{Q_{sap,k}}{A_{canopy,k}} \sum_{j=1}^N \sum_{i=1}^M \varepsilon_{i,j,k} f(x_i, y_j) \Delta x \Delta y \quad (5.12)$$

where $\Delta x \Delta y$ is the area of a grid cell; x_i and y_j are the coordinates at the center of a grid cell; $\varepsilon_{i,j,k}$ is an indicator function equal to one if any part of a tree in cluster k is located within that grid cell, and zero otherwise; and $A_{canopy,k}$ is the radial extent of the measured tree's canopy. Figure 5.5 shows an example of the source area function, $f(x_i, y_j)$, overlaid onto the map of the tree locations. This footprint was generated for daytime spring conditions, with an unstable atmosphere occurring at noon ($u^* = 0.7 \text{ m s}^{-1}$, $L = -89 \text{ m}$, $\sigma_v = 0.8 \text{ m s}^{-1}$, and $z_0 = 0.92 \text{ m}$). The value calculated using this method will be referred to as the stand transpiration using the “footprint” method.

Half-hourly values of q_{stand} were generated using these equations, the tower wind data, and the LIDAR tree location data. To create a fair comparison between this and the other methods of upscaling sap flow data, it was necessary to ensure that only times when the tower was primarily “sensing” in the study region were included. During the nighttime, stable conditions frequently forced the footprint entirely outside of the study area (Figure 5.5). These time-periods were excluded from the upscaling analysis, due to this problem, as well as the high levels of uncertainty associated with footprint modeling in stable conditions. Depending on the atmospheric conditions, this problem also

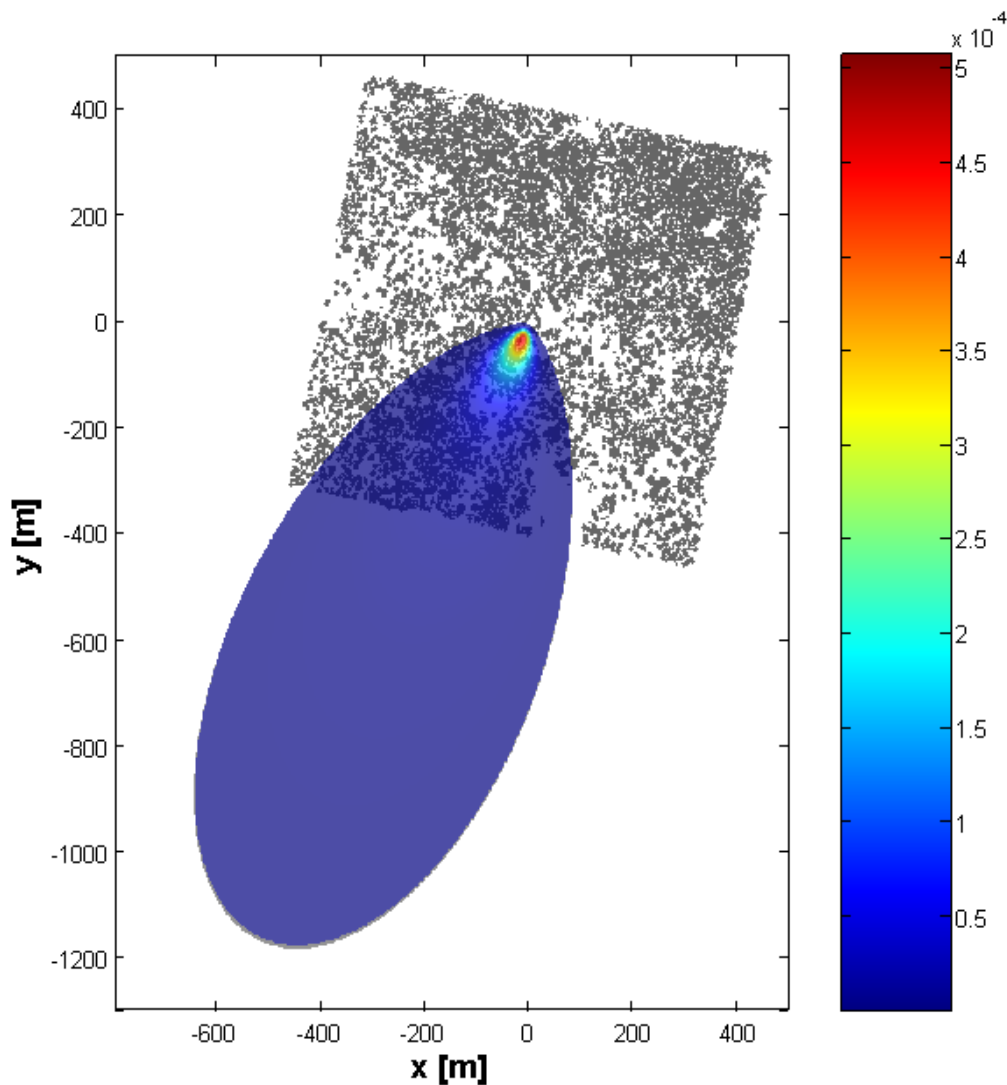


Figure 5.5: Example Flux Footprints for Tonzi Site

The top flux footprint was generated for noon on Day 141 (May 20, 2008), while the bottom was generated for midnight that night. The outer edge of the footprint represents the 90% flux boundary, i.e. 90% of the flux sensed by the tower is within the colored area. The footprint extends beyond the characterized area, which could lead to upscaling problems.

occasionally occurred during the day. To handle this issue, time-periods where less than 70% of the source area function was contained inside of the study area were eliminated from consideration. When more than 70% but less than 100% of the footprint was contained within the study area, the source area function was scaled to reflect this. For

instance, if 80% of the source area function was inside the study area, it was divided by

$$0.8: f_{scaled}(x_i, y_j) = f(x_i, y_j) / 0.8.$$

5.3 Results and Discussion

As previously suggested, upscaling from sap flow requires the synthesis of several elements, namely spatially referenced landscape and vegetation data and point measurements of individual tree transpiration. These factors must be combined, in a systematic manner, to yield a stand scale transpiration value that can be compared to latent heat data from an eddy-covariance system. Direct comparison is a must; while the sap flow data yields information covering the entire study area, eddy-covariance covers only a portion of it, the footprint.

In this section, we detail the results found at each step of this process, first discussing the sap flow dataset and its features. From there, we consider the representativeness of the clusters themselves and the eddy-covariance system: how well do these reflect the overall stand properties? We then compare the transpiration values found by both methods, describe the advantages each possesses, and detail the potential sources of discrepancy between the two. Finally, we provide suggestions for future refinements to sap flow upscaling and implementation of these upscaling techniques.

5.3.1 Sap Flow by Cluster and Season

Volumetric sap flow rates for each cluster medoid are shown in Figure 5.6, for each of the four, one-week focus periods. The rates are averaged by hour, to show their daily pattern. The peak values typically occur in June, and decrease as the season progresses. Sapwood area, as reflected in tree diameter, is very influential on volumetric

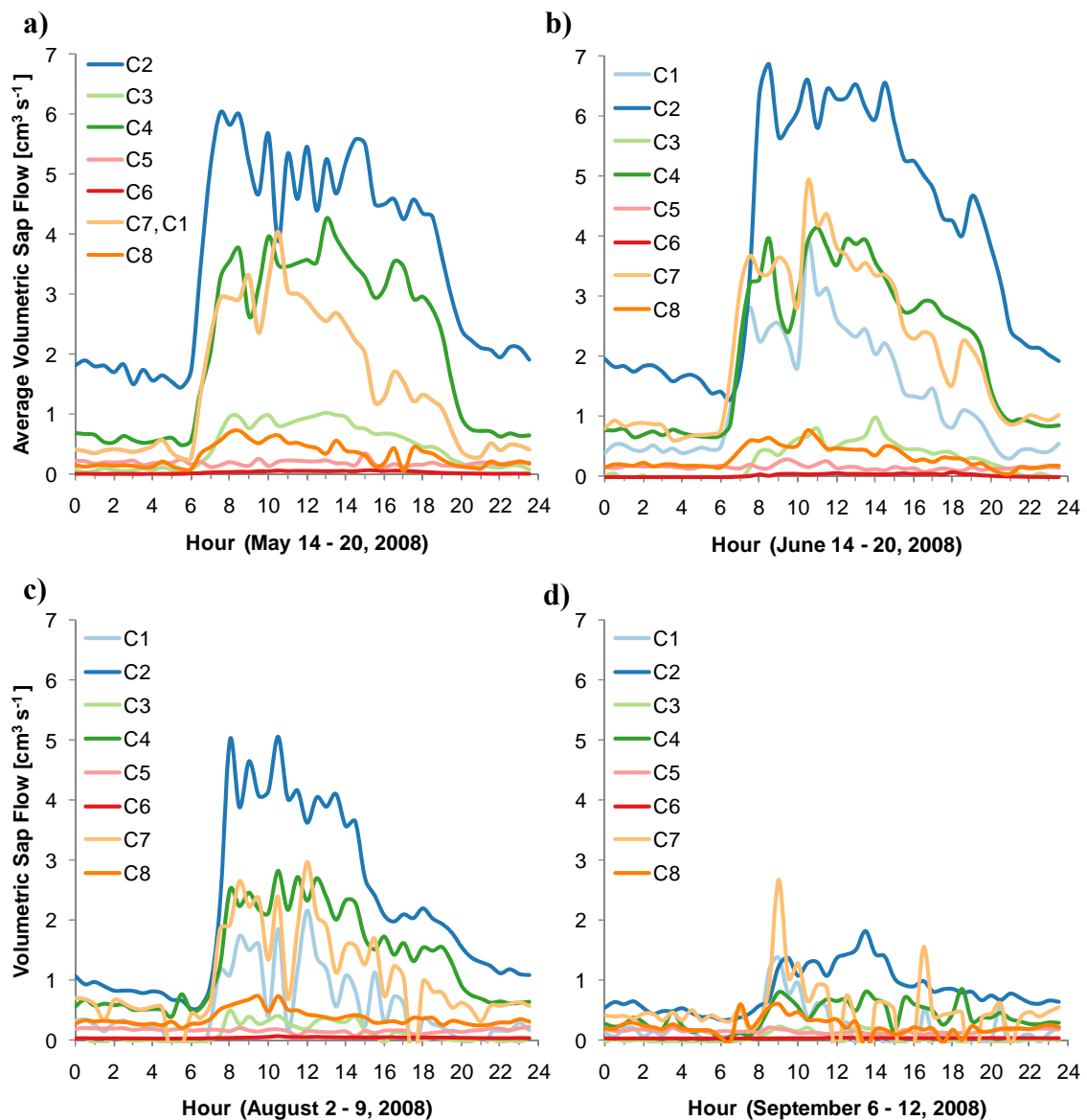


Figure 5.6: Cluster Sap Flow

Half-hourly sap flow rates, in $\text{cm}^3 \text{s}^{-1}$, are shown for week-long periods during May (a), June (b), August (c), and September (d). Sap flow follows a regular, diurnal cycle. Smaller trees transpire less; the medoid trees for Clusters 5, 6, and 8 are all under 0.20 m in diameter and their flow rates rarely exceed $1.0 \text{ cm}^3 \text{s}^{-1}$. The largest tree, the medoid for Cluster 2, has a transpiration rate six times higher.

sap flow rate, primarily because it is used in the upscaling process ($Q_{\text{tree}} = A_{\text{sapwood}}V_s$). As the largest diameter tree, the Cluster 2 medoid consistently shows the highest volumetric sap flow rate, from a maximum of $6.8 \text{ cm}^3 \text{ s}^{-1}$ in June to a minimum of $1.8 \text{ cm}^3 \text{ s}^{-1}$ in September. During the spring and summer months, these rates are roughly twice those of Clusters 1, 4, and 7, medium diameter trees with moderate to high soil moisture, and six times those of Clusters 5, 6, and 8, small diameter trees. As leaf senescence approaches, these rates begin to converge, likely because the sensors are less accurate at very low flow rates. The daily pattern of sap flow, if not its magnitude, is fairly consistent between clusters. Sap flow rates triple shortly after sunrise, plateau quickly, begin to decrease at midday (especially in the dry season), and taper off at sunset. During the nighttime, flow remains steady, but present, at about 20 to 30% of the daily peak values. Overnight flow rates also correspond to diameter; Cluster 2 has the highest rates, peaking at $2 \text{ cm}^3 \text{ s}^{-1}$ in June, decreasing to $1 \text{ cm}^3 \text{ s}^{-1}$ in August and $0.5 \text{ cm}^3 \text{ s}^{-1}$ in September. These nighttime flow rates are consistent with Fisher et al.'s previous observations at the site [2006] and are positively correlated with nighttime vapor pressure deficit (Figure 5.7). While it is possible that these flows represent the replenishment of water stores depleted during the daytime, two factors support the conclusion that they represent true dark transpiration: their correlation with nighttime vapor pressure deficit and the observation that during the dry season, pre-dawn water potentials do not typically equilibrate with soil and groundwater matric potential. (More information on predawn water potential can be found in Chapters 2 and 4.)

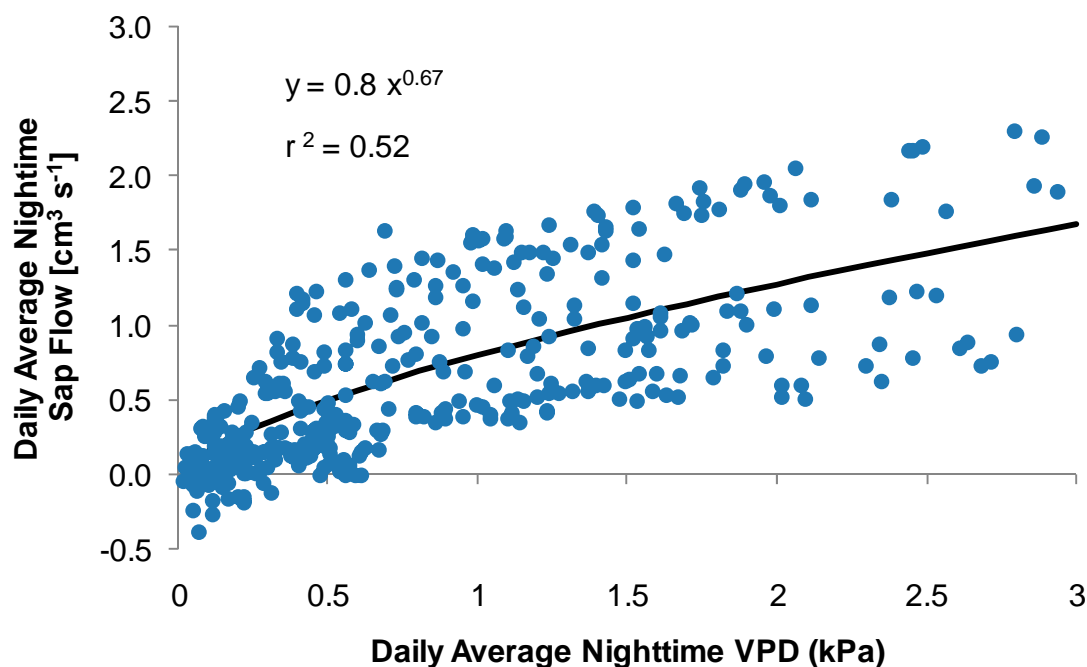


Figure 5.7: Relationship between Nighttime Sap Flow and Vapor Pressure Deficit
 The daily average of nighttime sap flow rate and nighttime vapor pressure deficit (VPD) are correlated, with low VPD corresponding to low sap flow. This relationship was first noted at the study site by Fisher et al. [2006], and supports the conclusion that tree transpiration is occurring at night. The relationship is shown for Cluster 2, but also holds for the other trees that display nighttime sap flow.

5.3.2 Cluster Selection: Was it Representative of the Study Area?

In this work, trees had two important properties that we considered essential determinants of sap flow, based on literature reports: diameter and water environment. However, it was unknown, a priori, if these were applicable to this system or if the proposed method would accurately capture the variation in tree transpiration. To answer this, we need to look at two separate issues. First, did the clustering algorithm divide the trees into appropriate diameter and soil moisture combinations? Second, were the right tree properties selected for the analysis?

To answer the first question, a histogram of tree diameter was created for each cluster (Figure 5.8). Most clusters appear to be associated with only a small range of diameters, with a typical span of 0.14 m. Cluster 2 has a more extensive range, as it is associated with infrequently occurring, very large diameter trees. While the clusters represent the entire continuum of diameter, some overlap occurs between Clusters 5, 6, and 8 and between Clusters 1, 3 and 7. Here, we need to examine the differences in soil moisture, shown at right, in order to determine if they are representing trees in different hydrologic conditions. The soil moisture measurements at the medoid trees reveal the distinctiveness of Clusters 5, 6, and 8 (shown in red, orange, and pink); their mid-summer values range from 0.13 to 0.24 m³ m⁻³, equal to soil matric potentials of -0.35 and -0.06 MPa, respectively. The trees in Cluster 6 would traditionally be considered under water-stress, while those in Cluster 8 would not. The separation between Clusters 1, 3, and 7 is not as distinct. Clusters 1 and 7 have nearly identical soil moisture and diameter ranges, potentially signifying that their trees could be combined into one group and suggesting the question - how similar are their sap velocities?

Examining a plot of the sap flow from each of these clusters (Figure 5.9), we note that the sap flow velocity for Cluster 7 is approximately 30 cm h⁻¹ higher than for the much drier Cluster 3. This finding is consistent with the assumption that soil moisture differences will lead to different individual tree transpiration values. The measurement for Cluster 1, however, shows a poor quality diurnal signal, indicating sensor failure. The magnitude of the difference between the midday high and the nighttime low is small, and the signal of the probe was reduced to approximately one-fifth its usual strength. These problems indicated that the tree had begun to reject the

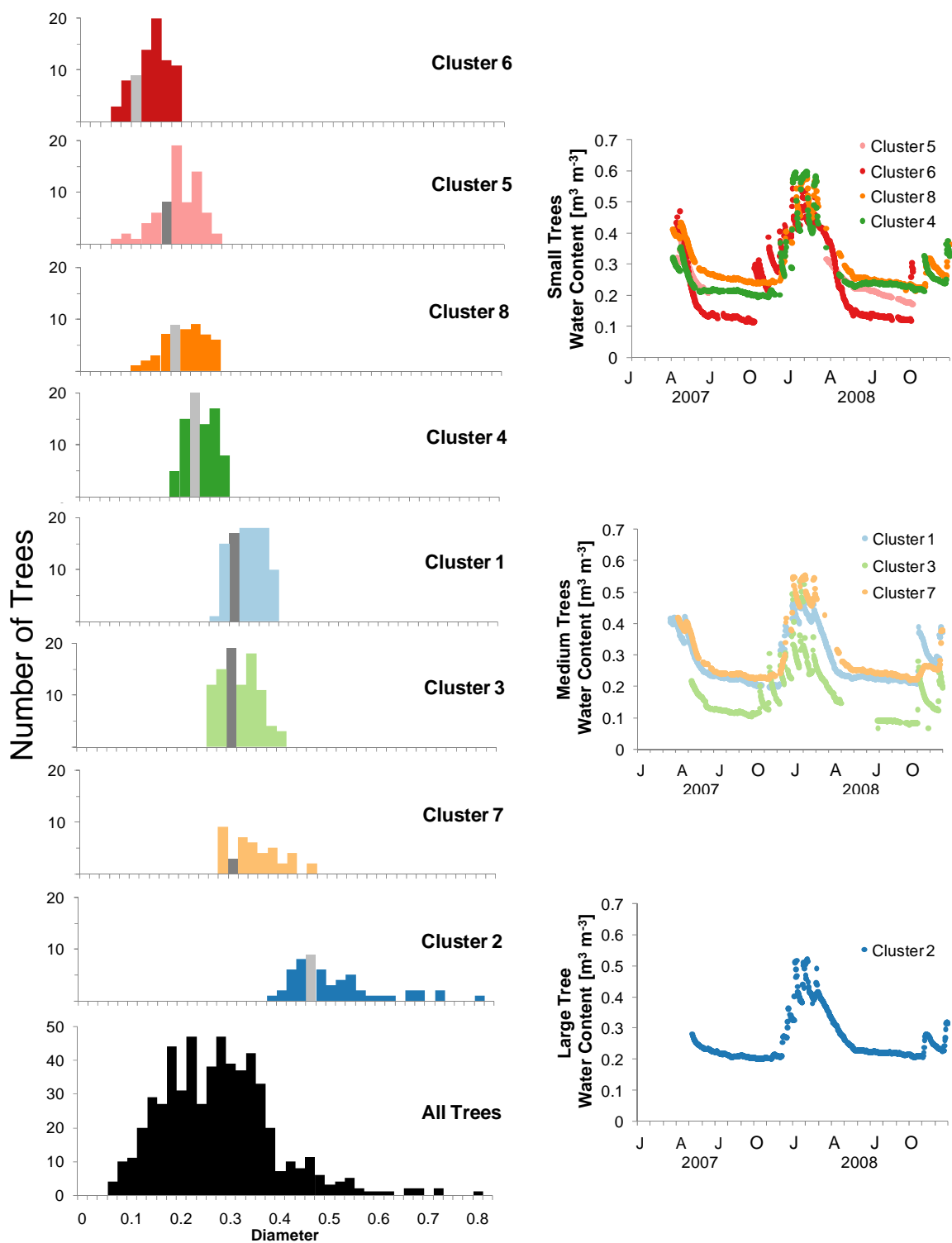


Figure 5.8: Statistical Distribution of Tree Diameter and Cluster Soil Moisture
 The diameter ranges of the trees in each cluster are shown on the left, while the soil moisture at each measurement station is shown on the right. In clusters that have very similar diameters (e.g. Clusters 5, 6, 8), soil moisture is often a distinguishing factor.

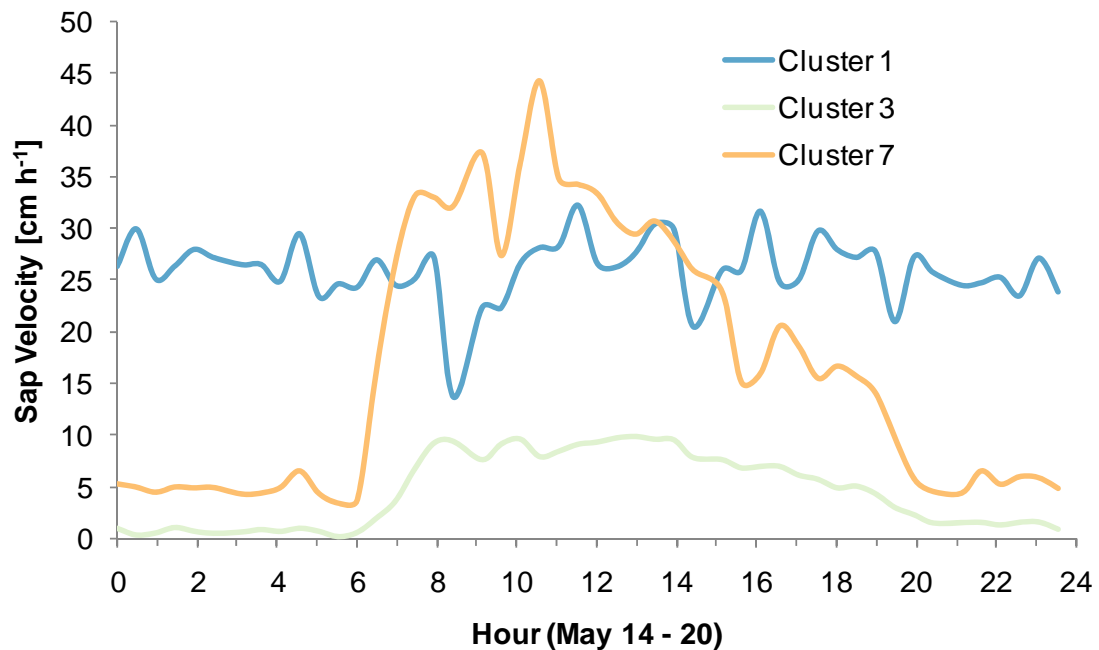


Figure 5.9: Comparison of Sap Flow from Midsize Trees

The diurnal signal in the Cluster 1 medoid tree is weak compared to that in the similar diameter trees (Clusters 3 and 7), indicating that wounding had prevented accurate measurements. The heat pulse probes for Cluster 1 were replaced in the Winter 2008, and as a result, the spring diurnal signal again resembled that of the other clusters.

sensor, forming a thick wound around it that buffered against the heat signal. When the probes were moved to a new location on the same tree, the signal once again returned to normal. Unfortunately, this failure was not discovered in time to be corrected for the 2008 growing season. To fill this data gap, it was assumed that Clusters 1 and 7 could reasonably be combined, and the Cluster 7 velocities were used as surrogates for Cluster 1 measurements.

Overall, the plots in Figure 5.8 suggest that the network design meets three important criteria: it covers a range of values across the stand, and combinations of values are, for the most part, not unnecessarily repeated.

The next question asks – how influential were the selected parameters on individual tree transpiration? The LIDAR data offers a range of tree properties; *a priori*, we selected diameter, elevation, and slope from a list that also included tree height, stem height, canopy radius, leaf area, leaf area index, and total tree biomass. Would another set of parameters correspond better to the observed variation in sap velocities among the measured trees?

To answer this question, we correlated total daily sap velocity for DOY 100 to 113 to the parameters measured by LIDAR, using a generalized linear model with a normal distribution and a log link function. A range of parameter combinations were tested and compared, aiming to minimize the deviance, a goodness-of-fit statistic based on the residual sum of squares. The parameters best able to explain the variability in the sap velocities were diameter, elevation, height, leaf area, and canopy radius (Figure 5.10).

From these, the following equation was developed to predict the velocity at any given tree:

$$\log(V_s) = 17.9 * Diameter - 2.4 * Elevation - 1.4 * Height + 0.005 * Leaf Area + 1.0 * Canopy Radius + 407 \quad (5.13)$$

where V_s is in cm d^{-1} , leaf area is in m^2 , and the remaining parameters are in m. In order to avoid auto-correlation, velocities were used instead of volumetric flow rates. The parameters were developed using data from odd-number days, and tested against data from even-numbered days, as shown Figure 5.10.

The influence of the additional parameters indicates that soil moisture and diameter are not, as presumed, the only controlling factors on tree sap velocity. The

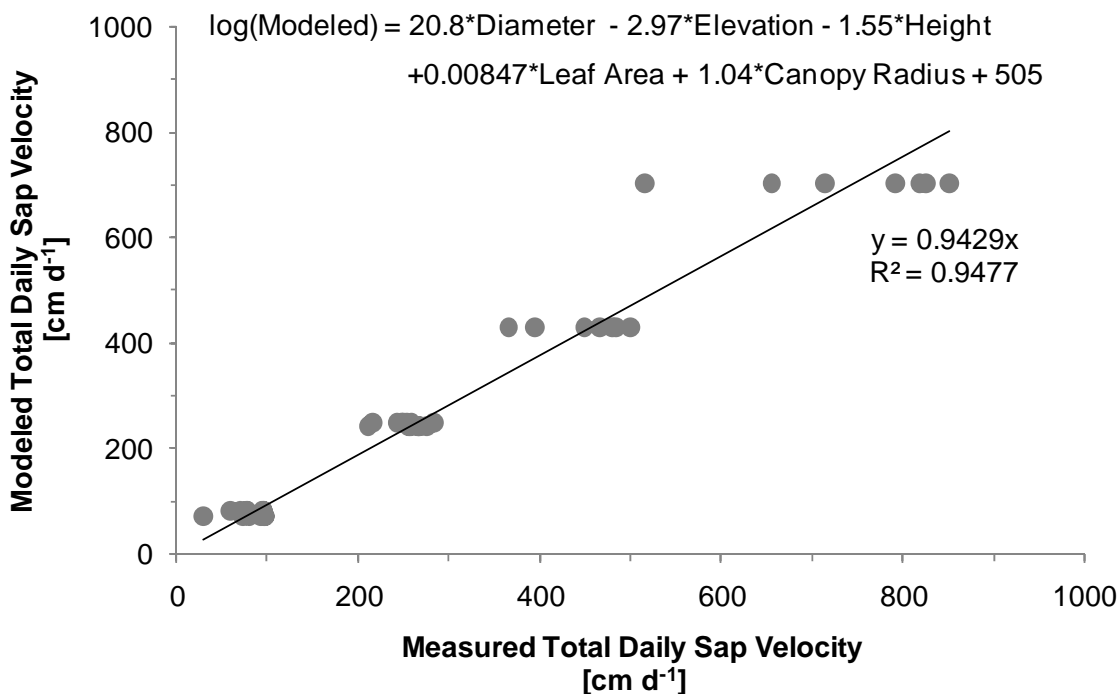


Figure 5.10: General Linear Model of Sap Velocity

Sap velocity can be modeled as a function of multiple tree parameters found by LIDAR. In the original cluster design, diameter, elevation, slope, and sand content were used. These results suggest that a combination of diameter, elevation, tree height, leaf area, and canopy radius may have been more suitable.

need to include leaf area and canopy radius implies that the light environment of individual trees is also an important consideration. The inclusion of height suggests that tree age, and potentially access to groundwater, is another factor. Further work should be done to add the depth to water table to the analysis, since blue oaks are known to use significant amounts of groundwater during the summer months (Chapter 4).

One caveat to this analysis is that the trees measured cover only a limited portion of the parameter space for many of the variables. For instance, the range of leaf areas is 2.5 to 140 m² in the sampled trees, while the overall range in the 200 m x 200 m domain is 0.15 to 400 m². Thus, the model cannot be used to predict the transpiration of trees

significantly out of the measured range; it produces spurious, non-physical values (for example, $V_s > 400 \text{ cm d}^{-1}$). An additional concern is that the model is over-fitted, given that there are only seven values for the dependent variable at any point in time, but there are six parameters. Rigorous hypothesis testing should be performed to determine if this number can be successfully reduced, and if any of the parameters, such as leaf area and canopy radius, are correlated. However, initial tests reveal that even when the model is reduced in complexity, the unrealistic transpiration values still occur.

5.3.3 Is the Tower Footprint Representative of the Study Area?

The next question is – how well does the eddy-covariance system measure the study area? Does its footprint reasonably represent the trees in this area? Answering this question is necessary to provide a fair comparison between the tower data and the upscaled sap flow data.

Figure 5.11 illustrates how the footprint of the eddy-covariance flux is occupied by trees of each cluster type. The proportion of the footprint occupied by each tree type is shown; this proportion can be represented by the equation:

$$p_k = \frac{\sum_{j=1}^N \sum_{i=1}^M \varepsilon_{i,j,k} f_{scaled}(x_i, y_j) \Delta x \Delta y}{\sum_{j=1}^N \sum_{i=1}^M f_{scaled}(x_i, y_j) \Delta x \Delta y} \quad (5.14)$$

The canopy coverage is 53% over the entire study area, so the tree-covered proportion of the footprint should be similar, if it is indeed representative of the study area. Looking at the graph, we find that the tree-covered proportion of the footprint is most commonly between 45 and 50% and rarely exceeds 53%. This indicates that the tower could be sampling from a slightly less dense region, potentially underestimating the flux.

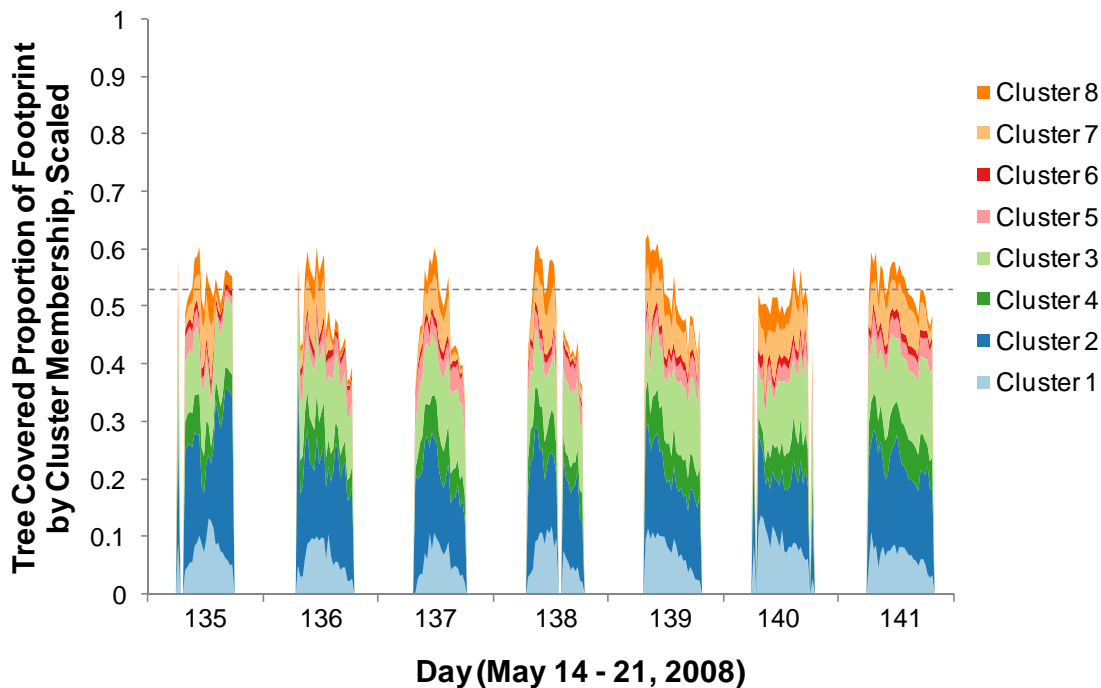


Figure 5.11: Proportion of Footprint Covered by Trees

The location and extent of the eddy-covariance footprint depends on the wind direction and the stability of the atmosphere, thus the trees contained within the footprint will vary temporally. This figure shows the proportion of the footprint covered by tree canopy (as opposed to openings in the canopy), broken down into the types of trees contained within it. Approximately 53% of the study area is covered by tree canopy, as indicated by the dashed line; to be representative of the study area, the footprint should approximate this coverage.

How do the trees in the footprint area compare, then, to the trees in the study area? Does the footprint upscaling give more weight to certain types of trees over others? Table 5.2 shows how the footprints found typically weight each tree cluster, as compared to the weighting of each cluster over the entire study area. In all months, the large, Cluster 2 trees are underweighted; while they represent 51% of the total canopy area, the footprints show them as only 24 to 30% of the canopy area sensed by the tower. This difference is due to the location of the footprint, which most frequently covers the lower left quadrant of the study area. However, the upper right quadrant contains the

Table 5.2: Weight of Cluster Contribution to Canopy Area

Weight		1	2	3	4	5	6	7	8
Study Area		0.03	0.51	0.23	0.05	0.11	0.02	0.02	0.02
Footprints	May	0.14	0.30	0.22	0.11	0.06	0.03	0.09	0.03
	June	0.16	0.27	0.23	0.10	0.06	0.03	0.09	0.06
	August	0.16	0.24	0.23	0.11	0.06	0.03	0.11	0.06
	September	0.16	0.24	0.22	0.11	0.06	0.03	0.11	0.06

highest concentration of Cluster 2 trees, both visibly and quantitatively (Figure 5.3).

The tower only infrequently samples from this quadrant. The footprint also over-represents the small trees in Cluster 5 and medium trees in Clusters 1 and 7.

Thus, the eddy-covariance system samples more trees that have small and medium diameters (8 to 30 cm) and fewer trees that have large diameters (>40 cm). As shown in Figure 5.6, the Cluster 2 medoid tree had a rate of transpiration approximately $3.5 \text{ cm}^3 \text{ d}^{-1}$ higher than the Cluster 1 medoid. If the eddy-covariance system were sampling from a more representative area, the actual stand flux could be higher than the measured value. These results also suggest that, in regards to transpiration, the canopy and landscape is much less homogenous than previously assumed.

5.3.4 Comparison of the Tower and Sap Flow Stand Transpiration

Hourly values of stand transpiration during the focus periods are shown in Figure 5.12. During May, the tower and footprint data correspond well, both showing a diurnal peak flux of 0.17 to 0.19 mm h^{-1} . The sapwood area method underestimates this flux, showing a peak rate of 0.1 mm h^{-1} . This behavior is similar to that noted earlier by Kiang [2002]. However, the match between the footprint method and the tower suggests

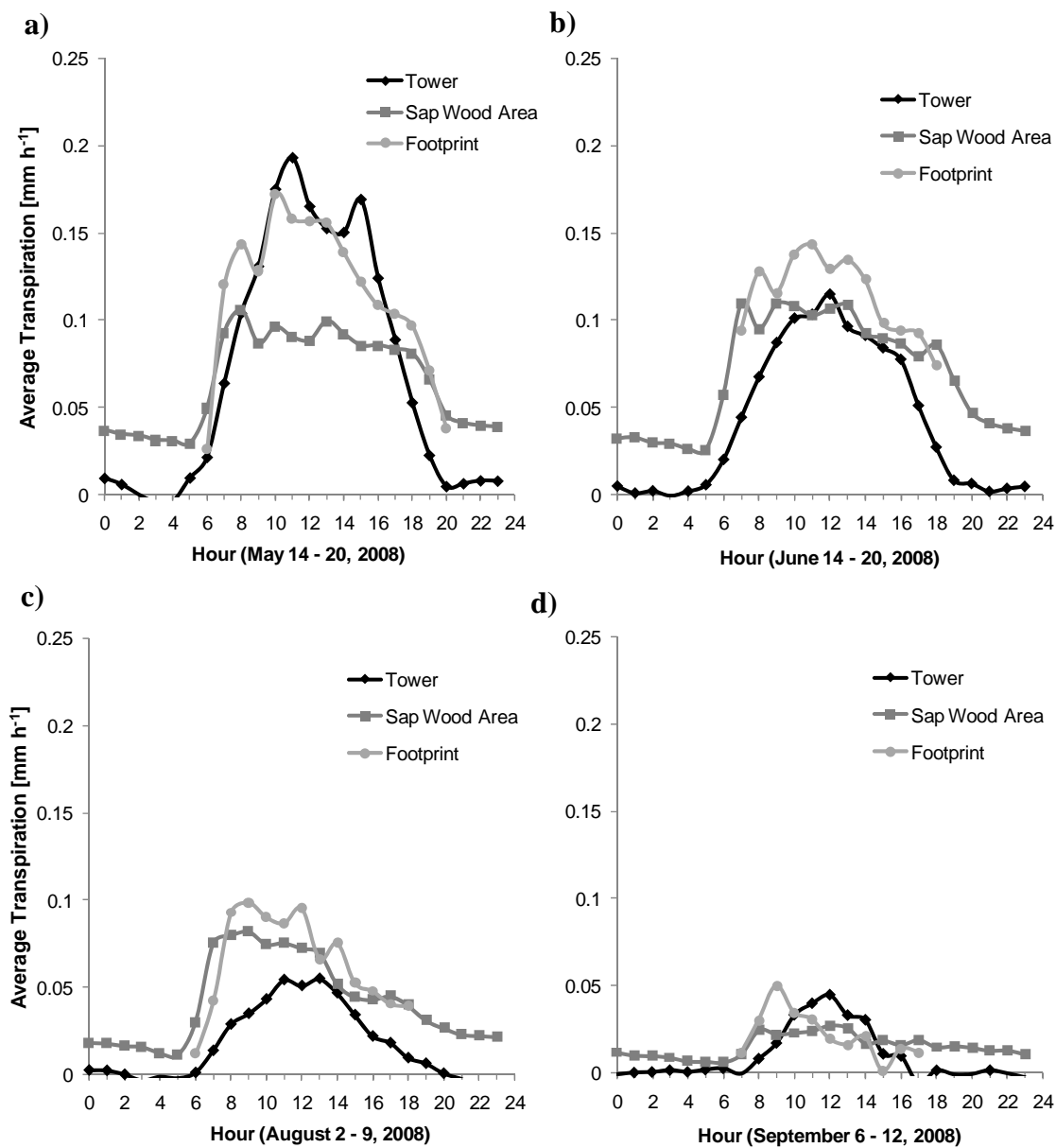


Figure 5.12: Hourly Stand Transpiration for Selected Periods
 A comparison of the stand transpiration flux measured by the eddy-covariance system (tower) and the two methods of upscaling the sap flow data (Linear and Footprint) for May (a), June (b), August (c), and September (d).

that instead of being caused by the factors previously hypothesized, the upscaling problems were due to the mismatch between the study area and the footprint area.

As with individual tree sap flow, transpiration decreases as the summer progresses. During June and August, both upscaling methods predict fluxes greater than those observed at the tower, with transpiration extending further into the mornings and evenings and peaking at rates around 0.04 mm h^{-1} higher. The shape of the diurnal pattern for the sapwood area method is much flatter than the others, with rates quickly reaching their maximum in the morning and continuing at that rate until midday.

Looking at transpiration on the daily scale (Figure 5.13), we find that the sap flow upscaling preserves the seasonal trends seen at the tower: low tree transpiration in the winter, increasing after leaf out (DOY 78) to a spring/wet season peak of approximately 1.5 to 2.0 mm d^{-1} , and rapidly decreasing to summer values between 0.2 and 0.5 mm d^{-1} as the dry season begins and the soil moisture is depleted. The sapwood upscaling methods continue to predict lower transpiration in spring and higher transpiration in the summer, as compared to the tower. The daily values are moderately well correlated, with $r^2 = 0.6$ between the tower and the sapwood area method, and $r^2 = 0.68$ between the tower and the footprint method.

While the eddy-covariance and sap flow transpiration values are in general agreement, three problems may be contributing to the discrepancies between them: (1) the tower may not be sampling a portion of the site that is representative of the overall study area; (2) the difference between the understory and overstory latent heat flux may

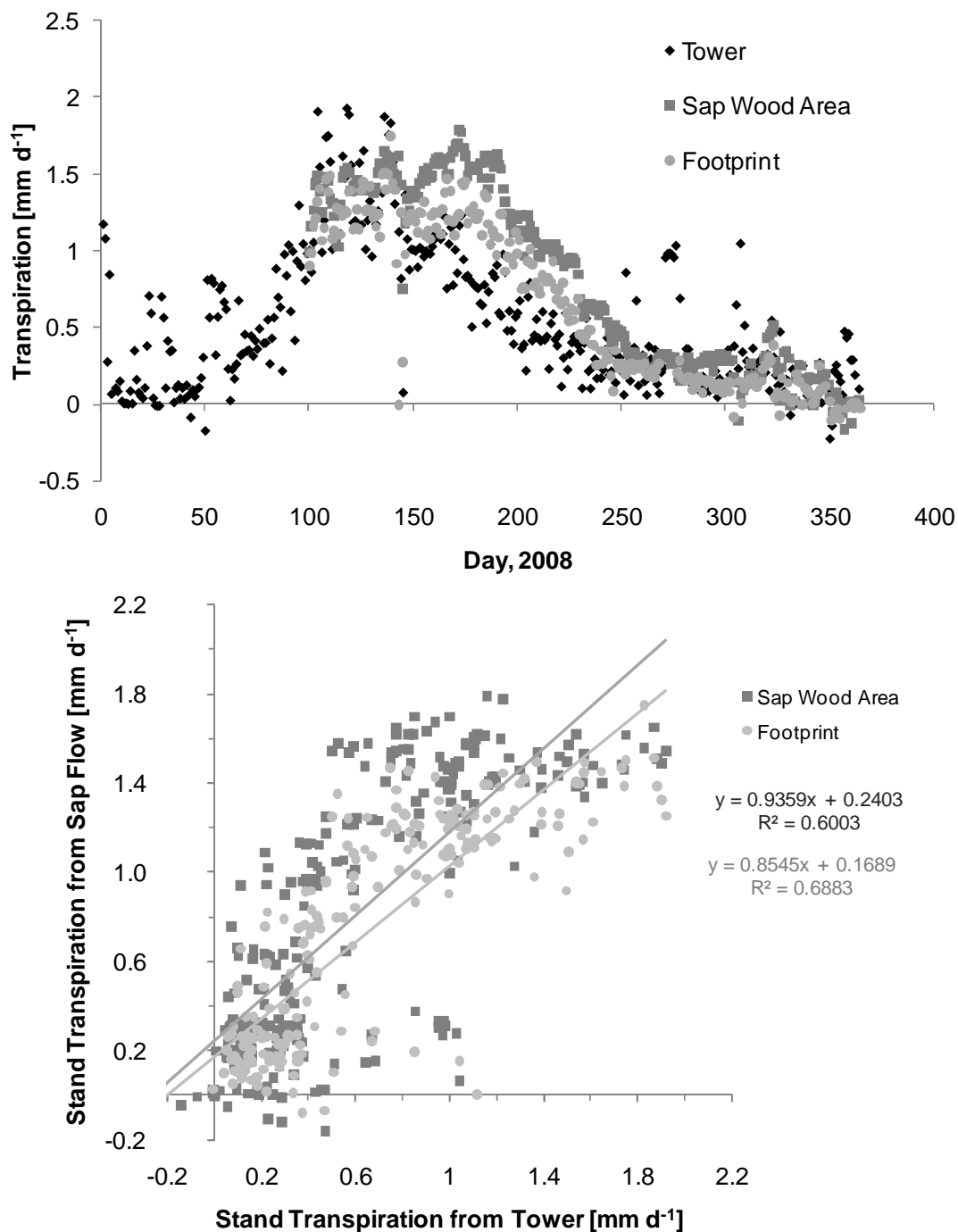


Figure 5.13: Daily Stand Transpiration

Top: The annual pattern of transpiration is captured by both upscaling methods, although it is slightly underestimated during April, May and June, and overestimated during July and August. **Bottom:** Daily transpiration values are moderately well correlated for both sap flow upscaling methods. The exclusion of nighttime fluxes from the footprint method improves its correlation, as does its ability to more accurately predict maximum flux in May and June.

not be an accurate representation of tree transpiration; and (3) pine trees are not included in the upscaling. Alternatively, issues with the velocity to tree upscaling step (Section 5.2.3) may exist, if the depths measured are insufficient to characterize the radial velocity profile or if the literature values for stem moisture content or wood density are inappropriate for the site.

The first complication is that the tower and the upscaled footprint fluxes are not representative of the entire stand (Table 5.2), particularly in that they tend to over-represent medium trees in wet areas (Clusters 1 and 7) at the expense of larger trees (Cluster 2). This observation runs contrary to Oishi et al.'s analysis [2008]; they speculate that in upscaling studies, mischaracterization of the footprint area is not the likely cause for difficulties, and that nocturnal water loss contributes much more to the underestimation of transpiration flux. However, they note that this is a particular problem when using Granier style sensors, which cannot resolve low, nighttime sap flow rates. Our use of Burgess style sensors prevents this, and in fact leads to a higher overnight flux than the tower data suggests.

The second possible source of error lies in the calculation of tree transpiration from eddy-covariance data. In order to find this value, we subtracted the latent heat flux measured by the understory (1 m) tower from the flux measured by the overstory (23 m) tower. Ideally, this should isolate the tree transpiration from the soil and grass evapotranspiration, but it is subject to considerable uncertainty.

The last problem relates to the presence of pine trees at the site. When the observation network was originally designed, they were not segregated from the oak

trees, as we assumed that they would not greatly affect the overall flux, since they were scarce and their sap flow was relatively low. In light of the upscaling challenges, we have decided to revisit this assumption. Previous studies have indicated that daily peak pine flow rates (v_s) at the site are around 3 cm h^{-1} for May and around 0.5 cm h^{-1} for August, and that the pines tend to be located in wet conditions [Kiang, 2002]. Given that the mean diameter for the grey pine trees on site is 0.25 m, the average pine tree will transpire at a rate of $0.22 \text{ cm}^3 \text{ s}^{-1}$ in May and $0.04 \text{ cm}^3 \text{ s}^{-1}$ in August. In comparison, Cluster 4, a similar size oak in wet conditions, would be producing $4 \text{ cm}^3 \text{ s}^{-1}$ in May and $2.8 \text{ cm}^3 \text{ s}^{-1}$ in August. As a result, the upscaled transpiration may be too high, depending on the exact number of pine trees present and their soil environment. This effect may be particularly strong if many of the large diameter trees noted in the upper right quadrant of the study area are in fact pine trees, and not oaks (Figure 5.3).

As discussed earlier, properly measuring sap velocities as a function of depth into the tree is important to upscaling. In this work, we observed some variation in v_s , with the deeper probes, located 2.8 cm into the tree, having slightly lower flow rates than the more shallow sensors, located at 0.8 cm. As an example, Figure 5.14 shows this trend for Cluster 7. Assuming that only the outside velocity had been used, the whole tree transpiration rate would have been 45% higher in May and 53% higher in August, roughly doubling both values. While this study was aimed at addressing an entirely different type of upscaling question, we speculate that these tree-scale issues may be as important. Some questions remain: Do we have a sufficient number of sampling points within and around the stem to characterize the flow? How do we quantitatively

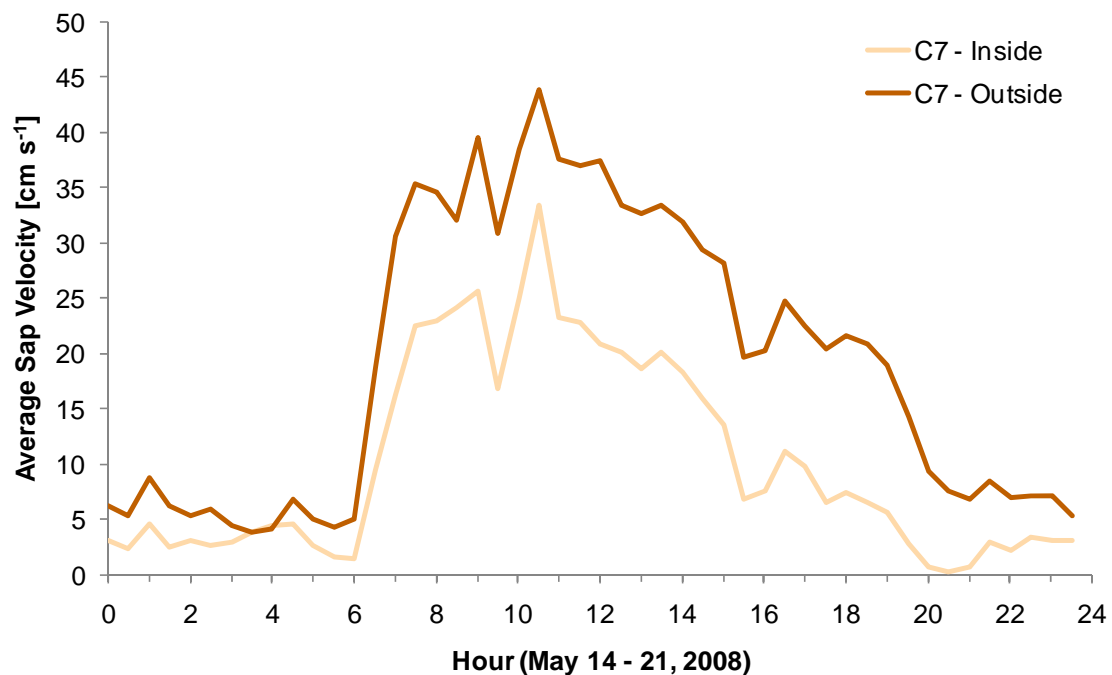


Figure 5.14: Comparison of Inner and Outer Sap Velocity Rates

The difference in inner and outer velocity is small, but has big implications for calculating the volumetric flow rate from an individual tree. In this case, if the inside probes had been neglected, the calculated flow rate would have been 45% higher.

determine “sufficient”? What impacts will mischaracterizing the radial profile have on the upscaled fluxes?

By examining the upscaling results, we can make further recommendations for cluster analysis in future implementations of this method. As noted earlier, the fluxes for the small trees (Clusters 5, 6, and 8) were, on average, an order of magnitude lower than the fluxes from the large trees. Was it necessary to measure these clusters? When their contributions to the total flux were removed completely from the upscaling calculations, the transpiration over the entire growing season was reduced by only 4%, from 192 mm to 184 mm. In contrast, when the flux from Cluster 2 was removed, the growing season transpiration was reduced by 230%, to 58 mm. This strongly suggests

that when resources are limited, they should be invested in better characterizing the transpiration from large, high-flow trees rather than including small diameter, low-flow ones.

Likewise, when considering the overall flux, it is slightly more important to characterize the variability associated with tree diameter than that associated with soil moisture. By combining clusters, we reduced the total number of groups to three, represented by only three of the sap velocity measurements. When the new groups were constructed such that they had similar soil moisture environments, we found that total transpiration only increased by 6 mm, or 3%. When combined by diameter instead, it increased by 12 mm, or 6%.

Finally, to refine the sap flow upscaling at this site, we have planned continued sap flow monitoring into the early summer of 2009. All probes have been moved to new locations on their trees to prevent a reoccurrence of the Cluster 1 wounding problem. A pine tree has been added to the measurement suite, and a census of pine trees will also be conducted. After monitoring is complete, tree cores will be collected for the purpose of measuring moisture content, dry density, and sapwood depth, and these values will be incorporated into future analyses. This additional data should help reduce the uncertainty associated with the conversion from heat pulse velocity to sap velocity.

5.4 Conclusions and Future Work

This chapter presents a framework for locating sap flow sensors to provide for a representative estimate for stand transpiration. Using geostatistical and artificial intelligence techniques, trees are separated into eight clusters with common properties.

One representative, or medoid, tree is measured within each cluster, and the water flow rate from this tree is used to represent the transpiration from all other trees in the cluster. The overall stand transpiration is calculated using the fluxes from each cluster and compared to the flux derived from eddy-covariance data.

The method for designing the sap flow network appears to be useful, covering the range of tree diameters and soil moisture conditions present on-site, in non-repetitive combinations. Soil moisture had a noticeable impact on sap flow; when comparing trees of similar diameters (e.g. Clusters 3 and 7), those in dry soil transpire at much lower flow than those in wet soil, particularly during the summer. However, based on the sap velocity data, more appropriate parameters could have been chosen for the original cluster analysis. A combination of tree diameter, height, elevation, leaf area, and canopy radius better explained the variability among the measured velocities. These potentially reflected the plant's energy environment and access to groundwater, rather than its local soil moisture availability.

Based on the upscaling results, sap flow shows promise as both a viable alternative and helpful supplement to eddy-covariance data. The ability to capture the nighttime fluxes of water vapor is perhaps the technique's strongest asset; without these measurements, the tower measurements are unlikely to capture up to 25% of the daily transpiration flux emitted during the growing season. Over the span of the 2008 season, this amounts to 53 mm of water lost from the subsurface that was not detected using eddy-covariance.

If this technique is used for future sap flow studies, we have several recommendations for its improvement. First, the system should be made more

redundant by measuring the two most representative trees per cluster, rather than one. This change would help prevent the whole system from functionally going “off-line” when the sensor on a single tree fails. Heater reliability should also be improved, as these fail more frequently than any of the other components. The sensors sets should be moved within the tree at regular, yearly intervals, to prevent wounding from causing signal loss. Additionally, before cluster analysis and network design, we strongly recommend conducting a pilot study aimed at identifying the tree and landscape features that most strongly control sap velocity. Once these parameters and their relative influence are established, cluster analysis can be performed to select the trees that are most representative of the controlling variables. Rather than focusing on characterizing all trees, special attention should be given to the large diameter trees which contribute disproportionately to the overall transpiration rate.

Finally, this research has raised two very important types of questions regarding the proper way to upscale sap velocities to stand transpiration rates:

- What is the most important step in the upscaling process? Is variation in the landscape merely a second-order effect? Can improper upscaling from sensor to tree scale overwhelm the gains made by improved landscape characterization?
- How can we test the validity of the upscaling method if the eddy-covariance flux is not “gold-standard” for comparison? When we have a discrepancy, how do we know if the tower or the sap flow system is wrong?

Future research will need to clarify these issues, before sap flow can be considered a sufficiently reliable method for measuring stand and landscape transpiration fluxes across a variety of terrains.

Chapter 6: Plant Water and Solute Uptake in Wastewater Recharge²

6.1 Introduction

California's Central Valley contains over 640 food-processing plants, which consume approximately 7.9×10^7 m³ of water per year [CLFP, 2007]. Nearly 80% of these processors discharge the resulting wastewater, which is typically high in organic carbon, nitrogen, and salts, to land [CVRWQCB, 2006], and many of these use land application as a treatment method. Ideally, the waste serves to both irrigate and fertilize crops grown in the disposal area, and the soil naturally attenuates the waste components before they reach the groundwater [Crites *et al.*, 1974]. Postulated mechanisms of attenuation include: microbial processes such as denitrification, cation exchange, crop nutrient uptake, and mineral precipitation [CLFP, 2007]. However, groundwater monitoring at some application sites has shown significant degradation of water quality [CVRWQCB, 2005], casting doubt on the efficacy of land disposal as a mechanism for attenuation.

California's regulations specify that groundwater quality may not be degraded by the discharge of waste, but do not currently specify limits to waste application rates or constituent concentrations [Cal. EPA, 2007]. Initial investigations revealed elevated salinity levels to be the most common form of groundwater degradation near land application sites, followed by concentrations of nitrogen compounds, namely ammonia and nitrate. Enforcement actions have been taken against multiple food processors

² This chapter is reprinted, with permission, from the original journal article: Miller, G. R., Y. Rubin, K. U. Mayer, and P. H. Benito, (2008), Modeling vadose zone processes during land application of food-processing waste water in California's Central Valley, *J. Environ. Qual.*, 37(5), S43-S57.

[*CVRWQCB*, 2005], and the regulatory boards have begun to re-examine the land disposal permitting process land [*CVRWQCB*, 2006]. California's Porter-Cologne Act [2006] requires that economic impacts be considered when stricter regulations on waste discharge are imposed [*Sunding and Zilberman*, 2005]. To support this end, an economic impact analysis is being performed and is based on a 30-year model of salinity in the region's groundwater as affected by the land application of food-processing wastes.

This portion of the study aims to develop and demonstrate a framework for modeling the transport and attenuation of these wastes in the vadose zone, in order to provide estimates of salinity loading suitable for use in the regional groundwater model of the Central Valley. These loading rates are a function of vadose zone attenuation processes, which are affected by site conditions, water table depth, waste application rate, and waste constituent concentrations.

The main challenge in modeling wastewater treatment through land application is the high level of variability present in both the waste stream and the disposal site characteristics over the Central Valley. Over five-hundred processors land discharge within the Central Valley, and each has its own characteristic waste stream and disposal practices. The soil and the geology vary highly in space, due to the presence of alluvial fans [*Burow et al.*, 2004]; for example, the vertical hydraulic conductivity varies by three orders of magnitude throughout the area [*Arkley*, 1964]. Additionally, few vadose zone measurements have been collected in discharge areas, and as a result, little data are available to constrain the model. This paper will discuss methods for simplifying the problem and addressing these issues by bracketing the range of possible outcomes,

focusing on the link between wastewater applied at the ground surface and the arrival of contaminants at the groundwater table. It will do this by introducing a conceptual model and then developing it into a 1-dimensional numerical model.

While this work is specific to food-processing waste streams, the modeling methods can be more broadly applied. Aquifer storage and recovery [Greskowiak *et al.*, 2005], bio-solids disposal [Brenton *et al.*, 2007], and septic systems [MacQuarrie *et al.*, 2001] all aim to treat or beneficially reuse waste through land application, and all contain similar contaminants of concern.

6.2 Methods

6.2.1 Conceptual Model

We developed a conceptual model that encompasses the fate and transport processes of the wastewater in surficial soils and underlying sediments. The conceptual model focuses on the vadose zone attenuation and transport of the main contaminants of concern (COCs) in the wastewater: labile organic carbon, nitrogen, and salts.

Concentrations of these COCs vary by both industry and processor. Waste streams representative of the four largest revenue industries in the Central Valley were analyzed in this study: tomato canning, meat packing and rendering, grape and wine production, and dairy processing (cheese and whey production). Table 6.1 shows the ranges of the average concentration of the primary COCs in the wastewater for these selected industries, taken from monitoring reports conducted by individual processors. Fixed dissolved solids (FDS) and labile organic carbon (OC) concentrations are high in most wastes ($>500 \text{ mg L}^{-1}$), and these concentrations generally vary more by processor than

Table 6.1: Concentration Ranges in Wastewater by Industry

Component	FDS[†] (mg L⁻¹)	Organic C, as BOD (mg O₂ L⁻¹)	Ammonium, as TKN (mg N L⁻¹)	Nitrate (mg N L⁻¹)
Wineries and grape processors	82–4300	42–6200	8.4–200	0.1–53
Tomato canner	430–4300	170–4400	3.1–520	nd–2.4
Cheese producers[‡]	nd–4800	570–5700	1.4–140	6.8–80
Meat packers	530–3300 [§]	18–1700	22–800	nd-2.3

[†]FDS, fixed dissolved solids; BOD, biochemical oxygen demand; TKN, total Kjehldahl nitrogen; nd, non-detect.
[‡]Cheese producer data from literature [Danalewich *et al.*, 1998]. All other data obtained from self-reporting by individual food processors.

industry. All industries discharge measurable amounts of nitrogen in their waste, although the tomato canning and meat packing industries typically release larger amounts of ammonia, while wastewaters from wineries and cheese producers contain larger amounts of nitrate.

Figure 6.1 summarizes the key processes constituting the conceptual model for the land application sites. Water flow through the system is dictated by the sources at the surface (precipitation, irrigation, and wastewater application), an evapotranspiration sink distributed equally through the 1 m root zone, and the flow reaching the bottom boundary condition at the groundwater table 15 m below the ground surface. A 1 m root zone depth was assumed to be representative of both corn, which has an average rooting depth of 0.84 m [Coelho and Or, 1998] and winter wheat, which has a maximum root depth between 0.5 to 1.0 m from December to March and 1.25 to 2.0 m during April and May [Gregory *et al.*, 1978]. For the Modesto area, Burow *et al.* [2004] report a range of

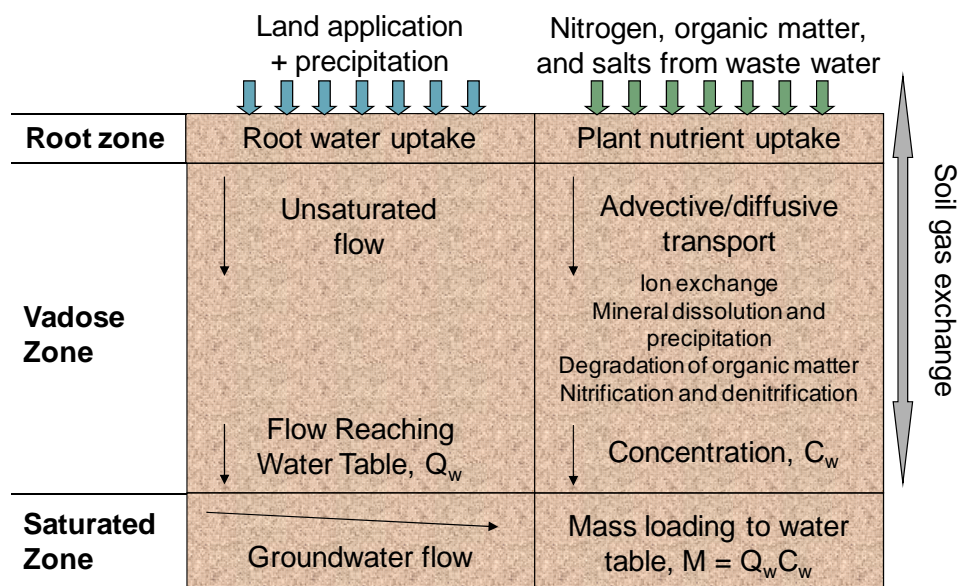


Figure 6.1: Conceptual Model of Land Application

Water flow-related processes are shown on the left, and chemical transport and attenuation processes are shown on the right. Soil gas exchange occurs by diffusion through the soil water and pore spaces. Although shown separately on the figure, these systems are coupled in the numerical model.

water table elevations from 10 to 35 m, which translates into a range in depth to groundwater of 1.5 to 38 m. Most food processing facilities are located in the center of this region (around the Highway 99 corridor), where the typical depth to groundwater is approximately 15 m.

Two biogeochemical systems are included: the nitrogen-carbon-oxygen (N-C-O) system and the major ions contributing to salinity. The N-C-O system, which describes the cycling of nitrogen and carbon compounds in the unsaturated zones, is influenced by the series of redox reactions shown in Table 6.2. The reactions are classified as aerobic (nitrification, respiration, and methane oxidation) or anaerobic (denitrification, manganese, iron and sulfate reduction, and fermentation) [Hunter et al., 1998; Langergraber and Simunek, 2005; MacQuarrie and Sudicky, 2001]. In natural systems,

Table 6.2: Biogeochemical Reactions and their Parameters

Reaction name and Equation	Rate coefficient	Half-saturation constants		Inhibition constants	
		K_{CH_2O} †	Other	$K_{inhibit,O_2}$	$K_{inhibit,NO_3}$
Aerobic Reactions	$\text{mol L}^{-1} \text{ s}^{-1}$	mol L^{-1}			
Nitrification $NH_4^+ + 2O_2 \rightarrow NO_3^- + H_2O + 2H^+$	2.0×10^{-9}	na	$K_{O_2} = 1.7 \times 10^{-5}$ $K_{NH_4} = 1.9 \times 10^{-4}$	na	na
Respiration $CH_2O + O_2 \rightarrow CO_3^{2-} + 2H^+$	2.0×10^{-10}	1.9×10^{-4}	$K_{O_2} = 4.7 \times 10^{-6}$	na	na
Methane oxidation $CH_4 + 2O_2 \rightarrow CO_3^{2-} + 2H^+ + H_2O$	1.0×10^{-9}	na	$K_{CH_4} = 1.0 \times 10^{-5}$ $K_{O_2} = 3.1 \times 10^{-6}$	na	na
Anaerobic reactions	$\text{mol L}^{-1} \text{ s}^{-1}$	mol L^{-1}			
Denitrification $CH_2O + \frac{4}{5}NO_3^- \rightarrow \frac{2}{5}N_2 + CO_3^{2-} + \frac{6}{5}H^+ + \frac{2}{5}H_2O$	5.0×10^{-10}	1.6×10^{-4}	$K_{NO_3} = 2.3 \times 10^{-5}$	1.6×10^{-5}	
Manganese reduction $CH_2O + 2MnO_2 + 2H^+ \rightarrow CO_3^{2-} + 2Mn^{2+} + 2H_2O$	5.0×10^{-12}	1.0×10^{-5}	na	5.0×10^{-8}	5.0×10^{-8}
Iron reduction $CH_2O + 4FeOOH + 6H^+ \rightarrow CO_3^{2-} + 4Fe^{2+} + 6H_2O$	2.0×10^{-12}	5.0×10^{-3}	na	3.1×10^{-6}	3.1×10^{-6}
Sulfate reduction $CH_2O + \frac{1}{2}SO_4^{2-} \rightarrow CO_3^{2-} + \frac{1}{2}HS^- + \frac{3}{2}H^+$	5.0×10^{-10}	1.1×10^{-4}	$K_{SO_4} = 1.6 \times 10^{-3}$	3.1×10^{-5}	1.6×10^{-5}
Fermentation $CH_2O + \frac{1}{2}H_2O \rightarrow \frac{1}{2}CO_3^{2-} + \frac{1}{2}CH_4 + H^+$	1.0×10^{-11}	1.0×10^{-3}	na	3.1×10^{-5}	1.6×10^{-5}

at a neutral pH, these reactions occur sequentially, in the order they are listed in Table 6.2 [Appelo and Postma, 2005]. We assume that the microbial communities necessary for mitigating these redox reactions are naturally present in the vadose zone before, or develop rapidly after, land application begins.

Organic material present in the waste provides the biodegradable, or labile, organic carbon (CH_2O) necessary for the progress of these reactions. The ratio of labile to recalcitrant organic carbon in wastewater varies by processor and industry. The literature reports ratios of 0.44 to 0.67 for fruit canning [Johns and Bauder, 2007], 0.25 to 0.78 for cheese making [Danalewich *et al.*, 1998], and 0.33 to 0.49 for tomato processing waste [Xu and Nakhla, 2006]. Data on organic carbon content in the wastewater is largely limited to the five-day biochemical oxygen demand (BOD_5). In the absence of more detailed total organic carbon data from the processing facilities, we limit our study to the modeling of readily biodegradable organic carbon, and assume that this organic carbon fraction can be represented by the BOD_5 . In this case, it is assumed that the consumption of one mole of BOD corresponds directly to the degradation of labile organic carbon (CH_2O), because the reaction taking place during BOD measurement is aerobic degradation, represented by the equation: $\text{CH}_2\text{O} + \text{O}_2 \rightarrow \text{H}_2\text{O} + \text{CO}_2$ [Nazaroff and Alvarez-Cohen, 2001].

Nitrogen is found in four primary forms in food waste: organically bound nitrogen, ammonia ($\text{NH}_{3(\text{aq})}$), ammonium (NH_4^+), and nitrate (NO_3^-). The sum of organic nitrogen, ammonia, and ammonium is measured as total Kjeldahl nitrogen (TKN), while nitrate is measured separately. We assume that all organic nitrogen is rapidly converted to ammonium [Savant *et al.*, 1987], and in the conceptual model, all TKN is represented as ammonium. This approach should create a worst case scenario for the simulated amount of ammonium or nitrate reaching the groundwater table because a) nitrogen is not allowed to escape to the atmosphere as ammonia during application and b) all nitrogen is initially present in the forms NH_4^+ or NO_3^- .

The term “salinity” encompasses multiple individual ion species and is commonly represented as either electrical conductivity (EC) or fixed dissolved solids (FDS). The direct measurement of the concentrations of ionic species in the waste is referred to as FDS, while the indirect measure of their charge is represented by EC. The major ions compromising salinity are: chloride (Cl^-), calcium (Ca^{2+}), magnesium (Mg^{2+}), potassium (K^+), sodium (Na^+), ammonium (NH_4^+), nitrate (NO_3^-), sulfate (SO_4^{2-}), and phosphate (PO_4^{3-}). Two carbonate species (CO_3^{2-} and HCO_3^-) are also significant contributors. The trace elements aluminum (Al^{3+}), manganese (Mn^{2+}), zinc (Zn^{2+}), copper (Cu^{2+}), and iron (Fe^{2+}) can also contribute to FDS [Appelo and Postma, 2005; Hillel, 2000]. As wastewater moves through the subsurface, cations in the soil solution are exchanged with those in clay minerals, altering the composition and concentration of the fixed dissolved solids present. For instance, if Mg^{2+} replaces Ca^{2+} on the cation exchange site, the concentration of Ca^{2+} in the pore water will increase, the concentration of Mg^{2+} will decrease, and the total FDS concentration (in mg L^{-1}) will increase, since the atomic weight of Ca^{2+} is greater than that of Mg^{2+} . Of the salinity components, the cations participating in these exchange reactions, in order of strength of attraction at a neutral pH, are Ca^{2+} , Mg^{2+} , Mn^{2+} , Fe^{2+} , K^+ , NH_4^+ , and Na^+ [Brady and Weil, 1999].

Additionally, six soil minerals are included: calcite (CaCO_3) because of its influence on carbonate equilibrium as well as manganese dioxide (MnO_2) and goethite (FeOOH) on account of their participation in organic carbon degradation in natural systems [Appelo and Postma, 2005]. The concentrations of calcite, iron and Mn-oxides were constrained by field data [Goldberg et al., 2005; USDA, 2006]. Siderite (FeCO_3),

rhodochrosite (MnCO_3), and amorphous iron sulfide (FeS) were included as solubility controls for the reaction products Fe(II) , Mn(II) , and S(-II) . Gypsum ($\text{CaSO}_4 \cdot 2\text{H}_2\text{O}$) dissolution is suspected to contribute to salinity problems in the Central Valley [*Schoups et al.*, 2005]. Precipitation and dissolution of this mineral phase was included, but its initial soil content was set to 0%, in order to reflect the most common conditions found in the present study area.

It should be noted that the relative predominance of a particular chemical species is pH-dependent. In the case of ammonia, it can either be found in the system as ammonia ($\text{NH}_{3(\text{aq})}$) or ammonium (NH_4^+). When in an aqueous solution, the relative concentrations of ammonia and ammonium are governed by the following equilibrium equation: $\text{NH}_3 + \text{H}^+ \leftrightarrow \text{NH}_4^+$. Given a pKa of 9.25 [*Lide*, 2007], the ammonium ion predominates in most wastewaters. For simplicity, the sum of these will be referred to as total ammonia, although they are distinguished in the numerical model. In the case of carbonate, it can be present as aqueous carbon dioxide ($\text{CO}_{2(\text{aq})}$) and carbonic acid (H_2CO_3), bicarbonate (HCO_3^-), or carbonate (CO_3^{2-}). Carbonic acid and aqueous carbon dioxide are predominant at $\text{pH} < 6.3$, bicarbonate at $6.3 \leq \text{pH} < 10.3$, and carbonate at $\text{pH} \geq 10.3$ [*Appelo and Postma*, 2005]. The sum of these species will be reported as total inorganic carbon (TIC), and carbon dioxide gas pressure will be reported separately.

The two systems (salinity and NCO) are loosely coupled though the ammonium, iron, and manganese ions, which sorb to soil and participate in the redox reactions. Root solute uptake within the top 1 m of soil also affects both systems, by removing essential plant nutrients (K^+ , NH_4^+ , NO_3^- , PO_4^{3-} , SO_4^{2-} , Ca^{2+} , Mg^{2+} , Zn^{2+}) and releasing carbonate (CO_3^{2-}) as a byproduct of respiration and nutrient uptake [*Tinker and Nye*, 2000].

Gas exchange and soil saturation also couple the systems. The gases carbon dioxide (CO_2), oxygen (O_2), nitrogen (N_2), methane (CH_4), and hydrogen sulfide (H_2S) are included in the model, are subject to transport through gas phase diffusion, and can participate in aqueous-gas equilibrium reactions. Ammonia (NH_3) gas transport was excluded due to its high solubility and predominant presence in the aqueous phase in hydrolyzed form as NH_4^+ . The presence of O_2 promotes the transformation of NH_4^+ to NO_3^- (nitrification) and inhibits the transformation of NO_3^- to N_2 (denitrification). Anoxic conditions can develop if microbial reactions consume the available oxygen more quickly than it can be replaced through diffusion. Additionally, the carbonate created as a byproduct of microbe mitigated redox reactions (Table 6.1) and plant nutrient uptake will, through equilibrium reactions, produce CO_2 gas. If this gas can readily escape the system, total inorganic carbon levels will decrease, also decreasing the total FDS concentration. The water content of the soil determines the ease at which these gases can diffuse to and from the atmosphere, necessitating vadose zone modeling.

6.2.2 Scenario Development

The conceptual model encompasses a wide range of simultaneously-occurring processes. Variations in the chemical composition of the wastewater in combinations with the hydrological conditions at the discharge site will affect the relative significance of the various processes in terms of dependent variables such as salinity and N fluxes to the water table. This wide range of combinations could be addressed by modeling each of the hundreds of discharge sites. An alternative is to identify several combinations of COCs and hydrologic conditions that can potentially bracket the dependent variables.

Table 6.3: Overview of Scenarios

Characteristic	Case 1	Case 2	Case 3
Saturation conditions	High	Low	Moderate
Saturation range, %	90 to 99	40 to 50	80 to 90
Ratio of K_{sat} to q_{waste}	~1	~10,000	~10
Fixed dissolved solids	High	High	Moderate to high
Labile organic carbon	High	Low	Low
Total ammonia	Low	Low	Low
Nitrate	Low	High	Low

K_{sat} , saturated hydraulic conductivity; q_{waste} , rate of wastewater application.

Such brackets are meaningful because they can provide best and worst case scenarios, which in turn are useful for management.

To limit the number of scenarios for analysis, we focused on salinity and N compounds. The difference between these two sets of compounds, for the purpose of process classification, is that salinity is affected by the same processes but with different levels of intensity, while N compounds may experience different process categories, depending primarily on the presence or absence of oxygen in the vadose zone. Thus, we identified 3 scenarios, defined by conditions that are most favorable or detrimental in terms of impact on N fluxes. These three scenarios can be augmented by different salinity profiles. The three scenarios selected are summarized in Table 6.3 and are described below. The “high” and “low” descriptors in Table 6.3 and in the following discussion indicate the concentrations of the chemicals of interest relative to the other dischargers in the industry.

Scenario 1 was designed to demonstrate the effects of the development of anoxic conditions at shallow depth and provides a worst case scenario for total ammonia loading to the aquifer. In this scenario, high levels of TKN, BOD, and FDS loading coupled with high water saturation maximize the total ammonia and salinity loading to the water table. Oxygen ingress is limited, inhibiting nitrification, the primary mechanism of ammonium removal.

Scenario 2 was constructed to show the effect of aerobic conditions throughout the unsaturated zone and provides a worst case for nitrate loading to the aquifer. When waste high in nitrogen (TKN + NO₃) and FDS levels and low BOD levels is coupled with low saturation conditions, the nitrate loading to the water table is maximized. Denitrification, which would otherwise convert nitrate to nitrogen gas, is inhibited by the presence of oxygen, which is a preferred electron donor, and is limited by available organic carbon, necessary for the microbe mitigated reaction. Nitrification, which is an aerobic processes and not dependent on organic carbon, continues to convert ammonium to nitrate.

Finally, Scenario 3 was created to demonstrate the conditions under which optimum nitrogen removal could be achieved. Here, the soil remains at approximately 80 – 90% saturation, and nitrification occurs in the upper portion, before all oxygen is consumed. Anaerobic conditions develop deeper within the soil profile, and denitrification can then occur. In this scenario, salinity remains moderate to high, as it is affected little by these processes.

Groundwater data collected in wells down-gradient of discharge sites provides support for the selection of these cases. Individual wells were loosely classified into

“scenarios”, based on the state’s water quality objectives for groundwater, 10 mg-N L⁻¹ for nitrate, 30 mg-N L⁻¹ for ammonia, and 500 mg L⁻¹ for TDS [Marshack, 2003]. Wells with low nitrate (<10 mg-N L⁻¹), high TKN (≥30 mg-N L⁻¹), and high FDS (≥500 mg L⁻¹) were classified as Scenario 1; those with low TKN (<30 mg-N L⁻¹), high nitrate (≥10 mg-N L⁻¹), and high FDS were classified as Scenario 2; and those with low nitrate and TKN but high FDS were classified as Scenario 3. For example, of the 19 wine and grape processors in the region with groundwater data, 5% were classified as Scenario 1, 58% as Scenario 2, and 26% as Scenario 3. Only 11% did not fall into one of these categories, typically due to low FDS levels. One caveat should be added; no consideration was given to background groundwater quality, which may or may not artificially elevate salinity and nitrate levels, depending on the location of the discharger.

6.2.3 Numerical Modeling

To estimate the water table loading of the COCs under these scenarios, a series of numerical simulations were performed using the multi-component reactive flow and transport code MIN3P [Mayer *et al.*, 2002]. Each simulation calculated the flow rate and concentration at the water table (15 m deep) over time using a 1-D, vadose zone column model with detailed biogeochemical interactions. From each of the industries included (tomato canners, dairy processors, wineries, and meat packers), representative waste streams were selected for modeling based on the requirements of each scenario, creating a total of twelve simulations. To select which waste stream best conformed to the scenario criterion, waste “footprint” diagrams were created for each industry. These diagrams graph the normalized average concentration for BOD, NO₃, TKN, and FDS for each discharger.

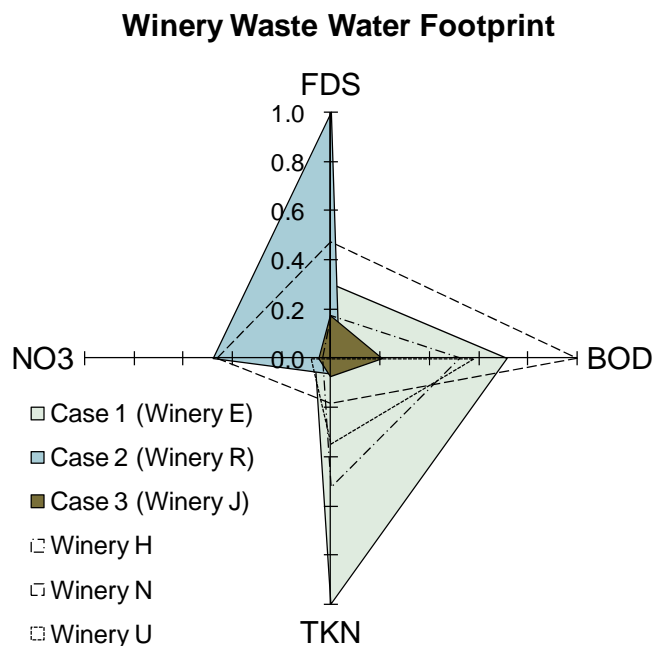


Figure 6.2: Footprint Analysis of Selected Wine and Grape Processors

The 2003 to 2005 average concentrations for each processor are normalized by the highest average concentration among all processors. Winery E wastewater was relatively high in biochemical oxygen demand (BOD) and total Kjeldahl nitrogen (TKN), while Winery R had higher fixed dissolved solids (FDS) and nitrate levels.

Figure 6.2 shows the footprint for the wine industry and the profiles matching each scenario. In the diagram, the 2003–2005 average concentrations for each processor are normalized by the highest average concentration among all processors. Of the 33 wine and grape processors that land apply wastewater, 26 had sufficient data available to be included in the footprint analysis, although only 6 of these are shown on the figure, for clarity.

While all four industries were included in the simulations, in this discussion, we will consistently return to the wine and grape industry as an example of the analysis. Similarities and differences in the modeling and results will be noted where appropriate.

6.2.3.1 Flow Inputs and Parameters

For the selected waste streams, discharger specific waste application rates (q_{waste}) were determined from permits issued [*Cal. EPA, 2007*], known as Waste Discharge Requirements (WDRs). To calculate the permitted wastewater application rate, q_{waste} (m s^{-1}), for each discharger, the maximum volumetric flow rate ($Q_{\text{permitted}}$) was divided by the minimum permitted application area ($A_{\text{permitted}}$). For most dischargers, the permissible long-term application rates ranged from 1×10^{-8} to $9 \times 10^{-8} \text{ m s}^{-1}$. The WDRs typically impose additional restrictions on the BOD loading rate, in order to prevent nuisance odors, citing the $112 \text{ kg ha}^{-1} \text{ d}^{-1}$ ($100 \text{ lb acre}^{-1} \text{ d}^{-1}$) rate recommended by the United States Environmental Protection Agency [*USEPA, 1977*]. In cases where the flow rate and the measured BOD concentration resulted in loadings above this limit, the flow rate was reduced as necessary, so that the simulations were indicative of processors compliant with the regulations.

Two soils were selected as representative of the range of saturated hydraulic conductivity (K_{sat}) in the study area: Delhi Sand ($1.4 \times 10^{-4} \text{ m s}^{-1}$) and Modesto Loam ($4.2 \times 10^{-7} \text{ m s}^{-1}$) [*Arkley, 1964; USDA, 2006*]. In the absence of more detailed data, ROSETTA [*Schaap et al., 2001*] was used to estimate the van Genuchten-Mualem parameters (S_r , n , α , l) of these soils, which are included in the equation for relative permeability k_r at a given saturation S [*Wosten and Van Genuchten, 1988*]:

$$k_r = S_e^{0.5} \left[1 - \left(1 - S_e^{\frac{1}{1-1/n}} \right)^{1-1/n} \right]^2 \quad (6.1)$$

where the effective saturation $S_e = (S - S_r)/(1 - S_r)$, S_r is the residual saturation, and n is a fitting parameter. The saturation, S , is calculated from the water retention curve, defined as a function of S_r , n , the fitting parameter α , and the pressure head, ψ :

$$S = S_r + \frac{1 - S_r}{(1 + \alpha\psi^n)^{1-1/n}} \quad (6.2)$$

To reach the desired saturation ranges (Table 6.3), the waste application rates were coupled with the properties for the appropriate soils (loam for Scenarios 1 and 3 and sand for Scenario 2), and K_{sat} for Scenarios 1 and 3 was reduced slightly, to $9 \times 10^{-8} \text{ m s}^{-1}$ and $2 \times 10^{-7} \text{ m s}^{-1}$, respectively. While these K_{sat} values do not represent the mean values for the soil, they are within the observed range for the study area [Burow *et al.*, 2004]. An effective porosity of 0.35 was used for both soil types.

Average monthly precipitation rates (q_{precip}) were calculated using the 1986-2006 data from the National Oceanic and Atmospheric Administration's (NOAA) Western Regional Climate Center data [2006]. All precipitation was assumed to infiltrate the top layer of soil; no corrections for run-off were performed. The monthly averages of reference evapotranspiration (ET_0) for Modesto, CA for 1987–2006 were obtained from the California Irrigation Management system data [Cal. Dep. Water Resour., 2006]. The evapotranspiration rates (q_{et}) were determined by multiplying monthly ET_0 with crop specific coefficients [Kang *et al.*, 2003], assuming an annual rotation of corn and winter wheat. When monthly evapotranspiration exceeded the combined waste application and precipitation rates, supplemental irrigation water was added at an appropriate rate ($q_{irr} = q_{et} - q_{precip} - q_{waste}$). These rates are shown in Table 6.4 for each scenario.

Table 6.4: Water Balance at Hypothetical Discharge Site

			Case 1		Case 2		Case 3	
Month	q_{precip}	q_{et}	q_{waste}	q_{irr}	q_{waste}	q_{irr}	q_{waste}	q_{irr}
	$\text{m s}^{-1} (\times 10^{-9})$							
Jan.	25	4.7	8.7	0	7.0	0	5.0	0
Feb.	25	12	8.7	0	7.0	0	0.39	0
Mar.	18	30	8.7	2.9	7.0	6.0	0.39	11
Apr.	8.4	66	8.7	50	7.0	56	0.39	59
May	7.2	73	26	41	11	56	0.39	67
Early June	1.5	40	26	14	11	29	0.39	40
Late June	1.5	32	26	4.5	11	20	0.39	31
July	0.018	76	26	51	11	66	0.39	77
Aug.	0.15	91	26	67	11	82	12	81
Sept.	1.5	54	26	27	11	42	12	41
Early Oct.	4.5	30	15	11	11	14	12	13
Late Oct.	4.5	14	15	0	11	0	12	0
Nov.	8.3	10	15	0	7.0	0	5.0	0
Dec.	19	4.6	8.7	0	7.0	0	5.0	0

q_{precip} , precipitation rate; q_{et} , evapotranspiration; q_{waste} , wastewater application rate; q_{irr} , irrigation rate

In order to keep the model tenable, reduce the complexity of the model inputs, and in light of very limited field data, several simplifying assumptions were made in regards to the water balance. First, monthly, rather than daily, precipitation and irrigation rates were used, drastically reducing the number of time-steps necessary. While the

effect of this temporal averaging on nitrogen dynamics is not well investigated, it has been shown not to cause significant errors in long-term studies of salinity [Schoups *et al.*, 2006]. Second, ET was not partitioned into soil evaporation (E) and plant transpiration (T), due to the inherent uncertainty associated with the E/T ratio. Measurements indicate that between 5 to 30% of ET is due to soil evaporation [Jara *et al.*, 1998; Kang *et al.*, 2003], and this proportion varies depending on site specific soil conditions and agricultural practices [Eastham *et al.*, 1999; Wang *et al.*, 2001]. Finally, we represented root uptake due to ET as a uniform sink throughout the rooting zone, avoiding detailed models of plant growth dynamics and root density distribution, which would have added additional parameters dependent on specific soil and climate conditions.

6.2.3.2 Chemical Inputs and Parameters

Model input concentrations were determined for each scenario based on discharger reported data. The BOD, FDS, TKN, and NO_3^- concentrations were averaged over a three-year period (2003–2005). When FDS was not available, it was estimated using the equation $\text{FDS (mg L}^{-1}\text{)} = 600 \times \text{EC (dS m}^{-1}\text{)}$ [Metcalf & Eddy *et al.*, 1991]. Using data from available records, the average fraction of FDS contributed by each salinity component was determined on an industry-specific basis. To obtain approximate component concentrations, the average FDS concentration was multiplied by the average fraction for each component. The input concentrations for wineries are shown in Table 6.5. This procedure was followed for all industries, except dairy and milk processing (i.e., cheese making), which has few, albeit high revenue, processing

Table 6.5: Model Input Concentrations for Wine and Grape Processors

Component (mg L ⁻¹)	Case 1	Case 2	Case 3
Calcium	80 [†]	250	46
Magnesium	30 [†]	95	17
Potassium	190 [†]	610	110
Sodium	220 [†]	690	130
Ammonium from TKN	260	15	17
Aluminum	nd‡	nd	nd
Manganese	0.50 [†]	1.6 [†]	0.29
Zinc	0.77 [†]	2.4 [†]	0.44
Copper	0.15 [†]	0.48 [†]	0.090
Iron	2.5 [†]	8.0 [†]	1.45
Carbonate	560	1800	320 [†]
Phosphate	16	50	9.0
Sulfate	120 [†]	370	67
Chloride	20	65 [†]	12
Nitrate	16	130	12
CH ₂ O from BOD	4400	230	1300
FDS	1360	4300	780
pH (unitless)	5.8§	8.7	6.4§
Oxygen (atm)	0.21	0.21	0.21

TKN, total Kjeldahl nitrogen; BOD, biochemical oxygen demand, [†] Ratio from fixed dissolved solids (FDS), [‡] nd, non-detect, [§] pH assumed to equal 6.4 after buffering, as required by permits.

plants in the Central Valley. The data used to analyze that industry was taken from literature [Britz *et al.*, 2005; Danalewich *et al.*, 1998].

High precipitation in the winter (48 to 66 mm month⁻¹) and high irrigation in late summer (36 to 210 mm month⁻¹) cause considerable dilution of the waste concentrations. For wineries, wastewater typically constitutes approximately half of all water entering the soil. Background chemical concentrations in rain and irrigation well water were obtained from the literature [*Appelo and Postma, 2005; Collett et al., 1999; Shelton and Miller, 1991*] and used as inputs to the model.

Within the Modesto area, the soil's cation exchange capacity (CEC) ranges from 0.1 cmol_c kg⁻¹ for the Delhi soil series to 4.0 cmol_c kg⁻¹ for the Meikle soil series [*USDA, 2006*]. For the simulations, a cation exchange capacity of 0.3 cmol_c kg⁻¹, and a dry bulk density of 1.5 g cm⁻³ was selected. Goldberg et al. [2005] measured manganese and iron oxide contents of 0.5 g kg⁻¹ and 6.6 g kg⁻¹, respectively, for a selection of Central Valley soils. It was assumed that approximately 10% of these oxides are bioavailable and that these mineral phases are reductively dissolved (Table 6.2). The soils also have a low to moderate calcite content (0 to 50 g kg⁻¹); a low value of 10 g kg⁻¹ was selected for the simulations.

Root solute uptake was modeled using a Michaelis-Menten formulation [*Barber, 1995*]:

$$I_x(t, z) = I_{x,max} \frac{C_x(t, z)}{K_x + C_x(t, z)} \quad (6.3)$$

where $I_x(t, z)$ ($\mu\text{mol cm}^{-2} \text{s}^{-1}$) is the total uptake rate of species x at simulation time t and depth z , $I_{x,max}$ ($\mu\text{mol cm}^{-2} \text{s}^{-1}$) is the maximum ion uptake rate, C_x is the species concentration, and K_x is the concentration for which the reaction rate is $0.5 \cdot I_{x,max}$ (mol cm^{-3}). The crop and species specific parameters were taken from literature

Table 6.6: Active Root Uptake Parameters

Nutrient	Corn parameters		Wheat parameters	
	$I_{x,\max}$ (mol cm ⁻² s ⁻¹)	K_x (mol L ⁻¹)	$I_{x,\max}$ (mol cm ⁻² s ⁻¹)	K_x (mol L ⁻¹)
Nitrate	1.0×10^{-12} †	1.0×10^{-5} †	4.8×10^{-13} §	2.7×10^{-5} §
Ammonium	1.0×10^{-12} †	1.0×10^{-5} †	6.5×10^{-13} §	5.0×10^{-5} §
Potassium	1.1×10^{-12} †	1.4×10^{-5} ‡	1.9×10^{-13}	7.0×10^{-6} †
Sulfur	3.0×10^{-13} ‡	1.0×10^{-5} ‡	NA [¶]	NA
Phosphorus	3.3×10^{-12} ‡	5.8×10^{-6} ‡	1.4×10^{-13} †	6.0×10^{-6} †
Magnesium	4.0×10^{-12} ‡	1.5×10^{-4} ‡	4.0×10^{-14} †	1.0×10^{-6} †
Calcium	1.0×10^{-12} ‡	4.0×10^{-3} ‡	1.6×10^{-13} †	5.0×10^{-6} †
Zinc	NA	NA	5.5×10^{-14} #	8.9×10^{-7} #

† Barber [1995]; ‡ Roose et al. [2001]; § Goyal and Huffaker [1986]; # Rengel and Wheal [1997]; ¶ NA, not available

[Barber, 1995; Goyal and Huffaker, 1986; Rengel and Wheal, 1997; Roose et al., 2001]

and are shown in Table 6.6. For the simulations, we assumed that these rates represented the maximum rates observed throughout the growing season, since most were collected during the first 10 to 20 days of plant growth. These baseline values of I_{\max} were then modified to vary with time, scaling them based on the measured nutrient accumulation rates reported in the literature [Barraclough, 1986; Seward et al., 1990]. Charge balance was maintained by introducing appropriate quantities of H⁺ and CO₃²⁻ into the soil solution when nutrients were removed; carbonate for anions and hydrogen for cations. Plants naturally exude these ions when taking up nutrients, in order to maintain electrical neutrality [Barber, 1995; Tinker and Nye, 2000].

The rates of the redox reactions shown in Table 6.2 were simulated using Monod-type rate expressions. For example, the equation to determine the rate of denitrification is:

$$R = k \left(\frac{[NO_3^-]}{[NO_3^-] + K_{NO_3^-}} \right) \left(\frac{[CH_2O]}{[CH_2O] + K_{CH_2O}} \right) \left(\frac{K_i}{[H^+] + K_i} \right) \quad (6.4)$$

where k is the effective rate coefficient, K_i 's are inhibition constants, and K_x 's are the half-saturation constants, and the concentrations are denoted by square brackets. The parameter values for the redox reactions were taken from ranges reported in the literature [Dincer and Kargi, 2000; Langergraber and Simunek, 2005; MacQuarrie and Sudicky, 2001; Mailloux *et al.*, 2002; Mayer *et al.*, 2001] and are shown in Table 6.2.

6.3 Results and Discussion

The simulations demonstrated 30 years of wastewater application, for compatibility with the aforementioned economic impact analysis. Breakthrough curves for the four primary contaminants of interest are shown in Figure 6.3 for the wine and grape industry. The time of first arrival of the tracer species chloride, was approximately 11.3 years for Scenario 1, 5.0 years for Scenario 2, and 13 years for Scenario 3. In Scenarios 1 and 3, not all labile organic carbon was consumed before the waste reached the groundwater, with 7430 and 470 mg L⁻¹ remaining. For all three scenarios, the pH at the groundwater table at year 30 was near neutral: 6.17 for Scenario 1, 7.02 for Scenario 2, and 6.53 for Scenario 3.

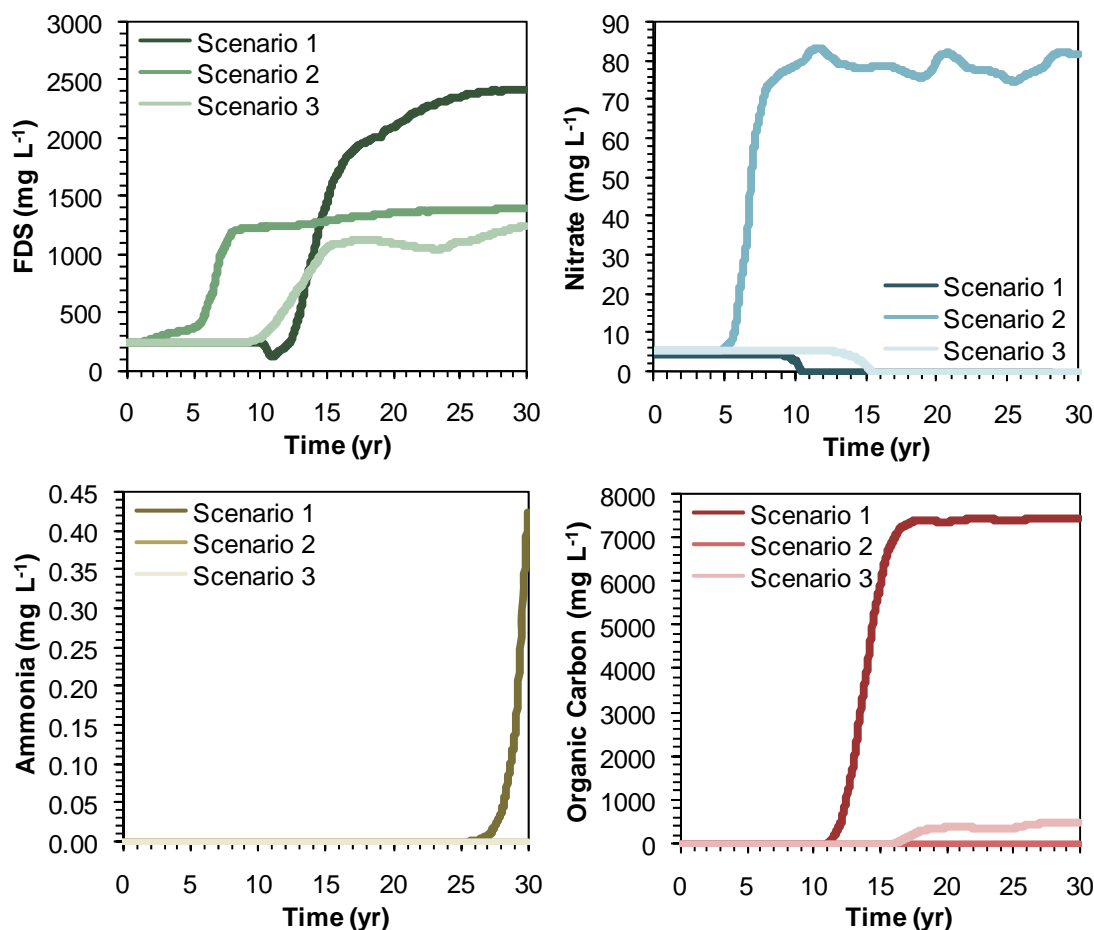


Figure 6.3: Breakthrough Curves of Contaminants Reaching the Water Table While nitrate, total ammonia, and organic carbon concentrations were dependent on the scenario, fixed dissolved solids (FDS) levels were consistently high.

6.3.1 Nitrogen Compounds

In Scenario 2 simulations, nitrate concentrations reached 82 mg L⁻¹, exceeding the 44 mg L⁻¹ (10 mg-N L⁻¹) water quality objective. The concentration of nitrate reaching the water table is 50 mg L⁻¹ lower than that in the wastewater, due to significant root uptake. Nitrate concentrations in Scenarios 1 and 3 remained below detectable levels, and total ammonia concentrations remained below detectable levels in Scenarios 2 and 3.

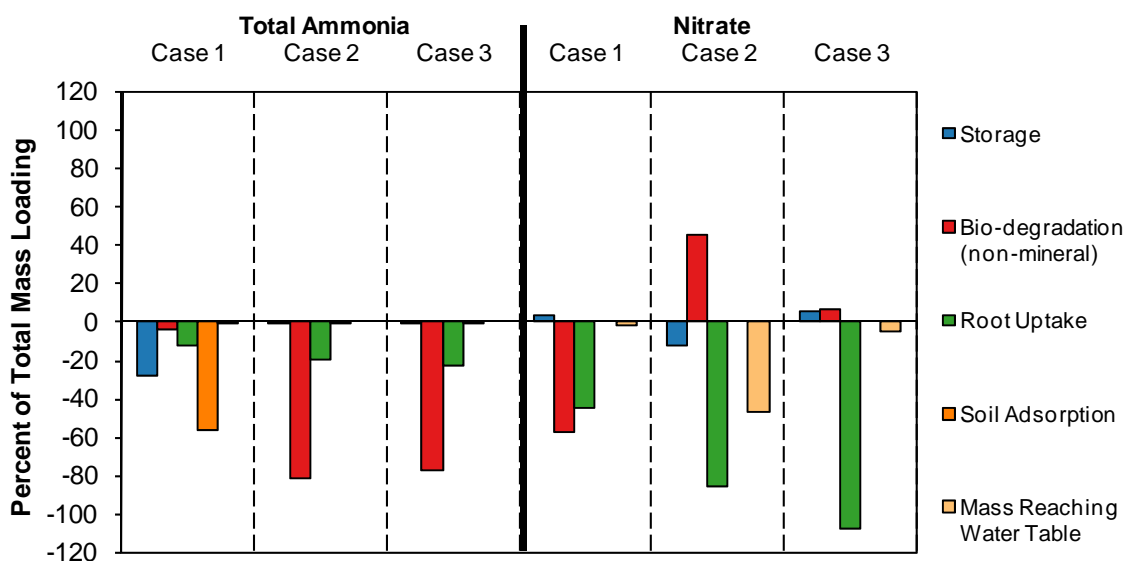


Figure 6.4: Nitrogen Mass Balance for Wine and Grape Industry

Mass balance of nitrogen compounds for wine and grape industry simulations after 30 yr. Root uptake and biodegradation strongly contribute to the decrease in total ammonia and nitrate reaching the water table. Under the optimal conditions modeled in Scenario 3, less than five percent of applied nitrate reaches the ground water.

Total ammonia concentrations in Scenario 1 began to increase at year 26, reaching 0.45 mg L^{-1} at 30 years. The breakthrough of total ammonia was retarded by approximately 15 years, as compared to the chloride tracer. This delay can be attributed to sorption, indicating that although the species arrival is slowed, the capacity of soil to attenuate ammonium in this manner is clearly finite. If the simulation was allowed to continue beyond the 30 year timeframe, total ammonia concentrations reaching the water table would be significantly higher.

The fate of nitrogen compounds in the system, shown in Figure 6.4, indicates the strong influence attenuation processes have over total ammonia and nitrate concentrations. Plant nutrient uptake removed between 12 and 23% of the applied total ammonia and 45 to 110% of the nitrate (100% of that applied at the surface plus a

portion of that converted from ammonium). Biodegradation typically played a larger role; in Scenarios 2 and 3, this process converted 81 and 77% of ammonium to nitrate.

In Scenario 2, this nitrate remained in the system, due to aerobic conditions, causing the overall nitrate reaching the water table to be 47% of that applied at the surface. In Scenario 3, the conditions were more favorable for denitrification. A large portion of the nitrate was either extracted by roots or converted to nitrogen gas, and only 5% of the nitrate applied reached the groundwater. Ammonium sorption had a small influence on Scenarios 2 and 3 because in these scenarios nitrification acted to remove it. In Scenario 1, where nitrification was inhibited, 56% of the total ammonia was removed via sorption. As the simulation time increased, the number of exchange sites where ammonium could replace a cation with less affinity for the soil decreased, causing NH_4^+ breakthrough to the water table (Figure 6.3). In the upper layers of the soil (0 – 10 m), total ammonia concentration exceeded 300 mg L^{-1} . When the simulation time was extended, total ammonia reached the water table, with concentrations near 100 mg L^{-1} by Year 40 and approaching a plateau at 440 mg L^{-1} in Year 51.

It should be noted that many dischargers treat their wastewater before application, in order to control BOD levels and prevent odor problems at the application site. In these cases, lower BOD levels may inhibit the microbial degradation of nitrate. To evaluate this effect, the BOD concentration in Scenario 3 was lowered to 5% of its original value (from 1500 mg L^{-1} to 70 mg L^{-1}), a level of BOD reduction consistent with wastewater treatment using the activated sludge process [Metcalf & Eddy *et al.*, 1991]. When Scenario 3 was rerun using the lower BOD levels, nitrate breakthrough, which did not occur in the original simulation, began to occur after 20 years. By Year 30, the

nitrate concentration at the water table had reached 9 mg L^{-1} . The impact of organic carbon removal on denitrification increased when assuming that 100% of the readily biodegradable fraction was removed during activated sludge treatment and that the remaining 5% of BOD was recalcitrant. In this scenario, the Year 30 nitrate concentration doubled to 20 mg L^{-1} . In both of these simulations, insufficient labile organic carbon was available for complete denitrification. While removal of BOD may have beneficial effects on land surface conditions, it can also negatively impact the attenuation of nitrogen compounds.

6.3.2 Salinity Reaching the Water Table

In all scenarios, estimated FDS levels began to exceed the water quality goals (500 mg L^{-1}) relatively quickly: 13, 5.9, and 12 years for Scenarios 1, 2, and 3, respectively, reaching a maximum of 2400, 1390, and 1250 mg L^{-1} at year 30. For the winery and grape processor scenarios, between 30 and 60% of the applied FDS over the 30 year period reached the water table (Figure 6.5). Attenuation by plant uptake and soil adsorption ranged from 10 to 20%; for Scenarios 1, 2, and 3, the total removal of FDS by these processes was 12, 14, and 18% of that applied, respectively.

The percent of applied FDS reaching the water table was not static throughout the simulations. When two five-year increments were examined (years 15 to 20 versus years 25 to 30), the FDS loading to the water table increased from 63 to 80% in Scenario 1, 35 to 37% in Scenario 2, and 85 to 90% in Scenario 3. The rise in loading was primarily due to the steady increase in the carbonate concentration from years 15 to 30 in Scenario 1 and years 20 to 30 in Scenario 3. Precipitation of calcium and carbonate into calcite delays breakthrough, acting as a buffer.

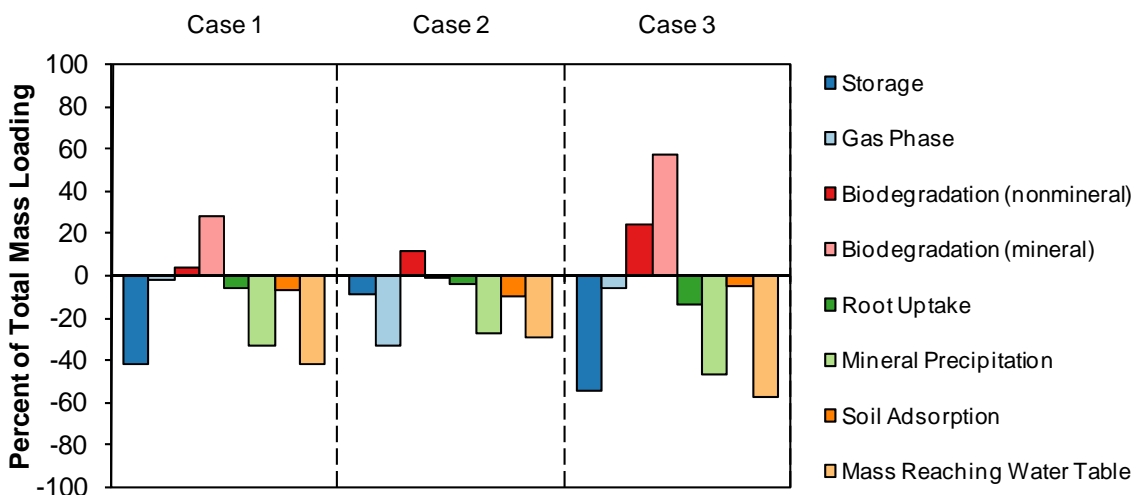


Figure 6.5: FDS Mass Balance for Wine and Grape Industry
 Mass balance of fixed dissolved solids (FDS) for wine and grape industry simulations after 30 yr. Between 30 and 60% of the FDS mass applied at the surface reached the water table.

Additionally, for Scenarios 1 and 3, the biodegradation rates of iron and manganese oxides changed as time progressed. (These reactions did not occur in Scenario 2 because of their anaerobic nature.) In years 15 to 20, both reactions were active, producing roughly 3.4 and $0.7 \text{ mol m}^{-2} \text{ yr}^{-1}$ of Fe^{2+} and Mn^{2+} in Scenario 1. By years 25 to 30, the supply of MnO_2 was nearly exhausted, and only $2.0 \times 10^{-3} \text{ mol m}^{-2} \text{ yr}^{-1}$ of Mn^{2+} were being released. If simulation time was extended past 30 years, the entire character of these systems could change, as iron oxide is exhausted and sulfate reduction or fermentation becomes the dominant method of organic carbon consumption, producing H_2S , CH_4 , and hydrogen ions.

Although high FDS levels damage crops and make groundwater resources non-potable, the composition, or species fraction, of FDS is also relevant. On the next page, Figure 6.6 shows the relative fraction of FDS contributed by each species. In drinking water, some species can cause health problems (Na^+ , NO_3^-), while others (Cl^- , SO_4^{3-} ,

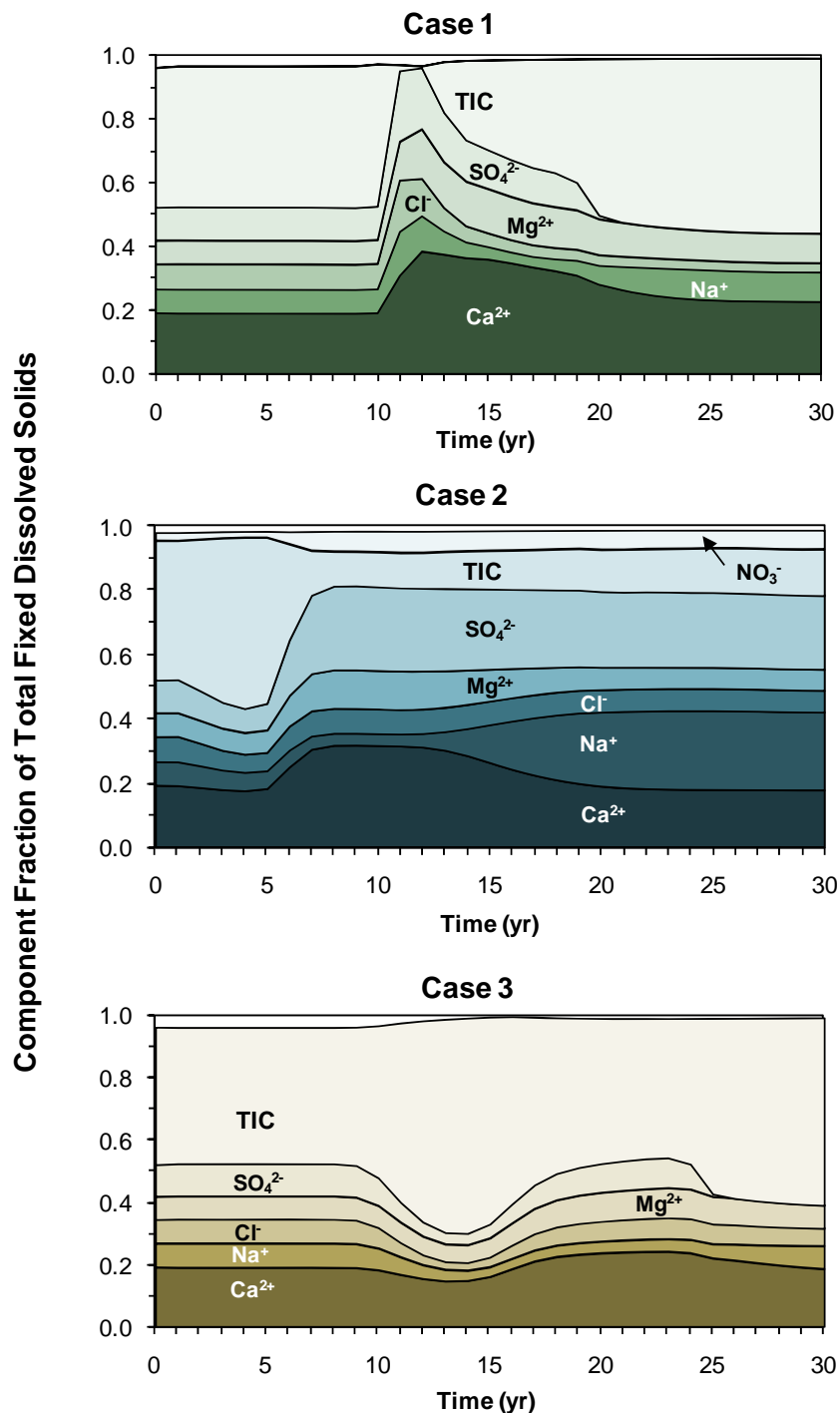


Figure 6.6: Fraction of FDS Contributed by Individual Components
 The distribution of these components depended primarily on input wastewater and soil water content. For scenarios with high water contents (1 and 3), outflux FDS was dominated by total inorganic carbon (TIC), since conversion into carbon dioxide and subsequent degassing were inhibited. Wastewater initially higher in sodium and chloride remained that way throughout the vadose zone.

CO_3^{2-}) cause hard water or create other aesthetic concerns [USEPA, 1992; 2003]. In irrigation water, Ca^{2+} , Mg^{2+} , and K^+ , are plant nutrients, while Na^+ and Cl^- are hazardous to crops at elevated levels.

The chemical composition of FDS is clearly a result of two factors: the proportion of the applied wastewater consisting of compounds which cannot be attenuated and the relative significance of attenuation processes versus carbonate production, which vary contingent on the saturation level. In Scenario 2, Na^+ and Cl^- account for over 30% of the FDS, mostly due to their relatively higher levels in the wastewater. For instance, sodium was present at 690 mg L^{-1} in Scenario 2 wastewater, and at 220 and 130 mg L^{-1} in Scenarios 1 and 3. The soil system has no mechanism for removing these ions, and they persist to the water table.

In Scenarios 1 and 3, total inorganic carbon (TIC) accounts for 55 and 60% of FDS, respectively. Approximately 8% of the TIC is released from the roots as plants consume nitrogen, phosphate, and sulfate in the waste, while the remaining 92% is generated by microbes as a result of the oxidation-reduction reactions. In contrast, TIC accounts for only 15% of FDS reaching the water table for Scenario 2, due primarily to the lower soil water content. A similar amount of TIC is produced in all scenarios (2.9 compared to 3.3 and $3.1 \text{ mol m}^{-2} \text{ yr}^{-1}$ in Scenarios 1 and 3), and due to the wastewater characteristics, a greater amount is applied at the land surface in Scenario 2 (9.6 versus 6.6 and $2.5 \text{ mol m}^{-2} \text{ yr}^{-1}$). However, the lower water content in Scenario 2 allows carbon dioxide (CO_2) gas to escape the system more readily. Equilibrium between CO_2 in the soil gas and TIC in the pore water must be maintained, allowing TIC levels in the system to decrease as CO_3^{2-} , HCO_3^- , and H_2CO_3 are converted to CO_2 . In this manner, over

60% of the TIC applied to or produced by the soil in Scenario 2 is lost to the gas phase. For Scenarios 1 and 3, the losses are much lower, 3 and 6 %, respectively.

While the lowered TIC levels may be beneficial to groundwater quality, release of carbon dioxide to the atmosphere can have environmental consequences, if sufficiently large. In Scenario 2, approximately 224 mol m^{-2} of TIC are converted to CO_2 over the 30 year life of the simulation, or $0.25 \text{ g-C m}^{-2} \text{ d}^{-1}$ being released into the atmosphere. However, net carbon uptake values of 7.9 and $13 \text{ g-C m}^{-2} \text{ d}^{-1}$ have been measured for corn and wheat fields, respectively [Baldocchi, 1994]. Thus, a field planted with corn or wheat and irrigated with wastewater would still be a net carbon sink; on average, the crops would sequester over thirty times the amount of carbon dioxide that the soil would produce.

6.3.3 Comparison to Groundwater Data

Ideally, the simulation results from the numerical model would be compared directly to vadose zone data. Unfortunately, little soil or lysimeter data is currently available, and it was not within the scope of this project to collect such a data set. However, many dischargers are required to monitor groundwater near their application sites, and this well data helps provide confirmation that the modeled FDS and NO_3^- concentrations are reasonable. Groundwater data for the wine and grape industry are extensive, and from these, histograms were created to show the distribution of concentrations in wells down-gradient of application sites (Figure 6.7). This approach has drawbacks, however, for two reasons. First, the concentration at the water table surface and the concentration in the groundwater are not analogous, primarily because mixing processes in the aquifer serve to dilute the wastewater. Second, it is difficult to

segregate ambient water quality problems from those directly caused by land application. If a discharger is located near another source of nitrate or FDS, the monitoring wells may be impacted even if the wastewater is not the cause. While a direct comparison is difficult to impossible, this method provides an approximate measure of the representativeness of the modeled values. Although a match between the computed and observed values does not validate the model, a mismatch would indicate problems with the modeling approach that need to be addressed.

Groundwater FDS concentrations from 65 wells ranged from non-detectable levels to 2100 mg L^{-1} . Scenario 1 predicted a slightly higher, but still reasonable level (2400 mg L^{-1}). Both Scenarios 2 and 3 predicted concentrations (1400 and 1300 mg L^{-1}) that occurred in six wells, near the high end of the range. Given that the waste streams selected for Scenarios 1 and 2 contained relatively high FDS levels, and that some dilution in the aquifer will occur, these results indicate that the simulations produced values that are in line with observations.

For the analysis of nitrogen (Figure 6.7), the wells were segregated into representatives of Scenario 1, 2 and 3, in the manner previously discussed. Only 5 wells, all located at one discharger, were classified as Scenario 1, indicating that although the scenario is possible, it occurs infrequently. A histogram for total ammonia concentrations could not be created due to limited data. From the remaining 60 wells, a histogram of nitrate concentrations was created, and on it, Scenarios 2 and 3 were reported separately. For Scenario 2 wells, nitrate concentrations ranged from 10 to 150 mg L^{-1} , with most reported concentrations between 10 and 30 mg L^{-1} . The modeled results were at the peak of this highly skewed distribution (18 mg L^{-1}). For Scenario 3,

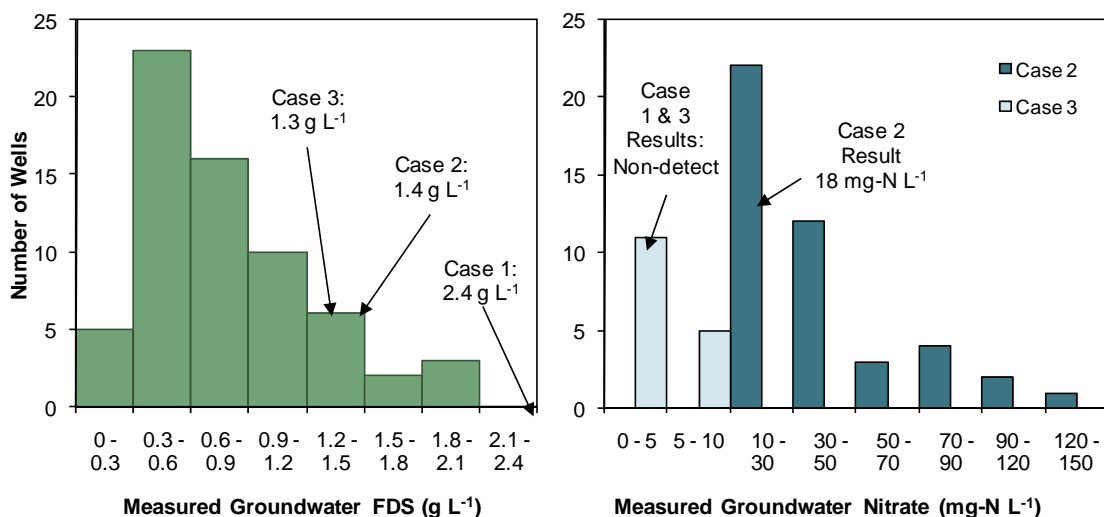


Figure 6.7: FDS and Nitrates Measured in Groundwater
 Histograms of measured fixed dissolved solids (FDS) and nitrate in ground water wells down-gradient of discharging wineries show that the measured ground water data is compatible with the modeled discharge concentrations, as indicated by the arrows.

the groundwater measurements ranged between non-detect and 10 mg L^{-1} , and the modeled results show non-detectable levels.

6.3.4 Root Zone Soil Salinity

The primary focus of this study is salinity and nitrogen loading to the groundwater, however, under some conditions, land application may lead to salinity build-up in the rooting zone. This buildup can lower crop yields, reducing ET, and in turn lead to increased levels of wastewater and plant nutrients (N, K, P, Mg, Ca) reaching the groundwater. According to Maas and Hoffman [1977], forage corn is stressed and yields begin to decrease above an $EC_e = 1.8 \text{ dS m}^{-1}$. Yields linearly decrease at a rate of 7.4% per 1 dS m^{-1} over this threshold level, meaning that they are reduced by approximately 25% at 5.2 dS m^{-1} . Wheat is more salt tolerant, with an initial threshold of 6.0 dS m^{-1} and a 25% decrease at 9.7 dS m^{-1} [Maas and Hoffman, 1977]. This section

aims to analyze the impact of increased soil salinity levels on crop yield, since it was not explicitly considered in the model.

One main determinant of soil salinity is the leaching fraction (LF), which represents the proportion of water applied (waste + precipitation + supplemental irrigation) that is not removed through root uptake. Low leaching fractions can lead to the accumulation of salts in the soil. In the Central Valley, precipitation occurs primarily during the winter, when evapotranspiration is low. This leads to low leaching fractions during the spring and summer months (March through August), when crops have the highest ratio of ET to applied water, and high leaching fractions during the fall and winter (November through February). A brief spike in leaching fraction occurs in June, when the wheat is harvested and the corn is planted. This pattern consistently repeats throughout the simulated time. Scenarios 2 and 3 have very similar patterns, although the leaching fraction is much lower in Scenario 2 (<0.5) likely due to the large difference in hydraulic conductivity.

To estimate the electrical conductivity of root zone soil, the equation $EC_{sw} = FDS/600$ was used [Asano *et al.*, 2007; Metcalf & Eddy *et al.*, 1991] where EC_{sw} is the electrical conductivity of the soil solution, in $dS\ m^{-1}$, and FDS is fixed dissolved solids calculated by MIN3P, in $mg\ L^{-1}$. To convert to soil salinity (EC_e), the soil solution salinity was divided by a factor of two, $EC_e = EC_{sw}/2$ [Asano *et al.*, 2007; Ayers and Westcot, 1985]. Figure 6.8 shows the simulated EC_e levels at 0.55 m for Scenario 1, for the 30-year simulation time (8a), highlighting the seasonal pattern (8b). The soil salinity follows a yearly pattern nearly opposite that of the leaching fraction (high in the summer and low in the fall), and the pattern is consistent throughout the simulation time for all

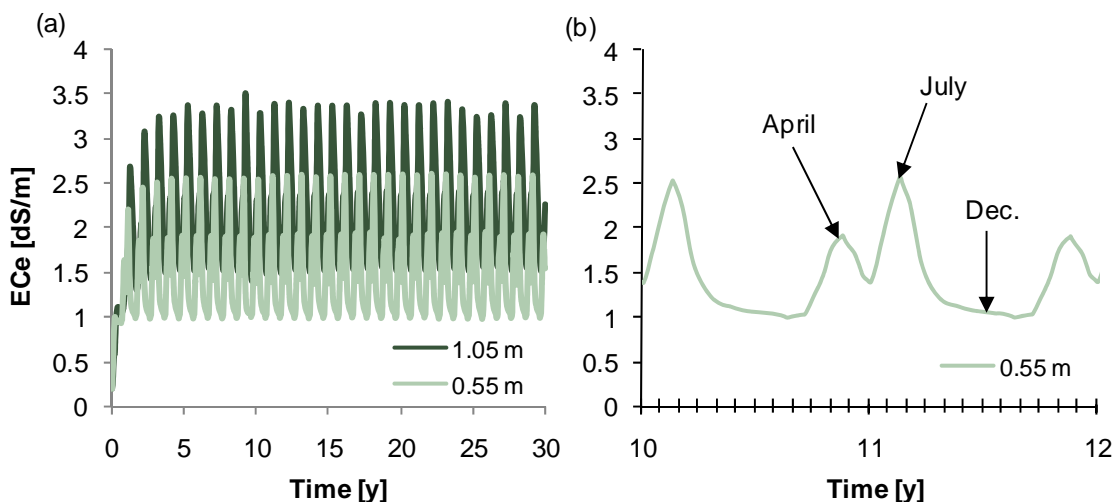


Figure 6.8: 30-year Simulated Soil Salinity for Scenario 2

(a) The seasonal pattern of soil salinity (EC_e) repeats regularly over the 30-yr simulation time. The lower portion of the root zone (>0.55 m below ground surface) had consistently higher salinity levels than the upper portion. (b) Peaks in soil salinity occur during April and July, when ET from the crops is highest. Salinity levels drop in the fall when ET begins to decrease.

three scenarios, with no buildup in salinity levels. Periodically elevated soil salinity levels ($EC_e > 2$) were noted in all three scenarios. Scenarios 1 and 2 are shown over the span of one year in Figure 6.9. Reductions in plant yield of up to 25% could be possible at these concentrations, but would primarily be limited to the corn crop grown between late July and early August or the wheat crop during March and April. The Scenario 1 simulation (Figure 6.9a) shows that the corn crops are subject to some salinity stress throughout their growing season, while wheat remains almost totally non-stressed. Due to the lower leaching fraction and the higher wastewater salinity levels in Scenario 2 (Figure 6.9b), the wheat becomes significantly stressed ($EC_e \approx 9 \text{ dS m}^{-1}$) during April, while the corn is stressed during July. Both crops remain relatively unstressed in the Scenario 3 simulations, with slight stresses ($EC_e < 2.5$) occurring to the corn crops during July. Additionally, in all scenarios, the high salinity levels occurred primarily in the

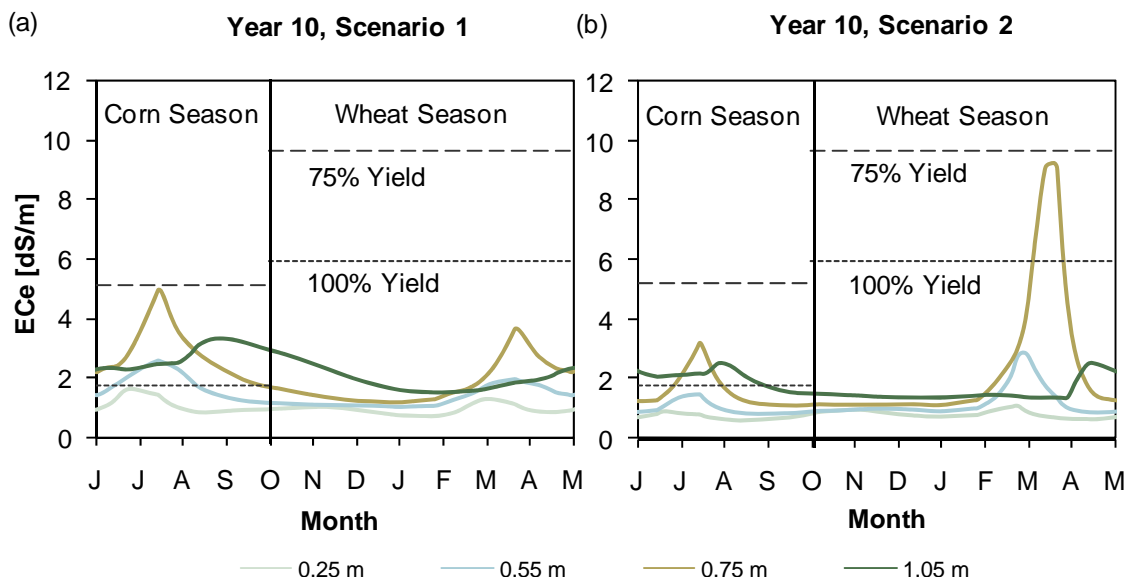


Figure 6.9: Year 10 Simulated Soil Salinity Levels

Soil salinity levels for Scenarios (a) 1 and (b) 2 during Year 10. Crop yield is not affected at $EC_e < 1.8 \text{ dS m}^{-1}$ for corn and $EC_e < 6.0 \text{ dS m}^{-1}$ for wheat, shown in the lower dotted lines. Yield decreases linearly as EC_e increases, with a 25% reduction at 5.2 dS m^{-1} for corn and 9.7 dS m^{-1} for wheat, shown in the upper dotted lines. In both scenarios, yield reductions between 0 and 25% potentially occurred during April and July.

lower root zone, between 0.75 and 0.105 m below the ground surface. This salinity difference between the upper and lower root zones could lead to water being preferentially removed from the upper soil layers.

Overall, these simulations show that crop yields may be periodically reduced by up to 25% due to salinity buildup in the lower root zone. This reduction could lower the ET and increase the leakage to the groundwater table, altering the FDS concentrations and loading rates to the groundwater table. It is likely, though, that conditions such as these may not be allowed to develop in an actual land application situation. From April to May, modeled irrigation, precipitation, and land application are nearly matched to the crop water uptake rates in Scenario 2, leading to a very low leaching fraction. It is

unlikely that land owners would permit the soil saturation to be reduced as greatly as the model predicts (0.2 – 0.3). Rather, in order to prevent crop stress, it is likely that additional irrigation water would be provided, leading to higher soil moisture, higher leaching fractions, and lower EC.

6.3.5 Model Sensitivity Analysis

As discussed previously, both the general, non-site-specific nature of the modeling approach and the lack of appropriate field data prevented the simulations from being tested directly. To better estimate the reliability of the model and provide guidance on future field studies, an analysis was conducted to determine the sensitivity of the model results to the input parameter values. While these types of analyses are well documented in the groundwater and vadose zone modeling literature [*Hill and Tiedeman, 2007; Vrugt and Neuman, 2006*], this application is only rarely conducted on *multicomponent reactive* transport simulations [e.g. *Spiessl et al., 2007*]. To perform the sensitivity analysis, we used a linear First Order-Second Moment (FOSM) type approach described by James and Oldenburg [1997] and briefly summarized here. This approach assumes that model outputs (z_i) can be estimated as a linear function of the uncertain model parameters (p_j), so that a Jacobian matrix (J) is formed where $J_{ij} = \partial z_i / \partial p_j$, i is the number of model outputs of interest, and j is the number of uncertain parameters. To calculate J, a forward finite difference approach is used where each of the parameters in the model is then perturbed “one-variable-at-a-time” by a constant fraction α , where $\partial p_j = \alpha p_j$, making the Jacobian equal to:

$$J_{ij} = \frac{\partial z_i}{\partial p_j} \approx \frac{z(p_j + \alpha p_j) - z(p_j)}{\alpha p_j} \quad (6.5)$$

Finally, a model sensitivity coefficient (χ) is computed from the results:

$$\chi_{ij} = \left| \frac{\partial z_i}{\partial p_j} \right| \frac{\sigma(p_j)}{\sigma(z_i)} \quad (6.6)$$

where $\sigma(p_j)$ and $\sigma(z_i)$ are the standard deviations of the parameters and outputs, respectively. The coefficient χ_{ij} can then be summed over i to obtain a total coefficient for each parameter (χ_j), which represents the combined sensitivity of each of the response metrics. The more sensitive the simulation results are to a parameter, the higher the value of χ_j becomes.

A sensitivity analysis was performed for both Scenario 1 and Scenario 2 simulations, in order to cover the range of saturation conditions which are known to cause very different model responses. For each of the scenarios in this analysis, N+1 simulations were required, where N = 73 parameters. (One simulation is required as a baseline and N simulations are needed to calculate model response to parameter changes.) For the response variables, we chose to use the following metrics: total mass of FDS, NO_3^- , NH_4^+ , and CH_2O released to the water table over the 30-year time-span and breakthrough concentration of each of these at the end of the 30-year simulation period. Since no estimate of $\sigma(p_j)$ was available for most of the parameters, we assumed that the coefficient of variation for each parameter (standard deviation divided by the mean) was equal to 1, meaning that $\sigma(p_j) \approx p_j$.

The model parameters were ranked according to their χ_j values, with higher values indicating higher sensitivity. The ten most influential model parameters and their

associated χ_j values are shown in Table 6.7. In both scenarios, the hydraulic parameters porosity, $\log(n)$, and $\log(\alpha)$ were among the most influential, for two potential reasons: first, because they controlled the oxygen levels in the soil, affecting which redox reactions would proceed, and second, because they controlled the overall water flow rate through the system, affecting dilution of the waste components and the residence time of the waste in the unsaturated zone. In part, the scenarios respond differently to parameter changes because of the non-linear behavior of the functions describing relative permeability and the water retention curve, Equations(6.1) and (6.2). Scenario 1 is highly saturated, and in that range of saturation, these functions are quite flat, so there is less sensitivity to $\log(n)$ and $\log(\alpha)$ as compared to Scenario 2, where these curves are much steeper. Due to this behavior, the applicability of the sensitivity analysis results to moderate (50-90%) and very low (<40%) saturation levels is limited. This limitation occurs since linear FOSM cannot be used to extrapolate to conditions outside of those tested, since the model is itself non-linear.

Taking porosity as an example, a 5% change in its value (from 0.35 to 0.37) resulted in lower FDS discharges to the water table over the 30-year period, with a decrease of 660 g (5%) in Scenario 1 and 310 g (2.5%) in Scenario 2. The change also reduced the final FDS breakthrough concentrations which were 2.65 mg L⁻¹ (0.1%) lower in Scenario 1 and 15.23 mg L⁻¹ (1%) lower in Scenario 2. For nitrogen, total ammonia reaching the water table was 0.02 g (52%) lower in Scenario 1 and nitrate was 17.56 g (2.5%) lower in Scenario 2. The decreases in final concentrations for each were 0.09 mg L⁻¹ (50%) for total ammonia in Scenario 1 and 0.57 mg L⁻¹ (0.7%) for nitrate in

Table 6.7: Ten Most Influential Model Parameters for Scenarios 1 and 2

Scenario 1						Scenario 2					
Parameter	χ_j^\dagger	$\chi_{\text{FDS};j}$	$\chi_{\text{NO}_3;j}$	$\chi_{\text{NH}_4;j}$	$\chi_{\text{CH}_2\text{O};j}$	Parameter	χ_j	$\chi_{\text{FDS};j}$	$\chi_{\text{NO}_3;j}$	$\chi_{\text{NH}_4;j}$	$\chi_{\text{CH}_2\text{O};j}$
θ_s	24.1	1.06	1.71	20.3	1.04	$\log(n)$	11.45	0.41	1.13	6.02	3.89
$\log(n)$	5.75	0.27	1.29	4.07	0.12	θ_s	7.18	0.71	0.66	2.95	2.86
$K_{\text{denit, pH}}$	4.48	0.06	3.29	1.11	0.02	$\log(K_{\text{sat}})$	4.75	0.29	1.30	1.92	1.24
k_{iron}	3.75	0.47	0.10	3.12	0.07	S_r	4.59	0.18	0.96	1.95	1.50
k_{denit}	3.11	0.08	0.39	2.60	0.05	$\log(\alpha)$	3.38	0.05	0.21	1.84	1.28
$I_{\text{max, Mg, corn}}$	2.53	0.11	0.14	2.22	0.05	k_{res}	2.54	0.03	1.24	0.04	1.23
$\log(\alpha)$	2.43	0.20	0.12	2.03	0.07	k_{nit}	2.22	0.05	1.10	1.05	0.02
$K_{\text{NH}_4, \text{corn}}$	2.39	0.08	0.13	2.16	0.02	$K_{\text{nit, pH}}$	2.03	0.09	0.66	1.27	0.01
$K_{\text{Mn, NO}_3\text{i}}$	1.95	0.09	0.11	1.68	0.06	$K_{\text{res, pH}}$	1.92	0.08	0.48	0.05	1.31
$I_{\text{max, Ca, wheat}}$	1.77	0.02	0.01	1.70	0.04	$K_{\text{res, CH}_2\text{O}}$	1.73	0.06	0.55	0.05	1.07

$\dagger \chi_j$, overall sensitivity coefficient, Eq. (6.6), and individual sensitivity coefficients for each component; θ_s , porosity; S_r , residual saturation; n , α , van Genuchten parameters, Eqs. (6.1) and (6.2); I_{max} , overall crop uptake rate of listed chemical (Eq. (6.3)); k , rate coefficient of redox reaction listed in subscript, Eq. (6.4); K , half-saturation constant of chemical for redox reaction or plant uptake, Eqs. (6.3) and (6.4).

Scenario 2. Overall, for the 5% change in porosity, the change to the output was less than 5% in all but one instance; the amount of total ammonia reaching the water table decreased by nearly 50% for Scenario 1.

In both scenarios, the slight change in porosity caused lower saturation levels, allowing additional ammonium to be degraded to nitrate. The model response to lower saturation was less pronounced in Scenario 2 than in Scenario 1, because the change in gas saturation was limited. In Scenario 1, the increased porosity led to the development of unsaturated conditions which made oxygen available, allowing ammonia oxidation to

begin to occur. Since high oxygen levels were already present in Scenario 2, the change in porosity and subsequent change in gas saturation did not have the same effect.

While the model was generally the most sensitive to the saturation controlling parameters, it also responded to changes in the biodegradation rate parameters. In Scenario 1, the parameters describing the anaerobic redox reactions were influential (Table 6.7), primarily the rate coefficients of denitrification (k_{denit}) and iron reduction (k_{iron}), the pH inhibition constant for denitrification ($K_{\text{denit,pH}}$), and the nitrate inhibition constants for manganese reduction ($K_{\text{Mn, NO}_3\text{i}}$). A similar model response was also noted with the plant uptake rates $I_{\text{max,Ca}}$ and $I_{\text{max,Mg}}$. All of these parameters primarily impacted the concentration and mass of NH_4^+ reaching the water table and had a smaller effect on FDS mass loading. This behavior is caused by the influence of these parameters on the presence of divalent cations (Fe^{2+} , Mn^{2+} , Ca^{2+} , and Mg^{2+}) in solution, which compete with NH_4^+ for exchange sites. As fewer of these competing cations are present in solution, more sorption of NH_4^+ occurs. Although the parameter values affecting biodegradation and plant uptake rates are highly uncertain, in particular half saturation and inhibition constants, these results suggest that the overall rates of these processes may have important secondary effects on NH_4^+ concentrations, and exemplify the highly coupled nature of the system under investigation.

In Scenario 2, the parameters associated with the aerobic redox conditions were most influential. The rate coefficients for respiration (k_{res}) and nitrification (k_{nit}) were controlling, as well as the pH inhibition constants for these reactions ($K_{\text{nit,pH}}$ and $K_{\text{res,pH}}$) and the CH_2O half-saturation constant for respiration ($K_{\text{res,CH}_2\text{O}}$). These biodegradation rate parameters, like those in Scenario 1, have a high degree of uncertainty associated

with their values. Additionally, the model showed less sensitivity to plant solute uptake parameters in Scenario 2, likely due to the longer residence time of water in the root zone.

In summary, the sensitivity analysis demonstrated that for these two scenarios, the model outputs were most influenced by the hydrogeologic conditions that controlled soil saturation levels, followed by the rates of the biodegradation redox reactions. This finding implies that in order to apply this model to a specific site and accurately predict breakthrough of FDS, nitrogen compounds, and labile organic carbon, the most important information will be detailed characterization of soil saturation conditions, either by direct measurement or through knowledge of waste application rates and hydrogeologic properties. The results of this analysis also confirm that parameters affecting overall contaminant degradation must be evaluated carefully, as their values can significantly affect the model outputs. Measurements of microbial nitrification, denitrification, and respiration rates in soils with high organic carbon loadings will thus be important, as well as knowledge of how these rates are inhibited by low pH.

6.3.6 Application to Additional Industries

Until now, the discussion of the results has been limited to the wine and grape processing industry for simplicity, but simulations have also been conducted for other industries including dairy processing, tomato processing, and meat packing. Generally, while some differences were clearly caused by higher or lower BOD, N, or FDS concentrations, most were attributable solely to the distribution of subcomponents of these systems, for instance the ratio of nitrate to total ammonia or of crop nutrients to Na^+ and Cl^- .

Overall, the pattern of response to each scenario was consistent between industries, but the magnitude of the concentration reaching the groundwater varied depending on the input wastewater composition. The breakthrough curves for all industries followed a pattern consistent with those shown in Figure 6.2. For nitrogen compounds, the concentrations at the water table were dependent on the characteristics of the waste stream: the wine industry showed the highest total ammonia levels, while dairy processors had the highest nitrate levels, and tomato canners had lower levels of both. For Scenario 2, dairy, tomato, and meat processors had higher mass loadings of nitrate appearing at the water table than were added via the wastewater: 110, 240, and 915%, respectively. The additional nitrate was produced through the oxidation of ammonium. In Scenario 2 for meat packers, the TKN concentration was approximately ten-times that of nitrate, leading to its nine-fold increase between the surface and the water table.

All simulations predicted FDS levels above the groundwater quality objectives, some up to 16 times higher. For tomato processors, 68–98% of FDS applied reached the groundwater. For dairy processors, this range was 70–110%, and for meat packers, it was 72–150%. The FDS mass was increased by the dissolution of soil minerals. The wine and grape industry had lower percentages (29–96%) due to the characteristics of its waste; the ratio of plant nutrient ions to non-nutrient ions was higher in winery waste than in the other waste streams. For tomato and dairy processors, almost 50% of the FDS concentration was attributable to sodium or chloride, while for wineries and meat packers, less than 30% came from these ions. Instead, potassium and carbonate were present in higher fractions.

6.4 Conclusions

Land application of food-processing wastewaters should not be viewed as a complete treatment strategy. Numerical modeling showed that when site and flow conditions were optimal, natural attenuation is able to remove nearly all of the nitrogen and a significant portion of the plant nutrients applied. For instance, Scenario 3 balanced the wastewater application rate (3.9×10^{-9} to $12.0 \times 10^{-8} \text{ m s}^{-1}$), the hydraulic conductivity ($2 \times 10^{-7} \text{ m s}^{-1}$), and a sufficiently deep water table (15 m below ground surface) to achieve both aerobic and anaerobic zones in the soil, conditions ideal for first converting ammonium to nitrate and then nitrate to inert nitrogen gas. The permitted application rates for all analyzed waste streams described were fairly consistent, between 1.0 and $9.0 \times 10^{-8} \text{ m s}^{-1}$, a pattern that has likely been intentionally designed. At application sites with high hydraulic conductivity (10^{-4} m s^{-1}), these rates will lead to aerobic conditions, promoting nitrification but inhibiting denitrification in the vadose zone and potentially creating elevated nitrate concentrations in the groundwater. The alternative, higher application rates or lower conductivity ($<10^{-7} \text{ m s}^{-1}$), has the potential to create either a total ammonia or a nitrate problem. The optimum management strategy shown in Scenario 3 is heavily dependent on site conditions that may be difficult to create in practice.

In most cases, treatment through land application did not reduce total salinity by more than 10–40%, and in some situations, salinity levels increased due to the microbial and plant production of carbonate ions and the dissolution of soil minerals. Reductions in FDS were only achieved when the applied wastewater had low sodium and chloride concentrations relative to its content of the nutrients potassium, phosphate, and nitrogen.

Crop nutrient uptake was not a panacea; while it reduced levels of some FDS components, it proportionally increased levels of carbonate. The portion of FDS composed of carbonate was lower in Scenario 2, due to its low saturation levels which promoted carbonate loss through CO₂ degassing.

In some simulations, organic carbon reached the water table. In practice, this could be prevented by reducing the application rates and allowing time for other reactions, such as iron and sulfate reduction, microbial respiration, or fermentation, to consume the excess organic carbon. However, if processors must use in-plant pretreatment to control effluent BOD levels, they should strongly consider options that leave levels of organic carbon in the waste that are sufficient to sustain denitrification in the vadose zone.

These results indicate that improvements in the quality of water reaching the underlying aquifer must start with careful site selection, strict flow rate controls, and alterations to the character of the wastewater itself. In future work, the first priority should be on using field and soil column data that is now becoming available to test, further validate, and calibrate the model. In the presence of supporting data, the model itself could also be modified to include microbial growth and decay and a more rigorous description of processes in the root zone. For example, the implementation of a more sophisticated model of root uptake that introduces the effects of high soil salinity levels on crop and microbial community health would allow an assessment of the impact of reduced nutrient uptake and biodegradation on the transfer of nitrogen compounds to the water table.

Chapter 7: Summary

The terrestrial water cycle is strongly controlled by the biosphere, with transpiration by plants serving as the dominant mechanism for the return of precipitation to the atmosphere. Ecohydrologists have studied the how water moves throughout the soil-plant-atmosphere continuum, but the influence of groundwater on plant processes has been largely neglected. This dissertation aimed to fill in several critical gaps in our knowledge of these processes in semi-arid systems, with a special emphasis on oak savannas in California.

Plant available soil moisture has long been considered the primary variable controlling plant water uptake, and extensive statistical models have been developed around this conceptualization. These models, when appropriately modified, can predict soil moisture distributions across a variety of conditions, as demonstrated in Chapter 2. However, finding appropriate parameters for them can be difficult. Using data available from large micrometeorological networks can help, but the processes of properly incorporating it had not been previously detailed. Two of the model parameters are not as readily estimated: the plant stress point and the maximum evapotranspiration under non-stressed conditions. While inverse modeling helped to estimate these, it became clear that more research was needed on the relationship between soil matric potential and water stress for the species in question. The traditional definition of stress, based on leaf water potential, was not useful in this context. Also apparent was the need for a groundwater uptake term in the stochastic formulations. At the Tonzi Ranch site, it was

clear that the oak trees were either far more adept at conserving water than other species, or they were able to obtain water from a source not included in the “bucket” model.

The question of groundwater uptake by the blue oaks at the Tonzi Ranch had long been pondered, but not definitively answered. To fully understand the ecohydrology at the site, we needed to know more about the groundwater system. The available literature provided a few answers: water was contained in the numerous fractures of the underlying crystalline rock, and the likely yield from wells placed in this rock was very low. In wells drilled for domestic and irrigation use, the depth to groundwater was highly variable and estimated at anywhere from 10 to 30 m. In order to extract water at sufficient rates, many owners had to drill wells upwards of 100 m deep, as was done at the Tonzi site. A previous study noted that blue oaks in nearby Placerville could access sources of water up to 24 m deep. Other interesting observations noted that the availability of nitrogen in site soils could be traced directly back to the decomposition of the parent rock material, having potential consequences for the site’s biogeochemical cycling.

Installing and monitoring test wells provided much more information. The depth to groundwater was determined to be approximately 10 m and varied by around 3 m both spatially and temporally. The flow rate was in the high range for metavolcanic rock, around 10^{-7} to 10^{-6} m s⁻¹. In one well, this varied with groundwater depth, by an order of magnitude, highlighting the importance of the fracture system. The depth to groundwater provided an encouraging sign for plant uptake, as did minute diurnal fluctuations in it that roughly corresponded to sunlit hours, reflecting daytime transpiration and nighttime rebound.

Exploring this connection further, we found that these fluctuations can be used to quantify the vegetation uptake rates in the oak savanna. Using a method developed in 1932, but only recently gaining popularity, the groundwater uptake was estimated to reach up to 20 mm per month during the dry summer season. In many cases, this was over 80% of the total stand evapotranspiration. The uptake acted as a buffer for the strongly bimodal precipitation patterns. When winter and spring stores of soil moisture were depleted, around April or May, it became necessary for the trees to start using deeper sources of water.

Supporting these conclusions were a host of other hydrological and biophysical data. Water potential data provided for a very novel analysis, based on thermodynamic arguments. It indicated that not only was it possible for the deeply rooted woody vegetation to transport the water to the leaves, it took relatively less energy to do so than it did for the plants to extract it from the dry soil. Water balances at the tree and the stand proved slightly less useful, as they were plagued with problems in determining leakage rates during the wet season. The individual tree water balances, however, did suggest some possible avenues for interesting future research.

These tree water balances were developed from the results of concurrent research at the site using sap flow measurement methods. We designed this portion of the research to improve the process of upscaling from these point measurements of individual tree transpiration to spatially integrated measurements of stand and landscape latent heat flux. Previous work on upscaling considered tree diameter or leaf area to be the only controls on an individual tree's transpiration capacity. The method typically consisted of measuring four or five randomly selected trees with a range of diameters

and multiplying the measured sap velocities by the stem or sapwood area densities for the stand. While this approach had some success in wet systems, it clearly neglected another intrinsic control on transpiration – the tree’s soil environment.

Instead of randomly selecting trees for observation, we designed a systematic method that would group trees into non-predetermined categories and identify one “representative tree” for each grouping. The sap flow in this tree was then measured and used to upscale to a stand level flux. The properties used to classify trees into groupings were diameter, soil sand content, slope, and elevation. The last three of these were included as proxies for the soil environment. The classification algorithm worked well to identify eight distinct groupings of trees without repetition, and these groupings showed distinctly different behavior. For instance, three trees of identical diameter but located in different soil environments were measured; the trees in both the drier and wetter environments had lower transpiration rates than the tree exposed to average soil moisture levels.

Upscaling the data to the stand level was done using several methods: a simple linear model, a more advanced power law scaling technique, and a method that accounted for the flux footprint of the tower. The simplest method proved to be the most reliable when the daily sums of transpiration were considered, more closely matching the latent heat flux from the eddy-covariance system. The power law method produced results that corresponded better to the tower data at the half-hourly scale. A lack of overlap between the tower’s footprint and the sap flow study area created problems with the final upscaling method. Modifications to the system were made after reviewing this

preliminary data set, and data currently being collected should produce better upscaling results.

Finally, we provided an example of an engineering application that required the integration of ecological, hydrogeological, and biochemical concepts into one modeling framework. Unlike previous work, this modeling effort extensively considered the effects of both crops and microbes on the vadose zone remediation of wastewater. The model indicated that potentially harmful components in the food waste, primarily salts, nitrate, and ammonia, could be reaching the underlying groundwater, but that breakthrough was highly dependent on the rate of water application. Varying levels of soil moisture benefited certain microbial communities, which in turn affected organic matter and nitrogen consumption. While this modeling application took place in an engineered system, the methods developed could also be very useful in studies of natural systems and their biogeochemical cycling.

Overall, this research highlights the importance of incorporating the hydrogeological perspective into studies of ecohydrology by considering the contribution of groundwater to plant transpiration, demonstrating the usefulness of geostatistical methods in study design, and creating a modeling framework for ecological engineering in the near sub-surface. This perspective will be valuable as research into groundwater dependent ecosystems continues, and as we increase our understanding of the potentially strong coupling between groundwater and land surface processes.

This work suggests several broad topics and numerous specific questions for future research:

- **Occurrence and functionality of groundwater dependent ecosystems**

How can we systematically identify and classify groundwater dependent ecosystems? How does phreatophytic vegetation control surface water and groundwater flow at the landscape level? What happens to dependant ecosystems when groundwater levels change?

- **Feedbacks in the Groundwater-Soil-Plant-Atmospheric Continuum**

What role do feedback effects between groundwater, vegetation, and the atmosphere play in permanently altering the hydroclimate of a region? How will altered ET affect local and regional precipitation? To what extent can groundwater level changes influence the surface energy balance and the lower atmospheric boundary layer?

- **Sustainable groundwater allocation for ecosystem services and human populations**

Can we balance the human demand for groundwater with the water needed to sustain ecosystems? How do we quantify the intrinsic value of ecosystem provided services?

Answering these questions will require the understanding of complex, integrated natural systems that is fundamental to ecohydrology, as well as the data, tools, and perspectives developed in this dissertation.

References

- AmeriFlux (2005), AmeriFlux Website, edited, Oak Ridge National Laboratory.
- Anthoni, P. M., et al. (1999), Carbon and water vapor exchange of an open-canopied ponderosa pine ecosystem, *Agr. Forest Meteorol.*, 95(3), 151-168.
- Appelo, C. A. J., and D. Postma (2005), *Geochemistry, Groundwater and Pollution*, 2nd ed., A. A. Balkema, Leiden, Netherlands.
- Arking, A. (1991), The radiative effects of clouds and their impact on climate, *B. Am. Meteorol. Soc.*, 72(6), 795-813.
- Arkley, R. (1964), Soil survey of the Eastern Stanislaus Area, California, *Soil Survey Series 1057, No. 20*, USDA Soil Conservation Service, Washington, D.C.
- Asano, T., et al. (2007), *Water Reuse: Issues, Technology, and Applications*, McGraw Hill, New York, NY.
- Ayers, R. S., and D. W. Westcot (1985), Water quality for agriculture, *FAO Irrigation and Drainage Paper 29, Rev. 1*, edited, Food and Agriculture Organization of the United Nations, Rome.
- Bachelet, D., et al. (2003), Simulating past and future dynamics of natural ecosystems in the United States, *Global Biogeochem. Cy.*, 17(2), 1045, doi:10.1029/2001GB001508.
- Baldocchi, D. (1994), A comparative study of mass and energy exchange rates over a closed C3 (wheat) and an open C4 (corn) crop: II. CO₂ exchange and water use efficiency, *Ag. Forest Met.*, 67, 291-321.
- Baldocchi, D., et al. (2001), FLUXNET: A new tool to study the temporal and spatial variability of ecosystem-scale carbon dioxide, water vapor, and energy flux densities, *B. Am. Meteorol. Soc.*, 82(11), 2415-2434.
- Baldocchi, D. D., et al. (2002), How the environment, canopy structure and canopy physiological functioning influence carbon, water and energy fluxes of a temperate broad-leaved deciduous forest-an assessment with the biophysical model CANOAK, *Tree Physiol.*, 22(15-16), 1065-1077.
- Baldocchi, D. D. (2003), Assessing the eddy covariance technique for evaluating carbon dioxide exchange rates of ecosystems: past, present and future, *Global Change Biol.*, 9(4), 479-492.

Baldocchi, D. D., et al. (2004), How plant functional-type, weather, seasonal drought, and soil physical properties alter water and energy fluxes of an oak-grass savanna and an annual grassland, *Agr. Forest Meteor.*, 123(1-2), 13-39.

Baldocchi, D. D., et al. (2005), Predicting the onset of net carbon uptake by deciduous forests with soil temperature and climate data: a synthesis of FLUXNET data, *Int. J. Biometeorol.*, 49(6), 377-387.

Baldocchi, D. D., and L. Xu (2007), What limits evaporation from Mediterranean oak woodlands—the supply of moisture in the soil, physiological control by plants or the demand by the atmosphere?, *Adv. Water Resour.*, 30(10), 2113-2122.

Barber, S. (1995), *Soil Nutrient Bioavailability: A Mechanistic Approach.*, Wiley, New York.

Barraclough, P. B. (1986), The growth and activity of winter-wheat roots in the field: nutrient inflows of high-yielding crops, *J. Agr. Sci.*, 106, 53-59.

Bates, B., et al. (2008), Climate change and water, *IPCC Technical Paper*, Intergovernmental Panel on Climate Change, Geneva, Switzerland.

Bauer, P., et al. (2004), Estimation of the evapotranspiration rate from diurnal groundwater level fluctuations in the Okavango Delta, Botswana, *J. Hydrol.*, 288(3-4), 344-355.

Betts, R. A., et al. (1997), Contrasting physiological and structural vegetation feedbacks in climate change simulations, *Nature*, 387(6635), 796-799.

Bleby, T. M., et al. (2004), A validation, comparison and error analysis of two heat-pulse methods for measuring sap flow in *Eucalyptus marginata* saplings, *Funct. Plant Bio.*, 31(6), 645-658.

Brady, N., and R. Weil (1999), *The Nature and Properties of Soil*, 12th ed., Simon and Schuster, Upper Saddle River, NJ.

Brenton, C. M., et al. (2007), Macronutrient and trace element leaching following biosolids application on semi-arid rangeland soils, *Arid Land Res. Manag.*, 21, 143-156.

Breuer, L., et al. (2003), Plant parameter values for models in temperate climates, *Ecol. Model.*, 169(2-3), 237-293.

Briski, F. (1977), Drilling log for irrigation well on Tonzi property, Briski Well Drilling, Ione, CA.

- Briski, F. (1989), Drilling log for domestic well on Tonzi property, Briski Well Drilling, Ione, CA.
- Britz, T., et al. (2005), Treatment of dairy processing wastewaters, in *Waste Treatment in the Food Processing Industry*, edited by L. Wang, et al., pp. 1-28, CRC Press, Boca Raton, FL.
- Brutsaert, W. (2005), *Hydrology: An Introduction*, Cambridge University Press, New York.
- Bucci, S. J., et al. (2004), Processes preventing nocturnal equilibration between leaf and soil water potential in tropical savanna woody species, *Tree Physiol.*, *24*(10), 1119-1127.
- Burgess, S. S. O., et al. (2001a), An improved heat pulse method to measure low and reverse rates of sap flow in woody plants, *Tree Physiol.*, *21*(9), 589-598.
- Burgess, S. S. O., et al. (2001b), Tree roots: conduits for deep recharge of soil water, *Oecologia*, *126*, 158-165.
- Burkett, V., et al. (2001), Potential consequences of climate variability and change for the Southeastern United States, in *Climate Change Impacts on the United States: A Report of the National Assessment Synthesis Team*, Cambridge University Press, Cambridge.
- Burow, K. R., et al. (2004), Hydrogeologic characterization of the Modesto Area, San Joaquin Valley, California, *SIR 2004-5232*, USGS, Reston, VA.
- Butler, J. (1997), *The Design, Performance, and Analysis of Slug Tests*, CRC Press, Boca Raton, FL.
- Butler, J. J., et al. (2007), A field investigation of phreatophyte-induced fluctuations in the water table, *Water Resour. Res.*, *43*, W02404, doi:02410.01029/02005WR004627.
- Cal. Dep. Water Resour. (2006), Modesto Station #71 Data: California Irrigation Management Information System, [Online], Available at: <http://www.cimtis.water.ca.gov/cimtis/welcome.jsp> .
- Cal. EPA (2007), California Central Valley Regional Water Quality Control Board Adopted Orders, [Online], Available at http://www.swrcb.ca.gov/rwqcb5/adopted_orders/index.html (verified 11 May 2007).
- Campbell, G., and J. M. Norman (1998), *An Introduction to Environmental Biophysics*, Springer-Verlag, New York.

- Campbell Scientific (1996), *Instruction Manual: CS615 Water Content Reflectometer*, Logan, UT.
- Canadell, J., et al. (1996), Maximum rooting depth of vegetation types at the global scale, *Oecologia*, 108(4), 583-595.
- Cavender-Bares, J., and N. M. Holbrook (2001), Hydraulic properties and freezing-induced cavitation in sympatric evergreen and deciduous oaks with contrasting habitats, *Plant Cell Environ.*, 24(12), 1243-1256.
- Caylor, K. K., and D. Dragoni (2009), Decoupling structural and environmental determinants of sap velocity: Part I. Methodological development, *Agr. Forest Meteorol.*, 149(3-4), 559-569.
- Center for Stable Isotope Biogeochemistry (2009), Referencing 18O water analysis, edited, [Online], Available at: http://ib.berkeley.edu/groups/biogeochemistry/ref_oxygen.php (verified 23 March 2009), Berkeley, CA.
- Cermak, et al. (2004), Sap flow measurements with some thermodynamic methods, flow integration within trees and scaling up from sample trees to entire forest stands, *Trees*, 18, 529-546.
- Chapman, R. H., et al. (1975), *Geophysical investigations in the Ione area, Amador, Sacramento, and Calaveras Counties, California*, California Division of Mines and Geology, Sacramento.
- Chavarro-Rincon, D. (2009), *Tree Transpiration Mapping from Upscaled Sap Flow in the Botswana Kalahari*, Ph.D. thesis, University of Twente.
- Chen, Q., et al. (2006), Isolating individual trees in a savanna woodland using small footprint LIDAR data, *Photogramm. Eng. Rem. S.*, 72(8), 923-932.
- Chen, X., et al. (2008), Observations and Stochastic Modeling of Soil Moisture Control on Evapotranspiration in a Californian Oak Savanna, *Water Resour. Res.*, 44, W08409, doi:08410.01029/02007WR006646.
- Chen, X., et al. (In preparation), On determining wood thermal diffusivity and probe geometry using in-situ heat response curves for sap flow measurements, *Tree Physiol.*
- Chima, G. S. (1990), *Mountain Counties Water Management Studies*, Dept. of Water Resources Central District, Sacramento, CA.

Clark, L. D. (1964), Stratigraphy and structure of part of the western Sierra Nevada metamorphic belt, California, *Geological Survey Professional Paper 410*, US Gov. Print. Off., Washington, D.C.

CLFP (2007), *Manual of Good Practice for Land Application of Food Processing Rinse Water*, California League of Food Processors, Davis, CA.

Coelho, E. F., and D. Or (1998), Root distribution and water uptake patterns of corn under surface and subsurface drip irrigation, *Plant Soil*, 206(2), 123-136.

Collett, J. L., et al. (1999), Spatial and temporal variations in San Joaquin Valley fog chemistry, *Atmos. Environ.*, 33(1), 129-140.

Cramer, V. A., et al. (1999), Transpiration and groundwater uptake from farm forest plots of *Casuarina glauca* and *Eucalyptus camaldulensis* in saline areas of southeast Queensland, Australia, *Agr. Water Manage.*, 39(2-3), 187-204.

Crites, R., et al. (1974), Experience with land treatment of food processing wastewater, in *Proceedings 5th National Symposium On Food Processing Wastes, Monterey, CA*, EPA-660/2-74-058, pp. 4 - 30, USEPA.

CVRWQCB (2005), *Staff Report: Regulation of Food Processing Waste Discharges to Land*, Central Valley Regional Water Quality Control Board, Cal. Dept. Water Resources, Rancho Cordova, CA.

CVRWQCB (2006), *Staff report: Update Regarding the Regulation of Food Processing Waste Discharges to Land*, Central Valley Regional Water Quality Control Board, Cal. Dept. Water Resources, Rancho Cordova, CA.

D'Odorico, P., et al. (2004), Probabilistic modeling of nitrogen and carbon dynamics in water-limited ecosystems, *Ecol. Model.*, 179(2), 205-219.

Dagan, G. (1978), Note on Packer, Slug, and Recovery Tests in Unconfined Aquifers, *Water Resour. Res.*, 14(5), 929-934.

Daly, E., et al. (2004), Coupled dynamics of photosynthesis, transpiration, and soil water balance. Part I: Upscaling from hourly to daily level, *J. Hydrometeorol.*, 5(3), 546-558.

Daly, E., and A. Porporato (2005), A review of soil moisture dynamics: from rainfall infiltration to ecosystem response, *Environ. Eng. Sci.*, 22, 9-24.

- Danalewich, J. R., et al. (1998), Characterization of dairy waste streams, current treatment practices, and potential for biological nutrient removal, *Water Res.*, 32(12), 3555-3568.
- Davies, J. A., and C. D. Allen (1973), Equilibrium, potential and actual evaporation from cropped surfaces in Southern Ontario, *J. Appl. Meteorol.*, 12(4), 649-657.
- Dawson, T. E. (1993), Hydraulic lift and water use by plants: implications for water balance, performance and plant-plant interactions, *Oecologia*, 95(4), 565-574.
- Dawson, T. E. (1996), Determining water use by trees and forests from isotopic, energy balance and transpiration analyses: The roles of tree size and hydraulic lift, *Tree Physiol.*, 16(1-2), 263-272.
- Dawson, T. E., et al. (2002), Stable Isotopes in Plant Ecology, *Annu. Rev. Ecol. Syst.*, 33(1), 507-559.
- Decagon Devices (2005), *Application Note: Generating a Soil Moisture Characteristic Using the WP4*, in [Online], Available at http://www.decagon.com/ag_research/literature/literature.php, (Verified 18 March 2009), Pullman, WA.
- Delta T Devices (1999), *ThetaProbe Soil Moisture Sensor User Manual*, Delta T Devices, Cambridge, UK.
- Detto, M., et al. (2006), Soil moisture and vegetation controls on evapotranspiration in a heterogeneous Mediterranean ecosystem on Sardinia, Italy, *Water Resour. Res.*, 42(8), W08419.
- Dincer, A. R., and F. Kargi (2000), Kinetics of sequential nitrification and denitrification processes, *Enzyme Microb. Tech.*, 27, 37-42.
- Dingman, S. L. (2002), *Physical Hydrology*, 2nd ed., Prentice Hall, Upper Saddle River, NJ.
- Dixon, H. H., and J. Joly (1894), On the ascent of sap, *Proc. R. Soc. B*, 186, 563-576.
- Domenico, P., and F. Schwartz (1998), *Physical and Chemical Hydrogeology*, 2nd ed., John Wiley & Sons, New York.
- Donovan, L. A., et al. (1999), Predawn disequilibrium between plant and soil water potentials in two cold-desert shrubs, *Oecologia*, 120(2), 209-217.

- Dragoni, D., et al. (2009), Decoupling structural and environmental determinants of sap velocity: Part II. Observational application, *Agr. Forest Meteorol.*, 149(3-4), 570-581.
- Driscoll, F. (1986), *Groundwater and Wells*, 2nd ed., Johnson Division, St. Paul, MN.
- Duffield, W. A., and R. W. Sharp (1975), *Geology of the Sierra Foothills Melange and Adjacent Areas, Amador County, California*, U.S. Govt. Print. Off., Washington, D.C.
- Eagleson, P. S. (1978a), Climate, soil, and vegetation: 1. Introduction to water balance dynamics, *Water Resour. Res.*, 14(5), 705-712.
- Eagleson, P. S. (1978b), Climate, soil, and vegetation: 3. A simplified model of soil moisture movement in the liquid phase, *Water Resour. Res.*, 14(5), 722-730.
- Eagleson, P. S. (1978c), Climate, soil, and vegetation: 4. The expected value of annual evapotranspiration, *Water Resour. Res.*, 14(5), 731-739.
- Eagleson, P. S. (1982), Ecological optimality in water-limited natural soil-vegetation systems: 1. Theory and hypothesis, *Water Resour. Res.*, 18(2), 325-340.
- Eagleson, P. S. (2002), *Ecohydrology: Darwinian Expression of Vegetation Form and Function*, Cambridge University Press, Cambridge, UK.
- Eamus, D., et al. (2006a), A functional methodology for determining the groundwater regime needed to maintain the health of groundwater-dependent vegetation, *Aust. J. Botany*, 54(2), 97-114.
- Eamus, D., et al. (2006b), *Ecohydrology: Vegetation Function, Water and Resource Management*, CSIRO Publishing, Collingwood, Australia.
- Eastham, J., et al. (1999), The influence of early sowing of wheat and lupin crops on evapotranspiration and evaporation from the soil surface in a Mediterranean climate, *Agr. Water Manage.*, 42(2), 205-218.
- Ehleringer, J., and C. B. Osmond (1989), Stable isotopes, in *Plant Physiological Ecology: Field Methods and Instrumentation*, edited by R. W. Pearcy, et al., Chapman & Hall, London.
- Feddes, R. A., et al. (2001), Modeling Root Water Uptake in Hydrological and Climate Models, *B. Am. Meteorol. Soc.*, 82(12), 2797-2809.
- Fernandez-Illescas, C. P., et al. (2001), The ecohydrological role of soil texture in a water-limited ecosystem, *Water Resour. Res.*, 37(12), 2863-2872.

- Fetter, C. W. (2001), *Applied Hydrogeology*, 4th ed., Prentice Hall, Englewood Cliffs, NJ.
- Fisher, J. B. (2006), *I. The Land-atmosphere Water Flux Across Plant, Ecosystem, Global and Social Scales, II. GIS and Spatial Analysis for Environmental Justice and Wildlife*, Ph.D. thesis, Environmental Science, Policy and Management, University of California, Berkeley.
- Fisher, J. B., et al. (2007), What the towers don't see at night: nocturnal sap flow in trees and shrubs at two AmeriFlux sites in California, *Tree Physiol.*, 27(597-610).
- Ford, C., et al. (2007), A comparison of sap flux-based evapotranspiration estimates with catchment-scale water balance, *Agr. Forest Meteorol.*, 145, 176-185.
- Freeze, R. A., and J. A. Cherry (1979), *Groundwater*, Prentice-Hall, Englewood Cliffs, NJ.
- Gedney, N., and P. M. Cox (2003), The sensitivity of global climate model simulations to the representation of soil moisture heterogeneity, *J. Hydrometeorol.*, 4(6), 1265-1275.
- Gedney, N., et al. (2006), Detection of a direct carbon dioxide effect in continental river runoff records, *Nature*, 439(7078), 835-838.
- Goldberg, S., et al. (2005), Prediction of boron adsorption by field samples of diverse textures, *Soil Sci. Soc. Am. J.*, 69(5), 1379-1388.
- Goyal, S. S., and R. C. Huffaker (1986), Uptake of NO₃⁻, NO₂⁻, and NH₄⁺ by intact wheat (*Triticum aestivum*) seedlings : I. Induction and kinetics of transport systems, *Plant Physiol.*, 82(4), 1051-1056.
- Granier, A. B., P.; Köstner, B.; Gay, L. W.; Najjar, G. (1996), Comparisons of xylem sap flow and water vapour flux at the stand level and derivation of canopy conductance for Scots pine, *Theoretical and Applied Climatology*, 53(1-3), 115-122.
- Gregory, P. J., et al. (1978), Water relations of winter wheat: 1. Growth of the root system, *J. Agric. Sci.*, 91, 91-102.
- Greskowiak, J., et al. (2005), The impact of variably saturated conditions on hydrogeochemical changes during artificial recharge of groundwater, *Appl. Geochem.*, 20(7), 1409-1426.

- Hatton, T. J., et al. (1995), Estimating stand transpiration in a Eucalyptus populnea woodland with the heat pulse method: measurement errors and sampling strategies, *Tree Physiol.*, 15(4), 219-227.
- Hibbard, K. A., et al. (2005), An analysis of soil respiration across northern hemisphere temperate ecosystems, *Biogeochemistry*, 73(1), 29-70.
- Hill, M., and C. Tiedeman (2007), *Effective Groundwater Model Calibration with Analysis of Data, Sensitivities, Predictions, and Uncertainty*, John Wiley & Sons, Hoboken, NJ.
- Hillel, D. (1998), *Environmental Soil Physics*, Academic Press, San Diego, CA.
- Hillel, D. (2000), *Salinity Management for Sustainable Irrigation: Integrating Science, Environment, and Economics*, World Bank, Washington, DC.
- Holloway, J. M., and R. A. Dahlgren (1999), Geologic nitrogen in terrestrial biogeochemical cycling, *Geology*, 27(6), 567-570.
- Hsieh, C.-I., et al. (2000), An approximate analytical model for footprint estimation of scalar fluxes in thermally stratified atmospheric flows, *Adv. Water Resour.*, 23(7), 765-772.
- Hunter, K. S., et al. (1998), Kinetic modeling of microbially-driven redox chemistry of subsurface environments: Coupling transport, microbial metabolism and geochemistry, *J. Hydrol.*, 209(1-4), 53-80.
- Huntington, T. G. (2006), Evidence for intensification of the global water cycle: Review and synthesis, *J. Hydrol.*, 319(1-4), 83-95.
- Irvine, J., et al. (2004), Age-related changes in ecosystem structure and function and effects on water and carbon exchange in ponderosa pine, *Tree Physiol.*, 24(7), 753-763.
- Jackson, R. B., et al. (1996), A global analysis of root distributions for terrestrial biomes, *Oecologia*, 108(3), 389-411.
- James, A. L., and C. M. Oldenburg (1997), Linear and Monte Carlo uncertainty analysis for subsurface contaminant transport simulation, *Water Resour. Res.*, 33(11), 2495.
- Jara, J., et al. (1998), Measurement of evapotranspiration and its components in a corn (*Zea Mays L.*) field, *Agr. Forest Meteorol.*, 92(2), 131-145.

- Jewett, D. G., et al. (2004), Geomorphic and hydrologic controls on surface and subsurface flow regimes in riparian meadow ecosystems, in *Great Basin Riparian Ecosystems: Ecology, Management, and Restoration*, edited by J. Chambers and J. Miller, Island Press, Washington, D.C.
- Johns, M. M., and J. W. Bauder (2007), Root zone leachate from high chemical oxygen demand cannery water irrigation, *Soil Sci. Soc. Am. J.*, 71(6), 1893-1901.
- Kang, S., et al. (2003), Crop coefficient and ratio of transpiration to evapotranspiration of winter wheat and maize in a semi-humid region, *Agr. Water Manage.*, 59(3), 239-254.
- Kaufman, L., and P. Rousseeuw (1990), *Finding Groups in Data: An Introduction to Cluster Analysis*, Wiley-Interscience, New York.
- Kiang, N. Y.-I. (2002), *Savannas and Seasonal Drought: The Landscape-leaf Connection Through Optimal Stomatal Control*, Ph.D. thesis, University of California, Berkeley.
- Kim, J., et al. (2006), Upscaling Fluxes from Tower to Landscape: Overlaying Flux Footprints on High Resolution (IKONOS) Images of Vegetation Cover, *Agr. Forest Meteorol.*, 136, 132-146.
- Klute, A. (1986), Water retention: Laboratory methods, in *Methods of Soil Analysis: Part 1. Physical and Mineralogical Methods, ASA Monograph Number 9*, edited by A. Klute, pp. 635-662, Am. Soc. Agron., Madison, WI.
- Knapp, A. K., et al. (2002), Rainfall variability, carbon cycling, and plant species diversity in a mesic grassland, *Science*, 298(5601), 2202-2205.
- Kueppers, L. M., et al. (2005), Modeled regional climate change and California endemic oak ranges, *P. Natl. Acad. Sci. USA*, 102(45), 16281-16286.
- Kumagai, T., et al. (2004), Water cycling in a Bornean tropical rain forest under current and projected precipitation scenarios, *Water Resour. Res.*, 40(1), W01104, doi:01110.01029/02003WR002226.
- Kumagai, T. o., et al. (2005), Sources of error in estimating stand transpiration using allometric relationships between stem diameter and sapwood area for *Cryptomeria japonica* and *Chamaecyparis obtusa*, *Forest Ecol. Manage.*, 206(1-3), 191-195.

- Laio, F., et al. (2001), Plants in water-controlled ecosystems: active role in hydrologic processes and response to water stress - II. Probabilistic soil moisture dynamics, *Adv. Water Resour.*, 24(7), 707-723.
- Laio, F., et al. (2002), On the seasonal dynamics of mean soil moisture, *J Geophys Res-Atmos*, 107(D15), 4272, doi:10.1029/2001JD001252.
- Lamontagne, S., et al. (2005), Groundwater use by vegetation in a tropical savanna riparian zone (Daly River, Australia), *J. Hydrol.*, 310(1-4), 280-293.
- Langergraber, G., and J. Simunek (2005), Modeling variably saturated water flow and multicomponent reactive transport in constructed wetlands, *Vadose Zone J.*, 4(4), 924-938.
- Lautz, L. K. (2008), Estimating groundwater evapotranspiration rates using diurnal water-table fluctuations in a semi-arid riparian zone, *Hydrogeol. J.*, 16(3), 483-497.
- Lewis, D. C., and R. H. Burgy (1964), Relationship between oak tree roots + groundwater in fractured rock as determined by tritium tracing, *J Geophys. Res.*, 69(12), 2579-2588.
- Lide, D. R. (Ed.) (2007), *CRC Handbook of Chemistry and Physics*, 88th ed., CRC Press/Taylor and Francis, Boca Raton, FL.
- Loheide, S. P., et al. (2005), Estimation of groundwater consumption by phreatophytes using diurnal water table fluctuations: a saturated-unsaturated flow assessment, *Water Resour. Res.*, 41(7), W07030.
- Loheide, S. P. (2008), A method for estimating subdaily evapotranspiration of shallow groundwater using diurnal water table fluctuations, *Ecohydrol.*, 1(1), 59-66.
- Loranty, M. M., et al. (2008), Environmental drivers of spatial variation in whole-tree transpiration in an aspen-dominated upland-to-wetland forest gradient, *Water Resour. Res.*, 44, W02441, doi:02410.01029/02007WR006272.
- Maas, E. V., and G. J. Hoffman (1977), Crop salt tolerance - current assessment, *J. Irrig. Drain. Div.*, 103, 115-134.
- MacQuarrie, K. T. B., and E. A. Sudicky (2001), Multicomponent simulation of wastewater-derived nitrogen and carbon in shallow unconfined aquifers: I. Model formulation and performance *J. Contam. Hydrol.*, 47(1), 53-84.

- MacQuarrie, K. T. B., et al. (2001), Numerical simulation of a fine-grained denitrification layer for removing septic system nitrate from shallow groundwater, *J. Contam. Hydrol.*, 52(1-4), 29-55.
- Maechler, M., et al. (2006), *The cluster Package, R Package Version 1.10.5*.
- Mailloux, M., et al. (2002), Evaluation of a carbon-source stimulated bioremediation technology for the remediation of nitrate-contaminated aquifer at an airport site, in *55th Canadian Geotechnical and 3rd Joint IAHR-CNC and CGS Groundwater Specialty Conferences* edited by D. Stolle, et al., Southern Ontario Section of the Canadian Geotechnical Society, Niagara Falls, Ontario.
- Mambelli, S. (2008), Unpublished Tonzi Ranch Oxygen Isotope Data, University of California, Berkeley.
- Marshack, J. B. (2003), *A Compilation of Water Quality Goals*, Cal. EPA - Central Valley Regional Water Quality Control Board, Rancho Cordova, CA.
- Marshall, D. C. (1958), Measurement of sap flow in conifers by heat transport, *Plant Physiol.*, 33(6).
- Martínez-Vilalta, J., et al. (2003), Sap flow of three co-occurring Mediterranean woody species under varying atmospheric and soil water conditions, *Tree Physiol.*, 23, 747-758.
- Massman, W. J., and X. Lee (2002), Eddy covariance flux corrections and uncertainties in long-term studies of carbon and energy exchanges, *Agr. Forest Meteorol.*, 113(1-4), 121-144.
- Mayer, K. U., et al. (2001), Reactive transport modeling of processes controlling the distribution and natural attenuation of phenolic compounds in a deep sandstone aquifer, *J. Contam. Hydrol.*, 53(3-4), 341-368.
- Mayer, K. U., et al. (2002), Multicomponent reactive transport modeling in variably saturated porous media using a generalized formulation for kinetically controlled reactions, *Water Resour. Res.*, 38(9), 1174-1195.
- McElrone, A. J., et al. (2003), The contribution of deep roots to the water cycle: Seasonal patterns of water uptake and hydraulic lift from below 7 m on the Edwards Plateau, Texas, *Eos Trans. AGU, Fall Meet. Suppl.*, 84(46), Abstract H32C-0581.
- Mcnaughton, K. G., and P. G. Jarvis (1984), Using the Penman-Monteith equation predictively, *Agr. Water Manage.*, 8(1-3), 263-278.

- Meinzer, F. C., et al. (2001), Regulation of water flux through tropical forest canopy trees: Do universal rules apply?, *Tree Physiol.*, 21, 19-26.
- Meinzer, F. C., et al. (2004), Converging patterns of uptake and hydraulic redistribution of soil water in contrasting woody vegetation types, *Tree Physiol.*, 24(8), 919-928.
- Metcalf & Eddy, et al. (Eds.) (1991), *Wastewater Engineering: Treatment, Disposal, and Reuse*, 3rd ed., Irwin McGraw-Hill, Boston, MA.
- Miller, G. R., et al. (2007), An analysis of soil moisture dynamics using multi-year data from a network of micrometeorological observation sites, *Adv. Water Resour.*, 30(5), 1065-1081.
- Miller, J. D., and G. J. Gaskin (1999), *ThetaProbe ML2x Principles of Operation and Applications*, 2nd ed., Macaulay Land Use Research Institute, [Online], Available at <http://www.delta-t.co.uk/products.html?product2005092818876>, (Verified 25 March 2009), Aberdeen, UK.
- Mitchell, J. F. B., and T. C. Johns (1997), On modification of global warming by sulfate aerosols, *J. Climate*, 10(2), 245-267.
- Monteith, J. L. (1965), Evaporation and environment: the state and movement of water in living organisms, in *Symposium of the Society of Experimental Biology*, pp. 205-234.
- Mualem, Y. (1976), A new model for predicting the hydraulic conductivity of unsaturated porous media, *Water Resour. Res.*, 12(3), 513-522.
- Naumburg, E., et al. (2005), Phreatophytic vegetation and groundwater fluctuations: A review of current research and application of ecosystem response modeling with an emphasis on Great Basin vegetation, *Environ. Manage.*, 35(6), 726-740.
- Nazaroff, W., and L. Alvarez-Cohen (2001), *Environmental Engineering Science*, John Wiley & Sons, New York, NY.
- NOAA Western Regional Climate Center (2006), *Modesto, California Monthly Total Precipitation*, Reno, NV, [Online], Available at: <http://www.wrcc.dri.edu/cgi-bin/cliMONtpre.pl?camode>.
- Nolin, A., and C. Daly (2006), Mapping “at-risk” snow in the Pacific Northwest, USA, *J Hydrometeorol.*, 7, 1164-1171.
- Noy-Meir, I. (1973), Desert Ecosystems: Environment and Producers, *Annual Reviews in Ecological Systems* 4, 25-41.

- O'Grady, A. P., et al. (2006), Groundwater use by dominant tree species in tropical remnant vegetation communities, *Aust. J. Bot.*, 54(2), 155-171.
- Oishi, A. C., et al. (2008), Estimating components of forest evapotranspiration: A footprint approach for scaling sap flux measurements, *Agr. Forest Meteorol.*, *In Press*, *Corrected Proof*.
- Onof, C., et al. (2000), Rainfall modelling using Poisson-cluster processes: a review of developments, *Stoch. Env. Res. Risk A*, 14(6), 384-411.
- Panshin, A. J., and C. De Zeeuw (1980), *Textbook of Wood Technology: Structure, Identification, Properties, and Uses of the Commercial Woods of the United States and Canada*, 4th ed., McGraw-Hill, New York.
- Parson, E. A., et al. (2001), Potential consequences of climate variability and change for the Pacific Northwest, in *Climate Change Impacts on the United States: A Report of the National Assessment Synthesis Team.*, Cambridge University Press, Cambridge, UK.
- Pielke, R. A. (2001), Influence of the spatial distribution of vegetation and soils on the prediction of cumulus convective rainfall, *Rev. Geophys.*, 39(2), 151-177.
- Porporato, A., et al. (2004), Soil water balance and ecosystem response to climate change, *Am. Nat.*, 164(5), 625-632.
- Porter-Cologne Act (2006), Porter-Cologne Water Quality Control Act, in *California Water Code, Division 7*, Cal. State Water Resources Control Board.
- Priestly, C., and R. Taylor (1972), On the assessment of surface heat flux and evaporation using large-scale parameters, *Mon. Weather Review*, 1000, 81-92.
- R Development Core Team (2006), *R: A Language and Environment for Statistical Computing*, R Foundation for Statistical Computing, [Online], Available at: <http://www.r-project.org/>.
- Rengel, Z., and M. S. Wheal (1997), Kinetic parameters of Zn uptake by wheat are affected by the herbicide chlorsulfuron, *J. Exp. Bot.*, 48(4), 935-941.
- Ripley, B. (1981), *Spatial Statistics*, John Wiley and Sons, Hoboken, NJ.
- Rodriguez-Iturbe, I., et al. (1999), Probabilistic modelling of water balance at a point: the role of climate, soil and vegetation, *Proc. R. Soc. Lond. A*, 455(1990), 3789-3805.

- Rodríguez-Iturbe, I., and A. Porporato (2004), *Ecohydrology of Water-controlled Ecosystems: Soil Moisture and Plant Dynamics*, Cambridge University Press, Cambridge, UK.
- Rodríguez-Iturbe, I., et al. (2007), Challenges in humid land ecohydrology: Interactions of water table and unsaturated zone with climate, soil, and vegetation, *Water Resour. Res.*, *43*, W09301, doi:09310.01029/02007WR006073.
- Rodríguez-Iturbe, I., et al. (2008), Stochastic water table dynamics in groundwater-dependent ecosystems, *Geophys. Res. Abstr.*, *10*, EGU2008-A-11747.
- Roose, T., et al. (2001), A mathematical model of plant nutrient uptake, *J. Math. Biol.*, *42*(4), 347-360.
- Rubin, Y. (2003), *Applied Stochastic Hydrogeology*, Oxford University Press, Oxford, UK.
- Sargent, C. S. (1885), *The Woods of the United States*, D. Appleton and Company, New York.
- Savant, N., et al. (1987), Effect of amounts and sequence of additions of urea and water on hydrolysis of surface-applied granular urea in unsaturated soils, *Nutr. Cyc. Agroecosys.*, *11*(3), 231-243.
- Schaap, M. G., et al. (2001), ROSETTA: a computer program for estimating soil hydraulic parameters with hierarchical pedotransfer functions, *J. Hydrol.*, *251*(3-4), 163-176.
- Schoups, G., et al. (2005), Sustainability of irrigated agriculture in the San Joaquin Valley, California, *J. Hydrol.*, *102*(43), 15352-15356.
- Schoups, G., et al. (2006), Evaluation of model complexity and space-time resolution on the prediction of long-term soil salinity dynamics, western San Joaquin Valley, California, *Hydrol. Process.*, *20*(13), 2647-2668.
- Schwarz, P. A., et al. (2004), Climatic versus biotic constraints on carbon and water fluxes in seasonally drought-affected ponderosa pine ecosystems, *Global Biogeochem. Cy.*, *18*(4), GB4007, DOI 4010.1029/2004GB002234.
- Scott, R. L., et al. (2004), Interannual and seasonal variation in fluxes of water and carbon dioxide from a riparian woodland ecosystem, *Agr. Forest Meteorol.*, *122*(1-2), 65-84.

Scott, R. L., et al. (2008a), The ecohydrologic significance of hydraulic redistribution in a semiarid savanna, *Water Resour. Res.*, 44, W02440, doi:02410.01029/02007WR006149.

Scott, R. L., et al. (2008b), Multiyear riparian evapotranspiration and groundwater use for a semiarid watershed, *J. Arid. Environ.*, 72(7), 1232-1246.

Seward, P., et al. (1990), Modeling potassium uptake by wheat (*Triticum-Aestivum*) crops, *Plant Soil*, 124(2), 303-307.

Shelton, L. R., and L. K. Miller (1991), Water-quality data, San Joaquin Valley, California, April 1987 to September 1988, *Open File Report 91-74*, USGS, Denver, CO.

Shuttleworth, W. J., and I. R. Calder (1979), Has the Priestley-Taylor equation any relevance to forest evaporation?, *J. Appl. Meteorol.*, 18(5), 639-646.

Singhal, B. B. S., and R. P. Gupta (1999), *Applied Hydrogeology of Fractured Rocks*, Kluwer Academic Pub., Dordrecht, The Netherlands.

Sketchley, H. R. (1965), *Soil Survey, Amador Area, California*, U.S. Dept. of Agriculture Soil Conservation Service, Washington, D.C.

Snyder, K. A., and D. G. Williams (2000), Water sources used by riparian trees varies among stream types on the San Pedro River, Arizona, *Agr. Forest Meteorol.*, 105(1-3), 227-240.

Spiessl, S. M., et al. (2007), Identification of key parameters controlling dissolved oxygen migration and attenuation in fractured crystalline rocks, *J. Contam. Hydrol.*, doi:10.1016/j.jconhyd.2007.09.002.

Stannard, D. I. (1993), Comparison of Penman-Monteith, Shuttleworth-Wallace and Modified Priestly evapotranspiration models for wildland vegetation in semiarid rangeland, *Water Resour. Res.*, 29(5), 1379-1392.

Strand, R. G., and J. B. Koenig (1965), *Geologic Map of California, Sacramento Sheet, Scale 1:250000*, California Division of Mines and Geology, Sacramento, CA.

Sunding, D., and D. Zilberman (2005), *A Guide to Consideration of Economics Under the California Porter-Cologne Act.*, California Resource Management Institute, Sacramento, CA.

Taliaferro, N. L. (1943), Manganese deposits of the Sierra Nevada, their genesis and metamorphism, in *Manganese in California, California Division of Mines Bulletin 125*,

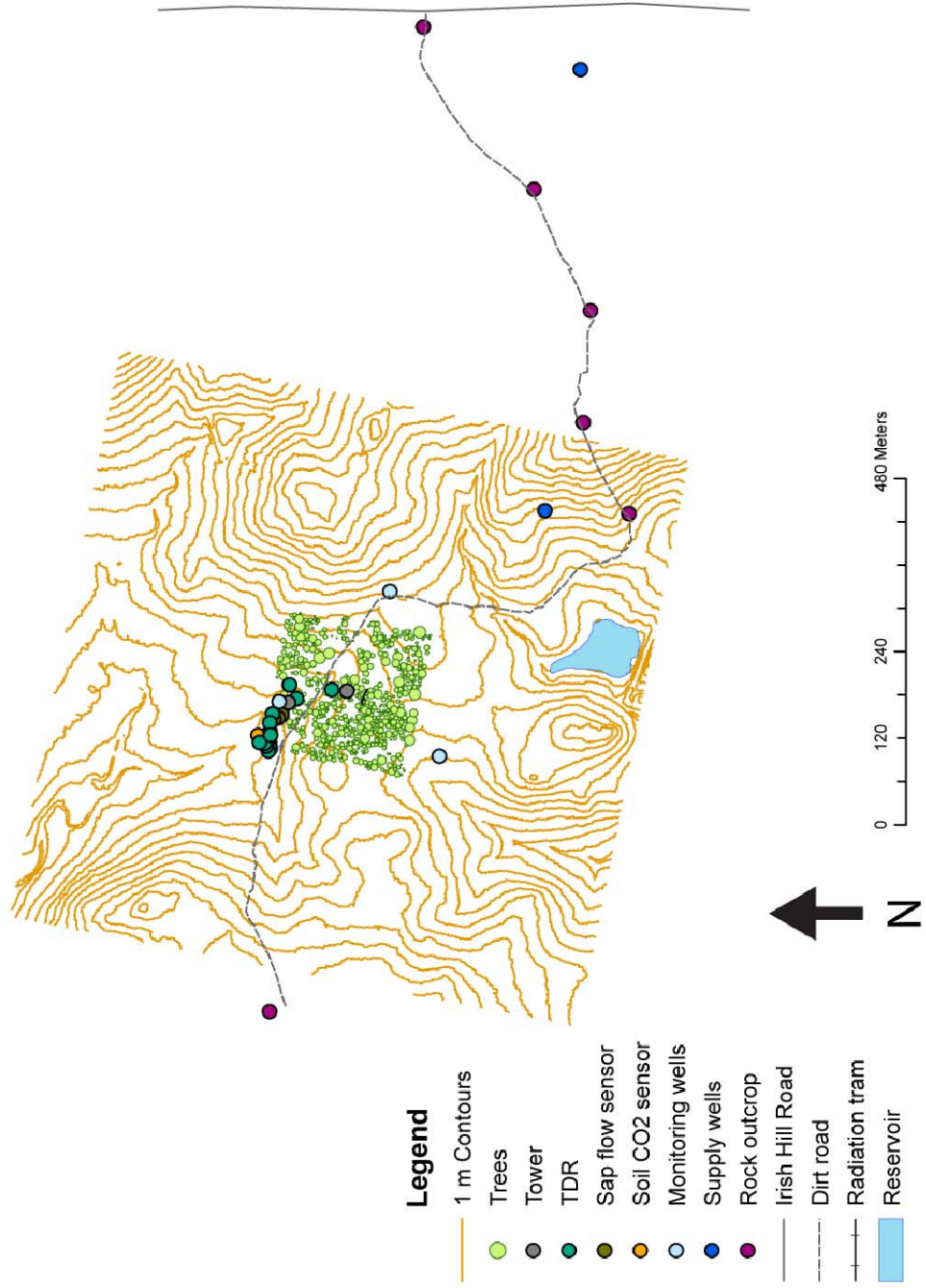
- edited by O. P. Jenkins, pp. 277-332, California Department of Natural Resources, San Francisco, CA.
- Tang, J. W., and D. D. Baldocchi (2005), Spatial-temporal variation in soil respiration in an oak-grass savanna ecosystem in California and its partitioning into autotrophic and heterotrophic components, *Biogeochemistry*, 73(1), 183-207.
- Tinker, P. B., and P. H. Nye (2000), *Solute Movement in the Rhizosphere*, Oxford University Press, New York.
- Turner, H. W. (1894), *Geologic Atlas of the United States, Folio 11: Jackson, California*, U.S. Geological Survey.
- Tyree, M. T. (1997), The Cohesion-Tension theory of sap ascent: current controversies, *J. Exp. Bot.*, 48(10), 1753-1765.
- USDA (2006), National Cooperative Soil Survey: Web Soil Survey, [Online], Available at: <http://websoilsurvey.nrcs.usda.gov/app/HomePage.htm>.
- USEPA (1977), Pollution abatement in the fruit and vegetable industry: wastewater treatment, *EPA-625/3-77-007C*, USEPA, Washington, DC.
- USEPA (1992), Secondary drinking water regulations: guidance for nuisance chemicals, *EPA810/K-92-001*, U.S. Environmental Protection Agency-Office of Groundwater and Drinking Water, Washington, DC.
- USEPA (2003), List of contaminants & their maximum contaminant levels (MCLs), *EPA 816-F-03-016*, U.S. Environmental Protection Agency - Office of Groundwater and Drinking Water, Washington, DC.
- Vertessy, R. A., et al. (1997), Estimating stand water use of large mountain ash trees and validation of the sap flow measurement technique, *Tree Physiol.*, 17, 747-756.
- Vincke, C., and Y. Thiry (2008), Water table is a relevant source for water uptake by a Scots pine (*Pinus sylvestris* L.) stand: evidences from continuous evapotranspiration and water table monitoring, *Agr. Forest Meteorol.*, 148(10), 1419-1432.
- Vrugt, J. A., and S. P. Neuman (2006), Introduction to the special section in Vadose Zone Journal: parameter identification and uncertainty assessment in the unsaturated zone, *Vadose Zone J.*, 5(3), 915-916.
- Wang, H., et al. (2001), Improving water use efficiency of irrigated crops in the North China Plain -- measurements and modelling, *Agr. Water Manage.*, 48(2), 151-167.

- Warren, J. M., et al. (2006), Hydraulic redistribution of soil water in two old-growth coniferous forests: quantifying patterns and controls, *New Phytologist*, 173, 753-765.
- West, A. G., et al. (2006), Water extraction times for plant and soil materials used in stable isotope analysis, *Rapid Commun. Mass Spectrom.*, 20(8), 1317-1321.
- West, G. B., et al. (1999), A general model for the structure and allometry of plant vascular systems, *Nature*, 400(6745), 664-667.
- White, W. N. (1932), A method of estimating ground-water supplies based on discharge by plants and evaporation from soil - results of investigations in Escalante Valley, Utah, *Water Supply Paper Report Number 659-A*, US Geological Survey.
- Williams, C. A., and J. D. Albertson (2004), Soil moisture controls on canopy-scale water and carbon fluxes in an African savanna, *Water Resour. Res.*, 40(9), W09302, doi:10.1029/2004WR003208.
- Wilson, K., et al. (2002), Energy balance closure at FLUXNET sites, *Agr. Forest Meteorol.*, 113(1-4), 223-243.
- Wilson, K. B., and D. D. Baldocchi (2000), Seasonal and interannual variability of energy fluxes over a broadleaved temperate deciduous forest in North America, *Agr. Forest Meteorol.*, 100(1), 1-18.
- Wilson, K. B., et al. (2001), A comparison of methods for determining forest evapotranspiration and its components: sap-flow, soil water budget, eddy covariance and catchment water balance, *Agr. Forest Meteorol.*, 106(2), 153-168.
- Wilson, P. L., et al. (1987), Fuelwood characteristics of northwestern conifers and hardwoods, *Research Bulletin No. 60*, Forestry Research Lab, Oregon State University, Corvallis, OR.
- Wosten, J. H. M., and M. T. Van Genuchten (1988), Using texture and other soil properties to predict the unsaturated soil hydraulic functions, *Soil Sci. Soc. Am. J.*, 52(6), 1762-1770.
- Wullschleger, S. D., et al. (2001), Transpiration from a multi-species deciduous forest as estimated by xylem sap flow techniques, *Forest Ecol. Manag.*, 143(1-3), 205-213.
- Xu, L. K., et al. (2004), How soil moisture, rain pulses, and growth alter the response of ecosystem respiration to temperature, *Global Biogeochem. Cy.*, 18(4).

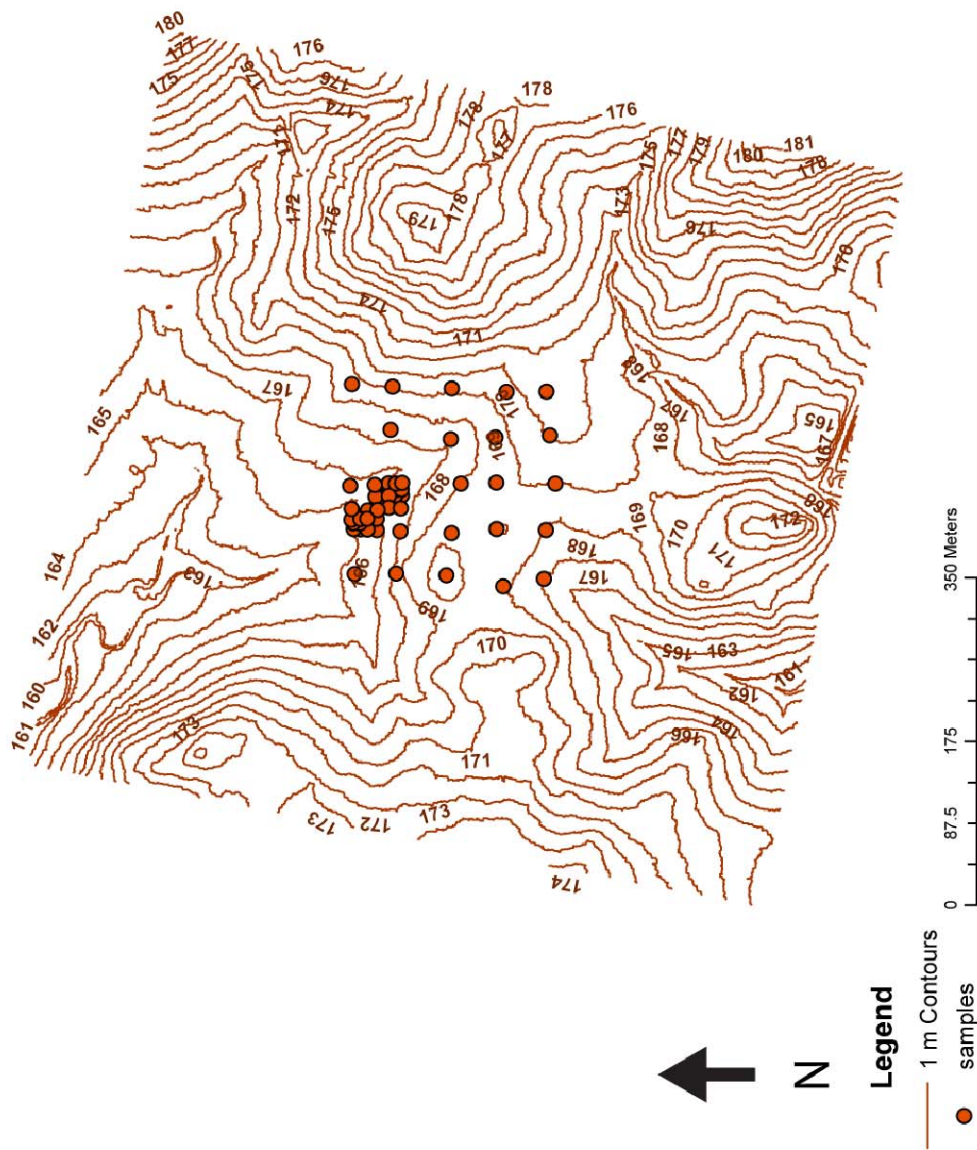
Xu, Z., and G. Nakhla (2006), Pilot-scale demonstration of pre-fermentation for enhancement of food-processing wastewater biodegradability, *J. Chem. Technol. Biotechnol.*, 81(4), 580-587.

Appendix A: Tonzi Ranch Maps

Tonzi Ranch Master Map



Tonzi Ranch Contour Plot



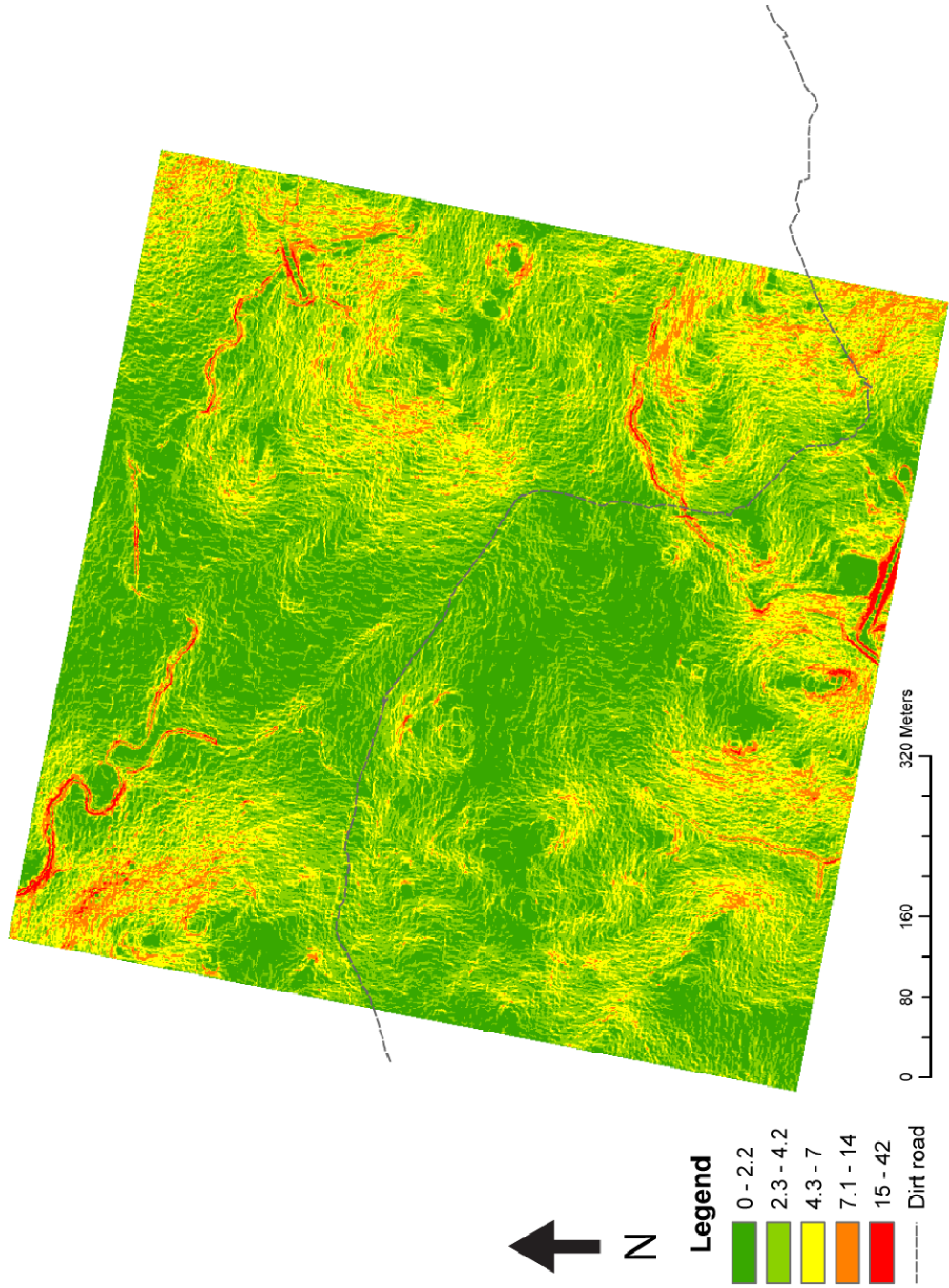
Legend

1 m Contours

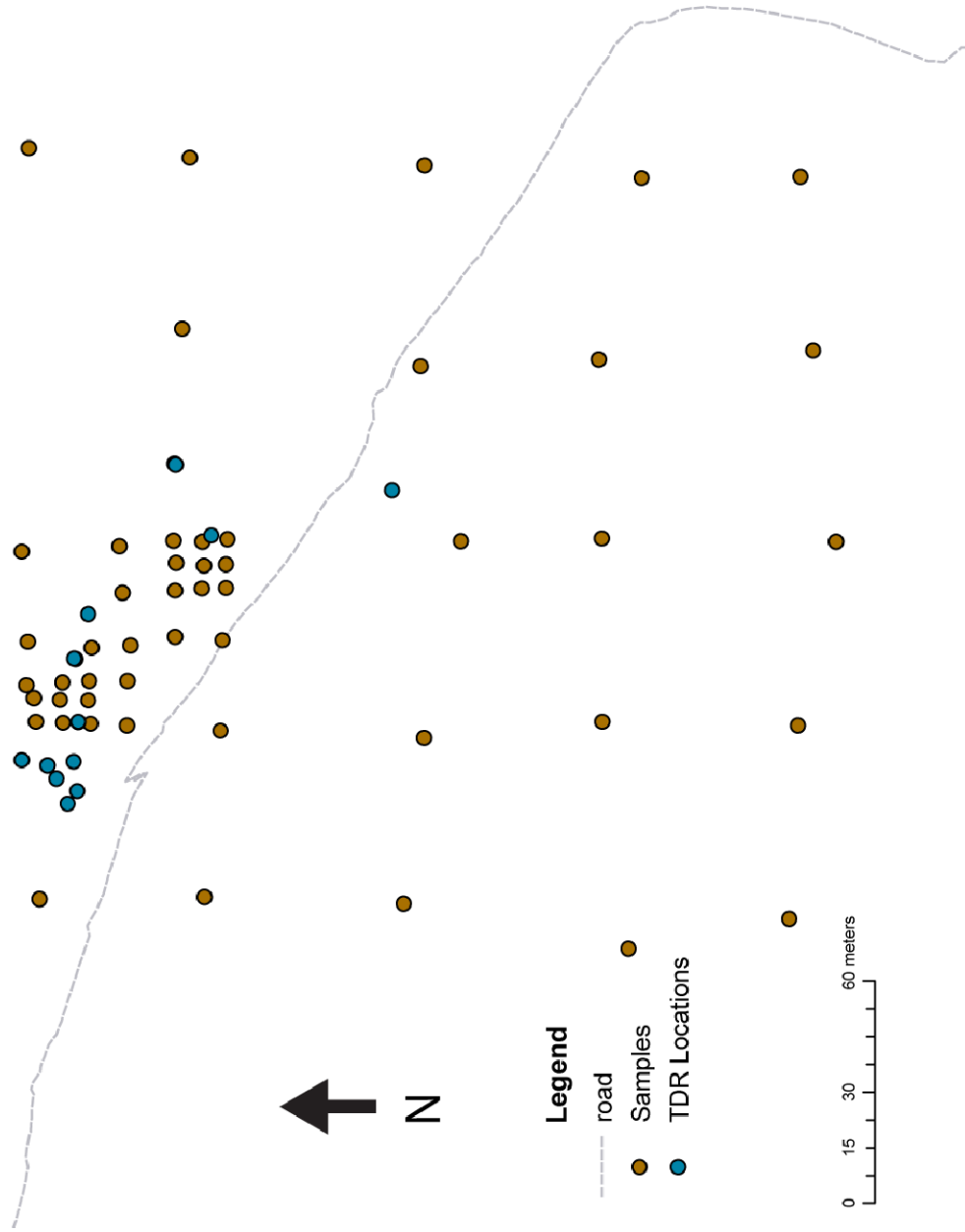
samples

0 87.5 175 350 Meters

Tonzi Ranch Slope



Tonzi Ranch Soil Measurements



Tonzi Ranch Trees and Instruments

